



Modélisation 0D - 1D de la chaîne d'air des moteurs à combustion interne dédiée au contrôle

Guillaume Martin

► To cite this version:

Guillaume Martin. Modélisation 0D - 1D de la chaîne d'air des moteurs à combustion interne dédiée au contrôle. Autre. Université d'Orléans, 2010. Français. NNT : 2010ORLE2065 . tel-00623122

HAL Id: tel-00623122

<https://theses.hal.science/tel-00623122>

Submitted on 13 Sep 2011

HAL is a multi-disciplinary open access archive for the deposit and dissemination of scientific research documents, whether they are published or not. The documents may come from teaching and research institutions in France or abroad, or from public or private research centers.

L'archive ouverte pluridisciplinaire **HAL**, est destinée au dépôt et à la diffusion de documents scientifiques de niveau recherche, publiés ou non, émanant des établissements d'enseignement et de recherche français ou étrangers, des laboratoires publics ou privés.

ÉCOLE DOCTORALE SCIENCES ET TECHNOLOGIES

LABORATOIRE PRISME

THÈSE présentée par :
Guillaume MARTIN

soutenue le : **15 Décembre 2010**

pour obtenir le grade de : **Docteur de l'Université d'Orléans**
Discipline : **Énergétique**

**Modélisation 0D - 1D de la Chaîne d'Air des MCI
dédiée au Contrôle**

-

**0D - 1D Modeling of the Airpath of IC Engines
for Control Purposes**

THÈSE dirigée par :
Pascal HIGELIN

Professeur, Université d'Orléans - PRISME

RAPPORTEURS :

Angelo ONORATI
Jan MACEK

Professeur, Politecnico di Milano, Energy Department
Professeur, Czech Technical University – Dept. of Automotive
and Aerospace Engineering

JURY:

Georges DESCOMBES Professeur, CNAM - Président du jury
David CHALET Maître de Conférences, Centrale Nantes, LMF-EMCI
Alain CHARLET Maître de Conférences, Université d'Orléans, PRISME
Vincent TALON Docteur, Renault SAS

Acknowledgments

This thesis was carried out within the advanced electronics research department at Renault SAS, in partnership with the Institut PRISME (Orléans University, France). The work has been financed via a CIFRE convention.

I thank M. Vincent Talon who defined the subject and provided me with technical inspiration during the last three years. I also want to thank M. Pascal Higelin, the advisor of this thesis, for the way he trusted on me and his guidance throughout the present research work. I would also like to express my thanks to M. Alain Charlet, who invested a great amount of his time for the support during the algorithms and test benches development.

I would like to express my thanks and gratitude to M. Angelo Onorati and M. Jan Macek for having agreed to review this thesis report, and to M. Georges Descombes and M. David Chalet for being members of the thesis committee.

In Guyancourt, I want to express my gratitude to MM. Luc Bourgeois, Hubert Béchard, Christian Taffin and Patrick Bastard for their trust and for the autonomy they allowed me for my research work. A wink to the Phd students 'coffee' team : David, Maria, Felipe, Maxime and last but not least Nicolas.

In Orléans, I would like to thank the test bench technical team, particularly Nicolas, Benoît, Bruno and Julien for their help during the development of the steady flow benches. I also want to thank M. Pascal Bréjaud for the many 'boundary condition' exchanges we had during the redaction of our paper.

In Nantes, I thank the Internal Combustion Engine team directed by M. Pascal Chessé for their help and the measurements performed on the turbocharger test bench.

Finally, I would like to thank my friends and relatives who experienced the side-effects of Phd life during the last three years : Daphné (rockin' it since 2003), my parents and sister, and my good ol' time friends : Vincent and Bb, Pebs, Pierre-Yves, Jb, Maxime and Seb.

*Il est vrai qu'en fait de systèmes
il faut toujours se réserver le droit de rire le lendemain de ses idées de la veille.*

*It's true that when it comes to systems
you must always reserve the right to laugh tomorrow at the ideas you had the night before.*

Voltaire - L'A.B.C. - 1768

Table of Contents

Table of Figures	xi
------------------	----

I Context and Stakes of the Study

1 Context of the study : control laws development of the Internal Combustion Engine (ICE)	3
1.1 Compliance to pollutant emissions limitations vs. production cost	3
1.2 Engine performance vs. fuel consumption	5
1.3 Reduction of the development time vs. R&D expenses	7
1.4 Impact on the engine control and its associated engine models	8
1.5 Role of the airpath regarding the control of modern engines	10
2 Goals and structure of the study	11
3 Key components and systems for the control of automotive engine airflow	13
3.1 Exhaust Gas Recirculation (EGR) loop	13
3.2 Superchargers	14
3.3 Poppet valves	17
3.4 Engine Control Unit (ECU)	18

II Gas exchange processes through turbochargers

4 Literature review	21
4.1 Extrapolation and interpolation of experimental turbocharger data maps	21
4.2 Building of turbocharger data maps based on turbomachinery equations	25
4.2.1 Turbomachine thermodynamical performance	25
4.2.2 Turbomachine fully-physical-based calculation	26
4.3 Thermal transfers within turbochargers	27
4.4 Gas exchange processes through turbochargers : proposed thesis developments	34
5 Experimental apparatus	35
5.1 Design of the test bench	35
5.2 Sensors	35
5.3 Visualization and post-treatment	37
5.4 Uncertainties	38
5.5 Tests	39

Table of Contents

6 Physics-based extrapolation of turbochargers data maps	41
6.1 Turbomachinery characteristic curves	41
6.1.1 Compressor characteristic curves	41
6.1.2 Turbine characteristic curves	43
6.2 Transposition of the characteristic curves to the turbocharger data maps	43
6.3 Development of a physical-based turbocharger data map-fitting method	46
6.3.1 Compressor model	47
6.3.2 Turbine model	50
6.4 Results and validation of the developed models	52
6.4.1 Application and results of the developed method on experimental data from suppliers	52
6.4.2 Validation of the extrapolation process with respect to turbocharger test bench data	57
7 Turbocharger thermal exchanges	59
7.1 Thermal exchanges calculation from measurements	59
7.1.4 Bearing friction model	62
7.2 Measurement results	66
7.2.1 Compressor data maps	66
7.2.2 Turbine data maps	67
7.2.3 Extrapolation of the compressor adiabatical data map	69
7.2.4 Study of the parameters influencing the heat transfers	71
7.3 Heat transfer modeling	74
7.4 Building process of the global turbocharger model	80
Conclusions of the work on gas processes exchange through turbochargers	83

III Gas Exchange processes through Flow Restrictions	85
-------------------------------------------------------------	-----------

8 Literature review	87
8.1 Pipe flow governing equations	87
8.2 Pipe flow governing equations resolution	89
8.2.1 Mean-value models	89
8.2.2 1-D spatial discretization schemes	90
8.2.3 multi-D spatial discretization schemes	92
8.3 ICE boundary conditions	93
8.3.1 The MOC applied to boundary conditions	94
8.3.2 Boundary conditions equations and hypotheses	98
8.4 Gas exchange processes : proposed thesis developments	104
9 Experimental apparatus	107
9.1 Cylinder head steady flow bench	107
9.2 Diaphragm steady flow bench	108
9.3 Cylinder transient flow bench	109
9.4 Numerical steady flow bench	110
10 Optimized MOC-based iterative schemes for the resolution of the non-homentropic boundary conditions	113
10.1 Expression of the Newton-Raphson algorithm for the entropy correction loop	113
10.2 Inflow case	114
10.2.1 Newton-Raphson algorithm built using $\lambda_{in,c}$ as the convergence variable	115
10.2.2 Newton-Raphson algorithm built using P as the convergence variable	116
10.2.3 Implementation of the proposed entropy correction loop resolution : inflow case	118
10.3 Outflow case	119
10.3.1 Isentropic outflow boundary resolution	120
10.3.2 Non-isentropic outflow boundary resolution	121
10.3.3 Creation of the datemap of κ	123
10.3.4 Implementation of the proposed iterative loop : outflow case	123

10.4 Convergence criterion choice	125
10.5 Convergence speed	126
11 Non-isentropic boundary condition models : data maps building and new developments	129
11.1 Inflow restriction models : Partially open-ends (POE)	130
11.1.1 Subsonic case : non-homentropic data maps building	131
11.1.2 Sonic case : non-homentropic data maps building	133
11.1.3 Non-homentropic inflow boundary data maps : direct analysis	135
11.2 Outflow restriction models : POE and nozzle	136
11.2.1 Subsonic outflow restriction boundary with momentum conservation : POE and nozzle data map building	138
11.2.2 Sonic outflow restriction boundary with momentum conservation : POE and nozzle data map building	139
11.2.3 Non-homentropic outflow boundary data maps : direct analysis	139
11.3 Complete non-homentropic flow resolution upstream and downstream a diaphragm	140
11.4 Poppet valve boundary condition	142
11.4.1 Inflow poppet valve	143
11.4.2 Outflow poppet valve	143
11.4.3 Poppet valve inflow/outflow data maps : direct analysis	144
12 Inflow / outflow restriction models : numerical and experimental validation	147
12.1 Partially open-end CFD results vs. boundary models data maps comparison	147
12.1.1 Inflow case	148
12.1.2 Outflow case	151
12.2 Experimental validation of the boundary models	152
12.2.1 Steady flow validation	152
12.2.2 Transient flow validation	156
Conclusions of the work performed on the gas exchange processes through flow restrictions	161
General conclusion	163
Conclusion and perspectives	165
Appendices	169
A : Compressible flow similitude	171
B : Compressor and turbine corresponding operating points	173
C : The Method of Characteristics	175
D : W_β^α numerical schemes	177
E : Gas models	179

Table of Contents

Table of Figures

1.1	European legislation emission limits for diesel engines.	4
1.2	Relative cost of the solutions to reduce ICE emissions. Source : [25]	5
1.3	Evolution of the consumption of the average power of vehicles in France (left) and of the average mass(right). Source : [25], [18]	6
1.4	Evolution of the consumption of the private vehicles in France (left) and of the average mileage for each vehicle category per year in France (right). PV : personal vehicle, CV : commercial vehicle. Source : [18]	6
1.5	Repartition of personal vehicles sales in France in 2009. Source : [18]	7
1.6	Typical calculation time of engine models. Adapted from [2].	9
3.1	Example of high pressure (HP) - low pressure (LP) EGR loops.	13
3.2	Left : Mechanical supercharger. Right : Comprex® wave supercharging device.	15
3.3	Automotive VGT turbocharger components. Adapted from [118].	15
3.4	Airflow through a variable geometry turbine.	16
3.5	Left : Side view of a centrifugal compressor. Right : h-S diagram of a centrifugal compressor.	16
3.6	Left : Side view of a centrifugal turbine. Right : h-S diagram of a centrifugal turbine.	17
3.7	Example of poppet valve flow.	18
4.1	Typical compressor (left) and variable geometry turbine (right) maps. Compressor and turbine operating range determined from engine mapping have been superimposed. Turbine map shows mass flow rate for 6 VGT settings.	22
4.2	Comparison between data from supplier maps (stars) and the Jensen extrapolation [69] (solid lines) for various compressor speeds.	23
4.3	Comparison between data from supplier maps (stars) and the Jensen extrapolation [69] (solid lines) for various turbine speeds (1 VGT position).	24
4.4	Speed characteristics triangle of a centrifugal compressor (left) and a centrifugal turbine (right)	25
4.5	Subsonic flow of viscous fluid around a NACA0012 wing. Upstream Mach number is set to 0.85 and $Re = 500$. On the left, iso-values of Mach number. On the right, longitudinal flow speed evolution along the capture line (red dotted line on the left figure). [27]	28
4.6	Mechanisms of heat transfer in/from the turbocharger. [118]	29
4.7	Non-dimensional temperature distribution of the casing walls of a turbocharger. Reference temperature is the maximum temperature at the turbine. [11]	30
4.8	Insulated turbocharger 5-part discretization and thermal exchanges. From [26]	32
4.9	Equivalent resistance scheme of an insulated turbocharger. From [26]	32
4.10	Simplification of the equivalent resistance scheme (Fig.4.9) of an insulated turbocharger. From [26]	32

Table of Figures

4.11 Final simplification of the equivalent resistance scheme (Fig.4.9) of an insulated turbocharger. From [26]	33
4.12 Chartflow of the 'Gas exchange processes through turbochargers' part.	34
5.1 Turbocharger bench with thermodynamical sensors positioning	36
5.2 Measurements uncertainties (in %) made on the turbomachine power estimation vs. the temperature difference across the turbomachines.	38
6.1 Speed characteristics triangle of a centrifugal compressor (left) and a centrifugal turbine (right)	42
6.2 Representation of the exchanged energies within a radial compressor	42
6.3 Representation of the exchanged energies within a radial turbine	43
6.4 Specific enthalpy calculated from supplier's data maps plotted as a function the corrected mass flow rate for various reduced shaft speeds and VGT positions. Compressor case (left), turbine case (right). Red lines provide the linear trends.	46
6.5 Evolution of $a(N_{turb})$ (right) and of $b(N_{turb})$ (left) regarding the compressor shaft speed (stars). Red line illustrates the data interpolation and the extrapolation towards low rpm values.	47
6.6 Specific enthalpy calculated from supplier's data maps plotted as a function	48
6.7 Left : Maximum efficiency per iso-speed of a radial compressor vs. turbocharger shaft speed (stars). The red line illustrates the result of a quadratic function curve fitting. Right : Illustration of the impact of the translation of the Δh_{is} curve on the maximum efficiency (black square on the right plot)	49
6.8 Evolution of $a(N_{turb})$ (right) and of $b(N_{turb})$ (left) regarding the turbine shaft speed (stars). Red line illustrates the data interpolation and the extrapolation towards low rpm values.	50
6.9 Typical turbine efficiency evolution in terms of rotational speed and mass flow rate. x axis is mass flow rate.	52
6.10 Turbocharger 1 : Compressor pressure ratio extrapolation results. Jensen's method (left) - Proposed method (right)	53
6.11 Turbocharger 2 : Compressor pressure ratio extrapolation results. Jensen's method (left) - Proposed method (right)	53
6.12 Turbocharger 3 : Compressor pressure ratio extrapolation results. Jensen's method (left) - Proposed method (right)	53
6.13 Turbocharger 1 : Compressor efficiency extrapolation results. Jensen's method (left) - Proposed method (right)	54
6.14 Turbocharger 2 : Compressor efficiency extrapolation results. Jensen's method (left) - Proposed method (right)	54
6.15 Turbocharger 3 : Compressor efficiency extrapolation results. Jensen's method (left) - Proposed method (right)	54
6.16 Turbocharger 1 : Turbine efficiency extrapolation results. Jensen's method (left) - Proposed method (right)	55
6.17 Turbocharger 2 : Turbine efficiency extrapolation results. Jensen's method (left) - Proposed method (right)	55
6.18 Turbocharger 3 : Turbine efficiency extrapolation results. Jensen's method (left) - Proposed method (right)	55
6.19 Turbine mass flow rate interpolation results. Jensen's method	56
6.20 Turbocharger 1 : Compressor pressure ratio and efficiency extrapolation combined to the Moore-Greitzer's surge model. Proposed method	56
6.21 Data from the turbocharger test bench. Compressor efficiency (left) - Compressor pressure ratio (right) - Model results for iso-speed lines lower than 90 krpm are fully extrapolated.	57

6.22 Data from the turbocharger test bench. Turbine efficiency (left) - Turbine mass flow rate (right) - Model results for iso-speed lines lower than 35 krpm are fully extrapolated. VGT opening =100%	57
7.1 Scheme of the heat and power exchanges within a non-adiabatical and insulated turbocharger. Considered case is for a turbine inlet temperature higher than the oil temperature and the compressor inlet temperature.	60
7.2 Representation of the experimental process to calculate heat exchanges within a turbocharger.	62
7.3 Considered axial forces (F) and torques (T) applied on the turbocharger rotor.	63
7.4 Comparison between the shaft power losses measured from the insulated adiabatical tests and the friction model results. The correlation line is plotted on the right.	64
7.5 Extrapolation of the friction power losses model for a change of temperature and rotational speed.	65
7.6 Comparison of the compressor pressure ratio and efficiency characteristics for various turbine inlet temperatures and various corrected shaft speeds.	66
7.7 Ratio between the adiabatical and the non-adiabatical measured efficiencies for various compressor corrected shaft speeds.	67
7.8 Comparison of the turbine corrected mass flow rate and efficiency characteristics for various turbine inlet temperatures and various corrected shaft speeds.	68
7.9 Close up on the 5500 rpm mass flow rate curve from Fig. 7.8	68
7.10 Ratio between the adiabatical and the non-adiabatical measured efficiencies. The dashed line is the extrapolation of the curve towards higher rotational speeds.	69
7.11 Heat transfers from the turbine (Q_T) and to the compressor (Q_C) and the oil (Q_O) plotted in the compressor system of coordinates. Two turbine inlet temperatures are considered : 573K and 773K.	70
7.12 Turbine transferred heat power Q_T and its ratio with respect to the turbine shaft power $\frac{Q_T}{W_{Tsh}}$ plotted regarding the turbine corrected mass flow rate. The provided rotational speeds are not corrected.	71
7.13 Compressor transferred heat power Q_C and its ratio with respect to the compressor shaft power $\frac{Q_C}{W_{Csh}}$ plotted regarding the compressor corrected mass flow rate. The provided rotational speeds are not corrected.	72
7.14 Correlation between the heat transfer powers at the compressor for two distinct VGT settings (20 and 100%) and two distinct turbine inlet temperatures : 573K and 773K.	73
7.15 Correlation between the heat transfer powers at the turbine for two distinct VGT settings (20 and 100%) and two distinct turbine inlet temperature : 573K (left), 773K (right).	74
7.16 Equivalent resistance scheme of an insulated turbocharger. From [26]	75
7.17 Final simplification of the equivalent resistance scheme (Fig.7.16) of an insulated turbocharger. From [26]	76
7.18 Left : Compressor thermal resistance with respect to the corrected mass flow rate and pressure ratio for various corrected shaft speeds. Right : Turbine thermal resistance with respect to the corrected mass flow rate for various corrected shaft speeds.	79
7.19 Oil flow thermal resistance with respect to the turbocharger shaft speeds.	79
7.20 Chartflow of the turbocharger model building process.	80
8.1 Control Surface for quasi-one-dimensional flow	87
8.2 Example of equivalent-volumes discretization of a turbocharged engine with an high pressure EGR loop.	90
8.3 Representation of the homentropic characteristics : Inflow (left) and Outflow (right).	94

Table of Figures

8.4	Benson entropy level definition (left). Non-homentropic Riemann variable definition (right)	96
8.5	Schematic representation of Benson's MOC iterative scheme	97
8.6	Schematic representation of the open-end inflow boundary condition	98
8.7	Schematic representation of the partially open-end inflow boundary condition	99
8.8	Schematic representation of the partially open-end outflow boundary condition	101
8.9	Schematic representation of an intra pipe sudden area change	102
8.10	Schematic representation of an intra pipe pressure drop device	102
8.11	Example of pipe junction : 'Y' type	103
8.12	Chartflow of the 'Gas Exchange processes through Flow Restrictions' part.	105
9.1	Cylinder head steady flow bench.	107
9.2	Left : System for the pressure measurement. Right : Interface between the pipe system and the intake side of the cylinder head.	108
9.3	Cylinder head steady flow bench.	108
9.4	Diaphragm steady flow bench.	109
9.5	Cylinder transient flow bench.	109
9.6	Considered geometries for the CFD simulation of partially open-ends (left) and poppet valves (right)	111
10.1	Benson entropy level definition (left). Non-homentropic Riemann variable definition (right)	114
10.2	Non-homentropic Riemann variable definition for the valve inflow case.	115
10.3	Data map of the pressure ratio expressed as a function of λ_{inc} , covering the entire valve opening ratio ϕ range (0 to 1). The stagnation state has been used as the reference state : $p_{ref} = p_0$, $a_{ref} = a_0$	117
10.4	Left : Evolution of $P^{\frac{\gamma-1}{2\gamma}}$ with respect to P. Right : Data map of the pressure ratio expressed as a function of λ_{inc} , covering the entire valve opening ratio ϕ range (0 to 1). The stagnation state has been used as the reference state : $p_{ref} = p_0$, $a_{ref} = a_0$	118
10.5	Chartflow of the proposed inflow entropy correction loop.	119
10.6	Non-homentropic Riemann variable definition for the valve outflow case.	120
10.7	Polytropic coefficient evolution with respect to the incident Riemann variable. The curves have been built using Eq.10.26 with $\Psi = 1$	122
10.8	Solutions of Eq. 10.35 (left) and Eq. 10.36 (right) for $\lambda_{in,c} = 1.07$ and $\phi = 0.75$, in the isentropic and non-isentropic cases. The non-isentropic curves have been built using the polytropic expression of Eq.10.26 with $\Psi = 1$	123
10.9	Chartflow of the proposed outflow iterative loop. Subsonic case.	124
10.10	Chartflow of the proposed outflow iterative loop. Sonic case.	125
10.11	Illustration of the impact of the convergence criterion value C_C on the creation of spurious oscillations at boundary. Left : The considered case is a rarefaction wave incident on a partially open-end. Right : Calculated static pressure at the boundary node for various values of C_C	126
10.12	Comparison of the number of iterations required by the studied convergence schemes. Subsonic test case with pressure ratio = 1.55. Convergence criterion : $C_c = 10^{-5}$. Left : Inflow valve model results. Right : Outflow valve model results.	126
11.1	Subsonic inflow valve models sound speed vs. entropy evolution - constant pressure model (left) - momentum conservation (right)	131
11.2	Sonic throat model : sound speed vs. flow entropy evolution	133
11.3	Matched nozzle model : sound speed vs. flow entropy evolution	134

11.4	Steady flow results comparison between boundary restriction models : subsonic case (left) and sonic case (right).	136
11.5	Spacial evolution of the static pressure for the subsonic inflow restriction models.	136
11.6	Subsonic outflow valve model considered system (left) and pressure distribution used to solve the momentum conservation (right)	137
11.7	Evolution of Ψ with respect to the outflow angle.	139
11.8	Steady flow results comparison between outflow boundary restriction models.	140
11.9	Considered system for the upstream/downstream restriction non-homentropic flow resolution. .	141
11.10	Left : impact of the downstream geometry ϕ_1 on the upstream non-dimensional flow velocity. Right : impact of the upstream geometry ϕ_3 on the downstream flow velocity.	142
11.11	Example of axi-symmetrical poppet valve flow structures in the inflow (left plot) and outflow (right plot) cases. Poppet valve models associated planes are also plotted.	143
11.12	Steady flow results comparison between the standard inflow models and the inflow poppet valve model : subsonic case (left) and sonic case (right).	144
11.13	Steady flow results comparison between outflow boundary restriction model and the outflow poppet valve model.	145
12.1	Considered geometries for the CFD simulation of partially open-ends : inflow (left) and outflow (right).	148
12.2	Steady subsonic flow results comparison between CFD and models.	148
12.3	Example of the static pressure evolution from the inflow partially open-end CFD results. . .	149
12.4	Steady sonic flow results comparison between CFD and the boundary models.	149
12.5	Left : sonic flow structure from the sonic throat assumption. Right : sonic flow structure from CFD observations	150
12.6	Steady sonic flow results comparison between CFD and the matched nozzle model.	150
12.7	Steady subsonic outflow results for an outflow sudden restriction. Left : Comparison between the CFD calculation and the isentropic model. Right : Comparison between the CFD calculation and the momentum resolution model with $\Psi = 1$	151
12.8	Steady subsonic for a 45° outflow nozzle. Left : Comparison between the CFD calculation and the isentropic model. Right : Comparison between the CFD calculation and the momentum resolution model with $\Psi = 0.5$	151
12.9	Non-studied flow restriction correlation : experimental setup in the case of the cylinder head flow bench.	152
12.10	Considered system for the inflow valve boundary validation.	153
12.11	Inflow poppet valve model results compared to flow bench data.	153
12.12	Considered system for the inflow valve boundary validation.	154
12.13	Outflow poppet valve model results compared to flow bench data.	154
12.14	Considered system for the complete upstream/downstream restriction model validation with respect to a diaphragm ($\frac{F_2}{F_{upst}} = \frac{F_2}{F_1}$).	155
12.15	Complete upstream/downstream restriction model results compared to the diaphragm flow bench data.	155
12.16	Considered system for the transient restriction models validation.	156
12.17	Comparison between the simulation and experimental results in the subsonic case ($P_{cyl} = 1.8$ bar) and a diaphragm / pipe section ratio ϕ of 0.67.	158
12.18	Comparison between the simulation and experimental results in the sonic case ($P_{cyl} = 4$ bar) and a diaphragm / pipe section ratio ϕ of 0.67.	158
12.19	Comparison between the simulation and experimental results in the subsonic case ($P_{cyl} = 1.8$ bar) and a diaphragm / pipe section ratio ϕ of 0.17.	159

Table of Figures

12.20 Comparison between the simulation and experimental results in the sonic case ($P_{cyl} = 4$ bar) and a diaphragm / pipe section ratio ϕ of 0.17.	159
12.21 Comparison between the results of the simulation using the outflow model from the literature ($C_d=1$) and the experimental results in the sonic case ($P_{cyl} = 1.8$ bar) and for a diaphragm / pipe section ratio ϕ of 0.67.	160

Nomenclature

a	[m.s ⁻¹]	Sound speed
A	[\cdot]	Non-dimensional sound speed
A_A	[\cdot]	Non-dimensional entropy level
d	[m]	Diameter
C	[m.s ⁻¹]	Velocity
C_p	[J.kg ⁻¹ .K ⁻¹]	Specific heat at constant pressure
e	[J.kg ⁻¹]	Specific energy
e₀	[J.kg ⁻¹]	Specific total energy
F	[m ²]	Pipe cross-section
F_{f/a}	[\cdot]	Fuel/air ratio
h	[J.kg ⁻¹]	Specific enthalpy
	[W.m ⁻² .K ⁻¹]	Heat exchange coefficient
h₀	[J.kg ⁻¹]	Specific total enthalpy
m	[kg]	Mass
M	[\cdot]	Mach number
N	[RPM]	Rotational speed
Nu	[\cdot]	Nusselt number
p	[Pa]	Pressure
p₀	[Pa]	Total pressure
P	[\cdot]	Pressure ratio
Q	[J.s ⁻¹]	Thermal transfer power
Q_{HV}	[J.kg ⁻¹]	Lower fuel heating value
Q_m	[kg.s ⁻¹]	Mass flow rate
r	[m]	Radius
R	[J.kg ⁻¹ .K ⁻¹]	Perfect gases constant
	[K.m ² .W ⁻¹]	Thermal resistance
Re	[\cdot]	Reynolds number
s	[J.K ⁻¹ .kg ⁻¹]	Entropy
S	[m ²]	Surface
t	[s]	Time
T	[Nm]	Torque
	[K]	Temperature
u	[m.s ⁻¹]	Particle speed
U	[m.s ⁻¹]	Tangential speed of blades
	[\cdot]	Non-dimensional speed of fluid
U_{int}	[J]	Internal energy
V	[m.s ⁻¹]	Speed of fluid in turbomachines
W	[J]	Work
	[m.s ⁻¹]	Speed of fluid in rotating systems of coordinates
Ẇ	[J.s ⁻¹]	Power

Greek

α	[°]	Angle
β	[°]	Angle
δ	[‐]	Dimensionless flow parameter
ϵ	[‐]	Emissivity
γ	[‐]	Specific heat ratio
η	[‐]	Efficiency
ρ	[kg.m ^{‐3}]	Density
ν	[m ² .s ^{‐1}]	Kinematic viscosity
μ	[N.s.m ^{‐2}]	Dynamic viscosity
μ_{th}	[‐]	Manometric head parameter
ϕ	[‐]	Section ratio
	[‐]	Dimensionless mass flow parameter
	[W]	Heat flux
φ	[W.m ^{‐2}]	Heat flux per unit of surface
ψ	[‐]	Dimensionless head parameter

Subscripts

0	Stagnation state
1	Compressor inlet static value
01	Compressor inlet total value
2	Compressor exit static value
02	Compressor exit total value
3	Turbine inlet static value
03	Turbine inlet total value
4	Turbine exit static value
04	Turbine exit total value
c	Corrected value
ext	Exterior conditions
g	Gas
i=[1...3]	Node location (pipe flow)
in	Ingoing or incident wave
n	Natural value
out	Outgoing or reflected wave
shock	Shock
t	Throat
w	Wall

Superscripts

n	Time level
it	Iterative step

Part I

Context and Stakes of the Study

Chapter 1

Context of the study : control laws development of the Internal Combustion Engine (ICE)

Motor vehicles are the most widespread means of transportation in Europe and in the US. The automotive vehicles equipped with internal combustion engines combine reliability and a low cost of the energy source. However, the main drawbacks of this propelling system are the pollutant emissions and the greenhouse gases combined to the increase of the cost of the power sources. The critical dependence of the modern means of transportation with respect to the availability of petroleum sources has been identified in the 70's. The first laws regarding pollutant emissions of the internal combustion engines have been created at the same time. This combination of decisions and events have lead to the reduction of the pollutant emissions and of the engine specific consumption. These results are based on strong research and development which are focused on engine efficiency, on combustion chemistry in order to prevent the production of pollutant and on the after-treatment systems.

At the same time, cars manufacturers have drastically decreased the development time of their vehicles, which allows to partially compensate the added cost of the R&D developments. This improvement of the development efficiency is more and more complex to achieve, as the associated system complexity is increasing. Indeed, the main R&D developments relative to the engine developments are linked to a compromise between the following parameters :

- the engine performance (power and torque).
- the engine consumption : many countries have introduced a vehicle efficiency evaluation in order to inform the customers. Consequently, a high fuel consumption might impair the future sales.
- the vehicle European legislation emission limits compliance.
- the engine production cost.

It is proposed in this chapter to get a general idea of these problems and to study how the engine control and its associated models are an answer to the developed issues.

1.1 Compliance to pollutant emissions limitations vs. production cost

The most restricting parameter in the development of an automotive engine has become the equilibrium between the compliance to European emissions legislation and the cost of the engine. There are 235 millions of personal vehicles on the roads in Europe [1], and this leads to the rejection of huge amounts of pollutant emissions in the air. In order to prevent the health issues and the effect on the environment, laws restricting

the cars emissions have been introduced. The evolution of the diesel legislation in Europe is shown on Fig. 1.1.

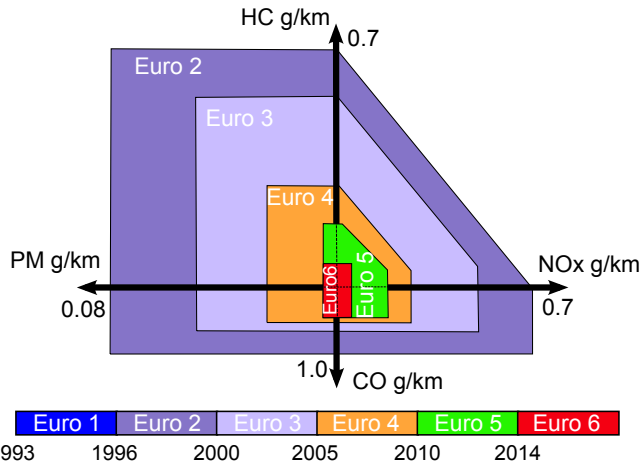


FIG. 1.1 – European legislation emission limits for diesel engines.

It appears that since 1995, the pollutant emissions limits have been drastically reduced. This had a global positive impact on the global emissions levels which are estimated each year, as shown on Fig. 1.1.

Chemical species	% of national emissions	evolution (%) since 1990
NOx	52	-42
CO	20	-85
PM	25	-30
Pb	0	-100
HC	57	+142

TAB. 1.1 – 2008 emissions in France of the road transportation sector and their evolution regarding 1990 levels. source : [25]

The exception comes from the HC level, which has increased even though the emission per vehicle has been decreased via the regulations. This shows that it is necessary to consider the problem globally : one should take into account the total mileage performed by the vehicles per year. The total mileage performed by all the cars on the roads in France has increased by 25% between 1990 and 2008 (source : [25]). Consequently, even in the case where the emissions are reduced for each single vehicle, this does not necessarily implies that the global emission levels are reduced.

In order to counterbalance the global increase of mileage performed by the vehicles, the pollutant emissions are being drastically reduced by law : the global emission limitations of Euro 6 will be, on average, 10 time lower than the Euro 2 levels, in the diesel case. In order to ensure the compliance to these limitations, the following technological solutions have been adopted :

- The control of the combustion. This is performed via the control of the chemical species which are introduced into the combustion chamber : air, fuel, recirculated exhaust gas and the way combustion occurs.
- After-treatment systems : filters and catalyzers are placed downstream the cylinder along the exhaust piping system to convert pollutant exhaust gases into safe chemical species.

These solutions have different pollutant emissions reduction efficiencies and also different costs :

It is estimated that the control of the combustion on automotive engines allows to cut the pollutant emission by up to 60%. Nevertheless, this performance is not sufficient to meet regulation limits, and after-

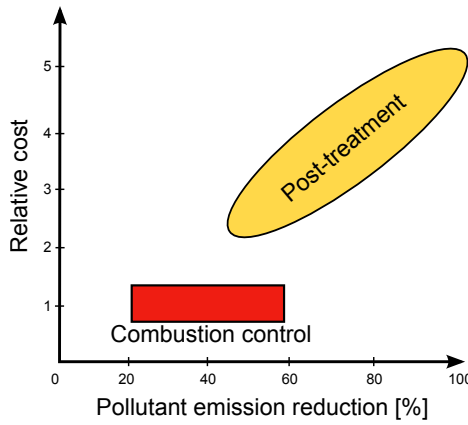


FIG. 1.2 – Relative cost of the solutions to reduce ICE emissions. Source : [25]

treatments devices have to be used. Such systems allow to reduce almost completely the pollutant emissions, but at a high cost (up to 5 times higher than the control of combustion). Consequently, the most economical solution is to prevent as much as possible the creation of pollutant emissions (via the control of combustion) in order to add as less as possible after-treatment devices. The 0D / 1D engine modeling tools have a central role in the development of the combustion control, especially regarding the flow rate of the species entering or exiting the cylinders. Models allow to get access to quantities which cannot be measured : for example, it is impossible to measure accurately the amount of recirculated exhaust gas which are entering the cylinder, but this quantity can be estimated by the means of models. As the 0D / 1D models provide a good compromise between accuracy and calculation time [122], [58], they appear to be a good choice for a engine control law development application. However, the drastic reduction of the emissions limits leads to high requirements in terms of model accuracy.

1.2 Engine performance vs. fuel consumption

Since the 1973 oil crisis, governmental incitations lead to a higher awareness of the consumers regarding the fuel efficiency of products. As a consequence, fuel consumption has become a crucial parameter in the choice of a car. However, comfort and security of the passengers have known an exponential demand. The main consequence of this evolution is the increase of the mass of the vehicles (+20% between 1995 and 2009 in France, see Fig. 1.4, right plot). This increase of the mass had a direct impact on the engine power required to preserve the dynamical performances of the vehicles : the average engine power has grown by 35% between 1995 and 2009 in France (Fig. 1.4, left plot). Despite this increase of the engine power, the average consumption has been decreased by 20% during the same period of time, which shows that great improvements have been achieved regarding the engine specific consumption (Fig. 1.3, left plot). Even though this improvement is spectacular, one should notice that this consumption reduction has been integrally compensated by the 25% increase of the road traffic (Fig. 1.3, right plot).

Fuel consumption reduction could be much more significant than the levels achieved today, however it is necessary to preserve a given level of performance to the car. In order to have a satisfying engine performance vs. consumption ratio, it is possible to work on the following parameters :

- the improvement of the engine efficiency..
- the reduction of the aerodynamical drag. Aerodynamical losses account for approximately 19% of the fuel consumption of a vehicle [55].
- the reduction of the tire rolling resistance. The losses at the road/tyre interface account for approxi-

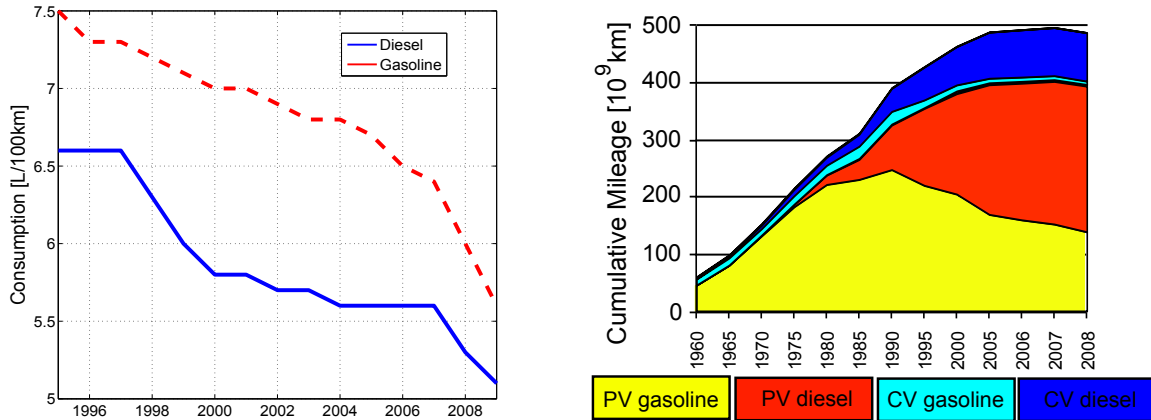


FIG. 1.3 – Evolution of the consumption of the average power of vehicles in France (left) and of the average mass(right). Source : [25], [18]

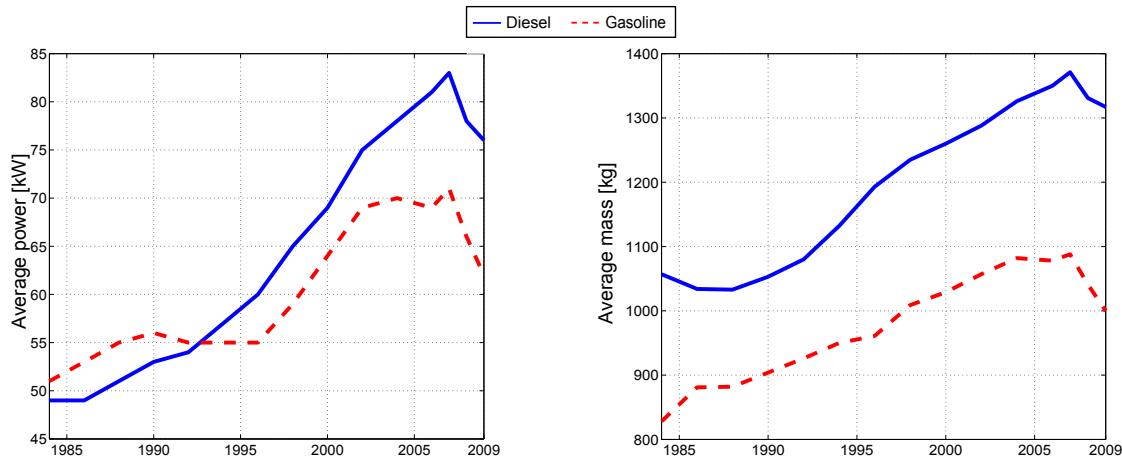


FIG. 1.4 – Evolution of the consumption of the private vehicles in France (left) and of the average mileage for each vehicle category per year in France (right). PV : personal vehicle, CV : commercial vehicle. Source : [18]

mately 21% of the fuel consumption of a vehicle [55].

- the reduction of the vehicle mass. Reducing the mass of a vehicle allows to reduce the rolling resistance and the requirement in terms of engine power. This phenomenon is visible on Fig.1.4 : since 2007, the average mass of the vehicles is decreasing along with the engine power. On the average, reducing the mass by 10% allows to decrease the fuel consumption by 10% (assuming a powertrain adaptation to the new weight [101]).

Now, a quick parametric study is proposed. A vehicle consuming 5.5L of fuel per 100km is considered. The vehicle is equipped with an engine having an average global efficiency of 30%. It is assumed that the engine efficiency is improved from 30 to 31%. This, leads to a fuel consumption reduction of 0.1774 L/100km (- 3.23%). The impact of the other parameters is studied in order to achieve the same fuel consumption decrease :

- reduction of the aerodynamical drag : it is necessary to decrease by 16.15% ($\frac{3.23}{0.19}$) the losses due to the aerodynamical phenomena.
- reduction of the rolling resistance : it is necessary to decrease by 15.38% ($\frac{3.23}{0.21}$) the losses due to the

tire contact.

- mass reduction : according to Pagerit [101], a reduction of 3.23% of the global vehicle mass is necessary.

It is concluded that the engine is the most sensitive parameter which allows to decrease the automotive fuel consumption, while the mass reduction is also an important parameter to consider. It appears that it will be much more difficult to have a comparable gain using the improvement of the road/tire contact or the improvement of the aerodynamical drag. In order to reduce engines consumption, the use of alternative technologies could also be considered. In recent years, systems such as the electrical/combustion engine hybrid motorization, the stop/start devices or the fully electrical powertrains show new trends in the reduction of the specific consumption. However, alternative propulsion technologies have a market penetration index which is still very low (less than 1.7% in France in 2009, see Fig. 1.5). Consequently, 'standard' technologies will probably stay one of the main lever allowing to reduce the fuel consumption reduction in the next 15 years.

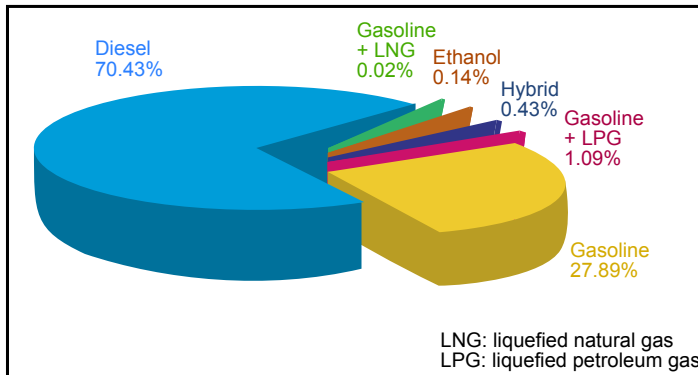


FIG. 1.5 – Repartition of personal vehicles sales in France in 2009. Source : [18]

1.3 Reduction of the development time vs. R&D expenses

From Fig. 1.1, one sees that the European legislation imposes a step forward in terms of pollutant emissions reduction of the engines every 5 years. This leads to an increase of the R&D work in order to comply with this mandatory schedule. It is necessary, from an economical point of view, to keep a balance between the investments and the sales revenues in order to preserve the potential benefits. The evolution of the R&D expenses and workforce between 2000 and 2009 is shown on Tab. 1.2 for PSA, Renault SAS and Volkswagen. These brands are the three biggest European car manufacturers in terms of worldwide sales [1]. Even though the strategy adopted by each group is different in terms of hiring and of expenses evolution, a strong re-enforcement of the R&D part for these brands is noticed. Around 5-6 % of the sales revenues is re-invested in the research, and the associated workforce can account up to 15% of the global number of employees. However, the research and development expenses and number of employees are not correlated : PSA has kept its R&D workforce almost stable, but the expenses have grown by 47%. Renault has reduced its research expenses by 9%, while the associated workforce has grown by 67%. The VAG group has, by far, the highest R&D budget and workforce in this study, but its worldwide sales level allows to reduce the impact of the R&D on the global balance.

In their annual reports published (sources : [107], [111], [132]), these firms state that the control of their R&D expenses will be crucial in the years to come. In order to reduce the R&D relative expenses while preserving the development schedule, the following solutions are adopted :

- Globalization of the production. This allows to make economies of scale. This requires from the brand to be implanted on many growing automotive markets, while preserving the sales level in the saturated

Manufacturer	Parameter	2009	2005	2000
PSA	R&D expenses (M€)	2148	1816	1461
	% of sales revenues	5.6	4	3.5
	R&D employees	17000	17000	14000
	% of total employees	13.9	12.2	10.9
Renault SAS	R&D expenses (M€)	1643	2264	1818
	% of sales revenues	4.9	5.5	5.8
	R&D employees	17881	12939	10700
	% of total employees	14.7	10.2	6.45
VAG	R&D expenses (M€)	5429	4075	4141
	% of sales revenues	5.8	4.3	4.8
	R&D employees	25583	22000	18375
	% of total employees	6.9	6.4	5.8

TAB. 1.2 – 2000-2009 evolution of some R&D-related parameters for PSA [107], Renault SAS [111] and VAG [132].

market countries (Europe, US).

- Improvement of the R&D efficiency. In this case, new processes and new tools are developed in order to improve the time efficiency.

1.4 Impact on the engine control and its associated engine models

The development of the engine control is crucial in order to reduce the pollutant emission and the fuel consumption. Today, the development of the engine control is based on 0D-1D engine models. Such models allow to develop the engine control laws and to validate them. Developing the models in terms of accuracy and time consumption has a direct impact on the engine control performance and on the R&D costs :

Reduced development time :

The use of modeling tools to evaluate the potential performances of engine control laws allows to reduce the need of experimental tests. The overall experimental process is generally demanding in terms of time and expenses. Using numerical tools in order to pre-evaluate the performances of a solution allows to use the experimental tests only as a final validation tool. As a consequence, the global development time and cost of a project can be decreased by introducing the modeling tools in the engines development process.

From a curative to a preventive engine control

Most of the engine control parameters are still determined by the means of data-maps. These data-maps are most of time only valid on the engine operating points and introduce errors under transient conditions. Consequently, additional correction data-maps are often introduced in order to take properly into account the physical parameters of the engine. Such an approach increases the structure complexity of the engine control. In the case where a dynamical model is implemented in the ECU, the external parameters are naturally taken into account by the model. This leads to a better estimation of the control values and an extension of the validity range.

Nevertheless the most interesting gain is obtained by developing a predictive control architecture rather than a curative control. The engine control based on static data-maps are curative : a sensor detects a non-optimal operating point, this information is then transmitted to the control unit in order to correct the behavior. The

use of models potentially allows to predict the evolution of a parameter. If this information is transmitted to the control unit, it is possible to stay in any case on the most optimal operating point as possible. Such approach has a very strong potential in the case of the pollutant emissions.

Consequently, it appears that the 0D-1D models are a cornerstone of the engine control development. Two parameters of the models have a strong impact on the compliancy of the model-based approach with the engine development process :

Model accuracy :

The degree of accuracy of the model directly impacts the control laws development. Indeed, reduced models are used to estimate the behavior of the real system and this estimation is then corrected regarding the feedbacks from the actual system (closed-loop system). In terms of validation process, a model in good agreement with the behavior of the 'real' system will allow to decrease the requirement of experimental tests. In the past years, the needs in terms of model accuracy has been strongly increased : in order to reach low pollutant emission and fuel consumption levels, the phenomena taking place in the engine must be modeled very finely.

Computation efficiency :

The increased complexity of the automotive engine has lead to the increase of the sub-models introduced in a complete engine model. Additionally, more accurate models generally require longer computation time. However, in order to stay competitive regarding experimental processes and to be implemented into the ECU, the calculation time of the modes must be kept as low as possible. This is generally performed by improving the introduced calculation schemes or by tuning the accuracy/computation time ratio.

Therefore, the development of the 0D-1D modeling tools can lead to interesting results in order to answer to the engine development problem. It is however necessary to find the optimal balance between the calculation time and the accuracy of the models in order to improve the efficiency of the R&D developments. Indeed, model-based developments are valid only if the models are in good agreement with the real system. Additionally, the models must require only low calculations time, in order to cope with the reduced development time. The launch of this thesis has been motivated by these requirements.

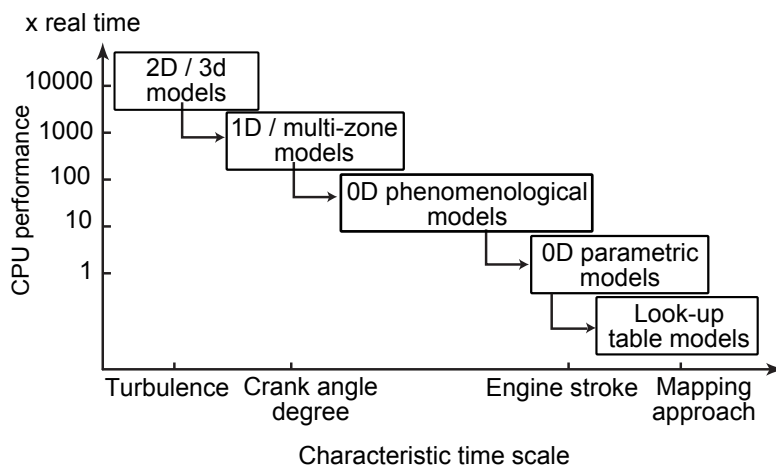


FIG. 1.6 – Typical calculation time of engine models. Adapted from [2].

1.5 Role of the airpath regarding the control of modern engines

The airpath has become a crucial part in the development of modern engines. The control of the airpath has a direct impact on the engine performance as well as on its pollutant emission level. Indeed, air system strategies allow to control the species which are introduced in the cylinder, which is a cost-effective way to reduce pollutant emissions. As a consequence, the automotive air systems have become increasingly complex in order to achieve pollutant reduction strategies and to allow fuel consumption reductions. Additional actuators have been introduced to control the intake and exhaust flow, which leads to an increase of the related engine control developments.

This increasing complexity of the air systems has an impact on the difficulty encountered to control the associated components (valves, throttles, turbochargers...) :

- The control of the pollutant emissions require to use accurate models in order to build satisfying observers.
- The increasing number of components involved in the engine air systems as well as the accuracy level requirement lead to longer computation time. Consequently, the optimization of the engine airpath models calculation efficiency is a crucial point.

Context of the study : main points

- The constraints imposed on the development of the automotive ICE come from the economical situation and the governmental regulations which are applied on the transport industry.
- In order to reduce the levels of pollutant emissions produced by road transportation, drastic emission limitations have been introduced in Europe. The most economical solution to comply to the pollutant emissions standards is to prevent as much as possible the creation of pollutant emissions. This allows to add as less as possible post-treatment devices, which are extremely costly to produce. Such approach can be achieved by controlling the species which are introduced in the cylinder.
- Fuel consumption is a crucial factor in the choice of a car. It appears that the most sensitive parameter to achieve fuel consumption reduction is the improvement of the engine efficiency.
- The three biggest European car manufacturers have globally known a great increase of their R&D expenses and workforce in the past decade. Nevertheless, improving the efficiency of the R&D processes is crucial in order to keep the development time and costs in agreement with the economical constraints of the automotive industry.
- These constraints have a direct impact on the engine control and its associated models. The development of these models can potentially provide an interesting solution in order to achieve a satisfying accuracy/computation time ratio :
 - Model-based developments are valid only if the models are in good agreement with the real system. As the engine systems are becoming more and more complex, this leads to an increase model accuracy requirement.
 - The models must require low calculations time, in order to cope with the reduced development time and to remain competitive regarding experimental tests.

Chapter 2

Goals and structure of the study

The previous chapter has underlined the increasing role played by the engine control and the air system in modern engines. Indeed, the actuators of the air system allow to control the chemical species which are introduced into the cylinder. The estimation of this parameter is crucial for the good progress of the combustion. It has been seen that the control of the combustion allows a cost-effective reduction of the pollutant emissions. Additionally, the model-based approach has a strong interest in terms of development time and cost. As a result, the present thesis will focus on the modeling of the airpath components for the engine control laws development and tuning processes. The main developments will involve the improvement of the following points :

- the modeling of the physical phenomena occurring through the air flow components. This parameter is crucial in order to provide predictivity to the models and to the engine control.
- the control of the models calculation time, which ensures the attractiveness and the efficiency of the model-based approach.
- the compromise between the models accuracy and the required experimental correlation to achieve this accuracy level. Many time-efficient models rely on experimental data to provide accurate results. This introduces additional costs and extend the development time.

It has been decided to focus the thesis on the components which are actuated in order to control the composition of the cylinder inflow / outflow. This means that the post-treatment devices won't be included in the present study. However, the turbochargers, throttles and valves models will be at the center of the thesis developments.

Structure of the manuscript :

The present document has been organized into two main parts :

1 : Gas exchange processes through turbochargers :

The first technical part of the thesis will focus on the turbocharger mean-value modeling.

The first chapter presents the literature review performed on the mean-values models of automotive turbochargers. The main turbocharger models structures are detailed. The advantages and limitations of these models are analyzed with respect to the control laws development process.

The turbocharger experimental apparatus which has been used in this thesis is detailed in the second chapter. A study of the accuracy level of the sensors is also proposed. The aim of the turbocharger tests was

to identify some physical phenomena and to get validation data.

The third chapter introduces the proposed radial turbine and radial compressor flow evolution models. The mathematical developments and the associated thermodynamical hypotheses are detailed. Models results are tested on three different turbochargers and compared to literature models results. Final validation is obtained from a comparison between the proposed model results and experimental data.

The fourth chapter addresses the modeling of the thermal exchanges within automotive turbochargers. Indeed, a non-negligible part of the heat from the turbine is transferred to the compressor.

2 : Gas exchange processes through flow restrictions :

The second technical part of the thesis is dedicated to the flow restriction modeling.

The first chapter is the literature review performed on the 0D and 1D models of automotive flow restrictions. The main automotive flow restriction models are introduced and their performances in terms of accuracy, predictivity and calculation time are analyzed. The main numerical schemes introduced in the literature papers in order to solve the aerodynamical boundary condition problem are also introduced. Finally, the concept of entropy correction is introduced.

In a second chapter, the experimental apparatus dedicated to the study of flow restrictions performance is detailed. Multi-dimensional CFD calculations are also introduced in this chapter as some of these results are used as 'reference' results in the following of the study.

The third chapter introduces the proposed developments regarding the iterative numerical schemes used in order to solve the boundary conditions problem. These numerical schemes have a strong impact on the calculation time and on the accuracy of the results.

The subject of the fourth chapter is the mathematical modeling of the flow restrictions. The proposed models are detailed, as well as the associated resolution processes. The equations and hypotheses introduced in order to build the models have a direct influence on the accuracy of the model. The equations also have an impact on the numerical schemes introduced to solve the boundary condition problem.

Finally, models results are compared to experimental results. This validation is performed in the case of steady and transient flows. This allows to differentiate the influence of the models mathematical equations from the numerical resolution schemes effects. Attention is focused on the accuracy level achieved without introducing any experimental corrective coefficient. The calculation time performance is also investigated.

Publications :

- 'Implementing turbomachinery physics into data map-based turbocharger models'. G. Martin, V. Talon, P. Higelin, A. Charlet, C. Caillol. *SAE Int. J. Engines* **2**(1) : 211-229, 2009.
- 'Physics-based diesel turbocharger model for control purposes'. G. Martin, V. Talon, T. Peuchant, P. Higelin, A. Charlet. *SAE paper* 2009-24-0123, 2009.
- 'Pressure ratio-based method for non-isentropic inflow valve boundary conditions resolution'. G. Martin, P. Brejaud, P. Higelin, A. Charlet. *SAE paper* 2010-01-1052, 2010.

Chapter 3

Key components and systems for the control of automotive engine airflow

The following part of the document will focus on the main actuated components of the engine. Components such as post-treatment devices also have an impact on the air flow, however it is intended to focus on the components which are actuated in order to control the evolution of the airflow. As a consequence, the following devices will be introduced : the EGR loops and the associated actuators, the supercharger devices and the poppet valves.

3.1 Exhaust Gas Recirculation (EGR) loop

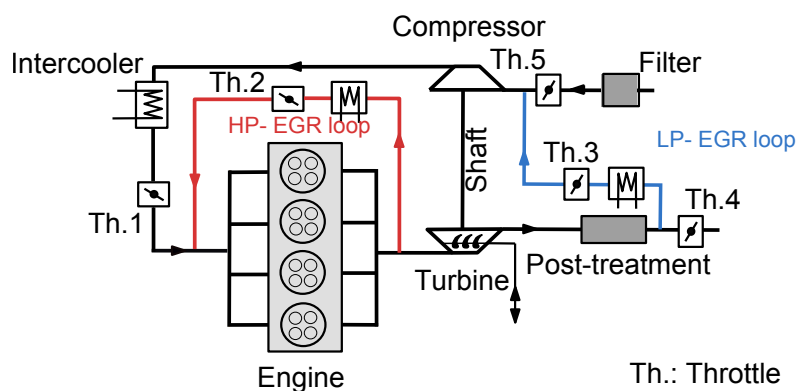


FIG. 3.1 – Example of high pressure (HP) - low pressure (LP) EGR loops.

The recirculation of exhaust gas towards the intake is a widespread technique in the diesel engine field. The introduction of burned gases inside the combustion chamber allows to decrease the oxygen concentration rate and the average gas temperature. These two effects lead to the reduction of NOx emissions. In the case of gasoline engines, the EGR loops are used to prevent knock combustion, which allows to reach higher loads. However, there is a counterpart to these improvements, as the decrease of the oxygen rate combined to the lower temperature lead to an increase of the soot emissions. EGR has also a negative impact on the fuel consumption, due to the slowdown of the combustion process speed and to the counter-pressure created at the exhaust. Two EGR architectures exist (see Fig.3.1) :

- High pressure EGR. This loop is the most classic architecture : a part of the gas flow is deviated from the exhaust system to the high pressures part of the intake piping system (downstream the compressor). The fact that the pressure upstream the turbine is generally higher than the pressure downstream the

compressor is used to establish the flow naturally. This system is regulated by the means of the EGR throttle $Th.2$, of the main throttle $Th.1$ and of the turbine variable geometry position.

- Low pressure EGR. Exhaust gas flow is deviated from downstream of the post-treatment devices ('clean' exhaust gas) towards upstream of the compressor. This system allows to achieve colder EGR and reduces the risk of compressor surge (compared to the HP loop). The LP loop is regulated by the means of the EGR throttle $Th.3$, of the exhaust throttle $Th.4$ and of a throttle placed upstream of the compressor $Th.5$.

It appears that such systems are complex to control, due to the high number of actuators and the fact that the system is looped.

3.2 Superchargers

The maximum power delivered by an engine for a given displacement is directly linked to the amount of fuel efficiently burned at each cycle inside the cylinder. This amount is limited by the quantity of air which can be introduced into the cylinders. Therefore, in order to increase the maximum power output of a given engine, the inlet air must be compressed to higher density than ambient conditions before entering each cylinder. This is shown ([61]) by the following equations (eq.3.1, eq.3.2) :

$$\dot{W} = \frac{\eta_f \cdot \eta_v \cdot N \cdot V_d \cdot Q_{HV} \cdot \rho_{inl} \cdot F_{f/a}}{2} \quad (3.1)$$

$$T = \frac{\eta_f \cdot \eta_v \cdot V_d \cdot Q_{HV} \cdot \rho_{inl} \cdot F_{f/a}}{4 \cdot \pi} \quad (3.2)$$

where \dot{W} and T are the power and torque output of the engine, η_v and η_f the volumetric and fuel conversion efficiencies, Q_{HV} is the lower fuel heating value, ρ_a is the inlet air density and $F_{f/a}$ is the fuel/air ratio. One can see that for the same engine architecture, supercharging will increase the maximum power and torque by increasing ρ_a , the other parameters remaining constant.

Supercharging can be achieved using several systems :

Mechanical superchargers

In this case, a positive displacement compressor is driven using mechanical power taken from the engine. Most of times, the link between the compressor and the engine is a belt direct-drive, which leads to issues in order to match the most efficient compressor speeds. The efficiency of these devices is relatively low (50%). This phenomenon combined to the direct-drive architecture means that an important part of the engine power is used to drive the compressor (15% on average). Finally, such devices are heavy and bulky. As a consequence, such supercharging system are not widely used in the automotive industry.

Pressure wave superchargers

Pressure wave supercharging uses wave action in order to compress intake air. The process is controlled by a cylindrical cell rotor whose speed is synchronized with the engine crankshaft speed. Individual cells alternately open and close the exhaust gas and fresh air apertures. When the aperture on the exhaust gas side is reached, pressurized exhaust gas flows into the cell and compresses the fresh air. As the cell rotor continues to rotate and reaches the aperture on the inlet side, the compressed air flows to the engine. Before the exhaust gas exits to the fresh air side, the aperture is closed again and the exhaust gas column is reflected before entering the engine. The exhaust gas exits at high speed sucking further intake air into the cell. Such system is complex to control and to integrate under the hood of modern cars. This device is consequently unusual in the automotive applications.

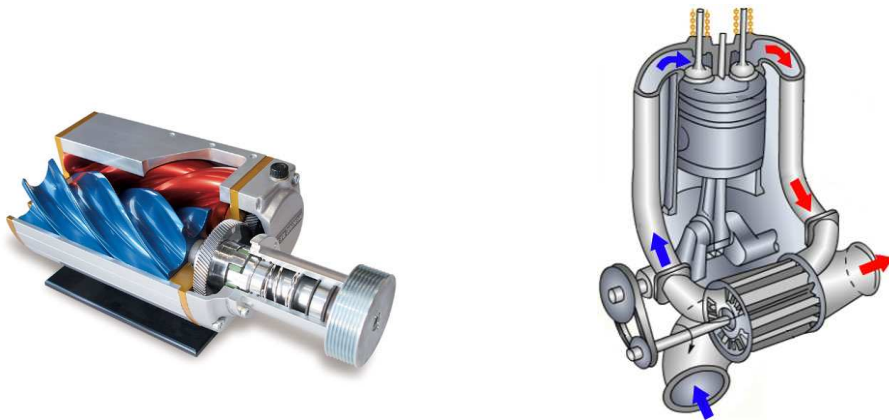


FIG. 3.2 – Left : Mechanical supercharger. Right : Comprex® wave supercharging device.

Turbochargers

A turbocharger is composed of a turbine and a compressor mounted on the same shaft (Fig.3.3). The turbine uses exhaust gases energy to drive the compressor which compresses inlet gases. In our study, we will only consider radial compressors and turbines since they are the only ones used in automotive applications. The turbine can either have a fixed or a variable geometry. In the case of a variable geometry turbine (VGT), pivoting nozzles are placed upstream of the turbine rotor. Such device changes the incident angle and the section of the exhaust flow channels. This has a direct impact on the amount of power transmitted to the shaft by the turbine. The main advantage of the VGT devices is to improve the response time of the turbocharger and to allow variable boost pressure control. The nozzles are moved by the means of a pneumatic or an electrical actuator.

Turbochargers provide an interesting compromise between cost, compactness and performance. Additionally, turbochargers have become key parts in the control of the exhaust gas recirculation. This explains why they are increasingly used on automotive applications in order to achieve supercharging.

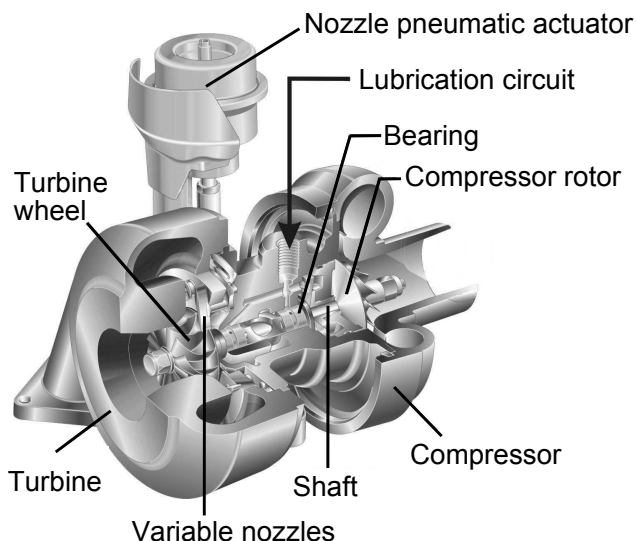


FIG. 3.3 – Automotive VGT turbocharger components. Adapted from [118].

Now, the compressor and turbine principles of operation are being detailed :

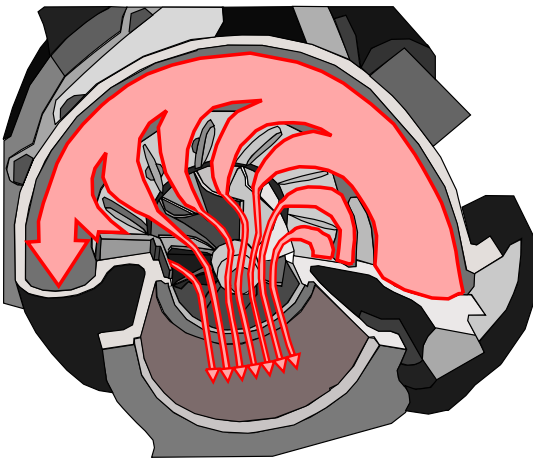


FIG. 3.4 – Airflow through a variable geometry turbine.

Compressor : A centrifugal compressor is composed of a static inlet, a mobile bladed rotor, a diffuser and a collector (Fig.3.5). The role of the collector is to bring compressed air to the engine air inlet system . The role of the rotor is to transfer energy between the turbocharger shaft and the fluid. The flow is deflected by the blades, this means that a reaction force is applied by the fluid to the rotor. For a better understanding of the physical processes taking place in the rotor area, a h-S (enthalpy - entropy) diagram is also drawn.

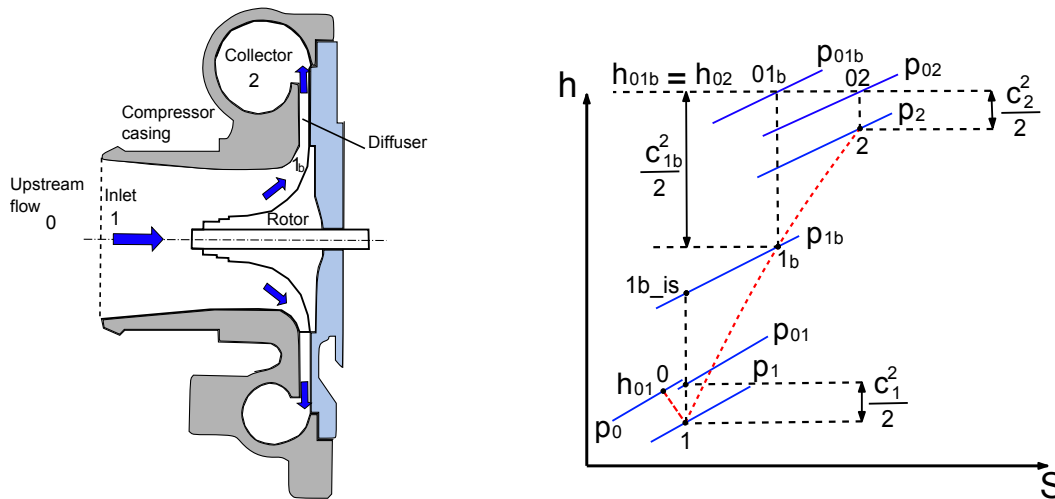


FIG. 3.5 – Left : Side view of a centrifugal compressor. Right : h-S diagram of a centrifugal compressor.

Inlet air is at pressure p_1 and speed C_1 . It is accelerated through the rotor up to speed C_{1b} . One can notice that static pressure p_{1b} has almost not increased (compared to p_1), but the kinetic energy has increased. This means that the gain of enthalpy through the rotor is due to the acceleration of the flow. After this first step, the fluid needs to increase its density, i.e. its pressure. That's the role of the diffuser, where an energy transfer occurs from kinetic to potential energy : the flow speed decreases along the diffuser to reach the value of C_2 whereas the static pressure increases to p_2 . At the final state, p_2 is almost equal to the final total pressure p_{02} . Entropy is created during the compression, which means that there are losses. Consequently a centrifugal compressor can be characterized by two parameters : the amount of energy transferred from the rotor shaft to the fluid (which is directly linked to the pressure drop across the compressor) and the efficiency of this process. The first law of thermodynamics allows to express this behavior via a mathematical

equation :

$$-\dot{W}_c = \frac{Q_m \cdot Cp \cdot T_{01}}{\eta_c} \left(\left(\frac{p_{02}}{p_{01}} \right)^{\frac{\gamma-1}{\gamma}} - 1 \right) \quad \eta_c = \frac{\left(\left(\frac{p_{02}}{p_{01}} \right)^{\frac{\gamma-1}{\gamma}} - 1 \right)}{\frac{T_{02}}{T_{01}} - 1} \quad (3.3)$$

Turbine : Turbocharger turbine is driven thanks to the energy of the exhaust gases. This energy is provided by the gases released by the exhaust valve and expanding toward the ambient pressure. As mentioned before, we will consider the case of radial flow turbines. Such devices are composed of a casing which collects exhaust gases, a nozzle with static or moving blades, and a rotor (Fig.3.6).

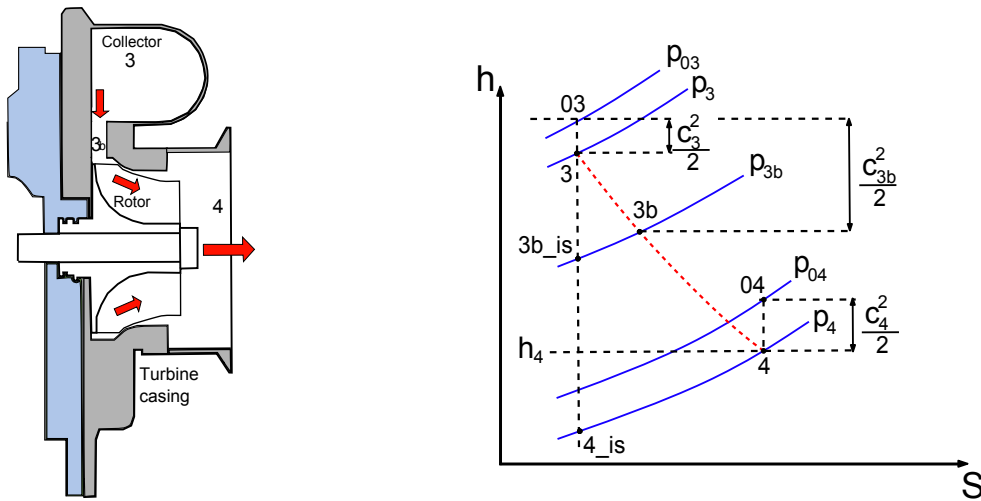


FIG. 3.6 – Left : Side view of a centrifugal turbine. Right : h-S diagram of a centrifugal turbine.

As in the compressor case, the h-S diagram of the thermodynamics processes through the turbine is plotted. The nozzle accelerates the flow to speed C_{3b} , which compensates the pressure loss ($p_{03b} \approx p_{03}$). In other words, it means that the total enthalpy h_{03b} is almost equal to h_{03} . Only the form of energy changes (pressure to kinetic energy) in the stator. The transfer of work occurs through the rotor, which is designed for minimum kinetic energy at the exit. Consequently, it is through the rotor that the total enthalpy exchange occurs ($h_{04} \ll h_{03b} \cong h_{03}$). VGT (Variable Geometry Turbines) are characterized by their nozzle having moving blades. For a full open nozzle, the area is maximal, so the flow is almost not accelerated. When the nozzle is almost closed, the area is minimum so maximum kinetic energy will be transferred through the rotor. The flow process is not isentropic for the flow through the turbine. Consequently a radial flow turbine can be characterized by two parameters : the amount of energy transferred from the fluid to the rotor shaft to the fluid and the efficiency of this process :

$$\dot{W}_t = Q_m \cdot Cp \cdot T_{03} \cdot \eta_t \cdot \left(1 - \left(\frac{p_{04}}{p_{03}} \right)^{\frac{\gamma-1}{\gamma}} \right) \quad \eta_t = \frac{1 - \left(\frac{T_{04}}{T_{03}} \right)}{1 - \left(\frac{p_4}{p_{03}} \right)^{\frac{\gamma-1}{\gamma}}} \quad (3.4)$$

3.3 Poppet valves

The valve is the most important restriction in the intake and exhaust system of internal combustion engines. They are indeed the main components which dictate the behavior of gas flow entering and exiting the cylinder. The introduction of variable valve timing (VVT) has allowed to develop innovative valve opening/closure laws in order to enhance the efficiency of the gas exchange processes. VVT devices combined

to turbocharger also allow to develop complex scavenging processes.

CFD and experimental tests have shown that the flow established at the valves is complex and dependent on the valve lift and the pressure ratio across the valve (see papers from Blair [6], Chen [22], Cheung [23] and Chalet [19]). At very low lifts, the flow remains attached to the valve head and seat. However at intermediate lifts, the flow separate from the valve head at the inner edge of the valve seat, leading to increased flow losses. The flow characterization of valves is generally performed using steady flow test benches. Blair et al. [9] have shown that the flow performance (mass flow rate for a given geometric flow area) can differ up to 40% from a valve geometry to another.

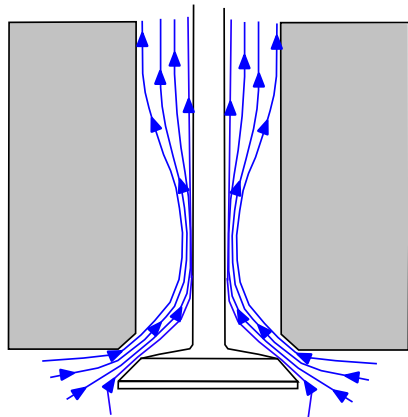


FIG. 3.7 – Example of poppet valve flow.

On standard engines, the valve opening/closure timing is imposed by the camshaft and is therefore fixed regarding the thermodynamical cycle occurring in the cylinder. In this case, the valve timing is optimized for a given operating point. Variable valve timing (VVT) by the means of multiple cam profiles, of eccentric actuation of the camshaft and of electro-hydraulic or electro-magnetic actuators has been introduced since the mid-90's. Description of these systems are available in the following papers by Matsuki [89], Flierl [44], Ferreri [42] and Picron [104]. VVT allows to adapt the valve timing to the operating point of the engine. This degree of freedom provides an additional lever to control the cylinder air flow, which can lead to a potential reduction of pollutant emission and fuel consumption for a given performance level.

3.4 Engine Control Unit (ECU)

The actuators of the engine air system are controlled by the Engine Control Unit. Modern ECUs use a microprocessor which can process the inputs from the engine sensors in real time. An electronic control unit is composed of a hardware and a software part. The hardware consists of electronic components on a printed circuit board. The software is stored in microcontrollers and synthesizes the engine control laws : the ECU receives inputs from sensors, and these data are processed in order to control the overall system. The control unit relies on static data-maps and on real-time models in order to command the actuators. The models and data-maps stored in the ECU have a direct impact on the control of the engine systems. It has been seen in the previous chapter that accurate models are a key in order to achieve predictive control.

Résumé : Contexte et enjeux de la thèse

L'automobile est le moyen de transport le plus répandu en Europe et aux États-Unis. Les véhicules équipés de moteurs à combustion interne combinent une fiabilité élevée à un faible coût de la source d'énergie. Néanmoins, les principaux inconvénients de ce système de propulsion sont les émissions de polluants, combinées à l'augmentation du prix des ressources d'énergie pétrolières..

Les premières lois sur les émissions polluantes des moteurs à combustion interne ont été créées dans les années 80. Ces décisions et événements ont conduit à la réduction d'émissions de polluants et de la consommation spécifique. Ces résultats sont le fruit d'évolutions qui ont été axées sur le rendement mécanique du moteur, sur le contrôle de la combustion et sur les systèmes de post-traitement. Dans le même temps, les constructeurs automobiles ont considérablement réduit le temps de développement de leurs véhicules, ce qui a permis de compenser partiellement le coût supplémentaire engendré par la recherche et développement. Cette amélioration de l'efficacité de développement est de plus en plus difficile à réaliser, car la complexité des systèmes associés est en hausse. En effet, les principaux développements en liens avec le moteur sont liés à un compromis entre les paramètres suivants :

- Les performances du moteur (puissance et couple).
- La consommation du moteur : de nombreux pays ont introduit une notation de la consommation du véhicule visible du client. Par conséquent, une consommation élevée peut nuire à l'image du véhicule, et donc sur son potentiel de vente.
- Le respect des lois gouvernementales limitant le rejet de polluants sur cycles normalisés..
- Le coût de production du moteur.

Il est proposé dans ce chapitre d'aborder de façon générale ces problématiques et d'étudier en quoi le contrôle moteur et les modèles mathématiques associés sont une réponse aux questions développées.

1.1 Respect des limites aux émissions de polluants par rapport aux coûts de production

Un des paramètres les plus limitants dans le développement d'un moteur automobile est devenu l'équilibre entre le respect des limites d'émissions polluantes et le coût de fabrication du moteur. Il y a 235 millions des véhicules personnels sur les routes en Europe, contribuant aux rejets de polluants dans l'air. Afin de limiter l'impact de l'automobile sur la santé et sur l'environnement, des lois limitant les émissions de polluant ont été mises en place. L'évolution de la législation diesel en Europe sont présentés sur la Fig. 1.1 : il apparaît que depuis 1995, les limites des émissions polluantes ont été considérablement réduites. Les limites d'émission de la norme Euro 6 sont, en moyenne, inférieures d'un facteur 10 aux normes Euro 2. Afin d'assurer le respect de ces limitations, les solutions technologiques suivantes ont été développées :

- Le contrôle de la combustion, qui est réalisée via le contrôle des espèces chimiques qui sont introduites

dans la chambre de combustion : l'air, le carburant, les gaz d'échappement recirculés. La manière dont la combustion se déroule est également étudiée.

- Les systèmes de post-traitement : dans ce cas, l'émission de polluants n'est pas évitée à sa source, mais des systèmes de filtres et catalyseurs sont placés en aval du cylindre, le long du conduit d'échappement.

Ces solutions présentent des efficacités diverses concernant la réduction des émissions, ainsi que des coûts de production différents. On estime que le contrôle de la combustion des moteurs automobiles permet de réduire les émissions de polluant d'un maximum de 60% (un niveau de 100% correspondant à une dépollution complète). Néanmoins, cette performance n'est pas suffisante pour répondre aux limites de la réglementation et des dispositifs de post-traitement doivent être utilisés. Ces systèmes permettent de réduire presque totalement les émissions de polluants, mais pour un coût relatif très élevé (jusqu'à 5 fois plus élevé que le contrôle de la combustion). Par conséquent, la solution la plus économique est d'éviter autant que possible la création d'émissions polluantes (via le contrôle de combustion) afin de réduire l'utilisation des systèmes de post-traitement. Les outils de modélisation moteur 0D / 1D peuvent jouer un rôle central dans le développement du contrôle lié à la combustion :

- Il est impossible de mesurer avec précision la quantité de gaz d'échappement recirculés qui entrent dans le cylindre. Cette quantité doit être évaluée par le biais de modèles [50].
- Les modèles 0D / 1D offrent un bon compromis entre précision et temps de calcul [122], [58].
- L'utilisation de modèles permet de réduire l'utilisation de bancs moteur, ce qui conduit à une potentielle réduction des coûts de développement.
- Cependant, la réduction drastique des limites d'émissions conduit à des exigences élevées en termes de précision de modèle.

1.2 Performances du moteur par rapport à la consommation de carburant

Depuis la crise pétrolière de 1973, la variation du prix des ressources pétrolières est largement relayé dans les médias. En outre, les incitations gouvernementales conduisent à une plus grande sensibilisation des consommateurs quant à la l'efficacité énergétique des produits. En conséquence, la consommation de carburant est devenue un paramètre essentiel dans le choix d'une voiture. Toutefois, dans le même temps, le confort et la sécurité des passagers ont connu une croissance exponentielle. La principale conséquence de cette évolution est l'augmentation de la masse des véhicules (+20% entre 1995 et 2009 en France, voir Fig. 1.4, graphique de droite). Cette augmentation de la masse a un impact direct sur la puissance du moteur nécessaire pour préserver les performances dynamiques des véhicules : la puissance moyenne des moteurs a augmenté de 35% entre 1995 et 2009 en France. Malgré cette augmentation de la puissance du moteur, la consommation moyenne a été diminuée de 20% durant la même période de temps, ce qui montre que des améliorations considérables ont été réalisées en ce qui concerne la consommation spécifique du moteur. Même si cette amélioration est spectaculaire, il faut noter que cette réduction de la consommation a été intégralement compensée par l'augmentation de 25% du trafic routier (Fig.1.3). La réduction de la consommation de carburant pourrait être beaucoup plus importante que les niveaux atteints aujourd'hui, mais il est nécessaires de préserver un certain niveau de performance. Afin de diminuer la consommation des véhicules routiers, il est possible de travailler sur les paramètres suivants :

- L'amélioration de l'efficacité du moteur. Afin d'améliorer ce paramètre, le travail est effectué sur la combustion, sur le remplissage et sur la réduction des frottements internes et ceux des accessoires.
- La réduction de la résistance au roulement. Les pertes à l'interface pneu/route représentent environ 21% de la consommation de carburant d'un véhicule [55].
- La réduction de la masse du véhicule. Réduire la masse d'un véhicule permet de réduire la résistance au roulement et le besoin en termes de puissance du moteur. Ce phénomène est visible sur la Fig. 1.4 :

depuis 2007, la masse moyenne des véhicules vendus en France est en baisse, tout comme la puissance des moteurs. En moyenne, une réduction de masse de 10% permet de diminuer la consommation de carburant de 10% (en supposant une adaptation de la transmission en encore avec la nouvelle masse [101]).

Une étude rapide paramétrique est proposée. Prenons un véhicule consommant 5.5L de carburant par 100 km. Le véhicule est équipé d'un moteur d'efficacité moyenne de 30%. Il est supposé que le rendement moteur est amélioré et passe de 30 à 31%. Cela conduit à une réduction de la consommation de carburant de 0,1774 L/100 km (3,23%). L'impact des autres paramètres est étudiée afin de parvenir à la même réduction de consommation de carburant :

- Optimisation de la traînée aérodynamique : il est nécessaire de diminuer de 16,15% les pertes dues à l'aérodynamique.
- La réduction de la résistance au roulement : il est nécessaire de diminuer de 15,38% les pertes dues au contact pneu/route.
- Réduction de la masse : d'après [101], une diminution de 3,23% de la masse du véhicule est nécessaire.

Il est conclu que le rendement moteur est le paramètre le plus sensible ne ce qui concerne la consommation de carburant, tandis que la réduction de masse reste un facteur également très influant. Il semble beaucoup plus difficile d'avoir un gain comparable à l'aide à l'amélioration de la résistance au roulement ou de l'amélioration de la traînée aérodynamique. Afin de réduire la consommation des moteurs, l'utilisation d'autres technologies est également envisagé. Ces dernières années, des systèmes tels que les systèmes hybrides, les dispositifs Stop/ Start / ou la motorisation entièrement électrique ont été développés et introduits sur le marché automobile. Cependant, les technologies de propulsion alternatives ont un indice de pénétration de marché que est encore très faible (moins de 1,7% en France en 2009, voir Fig. 1.2). Par conséquent, les technologies moteur dites 'standards' vont probablement rester l'un des principaux leviers de réduction de la consommation de carburant au cours des 15 prochaines années.

1.3 Réduction du temps de développement par rapport aux dépenses R & D

D'après la figure 1.1, on voit que la législation européenne impose un pas en avant en termes de dépollution des moteurs tous les 5 ans en moyenne. Cela conduit à une augmentation de l'aspect recherche et développement afin de se conformer à cette norme dans le temps imparti. Il est également nécessaire, d'un point de vue économique, de maintenir un équilibre entre les investissements et le chiffre d'affaires. L'évolution des dépenses R & D des dépenses et des effectifs entre 2000 et 2009 est indiquée sur le tableau 1.2 pour PSA, Renault et Volkswagen. Ces marques sont les trois plus grands constructeurs automobiles européens en termes de ventes dans le monde. Même si la stratégie adoptée par chaque groupe est différente en termes de recrutement et d'évolution des dépenses, une forte augmentation de la R & D (en investissement et/ou en effectif) est constatée depuis 2000. Néanmoins, dans leurs rapports annuels publiés (sources : [107], [111], [132]), ces entreprises affirment que le contrôle de leur dépenses R & D sera crucial dans les années à venir. Afin de réduire les dépenses en recherche et développement tout en conservant la tenue du calendrier de développement, les solutions suivantes sont adoptées il est nécessaire d'améliorer l'efficacité de recherche et développement. Dans ce cas, de nouveaux procédés et de nouveaux outils sont développés afin de d'améliorer l'efficacité globale.

1.4 Impact sur le contrôle moteur et les modèles moteurs associés

Le développement du contrôle moteur est crucial afin de réduire les niveaux d'émission de polluants et la consommation de carburant. Aujourd'hui, le développement du contrôle moteur est basé sur des modèles

de moteurs 0D-1D. De tels modèles permettent de mettre au point les lois de contrôle moteur et de les valider. Le développement des modèles en termes de précision et de temps de calcul a un impact direct sur la performance du contrôle moteur et sur la maîtrise des coûts de développement :

Réduction des temps de développement :

L'utilisation d'outils de modélisation pour évaluer les performances potentielles des lois de commande du moteur permet de réduire le nombre d'essais moteurs nécessaires à cette partie du développement. Les essais moteurs sont généralement coûteux en termes de temps et de dépenses. Le passage à des outils numériques dans le but de pré-évaluer les performances d'une solution permet d'utiliser les essais expérimentaux seulement comme un outil de validation finale. Par conséquent, le temps de développement global et le coût d'un projet peuvent être réduits par l'introduction des outils de modélisation dans le processus de développement des moteurs.

Passage d'un contrôle moteur curatif à un contrôle moteur prédictif : La plupart des paramètres de commande du moteur sont déterminés au moyen de cartographies. Ces cartographies sont la plupart du temps uniquement valable sur des points de fonctionnement stabilisés et introduisent des erreurs en transitoire. Par conséquent, des correctifs sont souvent mis en place afin de prendre correctement en compte les paramètres physiques du moteur. Cette approche accroît la complexité de la structure de la commande du moteur. Dans le cas où un modèle dynamique est mise en œuvre par l'ECU, les paramètres externes sont naturellement pris en compte par le modèle. Cela conduit à une meilleure estimation des valeurs de contrôle et une extension de la limites de validité. Mais le gain le plus important est obtenu par le développement de la commande prédictive plutôt que curative. Dans le cas d'un contrôle moteur basé sur des données statiques (cartographies), le contrôle est dit curatif : un capteur détecte un point de fonctionnement non optimal, cette information étant ensuite transmise à l'unité de contrôle afin de corriger le comportement. L'utilisation de modèles permet potentiellement de prédire l'évolution d'un paramètre. Si cette information est transmise à l'ECU, il est possible de rester en permanence sur le point de fonctionnement le plus optimal possible. Une telle approche a un très fort potentiel dans le cas de la réduction des émissions de polluants.

Par conséquent, il semble que les modèles 0D-1D sont la pierre angulaire du développement du contrôle moteur. Les deux paramètres suivants sont cruciaux concernant la validité d'une approche modèle pour le développement de moteurs :

Le degré de précision du modèle : Le degré de précision du modèle influe directement sur le développement des lois de commande. En effet, des modèles réduits sont utilisés pour estimer le comportement du système réel et cette estimation est elle-même utilisée pour le contrôlé du système réel. En termes de validation et de mise au point des lois de commandes, un modèle en bon accord avec le comportement réel du système permet de réduire les essais moteurs. Les besoins en termes de précision de modèles ont fortement augmenté : la réduction des émissions polluantes et de la consommation nécessitent aujourd'hui la prise en compte fine des phénomènes physiques du moteur.

Le temps de calcul : La complexité accrue des moteur a conduit à l'augmentation du nombre de sous-modèles mis en place dans un modèle complet du moteur. En outre, des modèles plus précis nécessitent généralement plus de temps de calcul. Toutefois, afin de rester compétitif, le temps de calcul des modèles doit être maintenu aussi bas que possible. Cette maîtrise du temps de calcul est généralement réalisée par l'amélioration des algorithmes de résolution ou par un réglage du ratio précision / temps de calcul.

Il est conclu que le développement d'outils de modélisation 0D-1D peut conduire à des résultats intéressants afin de répondre à la problématique du développement moteur. Il est cependant nécessaire de trouver

l'équilibre optimal entre le temps de calcul et la précision des modèles, en vue d'améliorer l'efficacité de la R & D. En effet, le développement par modèles n'est valable que si les modèles sont en accord avec le comportement du système réel. En outre, les modèles doivent être optimisés en termes de temps de calcul, afin de faire face à des temps de développement réduits. Le démarrage de cette thèse a été motivé par ces exigences.

2 Présentation des principaux composants et systèmes impliqués dans le contrôle de la chaîne d'air

Le système d'air est devenu un élément crucial dans le développement des moteurs modernes. En effet, ces systèmes sont devenus de plus en plus complexes afin d'adopter des stratégies de dépollution et pour permettre de réduire la consommation en carburant. Des actionneurs supplémentaires ont été introduits pour commander les flux aérodynamiques, ce qui conduit à une augmentation de la complexité du contrôle moteur. Les stratégies du système d'air sont au cœur du contrôle des espèces qui sont introduites dans le cylindre, et constituent donc un moyen rentable de réduire les émissions polluantes. Cette partie de la thèse portera sur les principaux éléments actionneurs du moteur. Des composants tels que les dispositifs de post-traitement ont aussi un impact sur le débit d'air. Il a néanmoins été décidé d'axer la thèse sur l'étude des éléments actionnés afin de contrôler l'évolution des débits gazeux du moteur. En conséquence, les dispositifs suivants seront présentés : les boucles EGR (et leurs actionneurs associés), les dispositifs de suralimentation et les soupapes.

2.1 Boucle EGR :

La recirculation des gaz d'échappement vers l'admission est une technique largement répandue dans le domaine du moteur diesel. L'introduction de gaz brûlés à l'intérieur de la chambre de combustion permet de diminuer la concentration d'oxygène et la température moyenne du gaz. Ces deux effets conduisent à la réduction des émissions de NOx. Dans le cas des moteurs à essence, les boucles EGR sont utilisées pour empêcher le cliquetis, permettant d'accéder à des charges plus élevées. Cependant, il y a une contrepartie à ces améliorations, car la diminution du taux d'oxygène combiné à la diminution de température va entraîner une augmentation de la production de suies. Les boucles EGR ont également un impact négatif sur la consommation de carburant, en raison du ralentissement du processus de combustion et de la contre-pression créée à l'échappement. Deux architectures EGR existent (on se référera à la figure 3.1 pour le schéma et la définition des indices) :

- Circuit EGR haute pression. Cette boucle est l'architecture la plus classique : une partie du débit de gaz est dévié du système d'échappement vers la partie haute pression de l'admission (en aval du compresseur). Le fait que la pression en amont de la turbine est généralement supérieure à la pression en aval de la compresseur est utilisé pour établir un flux naturel. Ce système est régi au moyens de la vanne EGR Th.2, de la vanne papillon Th.1 et de la position à géométrie variable de la turbine.
- Circuit EGR basse pression. Le débit de gaz d'échappement est dévié de l'aval du système de post-traitement (air recirculé dit 'propre') vers l'amont du compresseur. Ce système permet d'atteindre des températures plus froides et réduit le risque de pompage du compresseur (en comparaison de la boucle EGR haute pression). La boucle basse pression est régie au moyen de la vanne EGR Th.3, de la vanne à l'échappement Th.4 et d'une vanne placée en amont du compresseur Th.5.

Il apparaît que ces systèmes sont complexes à maîtriser, en raison du nombre élevé d'actionneurs et le fait que le système soit bouclé.

2.2 Systèmes de suralimentation La puissance maximale délivrée par un moteur d'une cylindrée donnée est directement liée à la quantité de carburant brûlée efficacement à chaque cycle. Cette quantité est limitée par la quantité d'air qui peut être introduite dans les cylindres. Par conséquent, et afin d'augmenter la puissance de sortie maximum de un moteur donné, l'air d'admission peut être compressé à une densité plus élevée que les conditions ambiantes avant d'entrer chaque cylindre. Pour un même moteur, la suralimentation augmente la puissance maximale et le couple maximum obtenus. Cette compression peut être effectuée au moyen des systèmes suivant :

Compresseurs mécaniques

Dans ce cas, un compresseur volumétrique est entraîné en utilisant la puissance mécanique prélevée au moteur. La plupart du temps, le lien entre le compresseur et le moteur est une courroie à entraînement direct, ce qui conduit à des problématiques afin d'obtenir des vitesses de rotation permettant d'atteindre des rendements satisfaisants. L'efficacité de ces dispositifs est en effet relativement faible (50%). Ce faible rendement associé à l'architecture à entraînement direct signifie qu'une partie importante de la puissance moteur est utilisé pour entraîner le compresseur (15% en moyenne). Enfin, ces dispositifs sont lourds et encombrants.

Compresseurs par onde de pression

Les systèmes de suralimentation par onde de pression utilisent l'action des ondes de pression afin de comprimer l'air d'admission. De tels systèmes sont complexes à contrôler et à intégrer sous le capot des voitures modernes. Ce dispositif est par conséquent inhabituel dans les applications automobiles.

Turbocompresseurs

Un turbocompresseur est composé d'une turbine et d'un compresseur montés sur le même arbre (voir Fig. 3.3). La turbine utilise l'énergie disponible pour entraîner le compresseur qui comprime les gaz d'admission. Dans notre étude, nous ne considérerons que les compresseurs et les turbines radiales, car seule cette architecture est utilisée dans les applications automobiles. La turbine peut être à géométrie fixe ou variable. Dans le cas d'une turbine à géométrie variable (VGT), des ailettes pivotantes sont placées en amont du rotor de la turbine. Ce dispositif permet de varier l'angle d'incidence et de la section des canaux d'écoulement des gaz d'échappement en amont du rotor turbine. Cela a un impact direct sur la quantité d'énergie transmise à l'arbre de la turbine. Le principal avantage de ces dispositifs est d'améliorer le temps de réponse du turbocompresseur et de permettre le contrôle de la pression de suralimentation. Les ailettes sont actionnées par le biais d'un actionneur pneumatique ou électrique. Les turbocompresseurs offrent un compromis intéressant entre le coût, la compacité et la performance. En outre, les turbocompresseurs sont devenus des éléments clés dans le contrôle de la recirculation des gaz.

Soupapes

Les soupapes sont des restrictions prépondérantes dans le système d'admission et d'échappement des moteurs à combustion interne. Ils sont en effet les principaux éléments qui dictent le comportement des flux de gaz entrant et sortant du cylindre. L'introduction de la levée variable des soupapes a permis de développer des lois d'ouverture / fermeture des soupapes permettant d'améliorer l'efficacité du processus d'échange de gaz. Les dispositifs de levée variable combinés aux turbocompresseurs permet aussi de développer des processus complexes de balayage. Les calculs aérodynamiques multi-dimensionnels et les tests expérimentaux ont montré que le flux créé au niveau des soupapes est complexe et dépend de la levée de soupape et du ratio de pression à travers la soupape (voir les papiers de Blair [6], Chen [22], Cheung [23] et Chalet [19]). Aux faibles levées, l'écoulement reste attaché à la tête de soupape et au siège. Cependant, dès les levées moyennes, le flux se sépare de la tête de soupape sur le bord intérieur du siège, conduisant à des pertes plus élevées. La caractérisation des flux de vannes est généralement effectuée à l'aide de soufflerie de culasse. Blair et al. [9]

ont démontré que la performance en terme de débit (débit massique pour une section géométrique donnée) peut varier jusqu'à 40% d'une géométrie de soupape à une autre.

Dans le cas le plus simple, la levée soupape est imposée par un arbre à came à géométrie fixe. Dans ce cas, le calage des soupapes n'est optimisé que pour un point de fonctionnement donné point, un compromis étant recherché pour les autres points de fonctionnement. Les système de distribution à levée variable par le biais de plusieurs profils de came, de décalage d'arbre à cames et des actionneurs électro-hydraulique ou électro-magnétique ont été mis en place depuis le milieu des années 90. Les descriptions de ces systèmes sont disponibles dans les papiers suivants : Matsuki [89], Flierl [44], Ferreri [42] et Picron [104]. Les systèmes à levée variable permettent d'adapter le calage des soupapes sur plusieurs points de fonctionnement du moteur. Ce degré de liberté constitue un levier supplémentaire pour contrôler le flux d'air du cylindre, avec un potentiel concernant la réduction des émissions de polluants et de la consommation de carburant pour un niveau de performance donné.

2.4 Contrôle moteur Les actionneurs du système d'air des moteurs sont commandés par le boîtier de contrôle moteur. Les calculateurs modernes utilisent un microprocesseur qui permet de traiter les entrées des capteurs du moteur en temps réel. Le logiciel de contrôle moteur est stocké dans des microcontrôleurs et synthétise les lois de commande du moteur. Le boîtier de contrôle reçoit les signaux provenant des capteurs, et ces données sont traitées afin de contrôler l'ensemble du système moteur. L'unité de contrôle se base sur des données cartographiques, ainsi que sur des modèles en temps réel pour commander les actionneurs. Il a été vu précédemment que des modèles précis sont essentiels pour parvenir à l'implémentation de commandes prédictives.

3 Objectifs et structure de l'étude

Les deux chapitres précédents ont souligné le rôle croissant joué par le contrôle moteur et le système d'air dans les moteurs modernes. En effet, les actionneurs du système d'air permettent de contrôler les espèces qui sont introduites dans le cylindre. L'estimation de ce paramètre est crucial pour le bon déroulement de la combustion. En outre, l'approche fondée sur modèles a un fort intérêt en termes de réduction des temps de développement et des coûts associés. En conséquence, la présente thèse portera sur la modélisation des composants pour le système d'air moteur. Les principaux travaux porteront sur les points suivants :

- La modélisation des phénomènes physiques se produisant au travers des restrictions de la chaîne d'air du moteur. Ce paramètre est crucial afin d'assurer la prédictibilité des modèles et du contrôle moteur qui en découle.
- La maîtrise du temps de calcul des modèles, ce qui assure l'attractivité et l'efficacité de l'approche par modèles plutôt que entièrement expérimentale.
- Le compromis entre la précision des modèles et la corrélation expérimentale requise pour atteindre ce niveau de précision. De nombreux modèles se basent sur des recalages expérimentaux afin d'allier précision du modèle et temps de calcul réduit. Cette étape introduit des coûts ainsi que du temps de développement supplémentaires.

Il a été décidé de concentrer la thèse sur les éléments qui sont commandés via des actionneurs de manière à contrôler la composition des flux gazeux entrant / sortant du cylindre. Cela signifie que les dispositifs de post-traitement ne seront pas inclus dans la présente étude. Toutefois, les turbocompresseurs, les restrictions et les modèles de soupapes seront au centre des développements de cette thèse

Structure de la thèse : Le présent document a été organisée en deux parties principales :

1 : Échanges gazeux au sein des turbocompresseurs :

La première partie technique de la thèse portera sur les modèles moyens (0D) du turbocompresseur.

Le premier chapitre présente l'étude bibliographique effectuée sur les modèles moyens des turbocompresseurs dédiés aux applications automobile. Les principales structures de modèles de turbocompresseur sont détaillées. Les avantages et les limites des modèles introduits sont analysés en regard de la problématique de développement de lois de commande et de mise au point.

Le dispositif expérimental utilisé pour l'étude des turbocompresseurs dans cette thèse est détaillé dans le deuxième chapitre. Une étude du niveau de la précision des capteurs est également proposée. Le but de ces tests de turbocompresseurs a été d'identifier certains phénomènes physiques et d'obtenir des données en vue de valider les modèles développés.

Le troisième chapitre introduit les modèles de turbines radiales et de compresseurs radiaux proposés dans cette thèse. Les développements mathématiques et les hypothèses thermodynamiques associées sont détaillées. les résultats des modèles sont testés sur trois turbocompresseurs différents et comparés aux résultats de modèles de la littérature. La validation finale est obtenue à partir d'une comparaison entre les résultats du modèle proposé et les données expérimentales.

Le quatrième chapitre traite de la modélisation des échanges thermiques dans les turbocompresseurs automobiles. En effet, une partie non négligeable de la chaleur à la turbine est transférée au compresseur, modifiant ainsi l'équilibre thermodynamique du turbocompresseur.

2 : Les échanges gazeux à travers les processus de flux de restrictions :

La deuxième partie technique de la thèse est consacrée à la modélisation des restriction de la chaîne d'air moteur.

Le premier chapitre présente l'étude bibliographique effectuée. Les principaux modèles de restrictions sont présentés et leurs performances en termes de précision, de prédictibilité et de temps de calcul sont analysés. Les principaux schémas numériques introduits dans la littérature afin de résoudre le problème aux limites sont également introduits. Enfin, la notion de correction d'entropie est introduite.

Dans un deuxième chapitre, le dispositif expérimental dédié à l'étude des restrictions est détaillé. Les modèles aérodynamiques multi-dimensionnels sont également introduites dans ce chapitre. Les résultats de ces calculs multi-D seront utilisés, dans certains cas, comme 'référence'.

Le troisième chapitre présente les développements proposés au sujet des schémas numériques itératifs numériques afin de résoudre le problème des conditions limites. Ces schémas numériques ont un fort impact sur le temps de calcul et sur la précision des résultats.

Le sujet du quatrième chapitre est la modélisation mathématique des restrictions de la chaîne d'air moteur. Les modèles proposés sont détaillés, ainsi que leur processus de résolution. Les équations et les hypothèses introduites afin de construire les modèles ont une influence directe sur la précision du modèle. Les équations ont également un impact sur les schémas numériques mis en place pour résoudre le problème aux

conditions limites.

Enfin, les résultats des modèles sont comparés aux résultats expérimentaux. Cette validation est effectuée dans le cas d'écoulements permanents et transitoires. Cela permet de distinguer l'influence des modèles mathématiques de ceux des schémas numériques. L'accent est mis sur le niveau de précision atteint sans introduire de coefficient correctif expérimental. Les performances en termes de temps de calcul sont également étudiées.

Publications :

- 'Implementing turbomachinery physics into data map-based turbocharger models'. G. Martin, V. Talon, P. Higelin, A. Charlet, C. Caillol. *SAE Int. J. Engines* **2**(1) : 211-229, 2009.
- 'Physics-based diesel turbocharger model for control purposes'. G. Martin, V. Talon, T. Peuchant, P. Higelin, A. Charlet. *SAE paper* 2009-24-0123, 2009.
- 'Pressure ratio-based method for non-isentropic inflow valve boundary conditions resolution'. G. Martin, P. Brejaud, P. Higelin, A. Charlet. *SAE paper* 2010-01-1052, 2010.

Part II

Gas exchange processes through turbochargers

Chapter 4

Literature review

Real-time models of turbochargers are usually based upon performance datamaps. These models are easy to put into place, require low CPU charge and are control-oriented. Data relative to compressor and turbine are read from tables : pressure ratio and efficiency are determined as functions of mass flow rate and rotary speed on two distinct data maps. A first method to build the data maps relies on experimental characterization from the suppliers. As only higher turbocharger rotational speeds data are mapped and as data are poorly discretized, specific extra-interpolation methods are implemented. A second method to build these data maps is based on turbomachinery equations resolution. The goal of this approach is to calculate the energy dissipation which occur through the compressor and the turbine. The two first parts of the present literature review will focus on these extrapolation methods and turbomachine models.

Some studies have shown that heat is transferred between the compressor, the turbine and the oil. This heat has a non-negligible effect on the turbomachines performances. Therefore, the direct use of the turbocharger data maps implies that the heat transfer conditions are the same than on the test bench. This is not the case on real application, where for example, the turbine inlet temperature is not a constant parameter. Based on these experimental observation, some turbocharger thermal models have been developed to take into account the heat transfers which occur inside the turbocharger. The last part of the literature review will be focused on these models and on experimental from the literature. results.

4.1 Extrapolation and interpolation of experimental turbocharger data maps

Moraal and Kolmanovsky [94] have investigated the reasons why extrapolation and interpolation techniques are required to use turbocharger experimental data maps. It appears that while engine mapping usually covers the entire operating range, the situation for the turbocharger is different. It is possible to obtain the performance characteristics from the supplier. However, turbocharger characteristics are typically only mapped for higher turbo speeds and pressure ratios, whereas the operating range on the engine extends down to 10krpm shaft speed and pressure ratios close to one. This is shown on Fig.4.1. As a result, standard interpolation methods generally fail to produce reasonable results outside the region where experimental data is available. In fact, due to the non-linear nature of the compressor and turbine characteristics, even interpolation through lookup tables has been found to cause unacceptable performances. This is the reason why some authors have introduced extrapolation and interpolation methods specifically for turbochargers.

The most widespread turbocharger data maps extrapolation method has been developed in 1991 by Jensen et al. [69]. This model is based on the non-dimensional parameters definition by Winkler [137] and Benson [4]. The compressor work is expressed in terms of the dimensionless head parameter, ψ which is defined in equation 4.1.

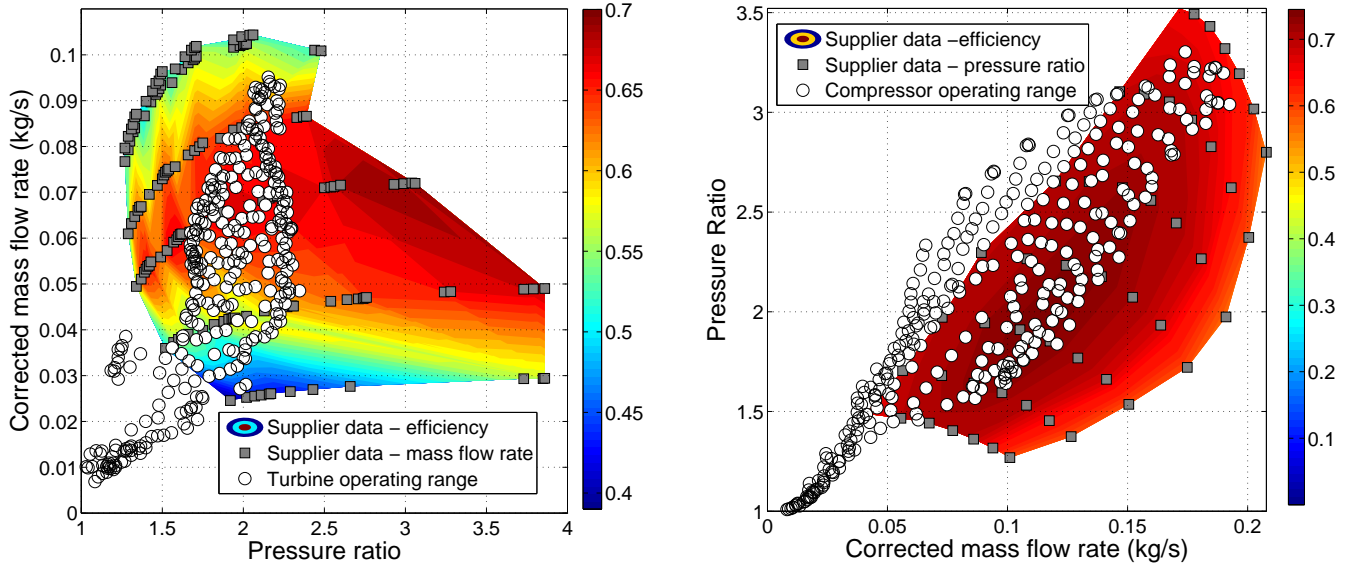


FIG. 4.1 – Typical compressor (left) and variable geometry turbine (right) maps. Compressor and turbine operating range determined from engine mapping have been superimposed. Turbine map shows mass flow rate for 6 VGT settings.

$$\psi = \frac{C_p T_{amb} \left[\left(\frac{p_{01}}{p_{amb}} \right)^{\frac{\gamma-1}{\gamma}} - 1 \right]}{0.5 U_c^2} \quad \text{with} \quad U_c = \frac{\pi}{60} d_c \omega_t \quad (4.1)$$

A dimensionless mass flow rate parameter is also introduced, in order to express compressor mass flow rate and Mach number at the inlet of the compressor :

$$\phi = \frac{Q_m}{\rho_{amb} \cdot \frac{\pi}{4} \cdot D_c^2 \cdot U_c} \quad M_{inl} = \frac{U_c}{\sqrt{\gamma R t_{amb}}} \quad (4.2)$$

Head parameter ψ , as well as the efficiency η_C can both be expressed as functions of the dimensionless flow rate ϕ and the inlet Mach number M_{inl} . For the head parameter, the following form was used :

$$\psi = \frac{k_1 + k_2 M_{inl} + k_3 \phi + k_4 M_{inl} \phi}{k_5 + k_6 M_{inl} - \phi} \quad (4.3)$$

The efficiency has been expressed as a second order dependent on ϕ for a given Mach number. The coefficient are then expressed as a function of the Mach number, as shown in equation 4.4.

$$\eta_C = \frac{a_1 + a_2 M_{inl}}{a_3 - M_{inl}} \phi^2 + \frac{a_4 + a_5 M_{inl}}{a_6 - M_{inl}} \phi + \frac{a_7 + a_8 M_{inl}}{a_9 - M_{inl}} \quad (4.4)$$

Parameters k_i et a_i are determined via least square method based on supplier data map. In their paper, Jensen and Kristensen point the issue that even though compressor interpolation provides good results for low rpm, the agreement is not as good for higher compressor speeds. This illustrated on Fig. 4.2. The second issue is that the overall model validity is linked to the accuracy of experimental data and on the algorithm. As the proposed extrapolation method is based on polynomial formulation and not on physical equations, the quality of extrapolated data is not guaranteed.

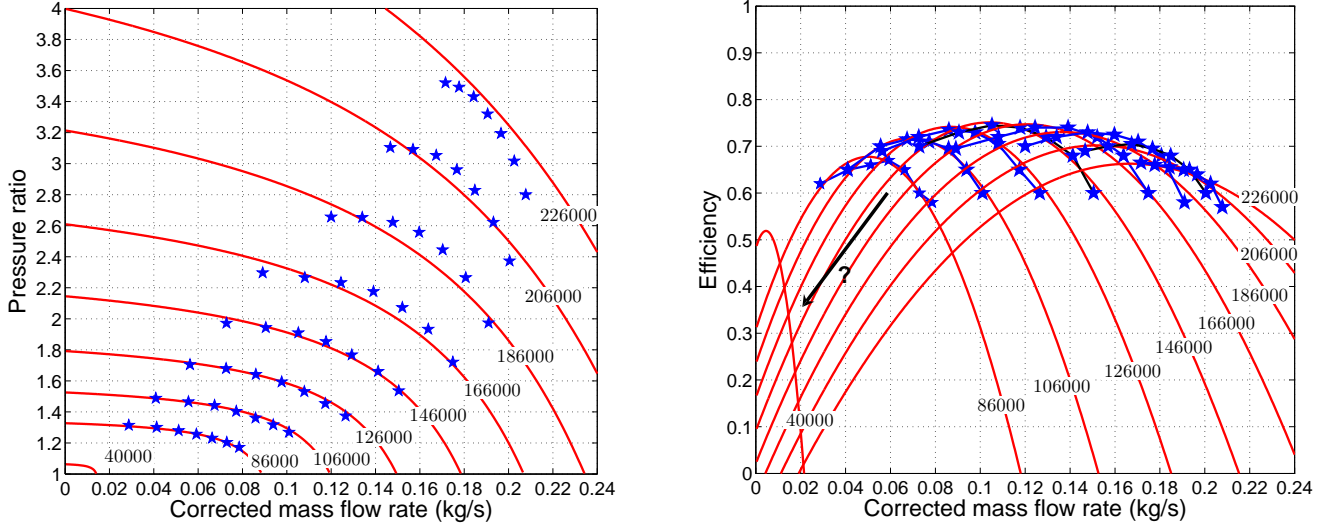


FIG. 4.2 – Comparison between data from supplier maps (stars) and the Jensen extrapolation [69] (solid lines) for various compressor speeds.

Regarding the processing of turbine data maps, the same global approach is used by Jensen. The idea is to model the turbine as a variable nozzle area (function of rotational speed and of pressure ratio across the turbine) to get the turbine flow (Eq.4.5, Eq.4.6). Differentiating two cases depending on P_{it} allows to take into account choked flow. In order to modify the nozzle area as a function of the entry parameters of the turbine model, Jensen introduced the empirical function developed in Eq.4.7 where parameters k_i are determined via a least square algorithm.

$$Q_m = F_t \sqrt{\frac{2\gamma}{\gamma-1} \left[\left(\frac{p_4}{p_{03}}\right)^{\frac{2}{\gamma}} - \left(\frac{p_4}{p_{03}}\right)^{\frac{\gamma+1}{\gamma}} \right]} \quad \frac{p_4}{p_{03}} > \frac{2}{\gamma+1}^{\frac{\gamma}{\gamma-1}} \quad (4.5)$$

$$Q_m = F_t \sqrt{\gamma \left(\frac{2}{\gamma+1}\right)^{\frac{\gamma+1}{\gamma-1}}} \quad \frac{p_4}{p_{03}} < \frac{2}{\gamma+1}^{\frac{\gamma}{\gamma-1}} \quad (4.6)$$

$$F_t = \frac{k_1 \cdot N_{turb} + k_2}{\frac{1}{P_{it}}} + k_3 \cdot N_{turb} + k_4 \quad (4.7)$$

The efficiency is essentially a function of the ratio between the isentropic expansion velocity and the turbine tip speed [4]. However and as noticed by Jensen et al., available efficiency data are most of the time available only for a narrow region. Fig.4.3 shows that it can be difficult to fit a quadratic function on regular data, particularly for higher rotational speeds. In this peculiar case, one can see that for higher rotational speeds, curves trends appear to be totally inadequate. In his paper, Jensen states that he had to impose end points for low and high values of the speed tips based on trends shown by Benson in his work [4]. Therefore, Jensen turbine efficiency treatment appears to be extremely dependent upon the quality of data. This method requires to be corrected 'by hand' by the user when trends can not be determined by the algorithm, which means that efficiency extrapolation is based on user's interpretation rather than physics. However, the same figure shows that turbine mass flow rate extrapolation is in excellent agreement with experimental data. In addition, as we know that pressure ratio should be of 1 for a nil mass flow rate, extrapolation towards lower rotational speed is not an issue.

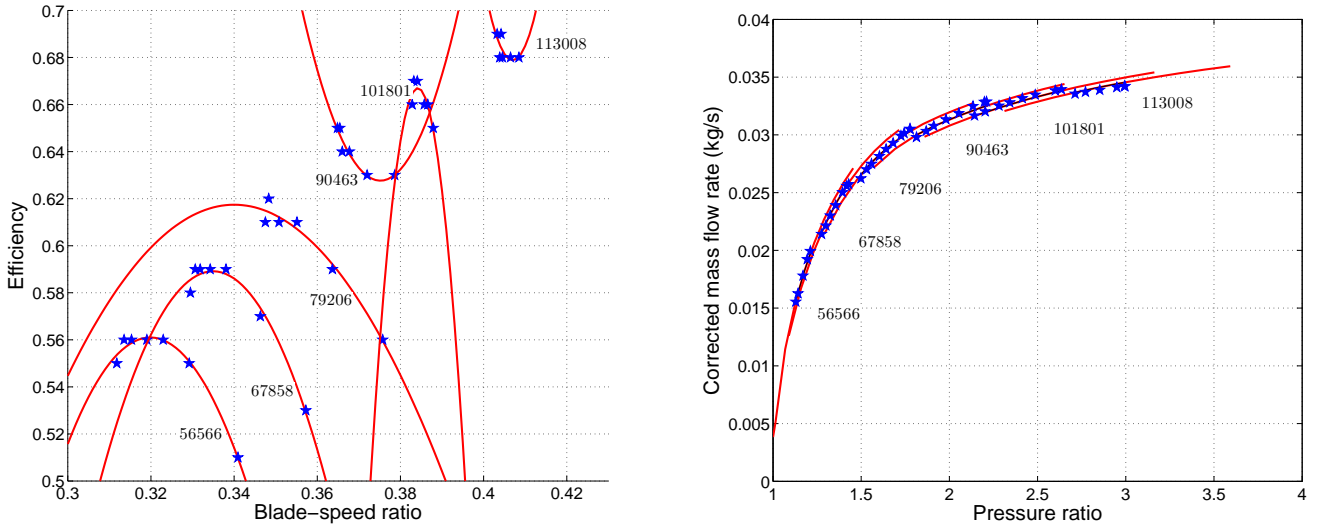


FIG. 4.3 – Comparison between data from supplier maps (stars) and the Jensen extrapolation [69] (solid lines) for various turbine speeds (1 VGT position).

While any of the turbine data maps extrapolation treatments found in the literature ([58], [94], [5],[63], [79], [54] are similar to Jensen's approach, other development of compressor models have been found. In his master's thesis [95], Mueller derives a compressor model from first principle and uses experimental data in order to parameterize its model. In the end, he proposes to model the head parameter ψ as a quadratic function of the dimensionless mass flow rate ϕ : $\psi = A\phi^2 + B\phi + C$, with coefficient A, B, C dependent upon blade tip speed U_C . From [94], it appears that this method requires as many fitting parameters as Jensen's method (9) and does not solve the accuracy issue at higher compressor rotational speeds. Additionally, extrapolation towards low speeds area produces inconsistent trends.

Kolmanovsky's compressor model detailed in [94] expresses the compressor flow parameter ψ as a function of compressor pressure ratio and turbocharger reduced speed. It implies the use of an exponential function, which allows to reduce the number of fitting parameters to 6. However, in the same way as Mueller's model, extrapolation towards low speed values appear to be unsatisfactory.

Some authors have tried to use neural networks ([94], [43]) to build a mean-value compressor model. They considered networks with one hidden layer and 3 to 5 neurons to represent compressor flow and efficiency maps. A network with n_u inputs (in our case $n_u = 2$ as inputs are mass flow rate and turbocharger shaft speed), one hidden layer containing n_n neurons and n_y outputs. In the case where two distinct neural networks are considered to build the pressure ratio and efficiency maps, each neural network will have one output ($n_y = 1$). In the case where the same neural network is used to build both data maps, there will be two outputs ($n_y = 2$). Such neural networks require $(n_u + n_y + 1) * n_n + n_y$ coefficients to be fitted. In the case where two distinct 5-neuron networks are built for the pressure ratio map and the efficiency map, a total of $2 * 21 = 42$ parameters have to be fitted, which is a large number when compared to the typical 25 – 40 points usually available on suppliers' data maps. In the case where the same network is built to produce both pressure ratio and efficiency (2 outputs), 27 parameters need to be fitted. But this large number of parameters is not the main drawback of neural networks applied to mean value modeling of compressors. Moraal [94] has shown that the convergence of the optimization process is not guaranteed, even when commercial codes toolboxes are used. Additionally, it is impossible to control in advance the quality of the extrapolated data, and more importantly, there is no criterion (excepting user's appreciation) to measure it.

This literature review of the existing turbocharger extrapolation/interpolation methods has shown that such methods rely only on few physical equations. Mathematical formulations are determined from experimental observations and parameters are determined by regressive analysis based on supplier's data maps. It appears that 1991 method developed by Jensen et al. [69] provides the most satisfying results among tested treatments. However, great improvements should be achieved regarding the extrapolation of compressor and turbine efficiency. The quality of the interpolation of compressor pressure ratio at higher rotational speeds should also be improved.

Interestingly, it appears that neural network do not seem suited for building such models. Indeed, most of the data map area needs to be extrapolated.

4.2 Building of turbocharger data maps based on turbomachinery equations

Analytical modeling of turbomachinery components and systems has been used for more than a century to develop new machines and understand internal flow states. The development of a 0D/1D turbomachine model based on physical equations can be divided in two parts :

- In a first step, isentropic performance (no losses) of the turbomachine is determined using thermodynamics and aerodynamics formulations.
- In a second step, the losses which occur within the turbomachine are determined using various types of models. By the combination of the isentropic performances and of the losses, it is possible to build complete performance data maps.

It is proposed in this section to review the main analytical models of turbochargers based on turbomachinery physical equations development.

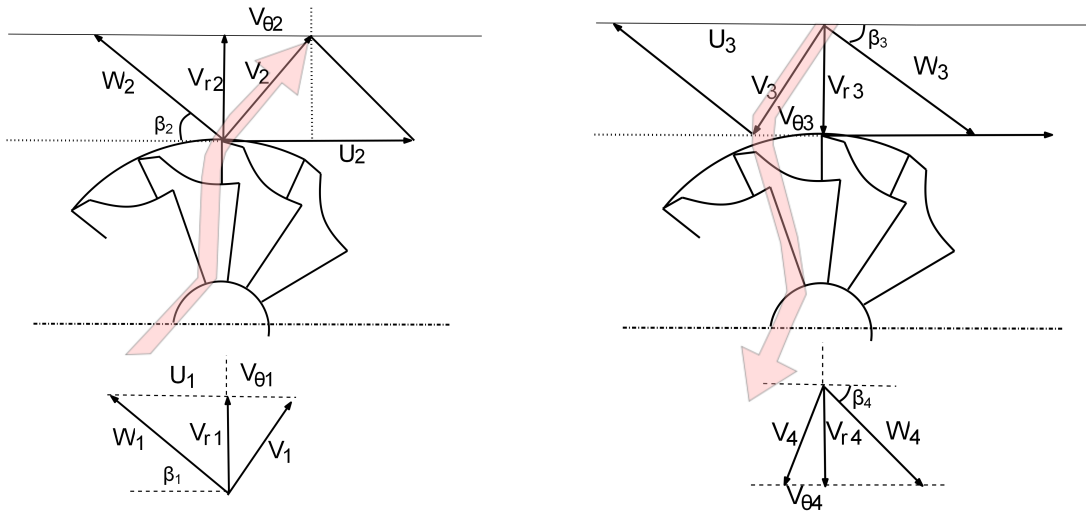


FIG. 4.4 – Speed characteristics triangle of a centrifugal compressor (left) and a centrifugal turbine (right)

4.2.1 Turbomachine thermodynamical performance

The formulation of the enthalpy change across radial turbomachines will be developed in this subsection. The notations introduced for the compressor case are explained below. They can be extended to the turbine

case without difficulty. On Fig.4.4, U is the tangential speed of blades, V is the absolute speed of the fluid exiting the rotor, W is the speed of the fluid in the system of coordinates linked to the rotor (ie. it rotates). We can define between these parameters what is called the two triangles of the characteristic speeds for a centrifugal compressor : subscript '2' is related to the values at the exit of the rotor, while subscript '1' is related to the entering ones. The angles β_1 and β_2 are the geometric angles of the blades at the inlet and the exit of the rotor, so they are fixed for a given compressor. Considering the parameters introduced just above, we can now develop Euler's equation applied to turbomachines (ref [106]). First of all, we can express the torque applied on the blades by the flow, related to the mass flow rate, and then deduce Eq.4.9 from Euler's equation in the case of the compressor :

$$T_{comp} = \dot{Q}_m \cdot (r_2 V_{\theta 2} - r_1 V_{\theta 1}) \quad (4.8)$$

$$\Delta h_{comp} = U_2 V_{\theta 2} - U_1 V_{\theta 1} \quad (4.9)$$

Indexes 3 and 4 provide the equivalent parameters for the turbine case (Fig.4.4, right). The equivalent development as in the compressor case provide the following equation for the turbine :

$$T_{turb} = \dot{Q}_m \cdot (r_4 V_{\theta 4} - r_3 V_{\theta 3}) \quad (4.10)$$

$$\Delta h_{turb} = U_4 V_{\theta 4} - U_3 V_{\theta 3} \quad (4.11)$$

One can see from the previous equations that the performances of the compressor and of the turbine are directly linked to the turbocharger speed (via U) and to the flow tangential speeds. Upstream flow tangential speeds $V_{\theta 1}$ and $V_{\theta 3}$ are determined from the upstream flow conditions. Downstream flow tangential speeds $V_{\theta 2}$ and $V_{\theta 4}$ are dependent upon the turbomachines geometry. These speeds need to be determined in order to calculate the turbomachine performances. In fact, a rigorous and widespread method [66] is to calculate the turbocharger performances by the resolution of the complete 1D -OD flow solution : 1D aerodynamical equations are solved in a rotational system of coordinates and then coupled to the turbomachinery flow losses models.

4.2.2 Turbomachine fully-physical-based calculation

The first step in order to build a fully-physical 1D-0D model of a turbocharger is to solve the isentropic flow equations. These equations are the 1D mass, energy and momentum conservation laws. They must be written in the case of a rotational flow. The development of such equations in the turbocharger case are detailed by Bozza [15]. Once this 'ideal' flow is calculated, it is necessary to take into account the losses occurring within the turbomachine.

Losses models are based on experimental observations, which have been broadly accepted over the past years. The state of the art of the turbomachines losses modeling is precisely described by Japikse [66], and most of 1D turbocharger losses have also been described by Watson [134].

From the literature study, losses occurring within a radial turbomachine can be classified into the following sections :

- Profile or boundary shear layer losses. They are created by the mean of the thin viscous shear layer along flow passage surfaces. Some frictional losses model based on flow Mach number and on frictional coefficient estimation are detailed in papers by Watson [133], Ferguson[41] and Macek [82].
- Secondary flow losses. The transport of fluid elements of different velocity levels under turning pressure gradient causes the development of vorticity. Much of the kinetic energy associated to this process is dissipated. Models related to this type of losses within radial turbomachines have been developed by Dean et al. [68], [31] and Japikse et al. [65], [102].

- Clearance losses. Such losses are due to tip clearance spillage and leakage through seals. An example of leakage models is provided by Descombes [33], [34].
- Exit mixing losses. These losses take into account the non-uniformity in terms of flow speed of the blade wakes, as in the case of airplane wings. This leads to a drop of total pressure available after the blades. This is illustrated on Fig.4.5. The approach regarding this phenomenon has been developed by Stewart [120].
- Slip of the flow. Even though the air flow is guided by the blades, there will be a deviation between the exit angle of the flow and the geometric angle of the turbomachine blades. This deviation angle is dependent upon the number of blades (the more blades there are, the lower the deviation angle is) and upon the geometry of the blades ([106]). The slip factor expresses the ratio between the turbomachine blades tangential speed and the flow tangential speed : $\sigma = \frac{V_{theta}}{U}$. The slip factor is usually calculated by the mean of empirical formulations, and the most commonly used formulations are found in the following papers : [136], [121], [46] [106]. It appears that some of the other flow losses have an impact on the slip factor (i.e. secondary flow losses, exit losses). Therefore, their use combined to a slip factor model is subject to caution.
- Disk friction. When a disk is rotated in a fluid, there is a resistive torque generated by the tangential shear component between the disk and the fluid. Even though the aerodynamical phenomenon is similar to the profile losses case, it is important to distinguish the two processes and to take them into account. Ferguson showed some modeling results correlation in [41].
- Sonic flow losses. For highly accelerated flows, shock waves are created and entropy is generated. This phenomenon is naturally taken into account by a nozzle flow model, such as the one shown by Macek [82].
- Some authors [15], [96], [34] are also introducing an ‘incidence loss’ theory, which has been first introduced by Spannake [119]. According to Bozza, it is assumed that the kinetic energy associated with the flow component normal to the blade direction is completely dissipated at a constant pressure. Japikse [66] refers top this model as a ‘simplified and less physically-driven’ secondary flow losses model and that it would be unnecessary if the previous losses models could be properly implemented.

This overview shows that at least 6 distinct losses models should be implemented in order to build a physically-driven turbocharger losses model. The building of these models requires many data to be built, mainly the geometry of the turbocharger. When such models are correctly implemented, it is possible to get an estimation of the pressure ratio characteristics and of the efficiency within 10% of the test bench results. However, in most cases, specific geometry of the turbomachines are unknown.

In the case where the turbocharger data map is available, it is possible to correct the mathematical model. An interesting approach has bee adopted by Macek [82], [83], as he defined a simple physical model of a radial turbine in order to identify the parameters relative to the flow losses. These parameters are then determined via an optimization algorithm fed by the data maps provided by the turbocharger suppliers.

4.3 Thermal transfers within turbochargers

The first detailed analysis of the impact of thermal transfers on thermodynamical performances of turbochargers has been shown in 1981 by Rautenberg et al. [109] [110]. By the mean of experimental tests, they measured that compressor and turbine do not work adiabatically. Some of the turbine heat power is transferred towards ambient, center housing, compressor housing and hydrodynamical bearings. Those heat transfers imply turbine outflow temperature decrease, as well as compressor outflow temperature increase. From compressor and turbine thermodynamical equations 4.12 and 4.13, a decrease of turbine outflow temperature T_{04} due to heat losses (for a constant inlet temperature T_{03}) will artificially increase the turbine efficiency. In the same way, increase of the compressor outflow temperature T_{02} due to heat exchange will

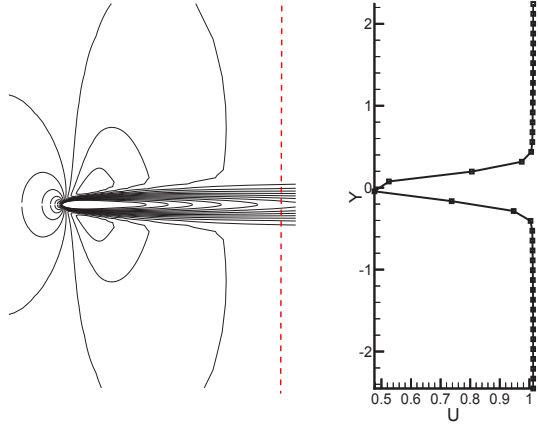


FIG. 4.5 – Subsonic flow of viscous fluid around a NACA0012 wing. Upstream Mach number is set to 0.85 and $Re = 500$. On the left, iso-values of Mach number. On the right, longitudinal flow speed evolution along the capture line (red dotted line on the left figure). [27]

artificially decrease its isentropic efficiency :

$$-\dot{W}_c = \frac{Q_m \cdot Cp \cdot T_{01}}{\eta_c} \left(\left(\frac{p_{02}}{p_{01}} \right)^{\frac{\gamma-1}{\gamma}} - 1 \right) \quad \eta_c = \frac{\left(\left(\frac{p_{02}}{p_{01}} \right)^{\frac{\gamma-1}{\gamma}} - 1 \right)}{\frac{T_{02}}{T_{01}} - 1} \quad (4.12)$$

$$\dot{W}_t = Q_m \cdot Cp \cdot T_{03} \cdot \eta_t \cdot \left(1 - \left(\frac{p_{04}}{p_{03}} \right)^{\frac{\gamma-1}{\gamma}} \right) \quad \eta_t = \frac{1 - \frac{T_{04}}{T_{03}}}{1 - \left(\frac{p_{04}}{p_{03}} \right)^{\frac{\gamma-1}{\gamma}}} \quad (4.13)$$

This means that effective compressor shaft power \dot{W}_{Csh} will differ from the compressor power estimated by the mean of temperature measurement \dot{W}_C . The same issue occurs at the turbine between turbine shaft power \dot{W}_{Tsh} and \dot{W}_T .

Rautenberg et al. have shown that turbine isentropic efficiency could be greater than 1 under given conditions and conclude that the turbine efficiency measured on a test bench when heat exchange occurs does not represent the aerodynamical quality of the turbomachine and should not be used to calculate the shaft power. From adiabatic tests and non-adiabatic tests comparison, they proposed a new efficiency formulation :

$$\eta_{C,adia} = \frac{\eta_{C,non-adia}}{1 - \eta_{C,non-adia} \cdot \varepsilon_C} \quad (4.14)$$

$$\eta_{T,adia} = \eta_{T,non-adia} - \varepsilon_C \quad (4.15)$$

$$\varepsilon_C = \frac{\Delta h_{C,adia}}{\Delta h_{C,isent}} \quad (4.16)$$

$$\varepsilon_T = \frac{\Delta h_{T,adia}}{\Delta h_{T,isent}} \quad (4.17)$$

Where isentropic enthalpy change for compressor and the turbine are respectively : $\Delta h_{is} = U_2 V_{\theta 2} - U_1 V_{\theta 1}$ and $\Delta h_{is} = U_4 V_{\theta 4} - U_3 V_{\theta 3}$. ε_C and ε_T are the endothermal and exothermal degrees of the compression and the expansion.

Similar observations and adiabatic efficiency formulations have been developed by Friberg et al. [48], and Frelin [47]. However, even though each developed model takes into account the change of efficiency due to heat exchange, it should be noticed that they are static models based on data maps and do not take into

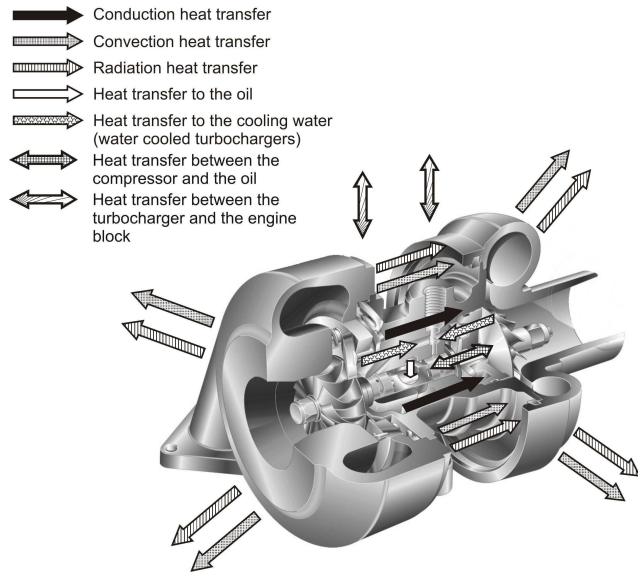


FIG. 4.6 – Mechanisms of heat transfer in/from the turbocharger. [118]

account transient heat exchange processes.

In order to deal with transient phenomenon, authors have introduced conduction, convection and radiation heat transfer models based on experimental or numerical correlation. These models are based on the link between the heat flow rate density $\varphi = \frac{\phi}{S}$, which is the heat flux per unit of surface [$W.m^{-2}$], to a difference of temperature. This relationship implies the introduction of the heat exchange coefficient h [$W.m^{-2}.K^{-1}$], which is the proportional coefficient between the heat flow rate density and the temperature difference (Eq.4.18).

$$\varphi = h (\Delta T) \quad (4.18)$$

This formulation allows to deal with the 3 types of heat exchange taking place within the turbocharger (Fig.4.6) : convective, conductive and radiative heat exchange processes :

Conduction heat transfer : Conduction transfers occur within the turbocharger as turbine casing and compressor casing are physically linked and conduction also occurs through the shaft. Cormerais [26] has shown in his thesis that the use of lump models both for turbine and compressor casing is a valid hypothesis. Lump models mean that the temperature is supposed to be uniform within compressor and turbine casing, which allows to reduce the problem to only one spatial dimension along the turbocharger shaft. Multi dimensional numerical studies [12], [13], [11], [26] have shown that the conductive heat transfer within turbochargers is essentially one-dimensional (Fig.5.1) .

For conduction exchange, thermal resistance $R = \frac{e}{\lambda S}$ is introduced and provides a relationship between the equivalent length of the casing e [m], the material of the casing conductivity λ [$W.m^{-1}.K^{-1}$] and the exchange surface. The use of Fourier's law (Eq.4.19) combined to steady state numerical or experimental data allows to identify the heat exchange coefficient h . Indeed, once φ is experimentally or numerically known for a given temperature difference ΔT , h can be directly calculated.

$$\phi = \varphi \cdot S = \frac{\lambda}{e} S \Delta T \Rightarrow h = \frac{\lambda}{e} \quad (4.19)$$

Once the heat exchange coefficient is known, a transient model is generally derived using lump models and

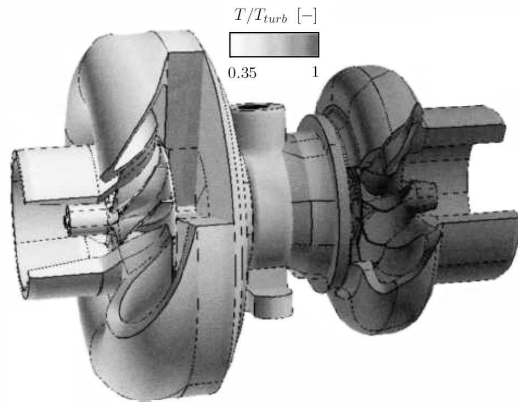


FIG. 4.7 – Non-dimensional temperature distribution of the casing walls of a turbocharger. Reference temperature is the maximum temperature at the turbine. [11]

the conservation of energy [26], [116], [118], [117]. For a given casing (compressor or turbine) at temperature T and submitted to an external temperature T_a via conduction heat exchange, Eq.4.20 can be derived and this allows to calculate the evolution of temperature T .

$$\rho.C.V \frac{\partial T}{\partial t} + hS(T - T_a) = 0 \quad (4.20)$$

Convective heat transfer : From [118], [26], [135], [12], [116] convective heat transfers occur in turbochargers. Firstly, there is convective heat exchange between casings and their respective flows (compressor and turbine). There is also convective heat transfers between turbocharger casing and ambient air. The heat flow rate is expressed by the Fourier equation expressed through the boundary layer : $\phi = \frac{\lambda}{\delta_T} S(T - T_a)$ where δ_T is the thickness of the boundary layer. As δ_T is not known in most cases, the heat transfer is generally expressed by the Newton equation : $\phi = hS(T - T_a) = \frac{T - T_a}{R}$, where $R = \frac{1}{hS}$ is the convective transfer equivalent resistance which is correlated experimentally. In this case, authors determined heat exchange coefficient h using Nusselt number correlations. Main Nusselt number correlations within turbomachines are found in [12], [70], [56], [16], [26]. Nusselt number $N_u = \frac{hD}{\lambda}$ is a non-dimensional number which is a function of the heat exchange coefficient h , of the fluid thermal conductivity λ [$W.m^{-1}.K^{-1}$] and of the duct diameter D . Based on experimental results, authors have built a correlation functions linking the Nusselt number to other non-dimensional parameters characterizing the flow, such as the Reynolds number R_e and the Prandtl number P_r . $R_e = \frac{\rho u_m D}{\mu}$ and $P_r = \frac{\mu c_p}{\lambda}$, where ρ is the fluid density, μ is the fluid dynamical viscosity and u_m the fluid mean value velocity.

$$N_u = F(R_e, P_r) \quad (4.21)$$

A typical Nusselt number correlation formulation is as following : $Nu = a.R_e^b.P_r^c$ where fitting coefficient a , b , c are determined from optimization algorithm. In the end, the determination of exchange heat coefficient h is performed as following :

1. From flow characteristics, R_e and P_r are calculated
2. Knowing correlation F , N_u is calculated
3. Using N_u definition, h is calculated

The main advantage of determining the exchange heat coefficient h by the mean of Nusselt number correlation is that the developed model takes into account the flow parameters which dictates the physical laws

of the convective process. The main drawback is that there are great deviations between calculated Nusselt numbers from each correlation found in the literature. The main example is provided in the case of an engine manifold study by Depcik [35], where deviations reach up to 100% of the Nusselt number estimation.

Radiative heat transfer : This type of heat transfer is modeled ([71]) via the Stefan-Boltzmann equation : $\phi = \epsilon\sigma S (T^4 - T_a^4)$, where ϵ is the casing emissivity [-] and σ is the Stefan's constant ($5.67e^{-8}W.m^{-2}.K^{-4}$). The emissivity is a function of the material, but also of the temperature. Tables providing emissivity values for turbocharger materials and their evolution regarding temperature are detailed in [71].

In order to identify heat transfer coefficients for convection, radiation and conduction, it is necessary first to measure heat transfers occurring between the compressor, the oil and the turbine. This is performed by the mean of an experimental process detailed by Baar et al. [3], Shaaban [118] and Cormerais [26] in their respective studies. This experimental method is based on adiabatic and non-adiabatic flows measurements comparison. In the case where turbocharger runs under insulated adiabatic conditions, compressor power determined from temperature measurement \dot{W}_C (Eq.4.12) is the same as the compressor shaft power \dot{W}_{Csh} as there is no heat exchange within the turbocharger. The same thing occurs at the turbine where $\dot{W}_T = \dot{W}_{Tsh}$. Under these conditions and for a constant shaft speed, the difference between compressor power and turbine power is due to losses occurring in the bearing. Therefore, adiabatical tests allow to build a losses model for the bearing.

When insulated but non-adiabatical turbocharger tests are run, 5 quantities need to be known in order to measure heat exchange. The five quantities are : compressor power determined from temperature measurement \dot{W}_C , compressor shaft power \dot{W}_{Csh} , turbine power determined from temperature measurement \dot{W}_T , turbine shaft power \dot{W}_{Tsh} and bearing power losses \dot{W}_B . \dot{W}_C and \dot{W}_T are directly determined from measurements, \dot{W}_B is estimated via the bearing losses model built from adiabatical tests. A major assumption made in [3], [118] and [26] is that compressor shaft power \dot{W}_{Csh} is not dependent upon heat exchanges, which means that heat exchanges are considered to occur in the collector, after the compression. Considering this assumption, \dot{W}_{Csh} is determined from the adiabatical compressor data map. Finally, turbine shaft power is determined via this loop $\dot{W}_{Tsh} = W_{non-adia} + \dot{W}_B$. Heat exchanges powers are determined by differentiation between effective turbomachines shaft power and power determined from insulated non-adiabatical tests. Introduced equations to determine heat exchanges within insulated turbocharger are shown below :

$$\dot{W}_{Csh,non-adia} = \dot{W}_{Csh,adia} \quad (4.22)$$

$$\dot{W}_{Tsh,non-adia} = \dot{W}_{Csh,non-adia} + \dot{W}_B \quad (4.23)$$

$$\dot{Q}_T = \dot{W}_{Csh,non-adia} + \dot{W}_B - \dot{W}_T \quad (4.24)$$

$$\dot{Q}_C = \dot{W}_{Csh,non-adia} - \dot{W}_C \quad (4.25)$$

The main issue regarding this experimental method is that heat exchanges are determined for a limited area of the global turbocharger operating range. Indeed, adiabatical tests require low turbine inlet temperature (generally $\sim 350K$). And as the specific enthalpy change across the turbine is directly linked to the turbine inlet temperature ($\Delta h_M = (1 - \frac{p_{04}}{p_{03}})^{\frac{\gamma-1}{\gamma}} Cp.T_{03}$), this means that the experiments won't cover the entire operating range. A way to compensate it would be to increase the pressure ratio across the turbine, but this proved to cause turbocharger failure.

Once heat exchanges are determined, some authors have shown that a practical way to build a transient heat exchange model is to build an equivalent resistance methods [26] or to use '1D' methods [26], [118], [116]. Both types of models use the lump model assumption for the turbine and the compressor casings. They also require the turbocharger to be discretized. An example of discretization of an insulated turbocharger is shown

on Fig.4.8 to 4.11 which are from Cormerais [26]. In this case, the author has divided the turbocharger into 5 subsystems : the turbine, the turbine plate, the central casing, the compressor plate and the compressor. At first (Fig.4.9), each equivalent resistance is explicitly detailed. However, by the mean of an electrical analogy, the global system is simplified to reach the final equivalent version shown on Fig.4.11. Depending on the number of temperature sensors and on their location, Cormerais shows that it is possible to use either the complex or the simplified resistance scheme. In the case of the '1D' method [26], [118], each subsystem is spatially discretized along the shaft dimension. However, Cormerais has shown that such a discretization does not provide significant accuracy improvement than the 0D resistance method.

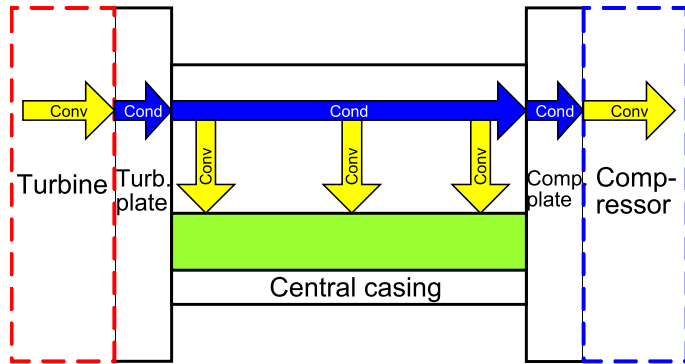


FIG. 4.8 – Insulated turbocharger 5-part discretization and thermal exchanges. From [26]

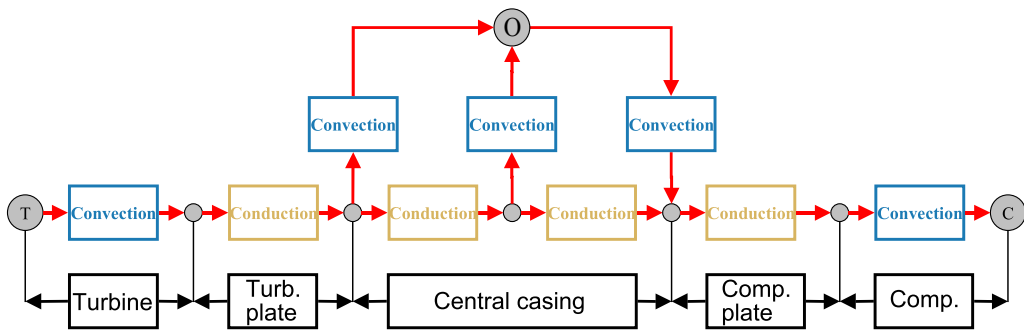


FIG. 4.9 – Equivalent resistance scheme of an insulated turbocharger. From [26]

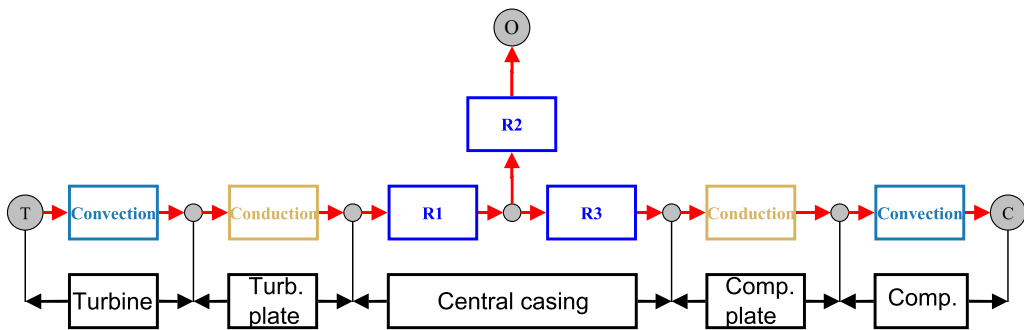


FIG. 4.10 – Simplification of the equivalent resistance scheme (Fig.4.9) of an insulated turbocharger. From [26]

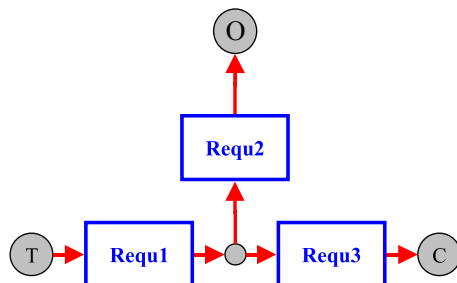


FIG. 4.11 – Final simplification of the equivalent resistance scheme (Fig.4.9) of an insulated turbocharger. From [26]

0D-1D turbocharger literature review : main points

The study of the main 0D-1D modeling approaches regarding the turbocharger has allowed to identify the following points :

- In order to comply with the real-time calculation processes, it is necessary to build a performance data map of the turbocharger. This data map is either based on the extrapolation of experimental data or on a complete mathematical modeling of the involved physical processes.
- Data maps provided by turbocharger suppliers do not cover the entire operating range of the turbomachines. Therefore, such data must be inter/extrapolated. This is performed by the mean of data map extrapolation treatments. These processes are essentially based on purely mathematical curve fitting methods, leading to uncertainties regarding the quality of the extrapolated data. The poor discretization level of the data map is also an issue, more specifically regarding the turbine efficiency.
- 0D-1D physical models of the turbocharger imply the development of many sub-models, mostly in order to determine the flow losses within the turbocharger. Such methods are now widely used in order to pre-determine the performance characteristics of the turbomachines. However, they require the knowledge of the specific geometry of the turbomachines, which is almost never the case. Indeed turbocharger suppliers generally do not provide such information.
- An interesting approach consists in building a physical model of the turbocharger in order to parameterize the equations. These parameters are consequently identified using the data maps from the suppliers.
- Many experimental studies have shown the impact of the heat transfers within the turbocharger on the temperature measure-based turbomachines efficiency. This error provides uncorrect performance simulation, mostly during transients. Heat transfers are identified via an experimental process based on adiabatical / non-adiabatical measurements. However, due to the lack of energy upstream the turbine in the adiabatical case, the operating range covered by this method is not complete.
- Thermal model of the turbocharger have been developed, mainly based on the identification of the heat transfer coefficients. An emphasis is made on the identification of the Nusselt number. However important discrepancies on the results have been found in the literature.
- Equivalent thermal resistance approach allows to achieve great simplification of the overall thermal model, while preserving a satisfying level of accuracy.

4.4 Gas exchange processes through turbochargers : proposed thesis developments

In the present part, the emphasis will be put on two specific points :

- **The extrapolation of the turbocharger datamaps :** The goal is to ensure the validity of the interpolated and extrapolated data. The physical equations of the turbomachinery physics will be developed and these developments will be used in order to build the compressor and turbine extrapolation schemes. By including more physics into these numerical processes, it is intended to improve the accuracy of the turbocharger model, mainly in the extrapolated operating range of the performance datamaps.
- **The turbocharger heat transfers identification and model building :** It is intended to take into account the heat transfers within a turbocharger in order to model the impact of these transfers on the turbocharger performance.

Structure of the 'Gas Exchange processes through Flow Restrictions' part : In this thesis, a turbocharger model will be considered as the composition of two complementary parts :

1. the performance datamaps of the turbocharger, which provide the thermodynamical characteristics of the compressor and the turbine. The development of more physical interpolation/extrapolation processes are directly linked to these datamaps.
2. the heat exchange model of the turbocharger. This model is considered as an 'add-on' of the datamap-based turbocharger model. It will correct the performances read from the datamaps in agreement with the thermodynamical states of the compressor, turbine and oil.

This structure is shown on Fig. 4.4. The developments associated to the compressor and turbine extrapolation process will be developed in the chapter 6. The heat transfers identification and model building will be detailed in chapter 7.

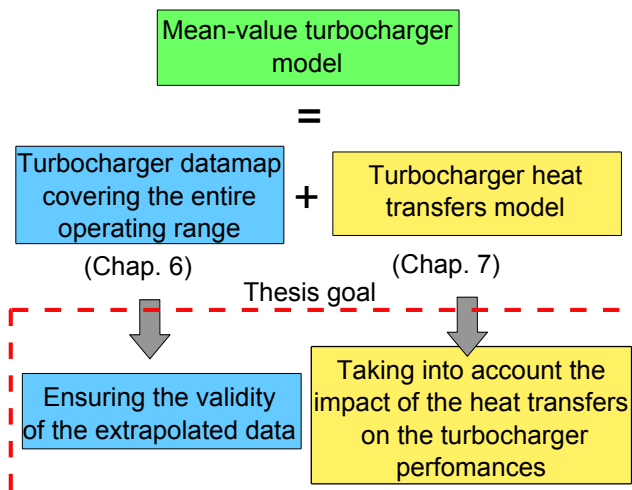


FIG. 4.12 – Chartflow of the 'Gas exchange processes through turbochargers' part.

Chapter 5

Experimental apparatus

The experimental campaign regarding the turbocharger has been performed at the Internal Combustion Engine Energy Research laboratory of the Ecole Central de Nantes, where a turbocharger test bench is being developed since 2002. The main interest of this test bench is that it allows to capture turbocharger behavior without having to run a complete engine.

5.1 Design of the test bench

The flow is established at the turbine by the mean of two industrial compressors, which allow to provide a flow rate up to $700m^3.h^{-1}$ at a pressure of 7 bar. The air flow is heated thanks to a 144 kW electrical heater, which allows to reach turbine inlet temperature up to 773K. The turbine inlet temperature is regulated via a loop between the air heater command and a temperature sensor located at the inlet of the turbine. The turbine mass flow rate is regulated via a vane located upstream of the air heater. A regulated vane is also located downstream the compressor, in order to command its mass flow rate / pressure ratio. An oil circuit has been put into place in order to provide the oil to the turbocharger bearing. Oil flow is regulated in terms of mass flow rate and of temperature. This is performed via a regulated valve and via a regulated oil-water heat exchanger. Mass flow rate sensors are located upstream of the turbine air heater and upstream of the compressor. The ducts upstream and downstream the compressor and the turbine are insulated in order to avoid heat losses and temperature gradients. In this study, only insulated turbocharger tests have been considered, therefore the turbocharger was insulated at any time.

5.2 Sensors

The temperature upstream and downstream the turbine and the compressor have been measured. The oil temperature upstream and downstream the turbocharger has also been acquired. Finally, oil and air mass flow rates have been measured, as well as the turbocharger shaft speed. Main sensors implementation is shown on Fig.5.1.

5.2.1 Thermal sensors

Temperatures upstream and downstream of the turbine and oil temperature have been acquired by the mean of 1mm diameter K thermocouples. This type of thermocouple has a discrepancy of measure of $\pm 1^\circ C$. Temperatures relative to the compressor have been measured with thermoresistive sensors, which have a measurement error of $\pm 0.6^\circ C$.

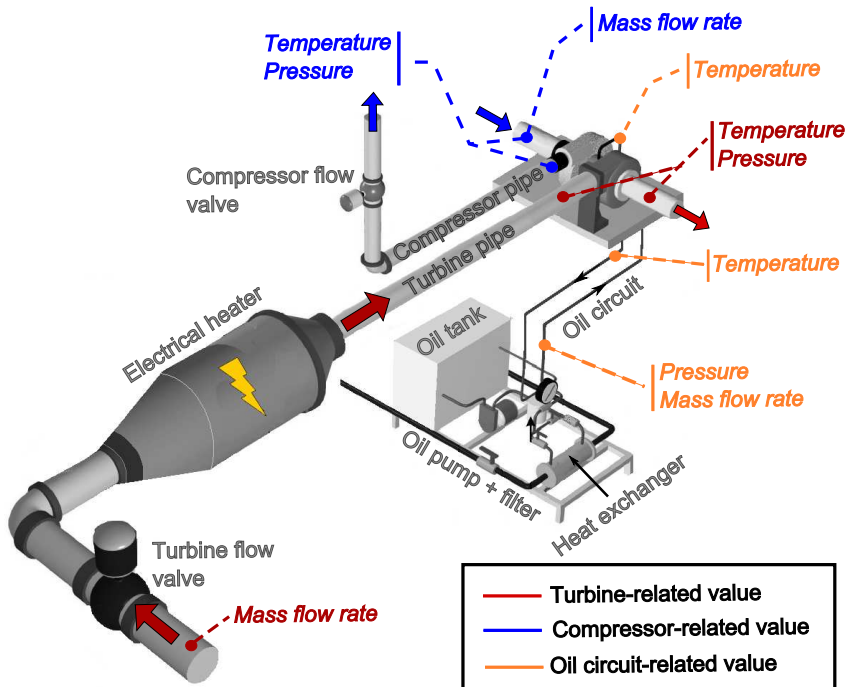


FIG. 5.1 – Turbocharger bench with thermodynamical sensors positioning

5.2.2 Pressure sensors

Pressure levels have been measured by HCX piezoresistive sensors from SensorTechnics. Accuracy is 0.1% of the full measurement scale. The following measurement scales have been used in order to reduce the measurement error :

- 5 bar relative at the turbine entry
- 2 bar relative at the compressor output
- 1 bar relative at the compressor entry
- 100 mbar relative at the turbine output

5.2.3 Mass flow rate

Air mass flow rates have been measured by Endress-Haiger proline t-mass 65F thermal mass flow measuring system. The maximum measured error is $\pm 1.5\%$ of the reading value.

Oil flow rate has been measured by a Microstream volumetric flow sensor from Bamo society. The accuracy of this sensor is 2% of the full scale. In our case, the full scale has been set to $45l/min$, which leads to an error of $0.015l/min$. In average, this is about 10% of the oil flow rate value.

5.2.4 Turbocharger rotation speed

The rotation speed of the turbocharger has been measured by an inductive sensor (Pico-turn) from Acam society. This sensor is introduced within the compressor housing. The measurement accuracy is ± 200 rpm.

The complete sensors list is summed-up in the following table :

Sensor type	Manufacturer	Model	Scale	Dispersion
Compressor entry pressure	Sensor technics	HCX piezo	0 – 1 bar	$\pm 0.1\% \text{ FS}$
Compressor output pressure	Sensor technics	HCX piezo	0 – 2 bar	$\pm 0.1\% \text{ FS}$
Turbine output pressure	Sensor technics	HCX piezo	0 – 0.1 bar	$\pm 0.1\% \text{ FS}$
Turbine entry pressure	Sensor technics	HCX piezo	0 – 5 bar	$\pm 0.1\% \text{ FS}$
Air mass flow rate	Endress-Hauger	T-mass 65F	0 – 0.5 kg/s	$\pm 1.5\% \text{ RV}$
Oil mass flow rate	Bamo	MicroStream	45l/h	$\pm 2\% \text{ FS}$
Turbine temperature	-	1mm K thermocouple	173 – 900 K	$\pm 1 \text{ K}$
Compressor temperature	-	thermoresistive sensor	223 – 773 K	$\pm 0.6 \text{ K}$
Turbocharger speed	Acam	Picoturn	-	$\pm 200 \text{ rpm}$

5.3 Visualization and post-treatment

Measurements are processed via a 6014 National Instruments card set to 200 kHz. The visualization and post-treatment software is Labview 7.1. As the sensors measure static temperatures and pressures and it is therefore necessary to recalculate the total pressures and temperatures :

$$T_{0x} = T_x + \frac{V_x^2}{2.Cp} \quad (5.1)$$

$$p_{0x} = p_x \left(\frac{T_{0x}}{T_x} \right) \quad (5.2)$$

It is also necessary to calculate the turbocharger reduced variables for the compressor (Eq.5.3 to 5.5) and the turbine (Eq.5.6 to 5.8) :

$$U_{redC} = U_C \sqrt{\frac{T_{ref}}{T_{01}}} \quad (5.3)$$

$$Qm_{redC} = Qm_C \sqrt{\frac{T_{01}}{T_{ref}} \frac{p_{ref}}{p_{01}}} \quad (5.4)$$

$$\tau_C = \frac{p_{02}}{p_{01}} \quad (5.5)$$

$$U_{redT} = U_T \sqrt{\frac{T_{ref}}{T_3}} \quad (5.6)$$

$$Qm_{redT} = Qm_T \sqrt{\frac{T_{03}}{T_{ref}} \frac{p_{ref}}{p_{03}}} \quad (5.7)$$

$$\tau_t = \frac{p_{03}}{p_{04}} \quad (5.8)$$

Finally, the turbomachines powers are calculated using the conservation of energy :

$$\dot{W}_C = Qm_C (Cp_2 T_{02} - Cp_1 T_{01}) \quad (5.9)$$

$$\dot{W}_T = Qm_T (Cp_4 T_{04} - Cp_3 T_{03}) \quad (5.10)$$

$$\dot{W}_O = Qm_O (Cp_6 T_6 - Cp_5 T_5) \quad (5.11)$$

5.4 Uncertainties

The analysis of experimental errors allows to determine the maximum error associated to the measurements. In order to achieve this study, the differential method of errors propagation is used [40]. This method is based on Taylor's theorem. It provides the maximal uncertainty u of a given n-parameters function $f(x_1, x_2, \dots, x_n)$ (Eq.5.12). c_i are the multiplicative coefficients of the parameters x_i .

$$u(f(x_1, x_2, \dots, x_n)) = \sqrt{\sum_{i=1}^n (c_i u(x_i))^2} \quad (5.12)$$

5.4.1 Uncertainties on the power calculation

As the C_p is assumed to be constant within the turbocharger, compressor and turbine power calculation can be expressed under the following formulation derived from Eq.5.9 and Eq.5.10 :

$$\dot{W} = Qm.Cp.\Delta T \quad (5.13)$$

Finally, the uncertainty regarding the turbomachines power is calculated in the following way :

$$u(\dot{W}) = W \cdot \sqrt{\left(\frac{u(Qm)}{Qm}\right)^2 + \left(\frac{u(\Delta T)}{\Delta T}\right)^2} \quad (5.14)$$

From the measurement errors definition provided by the suppliers, we know that the relative uncertainty on the mass flow rate is constant ($\pm 1.5\%$) on the full scale. However, as the absolute error made by temperature sensors is constant, the relative uncertainty will be dependent upon ΔT . From Eq.5.14, it is possible to plot the power uncertainties regarding the compressor and the turbine temperature difference :

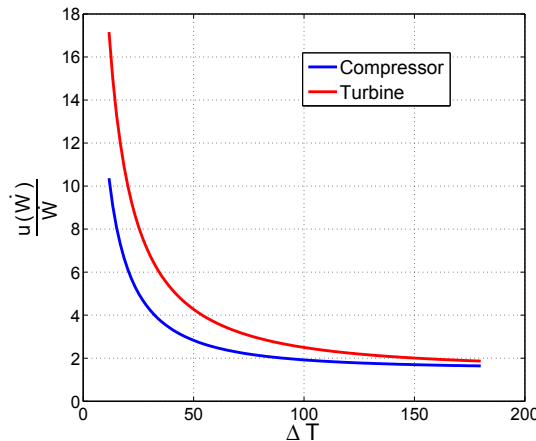


FIG. 5.2 – Measurements uncertainties (in %) made on the turbomachine power estimation vs. the temperature difference across the turbomachines.

The ΔT range has been determined from measurements. From this study, it appears that the measurement error is maximum for low temperature differences. Attention should be paid to the conclusions from results at very low load, i.e. for very small temperature change ($< 10K$) across the turbomachines.

5.4.2 Uncertainties on oil flow power measurement

From experimental observation, it appears that the lubricant oil exits the turbocharger casing as an oil mist. Therefore, the thermocouple measuring the temperature of the oil at the exit of the turbocharger casing

is placed in a biphasic flow. Such flow usually leads to high uncertainties on the temperature estimation. Consequently, the temperature of the oil exiting the turbocharger casing will be considered as unknown, which means that the value of \dot{W}_O (Eq. 5.11) won't be determined using experimental measurements in the following of the thesis.

5.5 Tests

The tests have been performed in order to characterize the turbocharger performances and their evolutions regarding heat transfers. The considered turbocharger is from BorgWarner with a variable turbine geometry dedicated to a 1.5 l. diesel engine application. The turbocharger tests covered the largest turbocharger operating range as possible, with shaft speed from 10 krpm to 200 krpm. Such tests allow to cover the lower area of the turbocharger operating range, usually not acquired by the suppliers. In order to take into account the heat transfers, two types of tests have been performed :

- Insulated and adiabatical tests. In this case, heat losses towards ambient air are drastically reduced and are neglected. The adiabatical condition definition is based on previous work by Cormerais [26] or Shaaban [118] : the turbine inlet temperature is tuned such that the 'flow mean temperature value' ($\frac{T_{inlet}+T_{outlet}}{2}$) calculated for the compressor, for the turbine and for the oil are equal.
- Insulated non-adiabatical tests. In this case, the turbocharger is still insulated, but no regulation on the turbine inlet temperature is done. Tests have been performed for the following turbine inlet temperature values : 573K and 773K.

Generally, a third type of test is performed : non-insulated non-adiabatical tests. Such tests allow to build heat transfers models between the turbocharger housing and the ambient air. In our case, it has been decided not to investigate this phenomenon. The main reason is that such heat transfers are highly dependent upon the under-hood environment and that the re-creation of such an environment seemed off-context of our study. Additionally, heat transfer from a mass of metal towards ambient air is a phenomenon with well-established formulations and correlations, which is not the case for heat transfers occurring within automotive turbochargers. Therefore, it has been decided to focus on this last aspect.

Chapter 6

Physics-based extrapolation of turbochargers data maps

It appears from the literature review that the existing methods developed in order to extrapolate turbochargers data maps have a major weakness regarding the accuracy of the extrapolated data. However, such methods are easy to put in place and do not require the extensive geometric knowledge of the turbocharger. On the opposite, fully-physical-based models take into account any phenomenon occurring within the turbocharger and are therefore robust regarding the extrapolation of the turbocharger data. However, they are very complex to build and imply a perfect knowledge of the turbocharger geometry.

The approach which has been developed is an attempt to combine the advantages of both methods :

- The use of mathematical curve fitting methods allows to simplify the building of the model.
- The development of the turbomachinery equations could provide robustness and a physical-based validation to the extrapolated data.

In order to achieve this, it has been decided to redevelop the basic turbomachinery equations and to identify which developments could be used in order to 'feed' the mathematical curve fitting methods.

6.1 Turbomachinery characteristic curves

It is possible to build the characteristic curves of the turbomachines by developing their thermodynamical equations. In the case of the pumps (fluid of constant density), it is possible to express some similitude coefficients known as the Rateau coefficients. Two of these coefficients can be adapted to the compressible flows case : the flow rate coefficient δ and the manometric head coefficient μ_{th} . An example of this development has been shown by Pluviose [106] for axial turbomachines. It is proposed here to adapt this approach to the radial turbomachines case.

6.1.1 Compressor characteristic curves

In the compressor case, the flow rate parameter and the manometric head parameter are expressed as : $\delta = \frac{V_r^2}{U_2^2}$ and $\mu_{th} = \frac{U_2 V_{\theta 2} - U_1 V_{\theta 1}}{U_2^2}$. The flow rate parameter δ expresses in a non-dimensional way the velocity speed at the exit of the rotor. The manometric head parameter μ_{th} expresses in a non-dimensional way the enthalpy change across the compressor. Fig.4.4 is re-plotted here under the reference Fig.6.1 in order to improve the readability of the section.

Starting from the Euler's equation, we can write that :

$$U_2^2 \cdot \mu_{th} = \Delta h = U_2 V_{\theta 2} - U_1 V_{\theta 1} \quad (6.1)$$

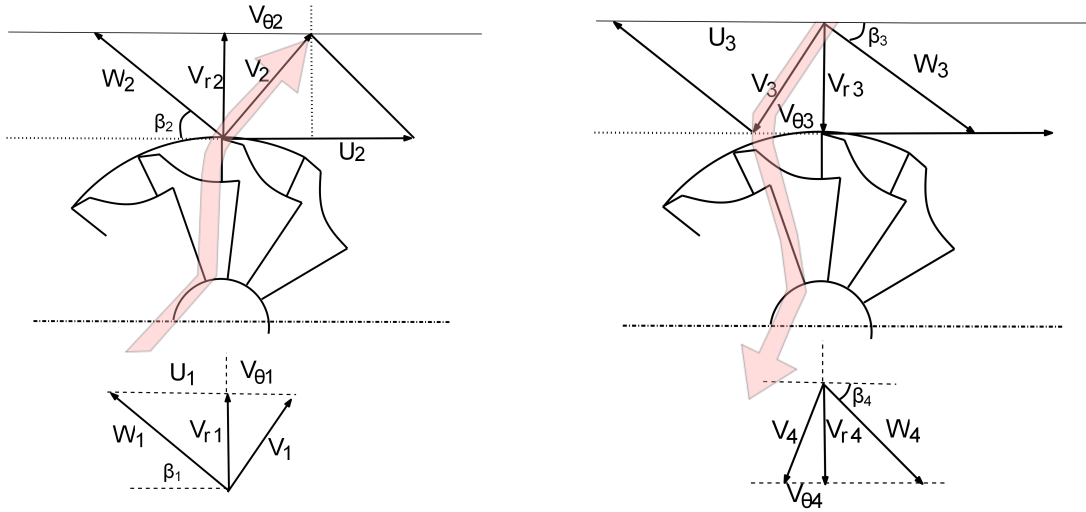


FIG. 6.1 – Speed characteristics triangle of a centrifugal compressor (left) and a centrifugal turbine (right)

In our case, we consider that the flow is irrotational when entering the rotor, which is almost the case in real applications ($V_{\theta 1} = 0$). Using the speed triangle in the compressor case, we find that : $V_{\theta 2} = U_2 - V_{r2}\cotan(\beta_2)$, which leads to the following equations :

$$\Delta h = U_2^2 - U_2 V_{r2} \cotan(\beta_2) \quad (6.2)$$

$$\frac{\Delta h}{U_2^2} = 1 - \frac{V_{r2}}{U_2} \cotan(\beta_2) \quad (6.3)$$

$$\mu_{th} = 1 - \delta \cdot \cotan(\beta_2) \quad (6.4)$$

In the system of coordinates δ, μ_{th} , the characteristic curve of a compressor is a negative slope line, with an ordinate at origin of 1. The theoretical slope of this line depends only on the geometry angle β_2 . The ratio between the specific enthalpy change Δh and the squared blade tip tangential speed U_2^2 is plotted on Fig.6.2 as a function of the flow rate parameter δ . The compression process is also plotted on a Mollier diagram where there is a non-isentropic pressure increase between P_1 and P_2 .

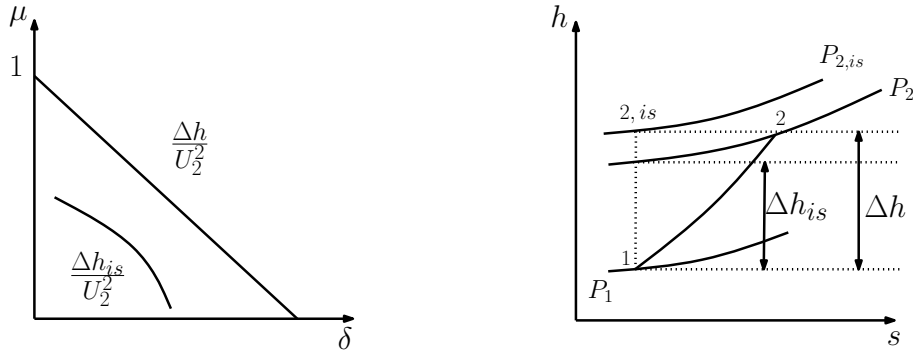


FIG. 6.2 – Representation of the exchanged energies within a radial compressor

In the case where the compressor would be isentropic, the isentropic pressure $P_{2,is}$ could be reached. One could also say that the isentropic compressor would require less specific energy to reach the pressure P_2 . This

isentropic enthalpy change is referred as Δh_{is} . Δh_{is} is lower than Δh as less specific energy is required to reach the same operating point. $\frac{\Delta h_{is}}{U_3^2}$ is also plotted in the δ, μ_{th} system of coordinates. Finally, it is possible to express the compressor isentropic efficiency η_{is} (Eq.6.5). η_{is} is always lower than 1.

$$\eta_{is} = \frac{\Delta h_{is}}{\Delta h} \quad (6.5)$$

6.1.2 Turbine characteristic curves

In the turbine case, the flow rate parameter and the manometric head parameter are expressed as : $\delta = \frac{V_{r3}}{U_3}$ and $\mu_{th} = \frac{U_4 V_{\theta 4} - U_3 V_{\theta 3}}{U_3^2}$. Developing the Euler's equation and considering that the flow is irrotational downstream the turbine ($V_{\theta 4} = 0$) allows to develop the following equations :

$$\Delta h = -U_3^2 + U_3 V_{r3} \cotan(\beta_3) \quad (6.6)$$

$$\frac{\Delta h}{U_3^2} = -1 + \frac{V_{r3}}{U_3} \cotan(\beta_3) \quad (6.7)$$

$$\mu_{th} = -1 + \delta \cdot \cotan(\beta_3) \quad (6.8)$$

The characteristic curve of the turbine is a line of positive slope and with an ordinate at origin of -1. As in the compressor case, this line is plotted in the system of coordinates in the system of coordinates δ, μ_{th} (Fig.6.3).

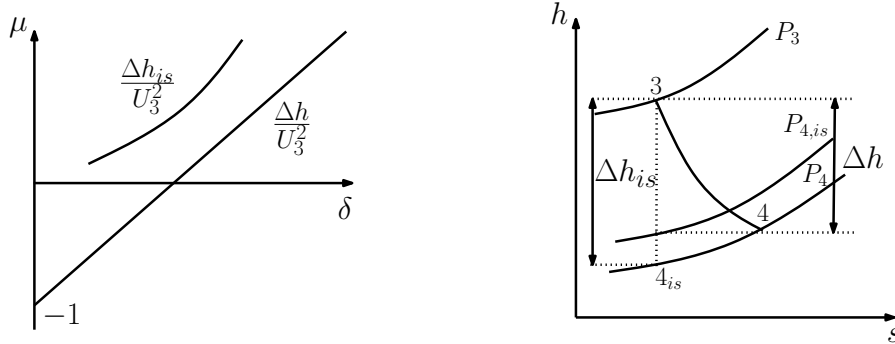


FIG. 6.3 – Representation of the exchanged energies within a radial turbine

It is also interesting to deal with the isentropic case. For a given specific energy, an isentropic turbine would require a smaller pressure decrease, therefore reaching a pressure $P_{4,is}$ greater than P_4 . One could also consider that for a given pressure decrease, an isentropic turbine would allow to recover more specific energy. This isentropic energy is expressed as Δh_{is} . This energy is higher than Δh . Finally, the isentropic efficiency of the turbine is defined as :

$$\eta_{is} = \frac{\Delta h}{\Delta h_{is}} \quad (6.9)$$

6.2 Transposition of the characteristic curves to the turbocharger data maps

From the previous developments, it appears that expressing the enthalpy change across a radial turbomachine in the δ, μ system of coordinates allows to identify a linear trend. This is an interesting property,

as linear mathematical expressions are well-suited for extrapolation processes. It is proposed in this part to transpose these observations to the data maps provided by the suppliers.

6.2.1 Compressor

In order to comply with the similitude theory, compressor data maps are usually provided in the following system of coordinates : the pressure ratio $\frac{P_{02}}{P_{01}}$ and the efficiency η_C are plotted as functions of the reduced mass flow rate $Qm_{redC} = Qm_C \sqrt{\frac{T_{01}}{T_{ref}} \frac{P_{ref}}{P_{01}}}$. Knowing the pressure ratio and the efficiency from the data maps, it is possible to calculate the enthalpy change across the compressor :

$$\Delta h = \frac{\left(\left(\frac{P_{02}}{P_{01}} \right)^{\frac{\gamma-1}{\gamma}} - 1 \right) Cp T_{01}}{\eta_C} \quad (6.10)$$

It appears that the tangential component $V_{\theta 2}$ of the fluid speed at the exit of the compressor (Fig.6.1) is imposed by the rotation speed of the blade tip. In fact, the blade speed ratio $\sigma = \frac{V_{\theta 2}}{U_2}$ is, at the first order, only dependent upon the geometry of the blades and on the rotation speed [66], [136], [106], [121]. Therefore, for a given blade tip speed U_2 , the tangential speed $V_{\theta 2}$ is constant. Consequently, the radial speed component V_{r2} is directly linked to the establishment of the flow within the blades of the rotor. From these observations, it appears that the mass flow rate through the compressor can be expressed in the following way [106] :

$$Qm_C = \rho_2 V_{r2} S_2 \quad (6.11)$$

$$Qm_{redC} = \rho_2 V_{r2} S_2 \sqrt{\frac{T_{01}}{T_{ref}} \frac{P_{ref}}{P_{01}}} \quad (6.12)$$

Where S_2 is the flow section [m^2] at the exit of the rotor. Introducing equation 6.12 into equation 6.2 provides the following relationship :

$$\frac{\Delta h}{U_2^2} = 1 - \frac{Qm_{redC}}{\rho_2 S_2 U_2} \cotan(\beta_2) \sqrt{\frac{T_{ref}}{T_{01}} \frac{P_{01}}{P_{ref}}} \quad (6.13)$$

Compressor characterization tests are performed by the suppliers at a constant inlet pressure P_{01} and a constant inlet temperature T_{01} . Additionally, the geometric blade angle β_2 and the rotor outflow section S_2 are constant. Finally, considering that the flow is 'observed' immediately after its exit of the rotor blades, it can be stated that the fluid has been accelerated but almost not compressed, as it has not entered the diffuser yet [61]. Therefore, we can consider that $\rho_2 = \text{constant} = \rho_1$. Introducing the constant term $K_C = \frac{\cotan(\beta_2) \sqrt{\frac{T_{ref}}{T_{01}} \frac{P_{01}}{P_{ref}}}}{\rho_2 S_2}$, we get :

$$\frac{\Delta h}{U_2^2} = 1 - \frac{Qm_{redC}}{U_2} K_C \quad (6.14)$$

For a given blade speed U_2 , Eq.6.14 provides a linear relationship between the specific enthalpy change across the compressor and the reduced mass flow rate from the data maps provided by the suppliers.

6.2.2 Turbine

Turbine's data maps are usually provided in the following system of coordinates : the pressure ratio $\frac{P_{03}}{P_{04}}$ and the efficiency η_T are plotted as functions of the reduced mass flow rate $Qm_{redT} = Qm_T \sqrt{\frac{T_{03}}{T_{ref}}} \frac{P_{ref}}{P_{03}}$. Unlike the compressor's data maps, the inlet pressure P_{03} is not constant. Knowing the pressure ratio and the efficiency from the data maps, it is possible to calculate the specific enthalpy change across the turbine :

$$\Delta h = \left(1 - \left(\frac{P_{04}}{P_{03}}\right)^{\frac{\gamma-1}{\gamma}}\right) Cp T_{03} \eta_T \quad (6.15)$$

As in the case of the compressor, the flow tangential speed $V_{\theta 3}$ is imposed by the blade tip tangential speed U_3 . Indeed, the blade speed ratio $\sigma = \frac{V_{\theta 3}}{U_3}$ is, at the first order, only dependent upon the geometry of the blades and on the rotation speed. This means that for a given rotational speed, the tangential speed $V_{\theta 3}$ is constant. Consequently, the radial speed component V_{r3} is directly linked to the establishment of the flow within the blades of the rotor, which allows to build equations 6.16 and 6.17. S_3 is the flow section [m^2] at the rotor inlet.

$$Qm_T = \rho_3 V_{r3} S_3 \quad (6.16)$$

$$Qm_{redT} = \rho_3 V_{r3} S_3 \sqrt{\frac{T_{03}}{T_{ref}}} \frac{P_{ref}}{P_{03}} \quad (6.17)$$

Combining Eq. 6.17 to Eq. 6.6 allows to develop the following relationship :

$$\frac{\Delta h}{U_3^2} = -1 + \frac{Qm_{redT}}{\rho_3 S_3 U_3} \cotan(\beta_3) \sqrt{\frac{T_{ref}}{T_{03}}} \frac{P_{03}}{P_{ref}} \quad (6.18)$$

In the case of the turbine, characterization tests are performed at a given inlet temperature T_{03} but for varying inlet pressures P_{03} . Therefore, the inlet density is varying from an operating point to another. Consequently, the inlet density ρ_3 cannot be assumed to be constant. However, the use of the terms introduced to reduce the mass flow rate allows to develop a constant expression :

$$\rho_3 = \frac{P_{03}}{R T_{03}} \quad (6.19)$$

$$\rho_3 \frac{P_{ref}}{P_{03}} = \frac{P_{ref}}{R T_{03}} \quad (6.20)$$

Introducing Eq. 6.20 into Eq. 6.18 :

$$\frac{\Delta h}{U_3^2} = -1 + \frac{Qm_{redT}}{S_3 U_3} \cotan(\beta_3) \sqrt{\frac{T_{ref}}{T_{03}}} \frac{R T_{03}}{P_{ref}} \quad (6.21)$$

$$\frac{\Delta h}{U_3^2} = -1 + \frac{Qm_{redT}}{S_3 U_3} \cotan(\beta_3) \frac{R \sqrt{T_{ref} T_{03}}}{P_{ref}} \quad (6.22)$$

As T_{ref} , T_{03} and P_{ref} are fixed to constant values by the suppliers, it is possible to introduce a constant term $K_T = \frac{R \cotan(\beta_3) \sqrt{T_{ref} T_{03}}}{S_3 P_{ref}}$:

$$\frac{\Delta h}{U_3^2} = -1 + \frac{Qm_{redT}}{U_3} K_T \quad (6.23)$$

For a given blade speed U_3 , Eq.6.23 provides a linear relationship between the specific enthalpy change across the turbine and the reduced mass flow rate from the data maps provided by the suppliers.

6.2.3 Building of the characteristic curves from a turbocharger data map

We have seen in the previous sections that a linear relationship could be built between the specific enthalpy change across the turbomachines and their reduced mass flow rate. In the following subsection, we are going to plot this evolution using data from the suppliers. From these data, it is possible to calculate the enthalpy change (Eq. 6.10 and Eq. 6.15) and to plot it as a function of the reduced mass flow rate. Considered turbocharger from a 1.9l direct injection diesel engine.

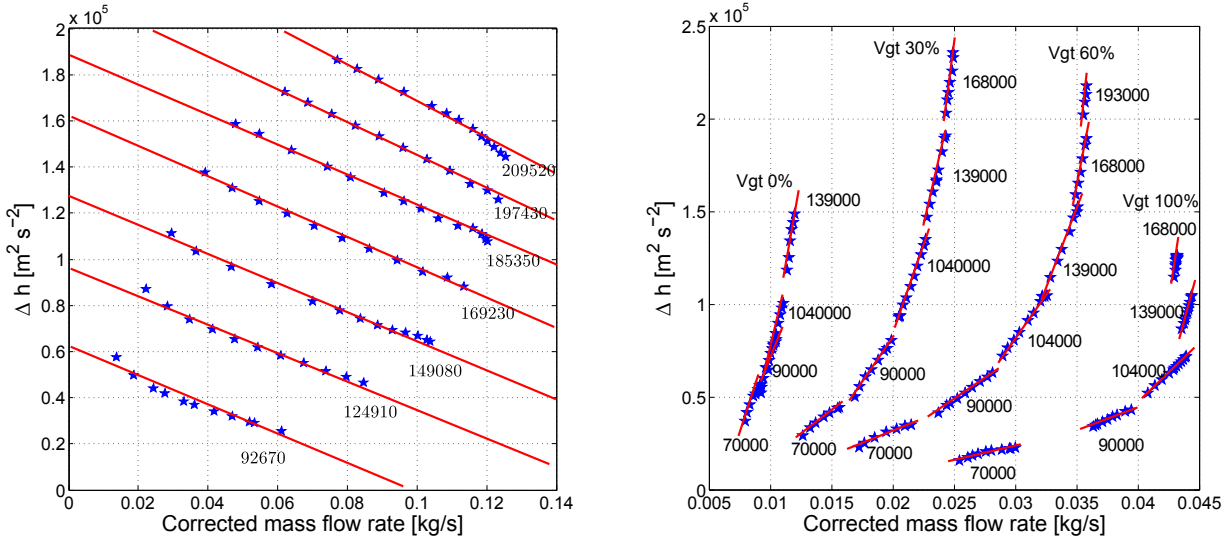


FIG. 6.4 – Specific enthalpy calculated from supplier's data maps plotted as a function the corrected mass flow rate for various reduced shaft speeds and VGT positions. Compressor case (left), turbine case (right). Red lines provide the linear trends.

Fig. 6.4 shows that the linear evolutions expressed by equations 6.14 and 6.23 are verified experimentally. The main outcome of this validation is that the linear expression of the specific enthalpy change could effectively be incorporated into a data map-fitting technique. The left plot on Fig. 6.4 shows that the complexity is increased in the case of the turbine. Indeed, it appears that the variable geometry requires an additional discretization of the data regarding the VGT position. In addition to this phenomenon, the covered operating range in terms of mass flow rate for each iso-speed line is a lot narrower for the turbine than in the compressor case.

6.3 Development of a physical-based turbocharger data map-fitting method

The following section will focus on the development of a turbocharger data map-fitting method embedding the previously-developed turbocharger characteristic curves. Emphasis has been put on keeping the

calculation time low and on the ease of use.

6.3.1 Compressor model

In order to build compressor's data maps, it is necessary to know, for a given mass flow rate Qm_C , the values of both the specific enthalpy change Δh and the specific isentropic enthalpy Δh_{is} change across the compressor. From Eq. 6.14, one knows that Δh can be determined from a linear relationship. Such linear trends are also convenient for the extrapolation of data. However, we have no indication regarding the shape of the evolution of Δh_{is} .

Δh determination :

From the experimental data, Δh is calculated using Eq. 6.10. It has been previously demonstrated that the evolution of Δh regarding the corrected mass flow rate rate is linear (Eq. 6.14). It is therefore possible to determine a set of parameters a and b , only dependent upon the rotary speed N_{turb} such that :

$$\Delta h = a(N_{turb}) Qm_{redC} + b(N_{turb}) \quad (6.24)$$

The coefficients $a(N_{turb})$ and $b(N_{turb})$ are determined by the mean of a least square method based on the supplier's data.

Δh extrapolation towards low Rpm values :

In order to calculate the values of Δh for low Rpm values, it is necessary to extrapolate the values of the coefficients $a(N_{turb})$ and $b(N_{turb})$. $b(N_{turb})$ is the ordinate at origin of Δh for each iso-speed curve. According to equation 6.14, the theoretical value of the ordinate at origin of Δh is U_C^2 . Therefore, one can write that :

$$b(N_{turb}) \sim N_{turb}^2 \quad (6.25)$$

Regarding the slope of the linear evolution of Δh , it appears from suppliers' data that $a(N_{turb})$ tends to be constant when reaching low Rpm values. This is illustrated on Fig. 6.5. Therefore, the extrapolated values of $a(N_{turb})$ towards low rpm region will be set to the value of the slope of the lowest iso-speed Δh line provided by the suppliers.

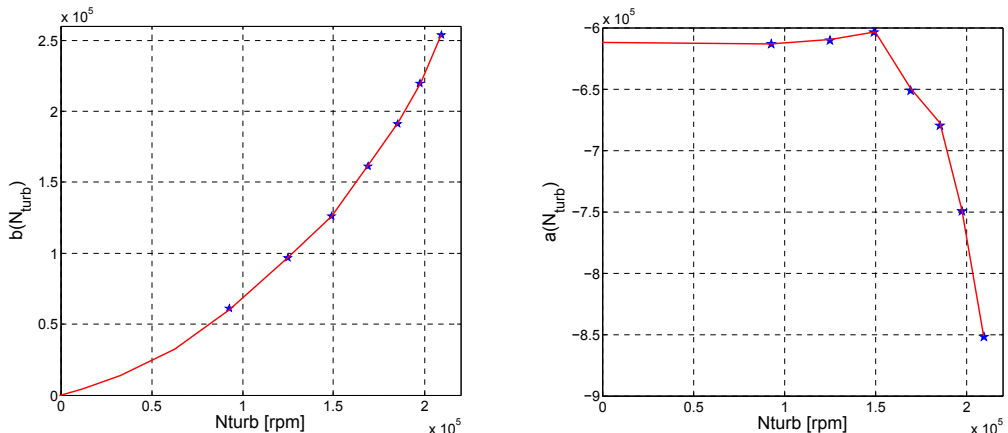


FIG. 6.5 – Evolution of $a(N_{turb})$ (right) and of $b(N_{turb})$ (left) regarding the compressor shaft speed (stars). Red line illustrates the data interpolation and the extrapolation towards low rpm values.

Δh_{is} determination :

As no information is available regarding the shape of Δh_{is} as a function of the corrected mass flow rate, it has been decided to use curve fitting method to determine this quantity. Going back to the literature review, one knows that Jensen et al. [69] have developed an interesting compressor's dimensionless head parameter ψ extrapolation method (Eq. 4.3). From its definition, the dimensionless head parameter is directly linked to the isentropic specific enthalpy change :

$$\Delta h_{is} = \left(\left(\frac{P_{02}}{P_{01}} \right)^{\frac{\gamma-1}{\gamma}} - 1 \right) CpT_{01} = 0.5\psi U_C^2 \quad (6.26)$$

Therefore, Jensen's method would theoretically be suited to determine Δh_{is} from suppliers' data maps. However, this technique provides poor accuracy for the higher rotational speeds. In order to correct this behavior, a modified version of the Jensen's method has been introduced : the data map of the compressor is discretized as shown on Fig. 6.6.

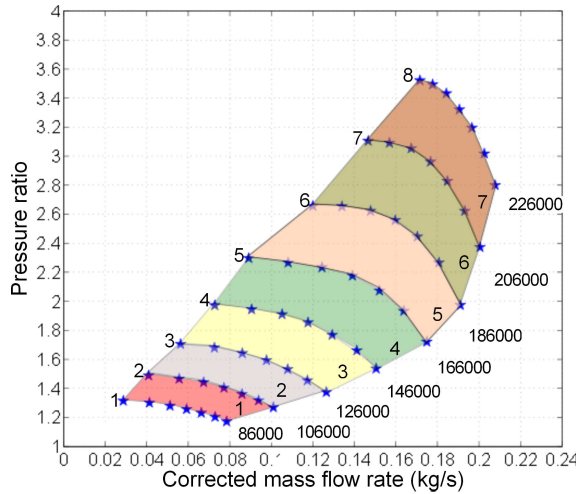


FIG. 6.6 – Specific enthalpy calculated from supplier's data maps plotted as function

In the case there are n_N iso-speed curves provided by the suppliers, n_N sets of Jensen's coefficients are created (one set for each iso-speed) :

$$\psi_{zone_{1i}} = \frac{k_{1i} + k_{2i} \cdot M_{inl_i} + k_{3i} \cdot \phi + k_{4i} \cdot M_{inl_i} \cdot \phi}{k_{5i} + k_{6i} \cdot M_{inl_i} - \phi} \quad i = 1 : n_N \quad (6.27)$$

The operating range of the compressor provided by the supplier can be divided into $n_N - 1$ zones. In order to ensure the continuity of the solution, a linear interpolation is performed between the parameters from the 2 iso-speed curves delimiting a zone. For example, solutions in the zone number 3 on Fig. 6.6 will be calculated using linear interpolations between the coefficients set $k_{13} \rightarrow k_{63}$ and the coefficients set $k_{14} \rightarrow k_{64}$. Once the dimensionless head coefficients ψ are determined, Δh_{is} is calculated using Eq. 6.26.

Δh_{is} extrapolation towards low Rpm values :

Moraal et.al [94] have shown that Jensen's treatment allows to preserve the correct ψ curve shapes, even in the extrapolation zone. However, no physical equation or observation allows to ensure the validity of the extrapolated data. In order to correct this, an iterative method has been developed.

From experimental data, it has been noticed that the maximum compressor isentropic efficiency for a given rotational speed shows a quadratic dependency regarding the turbocharger shaft speed. This trend has been observed on any radial compressor tested during this thesis (~ 10). An example of this curve and of its extrapolation is shown on Fig. 6.7.

From this observation, it is possible to build an iterative scheme in order to ensure the physical validity of the extrapolated Δh_{is} values :

1. A temporary Δh_{is} value is calculated using the discretized Jensen treatment. The coefficients from the first iso-speed curve ($k_{11} \rightarrow k_{61}$) are used in the extrapolated zone.
2. Using the extrapolated values of $a(N_{turb})$ and $b(N_{turb})$, the value of Δh is determined.
3. Knowing Δh_{is} and Δh , it is possible to calculate the corresponding isentropic efficiency : $\eta_C = \frac{\Delta h_{is}}{\Delta h}$. Efficiency vs. mass flow rate curves can therefore be constructed in the extrapolation area.
4. Once these curves are built, the maximum efficiency per iso-speed is calculated and compared to the max efficiency vs. turbocharger shaft speed quadratic curve. If the results are in good agreement, Δh_{is} values are definitive. If the case where the calculated maximum efficiency is not on the curve, the global Δh_{is} is vertically translated until agreement is achieved. This is illustrated on Fig. 6.7 : the modification of Δh_{is} directly impacts the value of the calculated efficiency η_C , therefore allowing to place the maximum efficiency (black square) on the quadratic evolution curve.

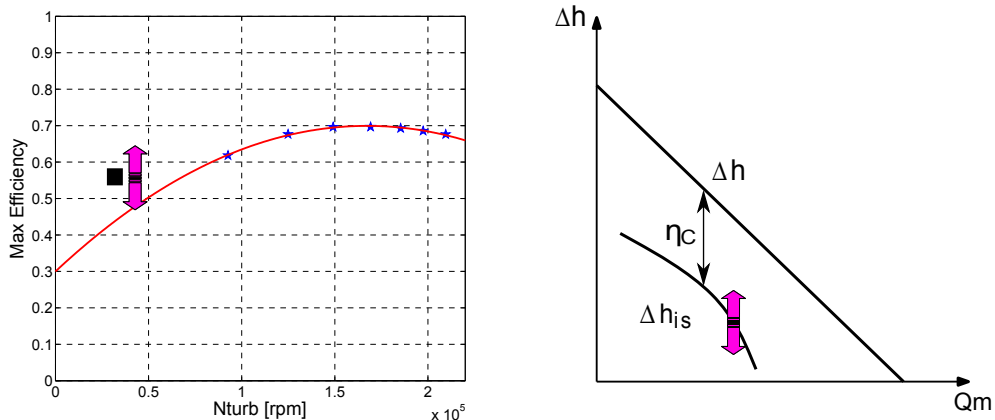


FIG. 6.7 – Left : Maximum efficiency per iso-speed of a radial compressor vs. turbocharger shaft speed (stars). The red line illustrates the result of a quadratic function curve fitting. Right : Illustration of the impact of the translation of the Δh_{is} curve on the maximum efficiency (black square on the right plot)

This treatment ensures the physical validity of the extrapolated compressor data by using the trend of the maximum isentropic efficiency as a physical criterion. The specificity of the developed method is that it is based on the fundamental relationship between Δh and Δh_{is} : $\eta_C = \frac{\Delta h_{is}}{\Delta h}$. It is interesting to notice that the existing curve fitting approaches dedicated to the compressor data maps are using two distinct treatments for the pressure ratio map and for the efficiency map [94], [69], [95], [58]. Therefore, such methods could potentially break the isentropic efficiency definition, which could lead to the following uncorrect relationship : $\eta_C \neq \frac{\Delta h_{is}}{\Delta h}$.

Compressor data maps creation :

Once the values of Δh and Δh_{is} are calculated for any corrected mass flow rate in the operating range, pressure ratio and efficiency data maps can be easily constructed :

- As Δh_{is} is known, the pressure ratio can be directly calculated using the following relationship :

$$\frac{P_{02}}{P_{01}} = \left(1 + \frac{\Delta h_{is}}{C_p T_{01}}\right)^{\frac{\gamma}{\gamma-1}}$$
- The isentropic efficiency is easily calculated : $\eta_C = \frac{\Delta h_{is}}{\Delta h}$. Unlike standard curve fitting methods, there is no need to develop a specific curve fitting treatment for the efficiency. It is naturally derived from the knowledge of the isentropic and non-isentropic specific enthalpy change values.

6.3.2 Turbine model

In order to build turbine's data maps, the values of both the specific enthalpy change Δh and the specific isentropic enthalpy Δh_{is} change need to be determined for a given mass flow rate Qm_T . As in the case of the compressor, we are going to use the linear relationship between Δh and the corrected mass flow rate Qm_{redT} to build the extrapolation process.

Δh determination :

From the suppliers's data, Δh is calculated using Eq. 6.15. As the evolution of Δh regarding the corrected mass flow rate rate is linear (Eq. 6.23), it is therefore possible to determine a set of parameters a and b , only dependent upon the rotational speed N_{turb} :

$$\Delta h = a(N_{turb}) Qm_{redT} + b(N_{turb}) \quad (6.28)$$

In the case where the turbine shaft is not rotating, no power is captured by the turbine even though mass flow rate is established. Therefore, the evolution of Δh vs. Qm_{redT} at $N_{turb} = 0$ is an horizontal line such that $\Delta h = 0$. Consequently, a and b are extrapolated towards lower rpm values such that : $a(0) = 0$ and $b(0) = 0$. Therefore, $b(N_{turb})$ will be extrapolated as a quadratic function reaching 0 at its origin. $a(N_{turb})$ is linearly extrapolated to reach 0 at its origin.

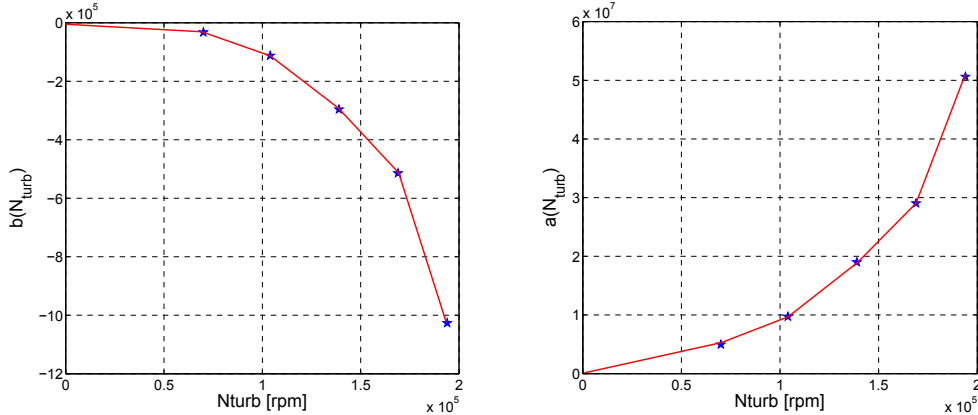


FIG. 6.8 – Evolution of $a(N_{turb})$ (right) and of $b(N_{turb})$ (left) regarding the turbine shaft speed (stars). Red line illustrates the data interpolation and the extrapolation towards low rpm values.

It is also important to notice that in the case where the turbine has a variable geometry, multiple sets of coefficients a and b will be calculated. There will be as many sets of a and b coefficients as there are VGT positions provided by the supplier. For example, if a supplier provides 7 turbine curves corresponding to 7 different VGT positions, then 7 sets of coefficients $a(N_{turb})$ and $b(N_{turb})$ will be determined.

Δh_{is} determination :

In order to calculate the evolution of $\Delta h_{is} = (1 - (\frac{P_{04}}{P_{03}})^{\frac{\gamma-1}{\gamma}})Cp T_{03}$ regarding the mass flow rate, it is necessary to have a relationship between the pressure ratio across the turbine $\frac{P_{04}}{P_{03}}$ and the corrected mass flow rate Qm_{redT} . Such relationship is provided by modeling the turbine as a flow through a nozzle. Jensen et al. [69] have, among others, demonstrated that such an approach was well suited for modeling the turbine flow. Additionally, this model will naturally tends to 0 when the pressure ratio reaches 1. Therefore, Jensen's approach will be directly used here (Eq. 6.29 to 6.31). Parameters k_i are determined via a least square algorithm. Once the relationship between the pressure ratio and the mass flow rate has been defined, it is possible to express the evolution of Δh_{is} vs. Qm_{redT} . Unlike in the compressor's case, there is no need to introduce a specific treatment to extrapolate Δh_{is} data towards lower rpm values. Indeed, as previously said, the nozzle model is based on a physical flow equation which describes well the behavior of the turbine for low pressure ratios.

$$Qm_{redT} = F_t \sqrt{\frac{2\gamma}{\gamma-1} \left[\left(\frac{p_4}{p_{03}} \right)^{\frac{2}{\gamma}} - \left(\frac{p_4}{p_{03}} \right)^{\frac{\gamma+1}{\gamma}} \right]} \quad \frac{p_4}{p_{03}} > \frac{2}{\gamma+1}^{\frac{\gamma}{\gamma-1}} \quad (6.29)$$

$$Qm_{redT} = F_t \sqrt{\gamma \left(\frac{2}{\gamma+1} \right)^{\frac{\gamma+1}{\gamma-1}}} \quad \frac{p_4}{p_{03}} < \frac{2}{\gamma+1}^{\frac{\gamma}{\gamma-1}} \quad (6.30)$$

$$F_t = \frac{k_1 \cdot N_{turb} + k_2}{\frac{1}{Pit}} + k_3 \cdot N_{turb} + k_4 \quad (6.31)$$

Turbine data maps creation :

From the previous developments, it is possible to build turbine data maps :

- The pressure ratio vs. mass flow rate data map is directly calculate using Eq. 6.29 and 6.30.
- Knowing the pressure ratio, the specific isentropic enthalpy change is calculated :

$$\Delta h_{is} = (1 - (\frac{P_{04}}{P_{03}})^{\frac{\gamma-1}{\gamma}})Cp T_{03}.$$
- Δh is determined from the linear extrapolations. Finally, the isentropic efficiency is calculated :

$$\eta_T = \frac{\Delta h}{\Delta h_{is}}.$$

Compressor and turbine models : recapitulation

- The development of the equations of the thermodynamical processes occurring within radial turbomachines has allowed to develop the linear relationship between the specific enthalpy change Δh and the corrected mass flow rates Qm_{redC} and Qm_{redT} . The output of these relationships is the expression of the linear coefficients $a(N_{turb})$ and $b(N_{turb})$, which allows to develop a physical-based interpolation and extrapolation treatment for Δh .
- The identification of the maximum efficiency vs. turbocharger shaft speed as a quadratic function allows to create a physical criterion in order to ensure the physical validity of the extrapolated Δh_{is} values for the compressor.
- An important point is that the fundamental equations of the isentropic efficiency $\eta_C = \frac{\Delta h_{is}}{\Delta h}$ and $\eta_T = \frac{\Delta h}{\Delta h_{is}}$ are at the basis of the developed treatment. Therefore, the calculated efficiency is directly impacted by the enthalpy change across the turbomachines. Both types of data maps (pressure vs. mass flow rate and efficiency vs. mass flow rate) are therefore linked, as in the case of phenomenological-based models. This ensures the physical consistency of the developed models.

6.4 Results and validation of the developed models

6.4.1 Application and results of the developed method on experimental data from suppliers

In this subsection, the curve fitting methods are tested on three different turbochargers (compressor + turbine) from the following applications : (1) : 2.0l diesel engine , (2) : 1.5l diesel engine and (3) : 1.2l gasoline engine. The data supplied by the manufacturer (stars) are superimposed onto extrapolation calculation results (plain lines). Extrapolation is performed to cover the entire mass flow rate / pressure ratios operating range. An extrapolation towards low rotational speeds is also performed to evaluate the robustness of the method. It must be noticed that turbine (1) is VGT, however, for convenience and as this has no influence on the calculation method, only results at a VGT opening of 50% are shown.

Results from the previously developed method are compared to Jensen's method results. Comparison is not performed for the turbine mass flow rate as this is the Jensen's method which is used in both cases (Fig. 6.19). Fig. 6.9 shows the typical efficiency evolution for turbines, based on measurements. On this figure, turbine rotary speed is expressed related to design speed (lowest speed is for coefficient 0.4, highest speed is for coefficient 1.0). It appears that the extrapolation results from the method developers in this thesis provides the correct trends for the turbine efficiency (Fig. 6.16 to Fig. 6.18). On the opposite, Jensen's method provides, for turbines 1 and 2, an unrealistic efficiency decrease : at low rpm, efficiency reaches 0 for pressure ratio values of about 2, which is not physical. In fact, it appears that the turbine data provided by the suppliers only cover a narrow range with respect to the blade speed ratio. Therefore, it is difficult for Jensen's method to capture the shape of the efficiency curve on the global operating range. On the other hand, the turbine efficiency method developed in this thesis relies on the identification of linear trends, which is much more robust in the case of narrow data range.

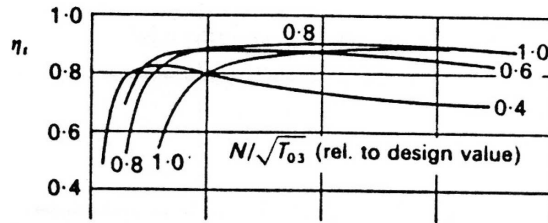


FIG. 6.9 – Typical turbine efficiency evolution in terms of rotational speed and mass flow rate.
x axis is mass flow rate.

From the results shown on Fig. 6.10 to Fig. 6.12, one can notice a strong improvement of the compressor pressure ratio inter/extrapolation accuracy. In the same time, the extrapolation of the compressor efficiency has also been improved (Fig. 6.13 to Fig. 6.15). One should notice that the left part of the extrapolated compressor characteristics are purely theoretical, as surge usually occurs at low mass flow rate values. However, it is possible to plug to the data maps a surge model. An example of this combination is shown on Fig. 6.20. Moore Greitzer's model allows to calculate the pressure ratio vs. mass flow rate values in the surge area [52], [53], [24], [93], [124]. The decrease of enthalpy change across the compressor has an impact on the isentropic efficiency. In the case of the thesis model, this naturally taken into account as the efficiency is defined as the ratio of the isentropic enthalpy change (not impacted by the surge) and the enthalpy change (calculated via the surge model). If Jensen's method would be used, the pressure ratio and efficiency data maps would be totally uncorrelated.

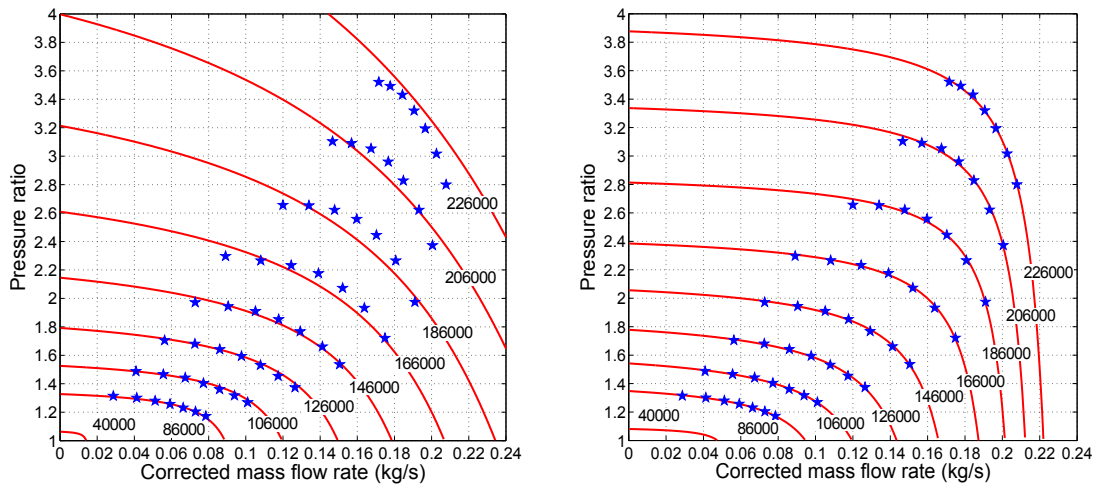


FIG. 6.10 – Turbocharger 1 : Compressor pressure ratio extrapolation results. Jensen’s method (left) - Proposed method (right)

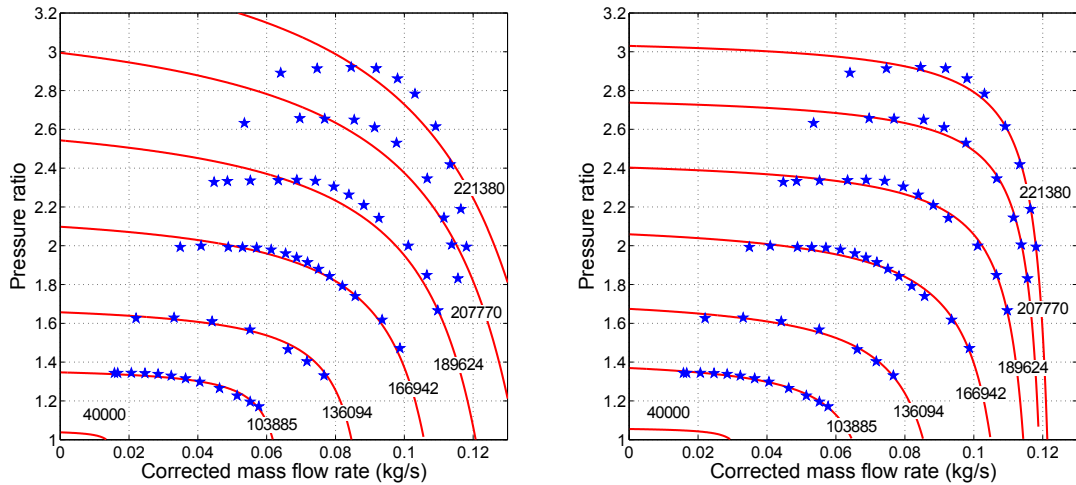


FIG. 6.11 – Turbocharger 2 : Compressor pressure ratio extrapolation results. Jensen’s method (left) - Proposed method (right)

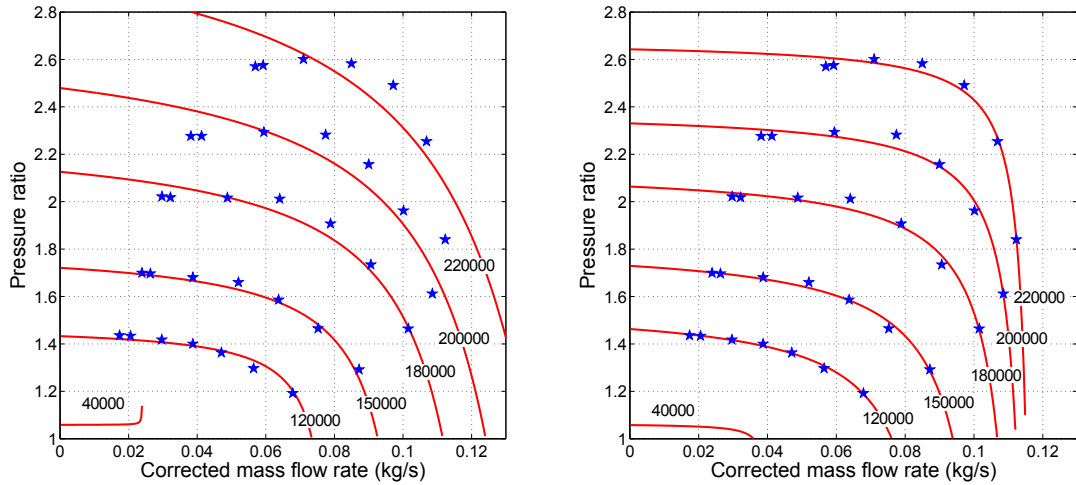


FIG. 6.12 – Turbocharger 3 : Compressor pressure ratio extrapolation results. Jensen’s method (left) - Proposed method (right)

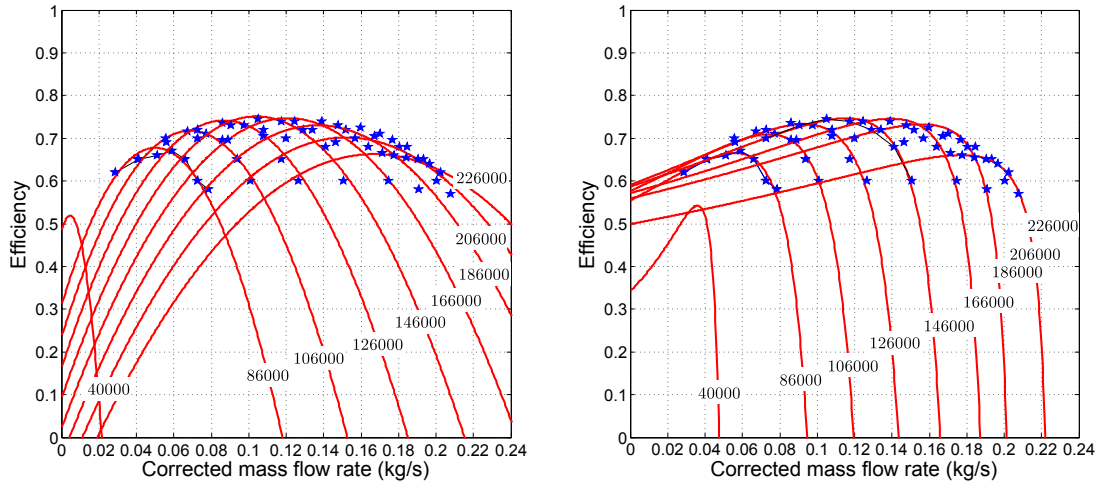


FIG. 6.13 – Turbocharger 1 : Compressor efficiency extrapolation results. Jensen’s method (left)
- Proposed method (right)

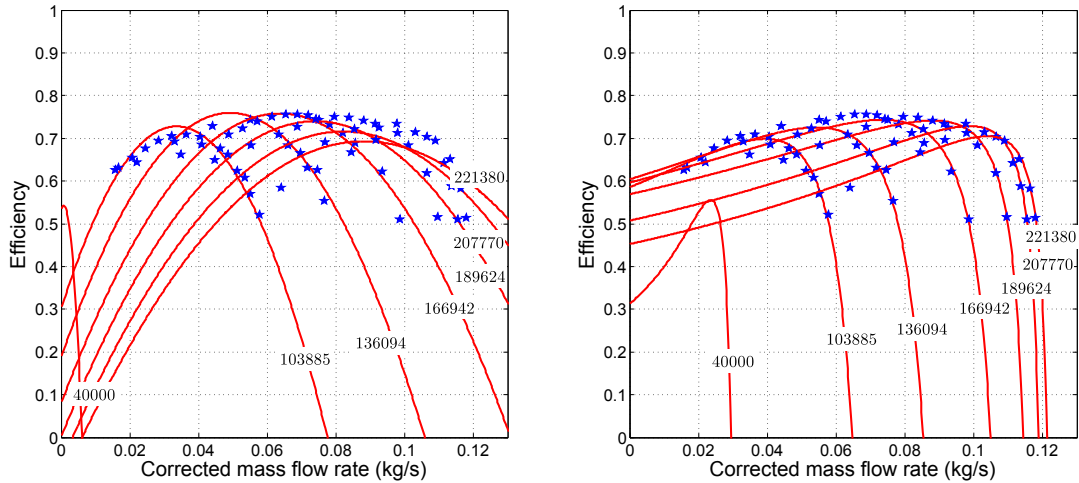


FIG. 6.14 – Turbocharger 2 : Compressor efficiency extrapolation results. Jensen’s method (left)
- Proposed method (right)

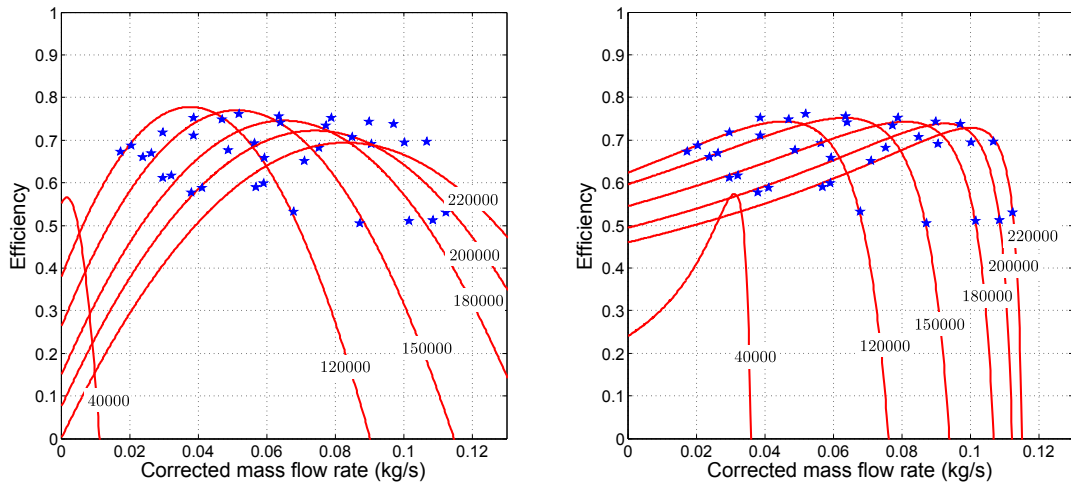


FIG. 6.15 – Turbocharger 3 : Compressor efficiency extrapolation results. Jensen’s method (left)
- Proposed method (right)

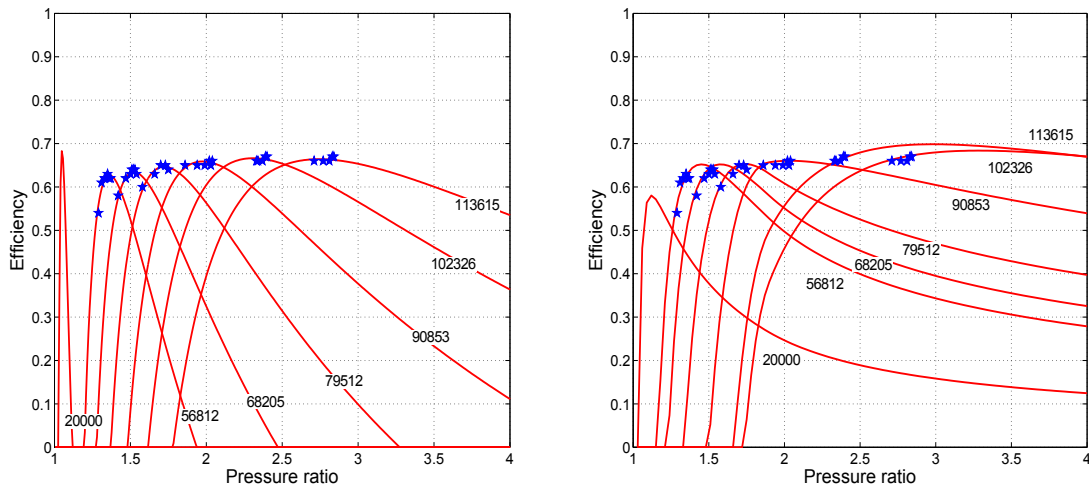


FIG. 6.16 – Turbocharger 1 : Turbine efficiency extrapolation results. Jensen’s method (left) - Proposed method (right)

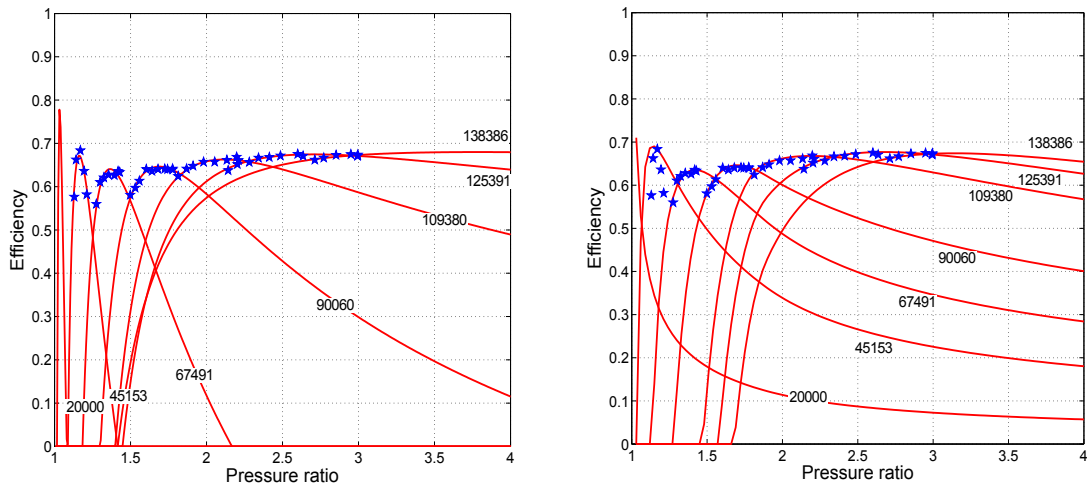


FIG. 6.17 – Turbocharger 2 : Turbine efficiency extrapolation results. Jensen’s method (left) - Proposed method (right)

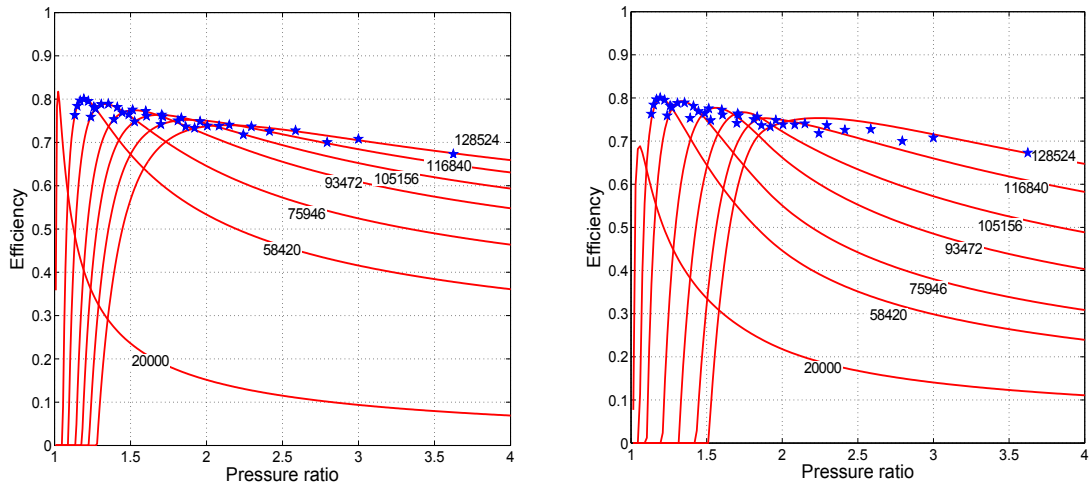


FIG. 6.18 – Turbocharger 3 : Turbine efficiency extrapolation results. Jensen’s method (left) - Proposed method (right)

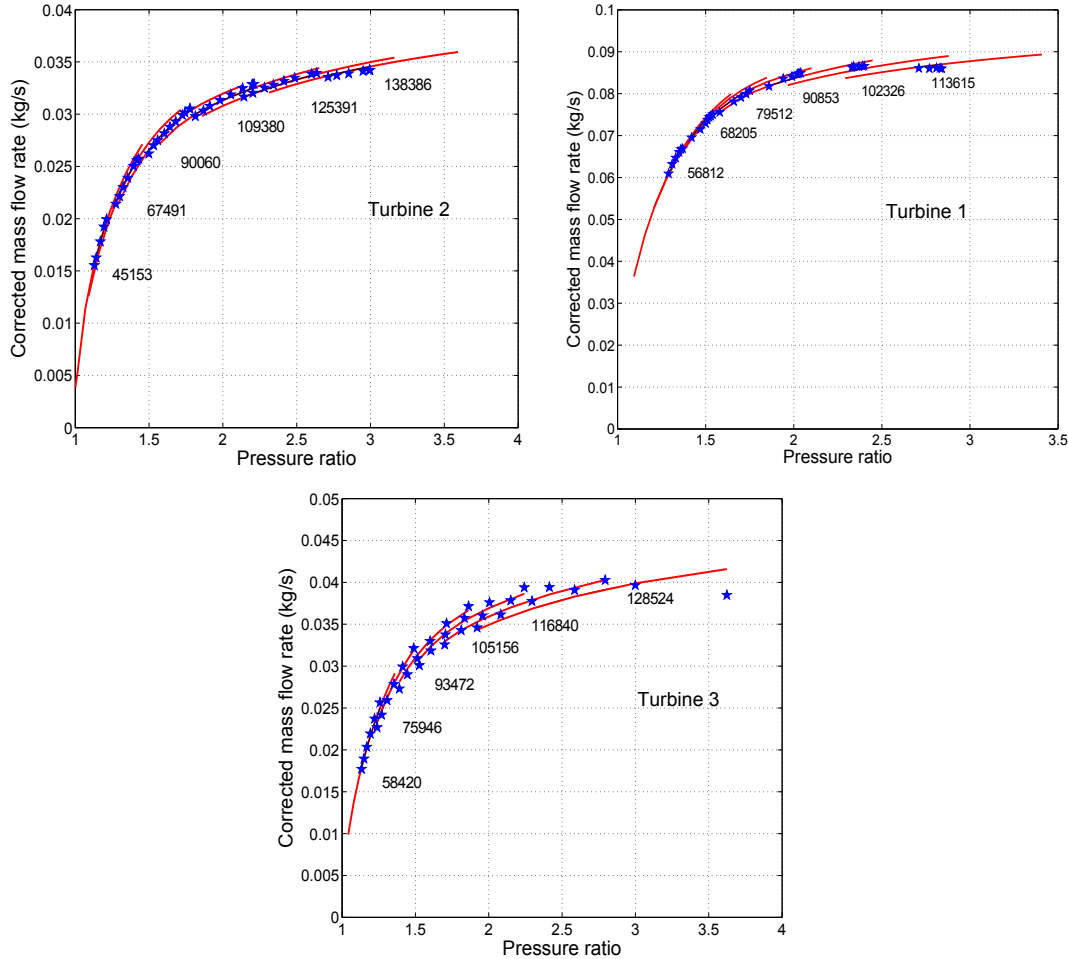


FIG. 6.19 – Turbine mass flow rate interpolation results. Jensen’s method

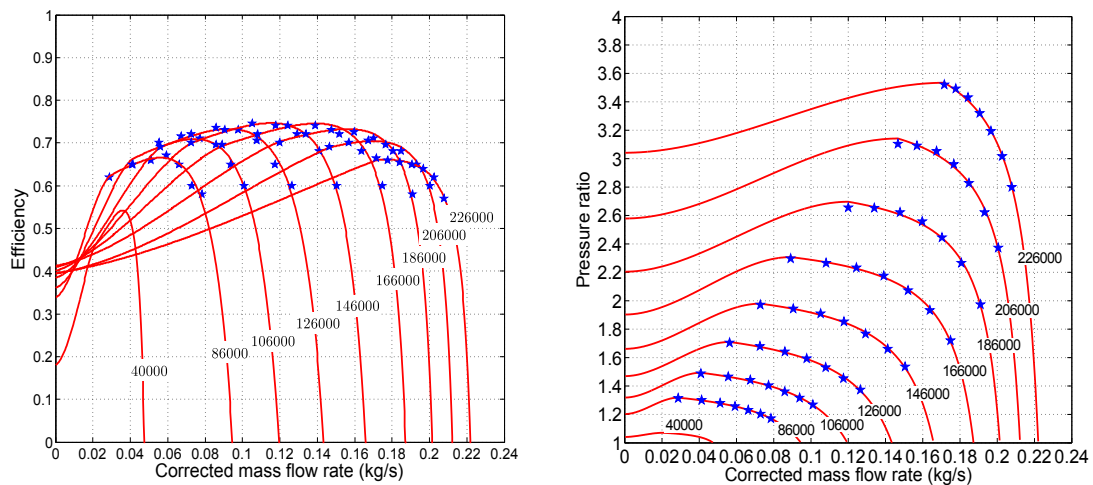


FIG. 6.20 – Turbocharger 1 : Compressor pressure ratio and efficiency extrapolation combined to the Moore-Greitzer’s surge model. Proposed method

6.4.2 Validation of the extrapolation process with respect to turbocharger test bench data

Figures 6.21 and 6.22 show the comparison between the measured data on the turbocharger test bench (previously described in the thesis) and the developed model results. The turbocharger test bench allowed us to measure operating point at low rotational speed. In order to validate the extrapolation process of the developed model, only higher iso-speed are used as inputs of the model. Compressor model is applied to compressor's data higher than 90 krpm, turbine model is applied to data higher than 35 krpm. Therefore, the lower part of the operating range is fully extrapolated and comparison can be made regarding the experimental data. Results are shown for a temperature of 773 K at the inlet of the turbine. This allows to be close to the supplier's test bench conditions. Turbine's efficiency reaches values higher than 1; this phenomenon is due to the heat exchange process and will be explained in the chapter dedicated to heat exchange modeling.

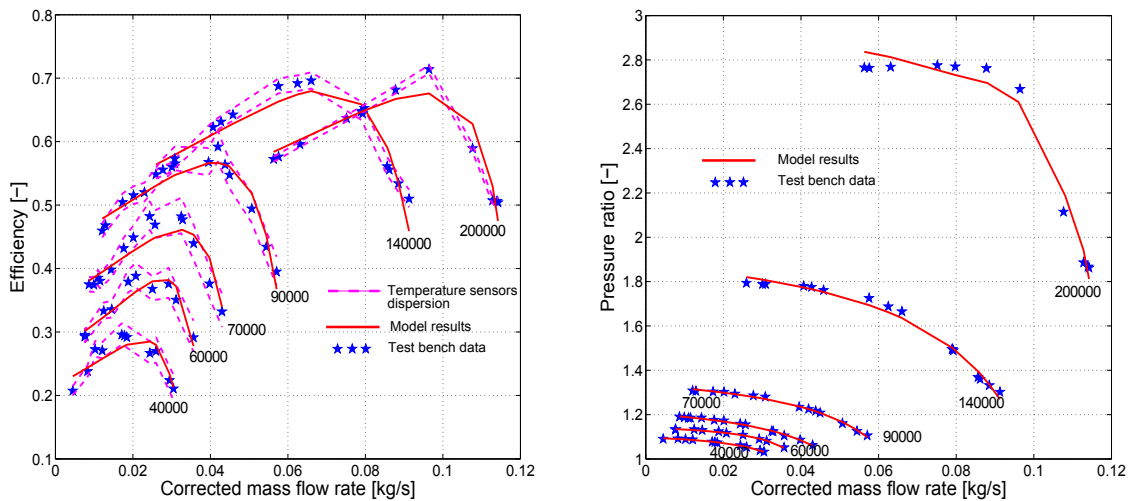


FIG. 6.21 – Data from the turbocharger test bench. Compressor efficiency (left) - Compressor pressure ratio (right) - Model results for iso-speed lines lower than 90 krpm are fully extrapolated.

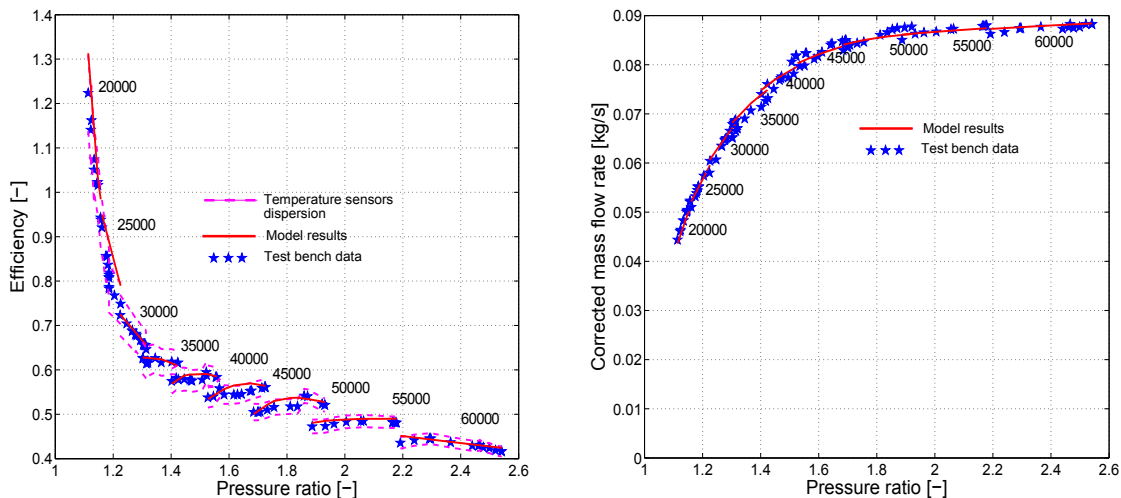


FIG. 6.22 – Data from the turbocharger test bench. Turbine efficiency (left) - Turbine mass flow rate (right) - Model results for iso-speed lines lower than 35 krpm are fully extrapolated. VGT opening = 100%

It appears that the results are in good agreement with the experimental data. The calculated efficiency is in most cases within the dispersion caused by the accuracy level of the temperature sensors. The pressure ratio vs. mass flow rate data maps also show a satisfying level of accuracy. The difference between the results of the model and the experimental data is always lower than 5%, even in the extrapolated range. The good results obtained in the extrapolated range of the data maps show that model is both robust and accurate. It would have been interesting to test other turbochargers on the test bench in order to validate extensively the extrapolation performances of the model. However, due to lack of time, this could not be achieved during the thesis.

Results of the developed turbocharger model : main points

- A new simple and accurate 0D model for automotive centrifugal compressors and turbines has been derived. This development has been motivated by the difficulty encountered with standard techniques to extrapolate the data maps of the turbomachines. Thanks to the use of mathematic curve fitting techniques and the introduction of turbomachinery physics, extrapolations are now robust and controlled by physical laws.
- The model has been tested on 3 different turbocharger data maps provided by the suppliers. A strong improvement of the compressor pressure ratio and efficiency data maps interpolation has been noticed. Additionally, the typical radial turbines efficiency trend is now respected.
- The extrapolation process of the model has been tested with respect to experimental data from a turbocharger test bench. This study has shown that the developed model is both robust and accurate. In the future, it should be interesting to test a wide range of turbochargers in order to completely validate the model in its extrapolation area.

Chapter 7

Turbocharger thermal exchanges

In the previous chapter, the interpolation and extrapolation methods for the turbocharger datamaps have been developed. Such datamaps allow to get in a simple and time-efficient way the performances of the compressor and the turbine in their entire operating range. However, the direct application of such a model does not take into account the heat exchange processes which occur within turbochargers. On test bench and under steady-flow conditions, a non-negligible part of the heat at the turbine is transferred to the compressor and the oil. The performance datamaps of the turbocharger take into account this heat transfer, but only for the specific conditions encountered on the test bench. In order to take into account the heat transfers in a physical way, the following process is introduced in this chapter :

- The development of the thermodynamical equations which allow to express the heat transfers within the turbocharger. These equations will be based on a one-dimensional assumption.
- The identification of the heat transfers on a specific application using test bench data and the equations which characterize the heat transfers.
- The development of a turbocharger thermal model in order to take into account the heat transfers under transient conditions.

7.1 Thermal exchanges calculation from measurements

The goal of this section is to detail the process and equations introduced in order to identify the heat exchanges occurring within an insulated but non-adiabatical turbocharger. The study will be based on the data from the turbocharger test bench measurements as referred in the test bench presentation chapter. Attention should be paid to make the distinction between the effective turbomachine shaft power (\dot{W}_{sh}) and the *apparent* power calculated via temperature measurements (\dot{W}).

7.1.1 Insulated and non-adiabatical turbocharger case : equations

The acquisitions have been performed under non-transient conditions, the compressor inlet temperature was approximately of 293K, the oil temperature was regulated at 353K and the turbine inlet temperature was set between 373K and 873K ($T_T > T_O > T_C$). Under these conditions, the results of the experimental and numerical studies detailed in [12], [13], [11], [26] show that the heat transfers can be considered as one-dimensional and that the heat is transferred from the turbine to the compressor (Q_C) and the oil (Q_O). This is shown on Fig. 7.1. Additionally, the turbine shaft power (\dot{W}_{Tsh}) is transferred to the compressor via the shaft (\dot{W}_{Csh}), even though some friction losses occur at the bearings (\dot{W}_F). The friction losses are transformed into heat and therefore the power gain for the oil flow due to heat exchanges and friction losses is expressed as :

$$\dot{W}_O = \dot{W}_F + Q_O \quad (7.1)$$

By the mean of the equilibrium of the powers on the shaft, the turbine shaft power is expressed in Eq. 7.2. Finally, the conservation of energy allows to write the heat exchange equation (Eq. 7.3).

$$-\dot{W}_{Tsh} = \dot{W}_F + \dot{W}_{Csh} \quad (7.2)$$

$$-Q_T = Q_C + Q_O \quad (7.3)$$

The apparent powers calculated by the mean of the temperature measurement take into account the power on the shaft and the heat transfers, which can be written as :

$$\dot{W}_T = Q_T + \dot{W}_{Tsh} \quad (7.4)$$

$$\dot{W}_C = \dot{W}_{Csh} - Q_C \quad (7.5)$$

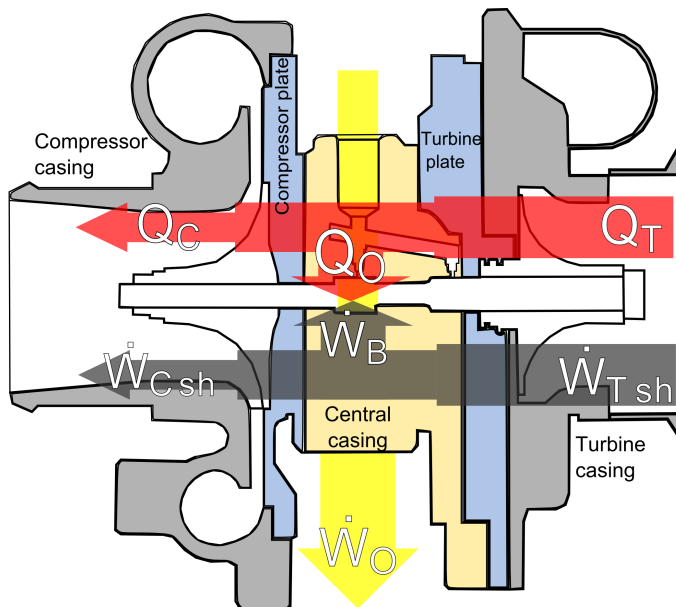


FIG. 7.1 – Scheme of the heat and power exchanges within a non-adiabatical and insulated turbocharger. Considered case is for a turbine inlet temperature higher than the oil temperature and the compressor inlet temperature.

Finally, from the previous equations development it is possible to get the system of 4 equations and 6 unknown quantities which should be solved in order to determine the heat exchanges (Eq. 7.6 to Eq. 7.9). The only known quantities are the values of \dot{W}_T , \dot{W}_C from the measurements. It should be noticed that a fifth equation ($Q_O = \dot{W}_F - \dot{W}_O$ from Eq. 7.1) could be added to the system, which would lead to a system of 5 equations and 6 unknown quantities. However, the uncertainties made on the measurement of \dot{W}_O are really high as the oil flow is biphasic at the exit of the turbocharger casing (oil mist). This uncertainty could heavily impact the determination of the other quantities, therefore the value of \dot{W}_O won't be introduced in the following developments.

$$Q_C = \dot{W}_{Csh} - \dot{W}_C \quad (7.6)$$

$$Q_T = \dot{W}_T - \dot{W}_{Tsh} \quad (7.7)$$

$$Q_O = -Q_C - Q_T \quad (7.8)$$

$$\dot{W}_F = -\dot{W}_{Tsh} - \dot{W}_{Csh} \quad (7.9)$$

The previous system can not be solved as there are more unknown quantities than there are equations. In order to get enough information to solve the system of equations, the insulated and adiabatical turbocharger tests are introduced.

7.1.2 Insulated and adiabatical turbocharger case : equations

In the adiabatical case, there is no heat exchange occurring within the turbocharger, therefore :

$$Q_T = Q_C = Q_O = 0 \quad (7.10)$$

From this, Eq.7.1, Eq.7.6, Eq.7.7 and Eq.7.9 are now reduced to the following system of equations :

$$\dot{W}_O = \dot{W}_F \quad (7.11)$$

$$\dot{W}_{Csh} = \dot{W}_C \quad (7.12)$$

$$\dot{W}_{Tsh} = \dot{W}_T \quad (7.13)$$

$$\dot{W}_F = -\dot{W}_{Tsh} - \dot{W}_{Csh} \quad (7.14)$$

It appears that measurements performed in the adiabatical and insulated case allow to measure directly the shaft power of the turbomachines (Eq. 7.12, Eq. 7.13). Finally, the power lost to the bearings by friction is directly calculated via equation 7.14.

7.1.3 Combination of adiabatical and non-adiabatical tests : assumptions and introduced models

In order to calculate the heat transfers occurring within the turbocharger, the experimental process detailed by Baar et al. [3], Shaaban [118] or Cormerais [26] is used. This process is detailed in the literature review section. It relies on a comparative study of the compressor, turbine and oil powers between the adiabatic and non-adiabatic cases ($\dot{W}_{adia} \neq \dot{W}_{non-adia}$). It is assumed that the heat capacity at constant pressure C_p is constant through the turbomachine, therefore the powers of the compressor and the turbine are calculated using the following equations :

$$\dot{W}_C = Qm_C C_{p,air} \Delta T_{comp} \quad (7.15)$$

$$\dot{W}_T = Qm_T C_{p,air} \Delta T_{turb} \quad (7.16)$$

$$(7.17)$$

A major assumption made in [3], [118] and [26] is that compressor shaft power \dot{W}_{Csh} is not dependent upon heat exchanges, which means that heat exchanges are considered to occur in the collector, after the rotor. This hypothesis has been validated experimentally by Shaaban [118], as he showed that compressor heat exchanges occurring before the impeller are accounting for less than 3% of the total heat exchanges

within the compressor. Considering this assumption, \dot{W}_{Csh} is determined from the adiabatic compressor data (Eq. 7.18) and the heat exchange at the compressor is calculated via the equation 7.19.

$$\dot{W}_{Csh,non-adia} = \dot{W}_{Csh,adia} \quad (7.18)$$

$$Q_C = \dot{W}_{Csh,non-adia} - \dot{W}_C \quad (7.19)$$

Friction power losses \dot{W}_F are known in the adiabatic case (Eq. 7.14). In order to estimate this quantity in the non-adiabatic case, it is necessary to build a bearing friction model. The friction model uses a Petroff-based estimation of the power losses occurring in the oil bearings. The model is then calibrated using the adiabatic test results. The 7.1.4 subsection is dedicated to the development and the calibration of the bearing friction model.

Once the compressor and the bearing powers are known, it is possible to calculate the turbine shaft power by the mean of the power equilibrium (Eq. 7.20). Finally, once the turbine shaft power is known in the non-adiabatic case, the heat transfer at the turbine is calculated (Eq. 7.21).

$$-\dot{W}_{Tsh,non-adia} = \dot{W}_{Csh,non-adia} + \dot{W}_F \quad (7.20)$$

$$Q_T = \dot{W}_{T,non-adia} - \dot{W}_{Tsh,non-adia} \quad (7.21)$$

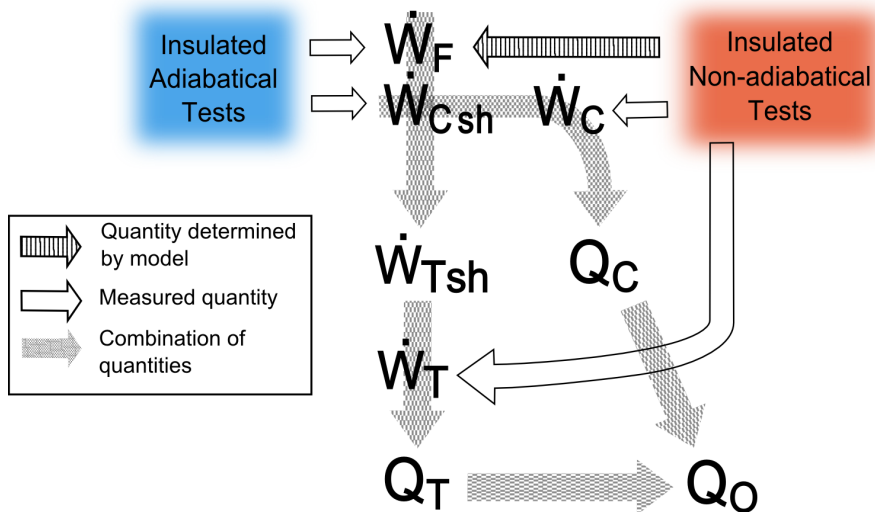


FIG. 7.2 – Representation of the experimental process to calculate heat exchanges within a turbocharger.

7.1.4 Bearing friction model

From insulated and adiabatical tests, it appears that there is discrepancy between the compressor shaft power \dot{W}_{Csh} and the turbine shaft power \dot{W}_{Tsh} . This difference is due to rotational friction power losses. The first source of rotational power loss is due to the viscous flow occurring within the oil bearings. The oil is submitted to shear stress because of the shaft rotation, creating a resistive torque : T_B . The second source of power loss is due to the axial stop : pressures applied on the compressor wheel and on the turbine wheel create axial forces (F_C and F_T on Fig. 7.3). Axial displacement of the shaft is restricted by the axial stop near the turbine wheel : contact force F_{ax_stp} is therefore established between the rotor shaft and the

turbocharger housing. As the shaft is rotating, this contact force will result in a resistive torque : T_{ax_stp} . Therefore, the friction power losses are divided into two contribution sources : the viscous friction occurring in the oil bearing and the contact friction due to axial stop forces. Both contributions need to be calculated in order to build the friction model : $\dot{W}_F = \dot{W}_{ax_stp} + \dot{W}_B$.

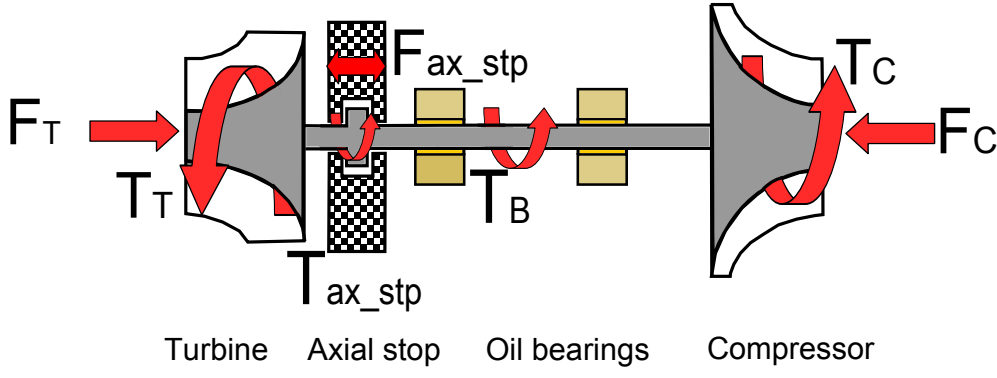


FIG. 7.3 – Considered axial forces (F) and torques (T) applied on the turbocharger rotor.

A major assumption made in the following developments is that the radial forces applied on the shaft have a negligible impact on the hydrodynamical flow in the bearing. This assumption is motivated by the following facts :

- The rotor shaft is dynamically balanced.
- The mass of the rotor is small ($< 100\text{g}$).
- As the compressor and the turbine casings are almost axisymmetrical, the pressure distributions on the fringe of the wheels are supposed to be uniform, therefore leading to no resultant radial forces applied on the wheels.

Consequently, the Petroff's formulation for viscous losses occurring within an oil bearing under negligible radial load will be used. The corresponding bearing resistive torque and the power loss deduced from this torque are expressed in Eq. 7.22 and 7.23. μ is the oil viscosity, R is the radius of the rotor shaft, B_w the bearing width and B_R the radial clearance of the bearing.

$$T_B = \frac{2\pi\mu N_{turb} R^2 B_w}{B_R} \quad (7.22)$$

$$\dot{W}_B = \frac{2\pi\mu N_{turb}^2 R^2 B_w}{B_R} \quad (7.23)$$

The axial stop torque and power losses are expressed in Eq. 7.24 and 7.25. f is the coefficient of friction between the shaft and the axial stop, which is dependent upon the oil viscosity, the rotational speed and the axial force difference. R_{ax_stp} is the contact length between the shaft and the axial stop.

$$T_{ax_stp} = (F_T - F_C) f(\mu, N_{turb}, \Delta F) \frac{R_{ax_stp}}{2} N_{turb} \quad (7.24)$$

$$\dot{W}_{ax_stp} = (F_T - F_C) f(\mu, N_{turb}, \Delta F) \frac{R_{ax_stp}}{2} N_{turb}^2 \quad (7.25)$$

The models found in the literature [118], [117], [26] have shown that it is unlikely to calculate the power losses of a rotating shaft by the only mean of a 0D model. It is indeed necessary to use a correlation between

a model and the experimental data. In our case, we have combined \dot{W}_B and \dot{W}_{ax_stp} expressions in a way which allows the introduction of two fitting coefficients k_1 and k_2 . One single set of coefficients is fitted using a least square algorithm and are determined from the insulated and adiabatical tests. These 2 coefficients include the constant terms due to the geometry of the system (R, B_w, \dots) as well as the model uncertainties. The values of k_1 and k_2 are not provided here due to confidentiality reasons.

$$\dot{W}_F = \mu N_{turb}^2 (k_1(F_T - F_C) + k_2) \quad (7.26)$$

$$\mu = 220.87 (T_{oil_mean})^{-2.0462} \quad (7.27)$$

$$T_{oil_mean} = \frac{T_{oil_in} + T_{oil_out}}{2} \quad (7.28)$$

The oil viscosity is calculated using a formula which approximates the dynamical viscosity of a 15W40 oil between 290K and 400K. The oil viscosity is calculated using the mean value of the oil temperature as defined in [118]. It has been previously explained that the value of the temperature of the oil exiting the turbocharger should be unprecise due to the oil mist created. However, this value is used for the oil viscosity determination, as some correction is performed via the experimental correlation of the k coefficients. The result of the correlated model compared to the adiabatical test results is plotted on Fig. 7.4. It appears that the calculated friction power loss is in good adequation with the test results. Around 95% of the modeled power losses results show less than 10% of error when compared to the experimental data.

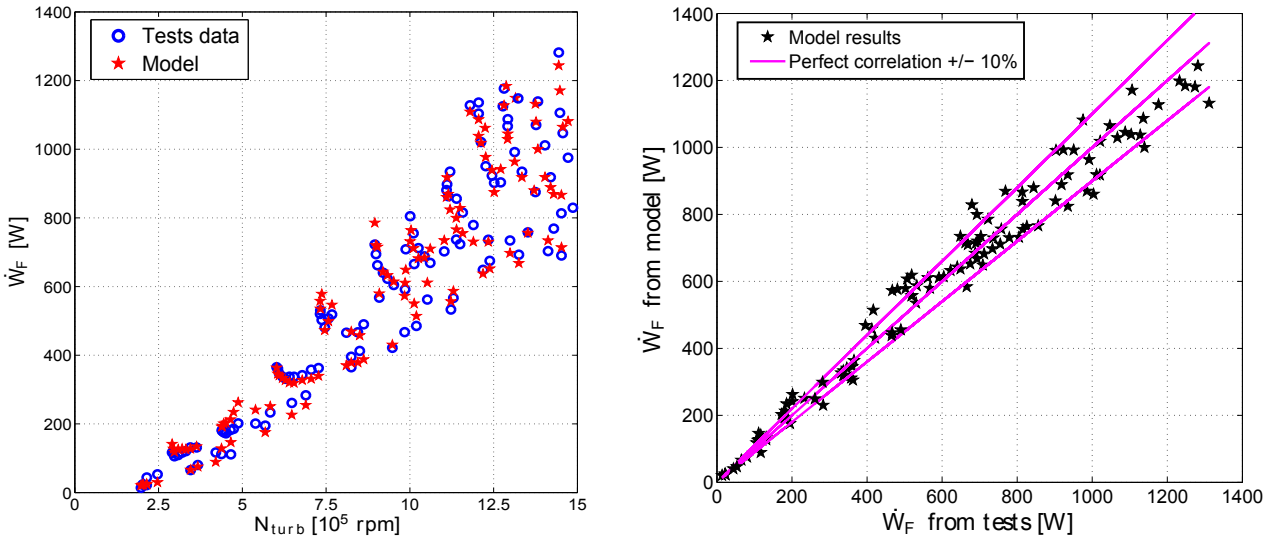


FIG. 7.4 – Comparison between the shaft power losses measured from the insulated adiabatical tests and the friction model results. The correlation line is plotted on the right.

It is also necessary to check the extrapolation behavior of the model. The results of this study is shown on Fig. 7.5, where the oil temperature or the rotational speed have been increased. Extrapolated data show that the physical trends are respected : an increase of the oil temperature causes the oil viscosity to decrease, therefore reducing the resistive torque. On the opposite, an increase of the shaft speed will cause further power losses to happen. It is impossible to compare extrapolated test results to some experimental data. Indeed, the friction power losses can only be determined under adiabatical conditions : therefore the oil temperature can not be changed and low turbine inlet temperature does not allow to reach higher rotational speeds. One should consequently keep in mind that the heat exchange calculation will heavily depend upon the shaft power loss model.

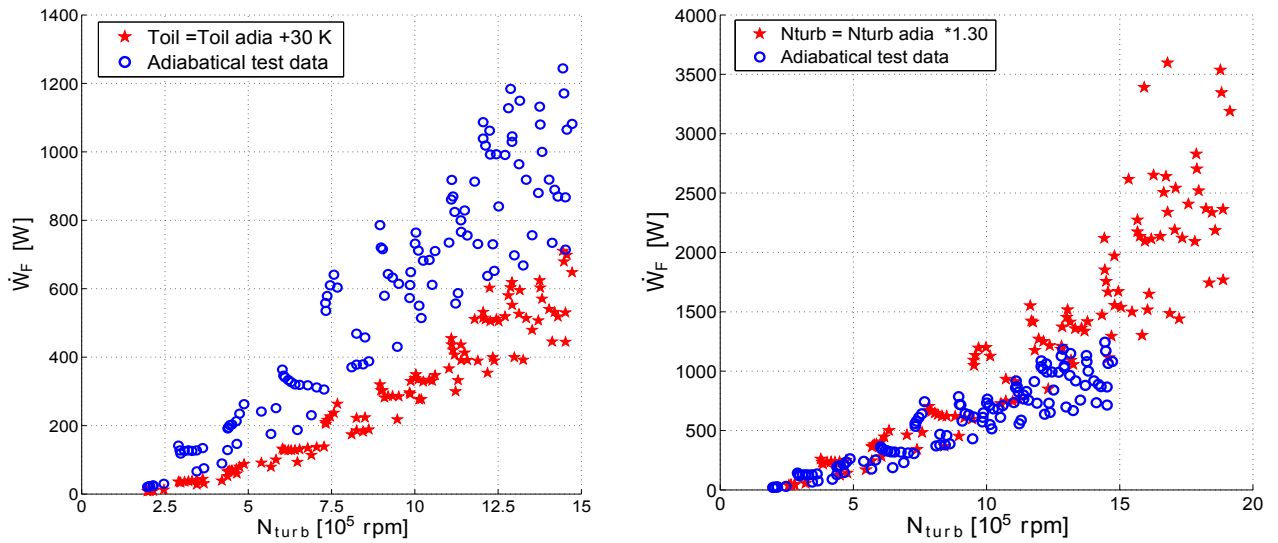


FIG. 7.5 – Extrapolation of the friction power losses model for a change of temperature and rotational speed.

Thermal exchanges equations and assumptions : recapitulation

The development of the main equations and assumptions introduced in order to determine thermal exchanges within a turbocharger has allowed to determine that :

- In order to identify the heat exchanges within a turbocharger, it is possible to build the heat exchange equations via a comparison between the insulated-adiabatical and the insulated non-adiabatical tests data.
- From this study, it appears that a system of equations with 6 unknown quantities need to be solved.
- As the friction power losses cannot be measured in the non-adiabatical case, it is necessary to build a friction power loss model. This model divides the friction power losses into two sources : 1 - the oil friction power loss within the oil bearing, based on Petroff's definition. 2 - The friction created by the axial force (due to the non-equilibrium of pressures in the compressor and in the turbine) applied on the axial stop.
- The heat transfer is assumed to be mono-dimensional, along the rotor shaft direction. This assumption is based on numerical and experimental studies found in the literature. The tests are performed with the following temperature distribution : $T_T > T_O > T_C$. In this case, the heat power is transferred from the turbine to the compressor and the oil. The equations introduced for the heat exchange identification are valid for this temperature distribution.
- The heat transfer at the compressor is assumed to occur after the rotor, in the compressor collector. This means that the shaft power of the compressor is assumed to be independent of the turbine inlet temperature. This assumption has been experimentally verified in the literature. Additional material confirming this hypothesis will be provided in the following section.

7.2 Measurement results

The results from the turbocharger tests previously introduced in the thesis are going to be detailed in this section. At first, the compressor and turbine characteristic data maps will be built in order to underline the impact of the turbine inlet temperature on the efficiency and on the pressure ratios. Secondly, the identified heat exchanges for the turbine, the compressor and the oil flow will be plotted and analyzed.

7.2.1 Compressor data maps

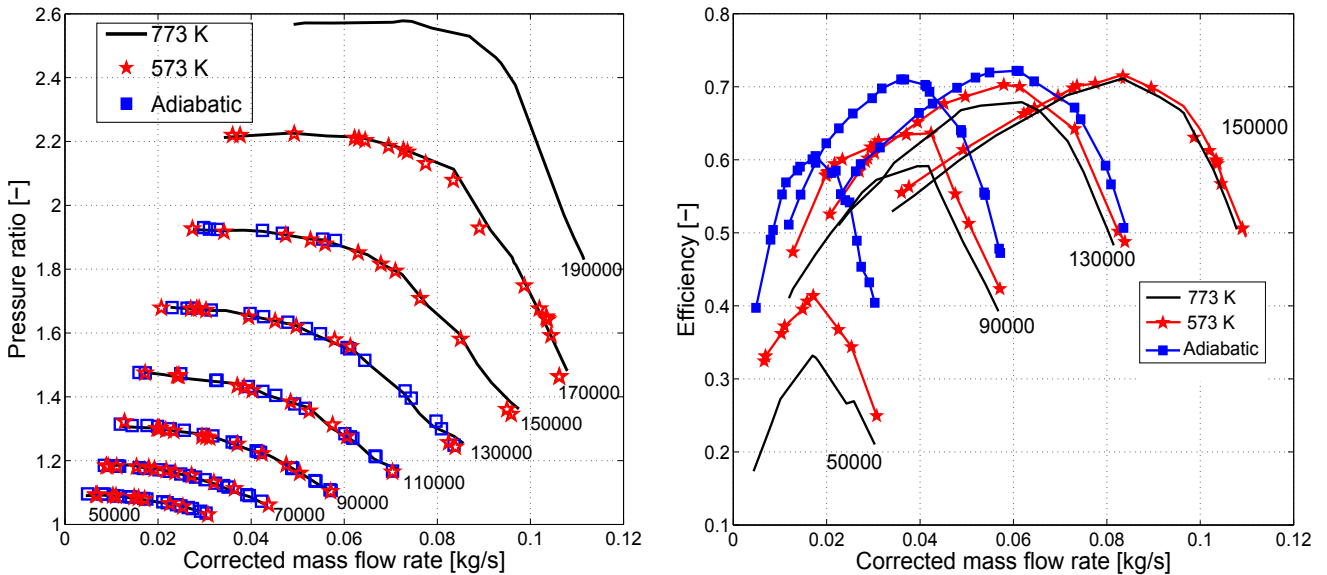


FIG. 7.6 – Comparison of the compressor pressure ratio and efficiency characteristics for various turbine inlet temperatures and various corrected shaft speeds.

Fig. 7.6 shows the impact of the turbine inlet temperature on the compressor characteristic curves. It appears that the pressure ratio vs. corrected mass flow rate is independent upon the turbine inlet temperature. On the other side, the efficiency is affected by the change of temperature at the turbine inlet. One can see that the higher the turbine inlet temperature, the lower measured compressor efficiency. These phenomena confirm that the heat exchange process at the compressor occurs after the rotor. From the left plot on Fig. 7.6, one can write that :

$$(1) \quad \left(\frac{N_{turb}}{\sqrt{T_{in}}} \right)_{Adia} = \left(\frac{N_{turb}}{\sqrt{T_{in}}} \right)_{573K} = \left(\frac{N_{turb}}{\sqrt{T_{in}}} \right)_{773K}$$

$$(2) \quad \left(\frac{P_{out}}{P_{in}} \right)_{Adia} = \left(\frac{P_{out}}{P_{in}} \right)_{573K} = \left(\frac{P_{out}}{P_{in}} \right)_{773K}$$

$$(3) \quad \left(Q_m \frac{\sqrt{T_{in}}}{P_{in}} \right)_{Adia} = \left(Q_m \frac{\sqrt{T_{in}}}{P_{in}} \right)_{573K} = \left(Q_m \frac{\sqrt{T_{in}}}{P_{in}} \right)_{773K}$$

The compressible flows similitude developments (Appendix A) show that these 3 equalities require the equality of the Mach number, of the Reynolds number and of the speed triangles of the compressor. The equality of the speed triangles means that there will be the same aerodynamical efficiency of the compression process through the rotor, therefore the isentropic efficiency of the compressor for the three turbine inlet temperatures is theoretically the same. However, the measured efficiencies show variations depending on the turbine inlet temperature. This is explained as follows :

- The acceleration of the flow through the rotor has the same efficiency for any turbine inlet temperature. This is demonstrated via the conservation of the compressor rotor speed triangles.

- There is some heat power transferred from the turbine to the compressor. This heat will cause an elevation of the compressor exit flow temperature, which has an impact on the measured efficiency :
$$\eta_c = \frac{\left(\left(\frac{P_{02}}{P_{01}}\right)^{\frac{\gamma-1}{\gamma}} - 1\right)}{\frac{T_{02}}{T_{01}} - 1}.$$
- As the efficiency of the process through the rotor remains constant for various turbine inlet temperatures, this means that the heat transfer from the turbine is effective *AFTER* the rotor. This shows that the heat transfer at the compressor occurs in the compressor collector. The main outcome of these observations is that the compressor shaft power (\dot{W}_{Csh}) is independent of the turbine inlet temperature. This confirms the assumption (taken from the literature) made in the previous sections in order to develop the heat transfer identification equations.

One can see on the left plot of Fig.7.6 that while the compressor operating range is entirely covered for a turbine inlet temperature of 773K, it is not the case in the lower turbine inlet temperature cases. In fact, it appears that the lower turbine inlet temperature, the narrower measured operating range. A low temperature flow upstream of the turbine has lower enthalpy than a hot flow, which means that less power will be potentially captured by the turbine. Consequently, less mechanical power is transferred via the shaft to the compressor.

On the left plot of Fig.7.6, it seems that the ratio between the adiabatic and non-adiabatic measured efficiencies is constant with respect to the compressor mass flow rate. Additionally, the difference of efficiency between the adiabatic and non-adiabatic cases decreases when the shaft speed increases, which means that the heat power transferred to the compressor tends to have a negligible influence at higher rotational speeds. These observations are confirmed on Fig. 7.7, where the ratios between the efficiencies measured in the adiabatic and the non-adiabatic cases are plotted.

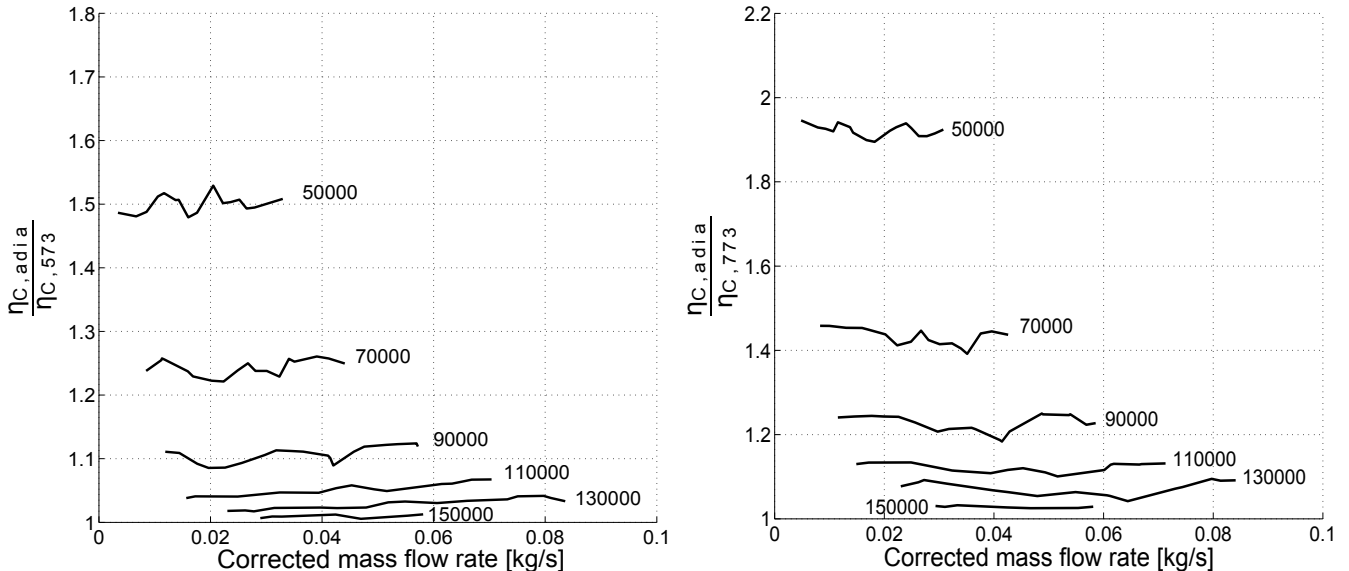


FIG. 7.7 – Ratio between the adiabatic and the non-adiabatic measured efficiencies for various compressor corrected shaft speeds.

7.2.2 Turbine data maps

Fig. 7.8 shows the impact of the turbine inlet temperature on the turbine characteristic curves. The left plot shows the corrected mass flow rate vs. the pressure ratio through the turbine for a VGT setting of 100. As in the compressor case, three cases are considered : the adiabatic case, a turbine inlet temperature of 573K

and a turbine inlet temperature of 773K. From the flow similitude theory (Appendix A), for a given shaft speed, the corrected mass flow rate characteristics should be independent of the turbine inlet temperature. It is not the case here, as the characteristic curves could not be exactly superimposed. This is particularly visible at higher rotational speed : the mass flow rate curves for the three turbine inlet temperatures at 55000 rpm are distinct, as shown on Fig. 7.9.

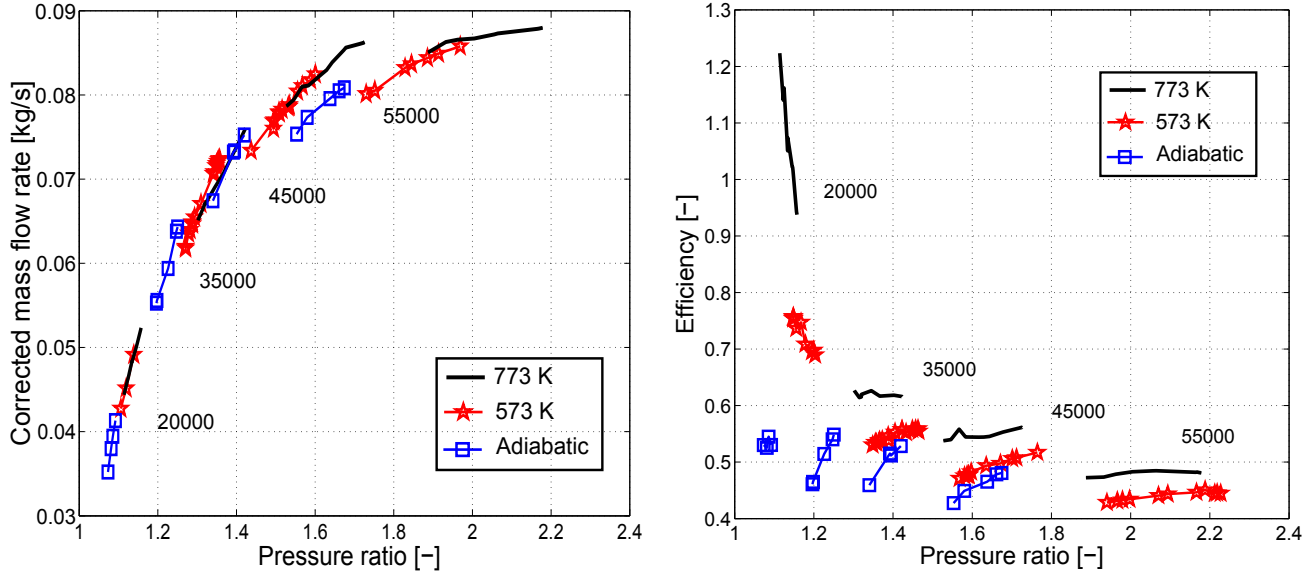


FIG. 7.8 – Comparison of the turbine corrected mass flow rate and efficiency characteristics for various turbine inlet temperatures and various corrected shaft speeds.

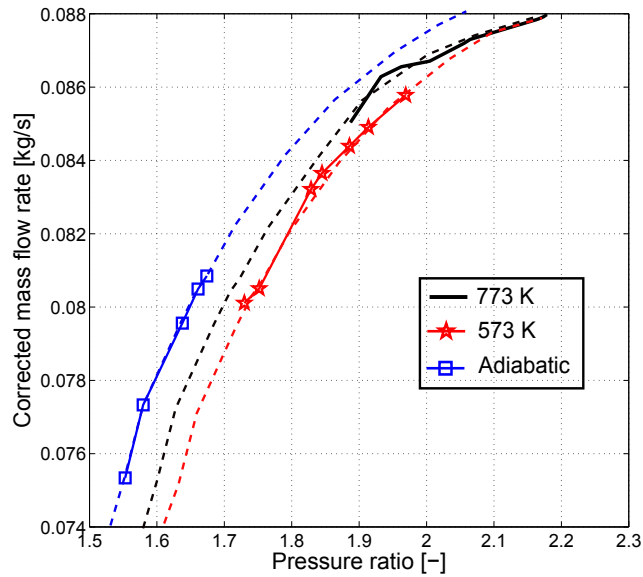


FIG. 7.9 – Close up on the 5500 rpm mass flow rate curve from Fig. 7.8

This means that unlike in the compressor case, the triangle of speeds is modified when the turbine inlet temperature is changed. Consequently, the flow process through the turbine rotor has different efficiencies with respect to the turbine inlet temperature. The turbine shaft power \dot{W}_{Tsh} is therefore also dependent on this temperature.

Interestingly, one can see on the right plot of Fig. 7.8 that the measured turbine efficiencies reach values

higher than 1 for higher turbine inlet temperature. Efficiency values higher than 1 are impossible to reach. Here, this is the effect of the turbine heat transfers which is seen : as some heat power is lost to the oil and to the compressor, the exit flow temperature of the turbine will be lower than in the adiabatic case. By looking at the turbine efficiency equation, it appears that this phenomenon increases the calculated efficiency :

$$\eta_t = \frac{1 - \left(\frac{T_{04}}{T_{03}}\right)^{\frac{\gamma-1}{\gamma}}}{1 - \frac{P_{04}}{P_{03}}}.$$

Higher turbine temperature leads to higher heat losses, and therefore higher flow temperature decrease, sometimes leading to non-physical efficiency values. Turbocharger manufacturers avoid this issue by including the shaft mechanical efficiency into the turbine data maps. Therefore, $\eta_{T,manuf} = \eta_T \times \eta_{shaft}$, which is always lower than 1 [26].

7.2.3 Extrapolation of the compressor adiabatical data map

As previously written, Fig. 7.6 illustrates that the adiabatical compressor data maps cover a restricted operating range. Then, the adiabatical characteristics of the compressor are required to determine both compressor and turbine shaft powers, and consequently the heat transfers. In order to extend the range of determination of the heat exchange powers, the compressor adiabatical data maps have been extrapolated. As the compressor respects the similitude theory, the pressure ratio curves are independent of the turbine inlet temperature. Therefore the compressor pressure ratio curves for a turbine inlet temperature of 773K are directly applied as the extrapolation of the adiabatical characteristics. Regarding the extrapolation of the efficiency, this approach cannot be used. However, Fig. 7.7 has shown that the ratio between the efficiencies determined in hot conditions and in adiabatical conditions are constant and tends to 1 when the shaft speeds is increasing. Consequently, it is possible to plot a curve of the ratio between the hot and adiabatical efficiencies dependent upon the shaft speed. The horizontal asymptote of this curves is 1 when the shaft speed tends to infinity, which allows a simple extrapolation of this curve (Fig. 7.10). In order to extrapolate the compressor adiabatical efficiency, the efficiency determined in hot conditions is used and multiplied by the adiabatical / hot ratio value read on the extrapolated curve.

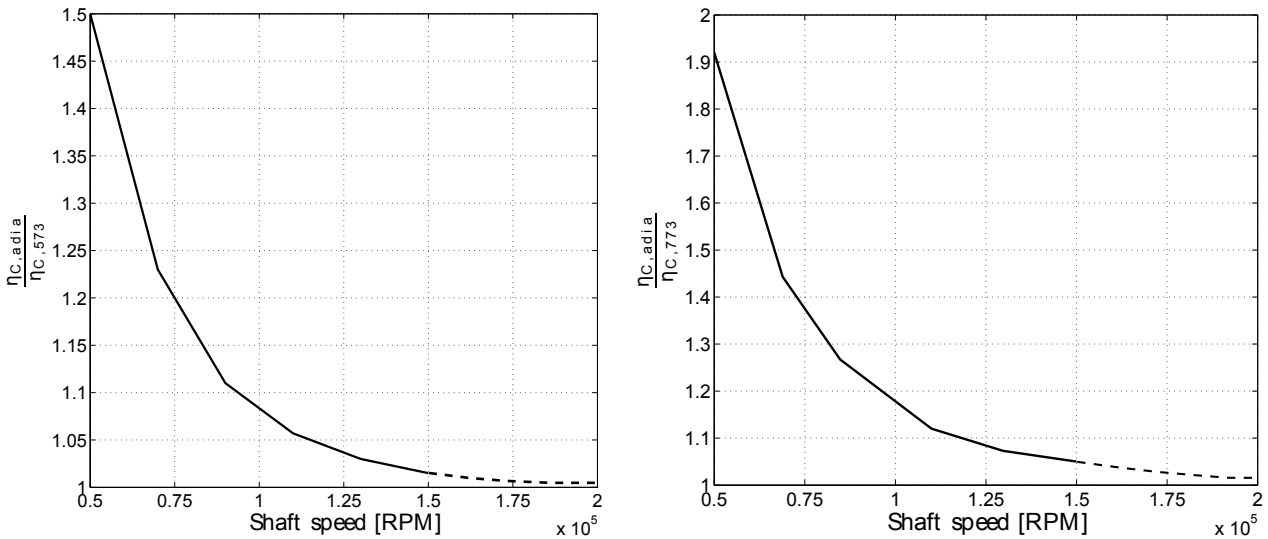


FIG. 7.10 – Ratio between the adiabatical and the non-adiabatical measured efficiencies. The dashed line is the extrapolation of the curve towards higher rotational speeds.

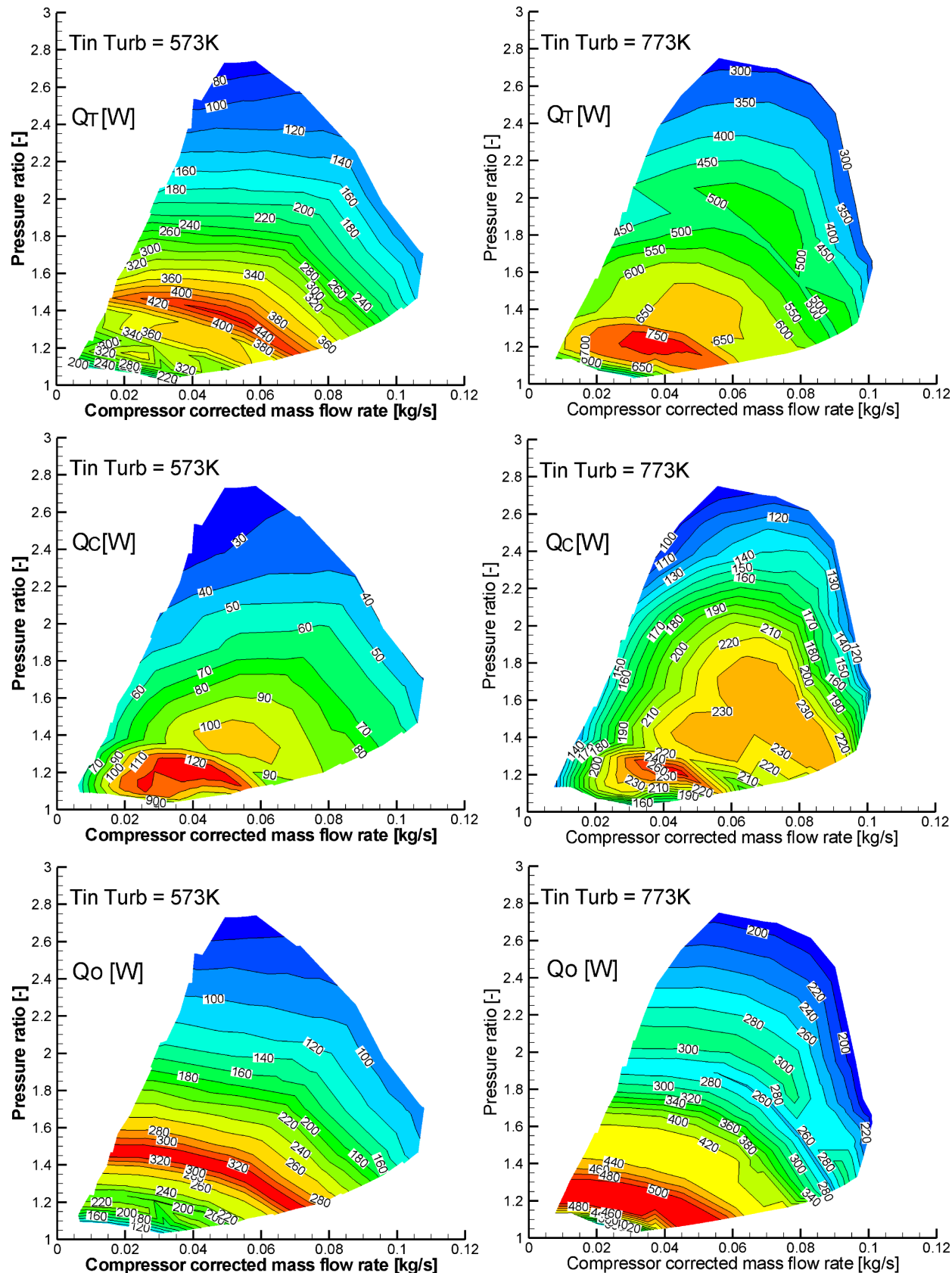


FIG. 7.11 – Heat transfers from the turbine (Q_T) and to the compressor (Q_C) and the oil (Q_O) plotted in the compressor system of coordinates. Two turbine inlet temperatures are considered : 573K and 773K.

7.2.4 Study of the parameters influencing the heat transfers

The heat power transferred within the turbocharger during the tests on bench has been identified using the previously-developed equations and assumptions (Eq. 7.15 to Eq. 7.26). In this section, the parameters which have an influence on the thermal exchanges evolution are studied. The results for a VGT setting of 100% are shown here (the impact of the VGT will be studied later in the thesis). It has been decided to plot on Fig. 7.11 the heat transfers results in the system of coordinates of the compressor mass flow rate vs. pressure ratio. The goal of this figure is to allow a direct comparison between each heat transfer. One must ensure that plotting the turbine heat transfer results into the compressor data map system of coordinates is a valid hypothesis. In fact, it is necessary to check if at a given compressor operating point (shaft speed + compressor shaft power + VGT setting), only one turbine operating point is corresponding. This point is addressed and justified in appendix B.

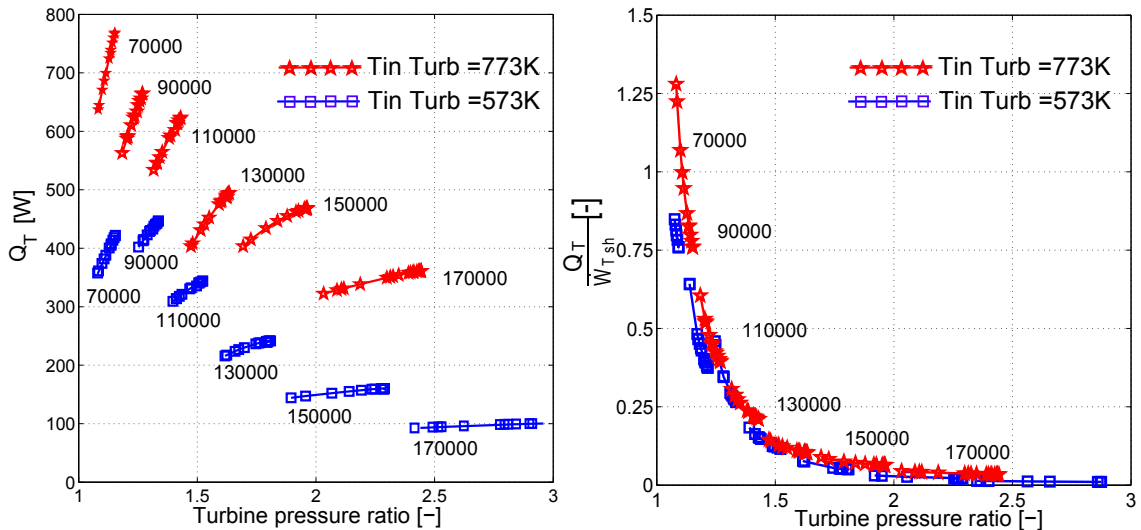


FIG. 7.12 – Turbine transferred heat power Q_T and its ratio with respect to the turbine shaft power $\frac{Q_T}{W_{Tsh}}$ plotted regarding the turbine corrected mass flow rate. The provided rotational speeds are not corrected.

On this plot, it is possible to see that the order of magnitude of the heat transfers within the turbocharger is 10^2 W. It is also interesting to notice that the heat power evacuated by the oil flow is generally higher than the power received by the compressor flow. The heat power evacuated by the oil flow is also heavily dependent on the shaft speed. The visual impression is that there is a strong correlation between the compressor and the turbine heat transfers, which is due to the heat transfer equilibrium obtained under stabilized conditions. The heat transfers are also plotted on Fig. 7.12 and 7.13. These figures show the evolution of the turbine and the compressor heat transfers with respect to their respective mass flow rates and the turbocharger shaft speed. For once in the thesis, the shaft speed values are not corrected, which allows a direct comparison between the turbine and the compressor cases. Fig. 7.12 and 7.13 are linked : each compressor operating point plotted on Fig. 7.13 has a corresponding point for the turbine case on Fig. 7.12. The correspondence is due to the shaft power equilibrium (more the bearing losses) between the compressor and the turbine under stabilized conditions. An example of the correspondence between the compressor and the turbine operating points is shown in appendix B.

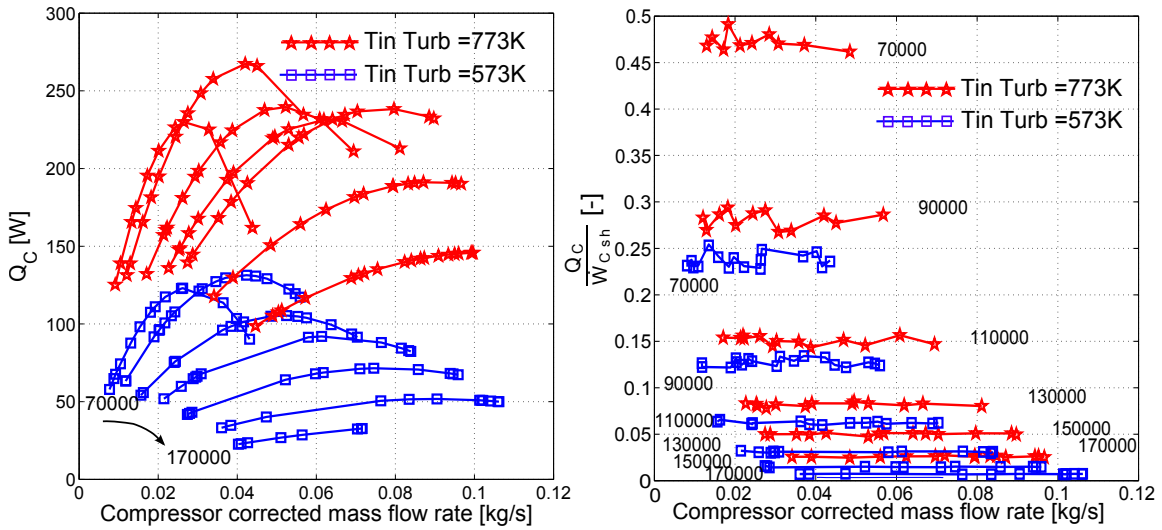


FIG. 7.13 – Compressor transferred heat power Q_C and its ratio with respect to the compressor shaft power $\frac{Q_C}{\dot{W}_{C,sh}}$ plotted regarding the compressor corrected mass flow rate. The provided rotational speeds are not corrected.

Turbine inlet temperature

As it could be expected, the heat power transferred from the turbine to the compressor and the oil increases with the turbine inlet temperature by raising the turbine inlet temperature T_{03} from 573K to 773K. The change of the value of T_{03} has an impact on both the compressor and the turbine heat transfers : for $T_{03} = 773K$, the maximum heat transfer power at the turbine (resp. at the compressor) is 750W (resp. 250W), while it is 400W (resp. 125W) at $T_{03} = 573K$. The ratio $\frac{Q_T}{\dot{W}_{t,sh}}$ is also impacted by the variation of the inlet temperature : the increase of the turbine heat losses Q_T is greater than the increase of the turbine shaft power. The same phenomenon occurs for the compressor.

Turbocharger shaft speed.

On the Fig. 7.11, it appears that the highest transferred heat power values are reached in the low rotational speeds operating range. This is confirmed on Fig. 7.12 and 7.13. It appears that increasing the turbocharger speed from 70kRPM to 170kRPM causes the average turbine heat power to decrease from approximately 750W to 350W for a turbine inlet temperature T_{03} of 773K (400W to 100W when $T_{03}= 573K$). In the case of the compressor, the heat transfers decrease from 250W to 140W (125W to 30W when $T_{03}= 573K$). In fact, at low rotational speeds, the turbine heat transfers amount for as much as 100% of the shaft power (50% in the case of the compressor). However, the heat transfers represent less than 5% of the shaft power when shaft speeds are higher than 150kRPM. This means that while heat transfers have a strong impact on the turbocharger performances at low RPM, it is not the case for higher rotational speeds where they are almost negligible.

Mass flow rate

The heat transfers at the compressor are dependent upon the mass flow rate (Fig. 7.13). Now, looking back at Fig. 7.7, it has been seen that the ratio between adiabatical and non-adiabatical compressor efficiencies are independent of the mass flow rate : $\frac{\eta_{C,adia}}{\eta_{C,non-adia}} = cst$. As the heat power transferred to the compressor is calculated using the following formulation : $Q_C = \dot{W}_C - \dot{W}_{C,sh}$, it appears that the heat over shaft power

ratio is expressed as :

$$\frac{Q_C}{\dot{W}_{Csh}} = \frac{\dot{W}_C}{\dot{W}_{Csh}} - 1 = \frac{\eta_{C,adia}}{\eta_{C,non-adia}} - 1 = cst \quad (7.29)$$

Therefore, the ratio $\frac{Q_C}{\dot{W}_{Csh}}$ is independent of the mass flow rate. This is confirmed by the Fig. 7.13 right plot.

The range of the turbine pressure ratio covered during tests is quite narrow for each iso-speed (Fig. 7.12, left plot). This is due to the compressor-turbine shaft power equilibrium and to the turbine characteristic curves, as shown on appendix B. However, it is possible to see dependency of the turbine heat transfers on the pressure ratio, and therefore the mass flow rate. This dependency decreases along with the turbocharger shaft speed, as the Q_T vs. pressure ratio curves slopes tend to be horizontal.

VGT setting

In his phd thesis report , Shaaban [118] has shown that the VGT position had no impact on the heat transfers towards the compressor. The same study has been performed here : the VGT setting has been set to 20% and the results are compared to the results for a VGT setting of 100%. In order to ensure that the heat transfers are compared at the same operating point, the following process is used :

- An operating point is chosen in the compressor data map.
- Using this operating point and the bearing loss models, the turbocharger shaft power is calculated. The corresponding turbine operating point is determined for VGT = 100% and VGT = 20%.
- Finally the heat transfers are compared. The correlation results are shown on Fig. 7.14 and 7.15.

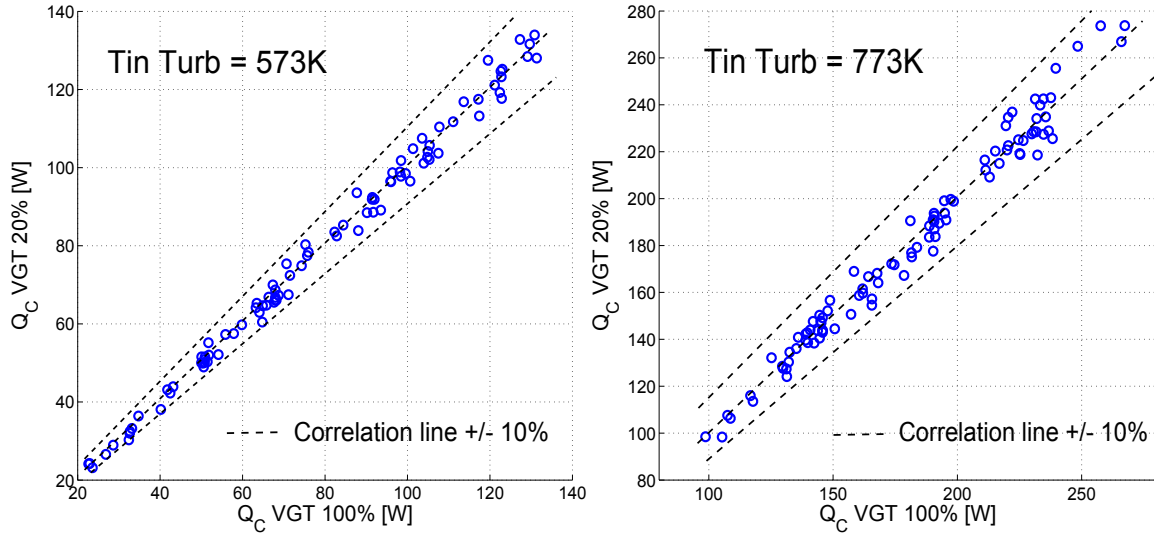


FIG. 7.14 – Correlation between the heat transfer powers at the compressor for two distinct VGT settings (20 and 100%) and two distinct turbine inlet temperatures : 573K and 773K.

The outcome of this study is that the heat transfers are almost not affected by the VGT setting, as the order of magnitude of the variation of the heat transfer powers is less than 10%. It is difficult to say whether this variation is due to an effective heat transfer variation or to an error in the shaft power loss calculation. However, as the impact of the VGT setting has only a minor impact on the turbine heat transfers, the position of the turbine nozzles will be considered as a negligible parameter in this study.

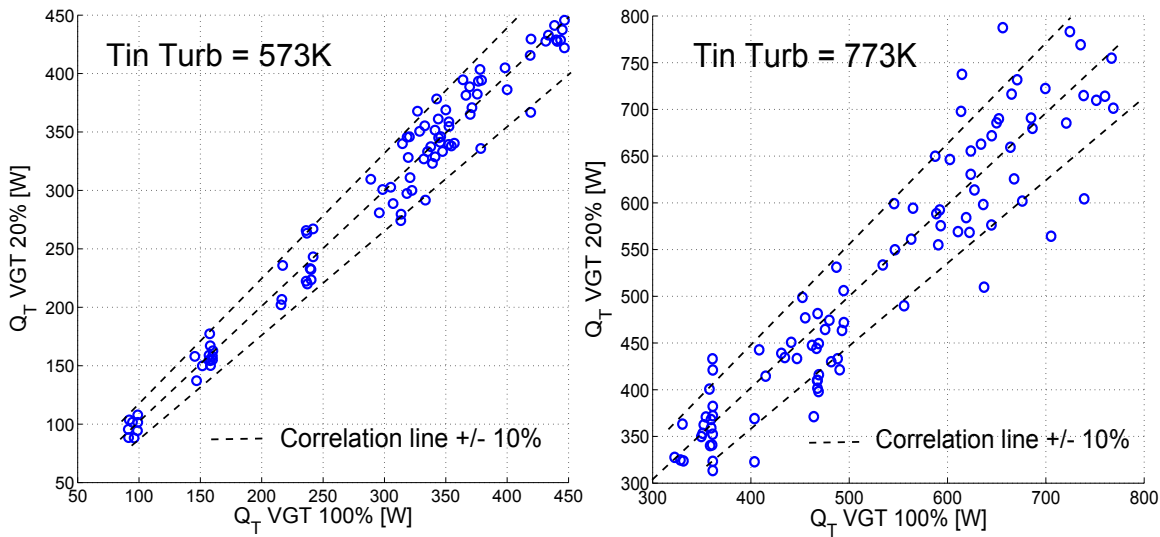


FIG. 7.15 – Correlation between the heat transfer powers at the turbine for two distinct VGT settings (20 and 100%) and two distinct turbine inlet temperature : 573K (left), 773K (right).

Turbocharger heat transfers study : recapitulation

- The impact of the heat transfers is visible on the turbomachines efficiencies : the measured compressor non-adiabatical efficiencies are lower than the measured adiabatical efficiency. The measured turbine non-adiabatical efficiencies are higher than the measured adiabatical efficiencies.
- It has been shown, via the similitude theory, that the heat transfers at the compressor occur after the rotor, while some heat losses occur at the turbine before the rotor.
- The heat transfer powers have been calculated from the adiabatical and non-adiabatical test bench data. It appears that at low RPM, the heat transfers represent an important part of the turbocharger power, as they can amount for as much as 100% of the mechanical shaft power. However, they tend to be negligible with respect to the shaft power for rotational speeds higher than 150kRPM.
- The VGT position has only a minor influence on the heat transfers.
- Under stabilized conditions, the compressor and the turbine heat transfers are heavily correlated. The measured heat transfers under constant conditions are dependent upon the temperature equilibrium, but also upon the operating point of the compressor/turbine association.

7.3 Heat transfer modeling

Now that the heat transfers have been studied, the final outcome of the study is to propose a way to model the impact of the heat transfers on the turbomachine performances. A simple model would be to use the created data maps of the heat transfer powers and to apply them to the data-map based turbocharger model. However, it has been seen that the heat transfers have been identified under peculiar conditions :

- Stabilized turbocharger shaft speed.
- Stabilized temperatures upstream and downstream of the turbomachines.
- Turbine inlet temperature higher than the oil temperature, which is higher than the compressor inlet temperature.

On a ‘real’ application, such conditions won’t be necessary met. Therefore, re-using the identified heat transfers will hardly produce sensible results. However, the identified heat transfers could be used as a

learning database combined to a heat transfer model. It has been seen in the literature review section that a pertinent way of modeling heat transfers is based on the heat transfers coefficient determination. In his thesis, Cormerais has developed an interesting approach in order to model the heat transfers within the turbochargers. This approach is based on the analogy between the heat transfer coefficients and the electric resistances. Considering an isolated mono-dimensional environment submitted to a difference of temperature ΔT , the heat transfer Q is created. From the electrical analogy, the following equivalent resistance R is associated :

$$R = \frac{\Delta T}{Q} \quad (7.30)$$

More precisely, the thermal resistance in the case of convective transfers is expressed in Eq. 7.31. The thermal resistance in the case of conductive transfers is expressed in Eq. 7.32. S is referring to the geometric thermal exchange surface, h is the convective coefficient, λ is the thermal conductivity.

$$R_{conv} = \frac{1}{hS} \quad (7.31)$$

$$R_{cond} = \frac{e}{\lambda S} \quad (7.32)$$

As detailed in the literature review, it is assumed that the heat transfers within the turbocharger are mono-dimensional. Additionally, Cormerais introduced the thermal resistance model of the turbocharger shown on Fig. 7.16 : The turbocharger is divided into three parts : the compressor, the central casing and the turbine. Some convective heat transfers occur between the turbomachines flow and their respective housings. Then, conductive transfers take place between the turbomachines plates and the central casing. The oil flow is also taken into account via convective heat transfers to the oil circuit. It is reminded that the test bench experiments have been performed using an insulated turbocharger, therefore no-heat loss towards the ambient air is considered. Such thermal resistance scheme introduces 9 thermal resistances, which must be determined from the experimental data. Using the analogy with the electrical theory, the Kirchhoff laws are introduced, which allows to reduce the system to only three thermal resistances (Fig.4.11). Intermediate steps between Fig. 7.16 and 7.17 are shown in the literature review. It is reminded that Cormerais did not notice significant improvement of the results by using a more complex thermal resistance scheme. Consequently, only three thermal resistances are considered in the following of the study.

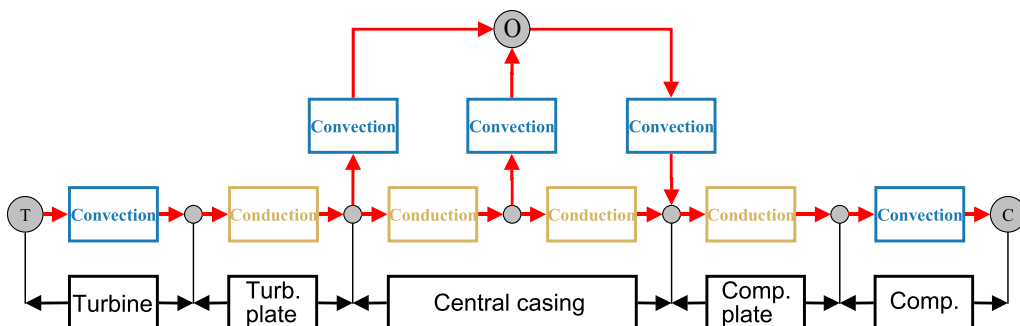


FIG. 7.16 – Equivalent resistance scheme of an insulated turbocharger. From [26]

The corresponding system of equations governing the heat transfers is described below, with T_{int} the theoretical temperature of the central point, which is at the interface of the three equivalent thermal resistances. T_T is the turbine inlet temperature and T_O the oil temperature before the oil flow enters the turbocharger casing. T_C is the compressor outflow temperature calculated using the adiabatic data maps. Indeed, it has been seen that compressor heat exchanges occur after the rotor, therefore after the compression.

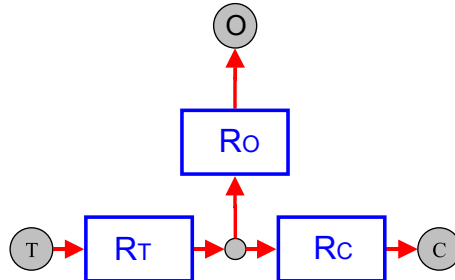


FIG. 7.17 – Final simplification of the equivalent resistance scheme (Fig.7.16) of an insulated turbocharger. From [26]

$$Q_C = \frac{T_{int} - T_C}{R_C} \quad (7.33)$$

$$Q_T = \frac{T_{int} - T_T}{R_T} \quad (7.34)$$

$$Q_O = \frac{T_{int} - T_O}{R_O} \quad (7.35)$$

$$-Q_T = Q_C + Q_T \quad (7.36)$$

Combining these four equations allows to determine a mathematical expression for T_{int} :

$$T_{int} = \frac{\frac{T_T}{R_T} + \frac{T_O}{R_O} + \frac{T_C}{R_C}}{\frac{1}{R_T} + \frac{1}{R_O} + \frac{1}{R_C}} \quad (7.37)$$

Using this expression, it is possible to express the heat transfer powers without introducing the virtual temperature T_{int} :

$$Q_C = \frac{1}{1 + \frac{R_C}{R_T} + \frac{R_C}{R_O}} \left(\frac{T_C}{-R_T - R_O} + \frac{T_O}{R_O} + \frac{T_T}{R_T} \right) \quad (7.38)$$

$$Q_T = \frac{1}{1 + \frac{R_T}{R_C} + \frac{R_T}{R_O}} \left(\frac{T_T}{-R_C - R_O} + \frac{T_O}{R_O} + \frac{T_C}{R_C} \right) \quad (7.39)$$

$$Q_O = \frac{1}{1 + \frac{R_O}{R_C} + \frac{R_O}{R_T}} \left(\frac{T_O}{-R_C - R_T} + \frac{T_T}{R_T} + \frac{T_C}{R_C} \right) \quad (7.40)$$

Eq. 7.38 to 7.40 show that each thermal resistance and each flow temperature have an impact on the global heat equilibrium of the turbocharger. This system of equations is derived from Eq. 7.33 to 7.36, which have an infinity of solutions for R_C , R_T and R_O depending on the value of T_{int} . T_{int} is a theoretical temperature, considered to be within the central casing, at the interface of the heat flows of the turbine, the compressor and the oil. In this work, T_{int} has been defined in the following way :

$$T_{int} = \frac{T_C + T_O + T_T}{3} \quad (7.41)$$

This formula will be used to determine the values of T_{int} , which are introduced into Eq. 7.33, 7.34 and 7.35 to determine the values of the thermal resistances.

Thermal resistances dependency

In order to build a thermal resistance model of the turbocharger, it is necessary to express the dependences of the thermal resistances regarding the physical parameters of the turbomachines flows. Two different methods have been considered to express the thermal resistance as a function of the flow characteristics :

1- *Nusselt number correlation* : From their definition (Eq. 7.31, and 7.32), the thermal resistances are directly linked to the convective and conductive heat transfers. For a given turbocharger, the geometry and the materials of the casings are constant, therefore the thermal conductivity λ remains constant. As the material conductivity is independent of the flows and of the thermal equilibrium, this parameter is naturally taken into account when the thermal resistances are calculated. However, the conductive heat transfers are directly impacted by the flow characteristics (Reynolds number, mass flow rate, viscosity). These convective heat coefficients are generally modeled via a Nusselt number approach. This approach is widespread in the study of the heat exchanges occurring within pipe flows or heat exchangers and is based on physical equations and experimental correlations. However, it has been shown in the literature review that even in the case of simple flows, the Nusselt correlations from various authors could show great discrepancies (up to 100% of difference [35]). In the case, the flow is very complex, which leads to an increased difficulty to fit the Nusselt number to the identified heat exchange coefficients. The main outcome of this issue is that authors of the literature papers have modified standard Nusselt formula to adapt to the turbocharger case. Additionally, there is often great differences between the turbocharger Nusselt number correlations from an author to an other one. In order to illustrate this phenomenon, three turbocharger Nusselt numbers are described. Busam's [16] Nusselt number definition is introduced :

$$Nu = aRe^b Re_{turb}^c Pr^d \quad (7.42)$$

$$Re = \frac{4Qm}{\mu\pi D} \quad (7.43)$$

$$Re_{turb} = \frac{\rho\pi RND}{30\mu} \quad (7.44)$$

where a,b,c,d are coefficients determined from least-square algorithm based on an experimental data. Re is the flow Reynolds's number and Re_{turb} an adaptation of the Reynolds's number to the turbomachines. Shaaban [118] has modified Busam's expression by adding a corrective term $Corr$:

$$Nu = aRe^b Re_{turb}^c Pr^d Corr \quad (7.45)$$

$$Corr = \text{Exp} \left(-e \left(Re_U^f Re^g Pr^h - \frac{i}{(Re + 1)^j} \right) \right) \quad (7.46)$$

Finally, Bohn et al. [12] introduced the following Nusselt number correlation for the turbochargers :

$$Nu = Nu_0 - \sqrt{a^2 - \frac{Re_C^2}{1 - (b e^{c T_{in}} + d T_{in})}} \quad (7.47)$$

where Re_C is a turbocharger Reynolds number taking into account the rotor geometry and a,c,b,d coefficient to be fitted. It is reminded that the Nusselt number definition for forced convection is the following one : $Nu = \frac{hD_h}{k_f}$ where h is the convective heat transfer coefficient, D_h the hydraulic diameter and k_f the fluid thermal conductivity. Therefore, the following process is used in the literature paper : once the heat transfer powers are known, the convective heat coefficients are identified on each operating point. Then, using the Nusselt number definition, authors develop the Nusselt number correlations in order to link the identified

convective heat transfer coefficients to the turbocharger flow parameters (mass flow rate, shaft speed...). Looking at each author's paper, it appears that the proposed correlations show an accuracy of $\pm 15\%$ with respect to experimental results and that they are only valid for the turbocharger used in their respective studies. Additionally, the Nusselt number correlations found in the literature papers are very different from the standard Nusselt number expression, and tend to become mathematical curve-fitting methods rather than physical models. Consequently it has been decided in this thesis to experiment a different approach than the Nusselt number correlation approach.

2- Data map building : The study of the Nusselt number correlations has shown that the heat transfer coefficients are generally expressed as functions of the Reynolds number. It has been seen in the similitude theory development in appendix A that the compressor and the turbine data maps respect the similitude conditions. The similitude theory applied to the turbomachines implies the conservation of the following quantities :

- Reynolds number
- Mach number
- Rotor triangle of speed

This means that each operating point expressed in the corrected turbomachines system of coordinates is specific of the flow conditions (Re , Mach, speed triangle). These flow characteristics take into account the parameters which have an influence on the heat exchange coefficients. Consequently, it appears that plotting the thermal resistances in the compressor and the turbine corrected system of coordinate is a valid hypothesis, as it implicitly links the thermal resistances to the flow conditions. The results are provided for the compressor and the turbine on Fig. 7.18, where the identified thermal resistances are plotted with respect to the corrected characteristics of the turbomachines. From this plot, one can see that in this system of coordinates, the thermal resistances are not dependent on the turbine inlet temperature. This behavior was expected : indeed, the convective heat transfer coefficients are dependent on the flow characteristics. Additionally, the similitude theory ensures that for a given corrected operating point, these characteristics are preserved. It is therefore valid to identify the same value for the thermal resistance at a given corrected operating point, independently of the turbine inlet temperature.

It has been seen previously that the compressor operating range is completely covered by the performed tests. However, this is not the case of the turbine, as the covered operating range is very narrow. This can be an issue in transient operation : as the shaft power equilibrium is not respected (the turbine and the compressor shaft power difference leads to the shaft speed to increase or to decrease), the turbine is sometimes operating outside the operating range covered during the stabilized tests. In order to overcome this issue, a linear dependency of the turbine thermal resistance with respect to the turbine corrected mass flow rate has been identified and is used to extrapolate the data.

The thermal resistance values are plotted regarding the shaft speed on Fig.7.19 . It appears that their values are dependent on the shaft speed and on the turbine inlet temperature. From [59], [90] and [77], these parameters have a combined effect on the oil flow within the bearing :

- The oil flow is directly linked to the the shaft speed of the turbocharger.
- The oil viscosity is dependent on the oil temperature. It appears that both the bearing friction losses and the heat flow from the turbine change the oil temperature within the bearing, therefore modifying the oil viscosity.
- The change of the oil viscosity directly impacts the excentricity of the shaft within the bearing, consequently changing the oil flow characteristics.
- The change of the oil flow characteristics has a strong influence on the heat exchange within the oil bearing.

In order to build a valid oil flow thermal exchange model, it is therefore necessary to take into account

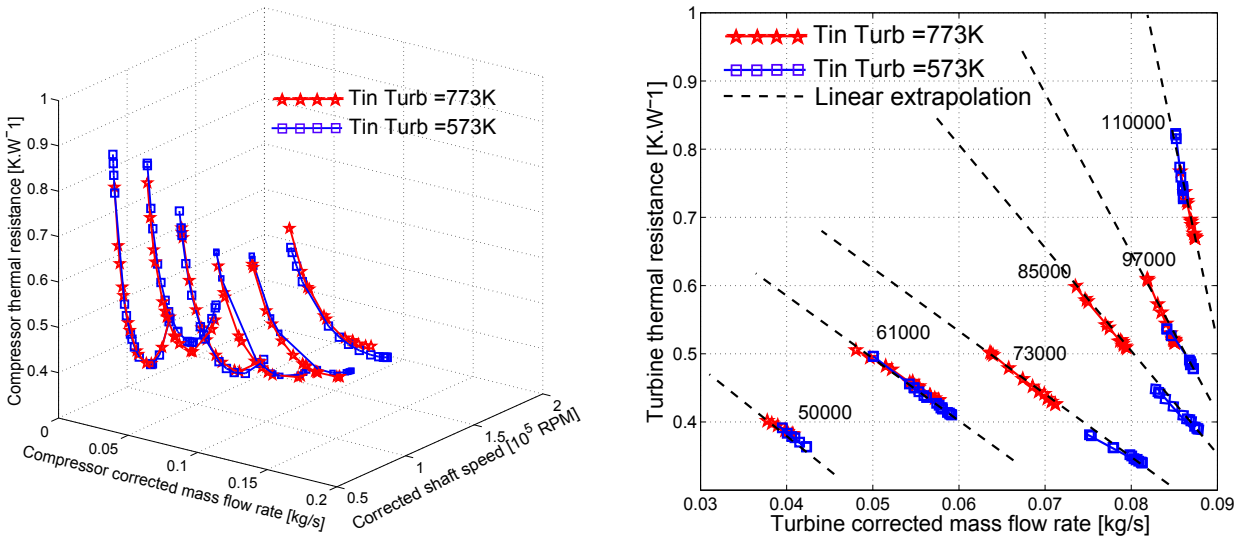


FIG. 7.18 – Left : Compressor thermal resistance with respect to the corrected mass flow rate and pressure ratio for various corrected shaft speeds. Right : Turbine thermal resistance with respect to the corrected mass flow rate for various corrected shaft speeds.

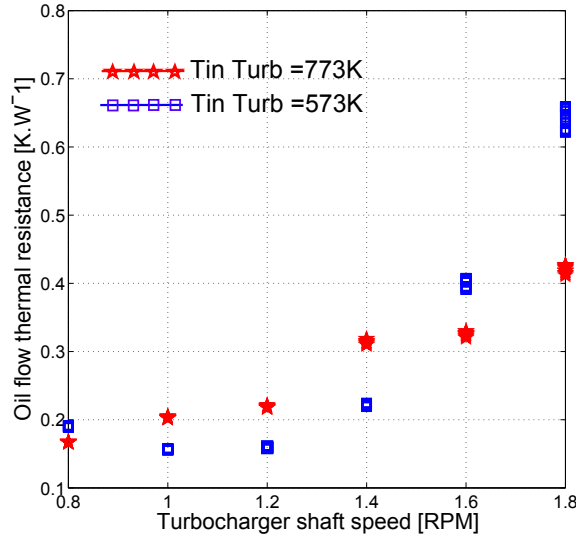


FIG. 7.19 – Oil flow thermal resistance with respect to the turbocharger shaft speeds.

the following parameters : the eccentricity of the shaft within the bearing, the impact of the heat on the oil viscosity, the oil mass flow rate. These parameters interact on each other, and it is therefore necessary to have access to a large experimental data base to correlate each sub-model [59]. In our case, the available data are not sufficient to build a model of the bearing oil flow and its associated heat exchanges. However, as the oil flow was regulated at a temperature of 360 K, a value similar to the oil temperature regulation on a real engine, the curves plotted on Fig. 7.19 will be used to estimate the oil flow thermal resistance. This approach is valid under the following conditions :

- Oil temperature regulated close to 360 K (before entering the turbocharger).
- Turbine inlet temperature between 573 and 773 K. For turbine inlet temperatures included between these values, the curves can be interpolated.
- Insulated turbocharger.

The main issue is that the data are only available for two turbine inlet temperatures (573 and 773K).

While it seems realistic to perform interpolation between these curves, extrapolating the data for lower or higher turbine inlet temperature appears to be an unreliable approach. Additional tests for different turbine inlet temperatures have been planned, but the test results were not available by the time of the redaction.

7.4 Building process of the global turbocharger model

The datemap extrapolation methods and the heat exchange model are two complementary developments. In reference to Fig. 7.20, the data map extrapolation allows to get the complete adiabatic data maps of the compressor and the turbine. Using these data maps allow to parameterize the bearing friction loss model and to get the adiabatic performances of the turbocharger. Combining the adiabatic and the non-adiabatic datamaps allows to identify the thermal resistance of the turbocharger. Finally, the 'real' performances of the turbocharger are calculated by combining the adiabatic performances to the heat exchange model.

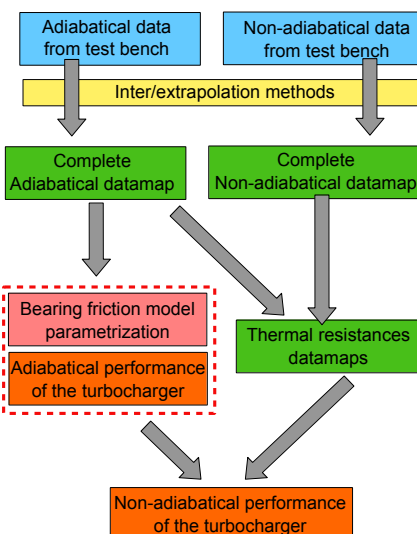


FIG. 7.20 – Chartflow of the turbocharger model building process.

Such approach allows to build a datemap-based model of a turbocharger and to take into account the heat transfers which affect the performances of the turbomachines. As the model relies on datamaps, the model runs in real-time. The main limitation of this approach is that it relies extensively on experimental data. This means that while the global structure of the model can be applied to any turbocharger, it is however necessary to perform new experimental measurements for each turbocharger in order to : 1- build the performances datamaps ; 2-identify the heat exchange model.

Turbocharger heat transfers model : main points

- The developments from Cormerais have been adapted to the present work. It has been decided to model the turbocharger as an equivalent scheme using three thermal resistances, as it is the best compromise between accuracy and complexity.
- The main equations and hypotheses introduced to identify the thermal resistances have been introduced and developed. These formulations show that each thermal resistance has an impact on the global heat equilibrium, which shows the complexity of the heat flow within the turbochargers. Using these developments, the thermal resistances have been identified using the test bench data.

- Even though the Nusselt number correlation is a valid approach in order to determine the dependency of the heat exchange coefficients regarding the turbocharger parameters. However, the complexity of the flow within radial turbomachines leads to Nusselt number correlations far from the standard formulations. The correlations found in the literature tend to become mathematical curve-fitting methods rather than physical models based on experimental data.
- An alternative approach in order to link the thermal resistances to the turbocharger flow parameters has been developed. Based on the similitude theory approach, it has been seen that expressing the thermal resistances values with respect to the corrected flow parameters is a valid hypothesis. Consequently, the values of the thermal resistances are expressed into a data map using the corrected mass flow rate and the corrected shaft speed as inputs. While the compressor operating range has been completely covered by the test bench test, it is not the case for the turbine. A linear extrapolation of the turbine thermal resistances has been proposed to extend the range of the available data. The main drawback of the data map approach is related to the oil flow thermal resistance. As the available data were not sufficient to build a model of the bearing oil flow and its associated heat exchanges, the oil flow heat resistances have been expressed in a data map with respect to the turbocharger data map. This approach is only valid under the temperature conditions of the study.

Conclusions of the work on gas processes exchange through turbochargers

This part of the thesis has been focused on the mean-value modeling of the automotive turbochargers. The guideline of the developments previously presented has been to include as much physics as possible into the models without leading to an increase of the calculation time.

Physics-based extrapolation of turbochargers data maps

The first proposed development has been to include the physical equations of the turbomachinery into the compressor and the turbine data maps extrapolation process. This development has been motivated by the difficulty encountered with standard techniques to extrapolate turbomachines data maps. Thanks to the use of mathematic curve fitting techniques and the introduction of turbomachinery physics, extrapolations are now robust and controlled by physical laws. The linear trend of the enthalpy evolution with respect to the mass flow rate has been used to provide some coherence and physical behavior to a mean-value model. This linear evolution has been demonstrated in the case where corrected quantities (corrected mass flow rate, corrected shaft speed) are used. Therefore, the linear extrapolations can be directly applied to the data maps provided by the turbocharger suppliers. This property is also used to express the turbomachines efficiencies without introducing complex curve fitting methods. More importantly, the proposed method in order to determine the efficiency respects the physical link existing between the isentropic and the real enthalpy change across a radial turbomachine.

This leads to a much more robust and accurate treatment of the data maps, while keeping the zero dimensional approach. Comparative application tests have been performed on three different compressors and turbine, showing that the method is general and more accurate than the standard method (particularly in the case of the efficiency estimation). Additionally, some tests performed on a test bench dedicated to the turbocharger has allowed to measure the compressor and the turbine characteristics in the operating range usually excluded from the suppliers data maps. The comparison between the extrapolated results from the model and the experimental results has shown that the developed method provides accurate extrapolated data.

Turbocharger thermal exchanges

The second proposed development focused on the thermal exchanges occurring within the automotive turbochargers. Even though the impact of this phenomenon on the turbocharger performances has been identified in the 1980s, the engine computational software generally do not take them into account. The study has been based on a turbocharger test bench allowing to measure the flow temperatures under stabilized conditions. The corresponding heat transfers have been identified by the mean of the heat exchange equations found in the literature. It has been seen that the efficiencies determined by the mean of the flow temperature measurements are not representative of the actual aerodynamical performances of the turbomachines.

Generally, this means that the compressor efficiency determined in hot conditions is under-estimated, while the turbine efficiency is over-estimated. The error can be important, as the heat power loss at the turbine represents more than 100% of the shaft power on some operating points. In the case of the compressor, the heat exchanges lead to an error of 50% on the shaft power. The impact of the heat exchanges is high at low rotational speed and becomes negligible at higher rotational speeds.

Data maps of the heat exchanges have been plotted, showing the strong correlation between the turbine and the compressor heat transfers. Such data maps cannot be used directly to model heat exchanges, as they are specific of the heat exchanges under steady flow conditions. However, the identified heat exchanges can be used to identify the thermal exchange coefficient of the compressor, the turbine and the oil flows. The adopted method has been to build an equivalent thermal resistance scheme of the turbocharger. An alternative approach in order to link the thermal resistances to the turbocharger flow parameters has been developed. Based on the similitude theory approach, it has been seen that expressing the thermal resistances values with respect to the corrected flow parameters is a valid hypothesis. Consequently, the values of the thermal resistances are expressed into a data map using the corrected mass flow rate and the corrected shaft speed as inputs. A major difficulty has also been identified, as a satisfying oil flow heat exchange model could not be built with the available data. A temporary solution, based on a data map, has been adopted, but is only valid for a restricted range of turbine inlet temperature.

Résumé : Echanges gazeux au sein des turbocompresseurs

1 Etude bibliographique

Les modèles temps réel des turbocompresseurs sont généralement basés sur des cartographies. Ces modèles sont faciles à mettre en place, nécessitent une faible charge CPU et sont compatibles avec un développement de lois de commande. Les données relatives au compresseur et à la turbine sont lues à partir de tables : le rapport de pression et le rendement sont déterminés en fonction du débit massique et de la vitesse de rotation sur deux cartographies de données distinctes. Une première méthode pour construire les cartographies s'appuie sur la caractérisation expérimentale. Les acquisitions ne sont généralement pratiquées qu'aux vitesses de rotations les plus élevées, et sont généralement peu discrétisées. Par conséquent, des méthodes spécifiques d'extrapolation et d'interpolation sont mises en œuvre.

Une deuxième méthode pour construire ces cartographies est basée sur la résolution des équations aérodynamiques des turbomachines. L'objectif de cette approche est de calculer les pertes aérodynamiques qui se produisent dans le compresseur et la turbine. Les deux premières parties de l'étude bibliographique porteront sur ces méthodes d'extrapolation et sur les modèles aérodynamiques des turbomachines.

L'utilisation directe des cartographies turbocompresseur ne permet pas de prendre en compte de possibles transferts thermiques au sein des turbocompresseurs. Cependant, certaines études ont montré qu'une partie non négligeable de la chaleur est transférée de la turbine vers le compresseur et le circuit d'huile. Sur la base de ces observations expérimentales, des modèles thermiques de turbocompresseurs ont été développés pour prendre en compte les transferts de chaleur. La dernière partie de l'étude bibliographique sera concentrée sur ces modèles d'échanges thermiques.

1.1 Méthodes d'interpolation et d'extrapolation des cartographies expérimentales des turbocompresseurs

La méthode la plus répandue concernant l'interpolation et l'extrapolation de cartographies de turbocompresseurs a été développée en 1991 par Jensen et al. [69]. Ce modèle est basé sur les paramètres sans dimension définis par Winkler [137] et Benson [4]. Des expressions polynomiales ont été développées en utilisant ces paramètres sans dimensions ainsi que sur des coefficients de corrélation. Les coefficients de corrélation sont déterminés par la méthode des moindres carrés sur une base d'apprentissage expérimentale. Cette base d'apprentissage est généralement une cartographie expérimentale des performances du compresseur et de la turbine. Les expressions mathématiques proposées par Jensen et al. sont présentées via les équations 4.1 à 4.7. Dans leur article, Jensen et al. précisent que même si l'interpolation des données fournit de bons résultats pour les faibles régimes de rotation, le niveau de précision n'est pas aussi bon pour les plus hauts régimes. Ce phénomène est illustré sur la figure 4.2. La deuxième limitation vient de la formulation même du modèle : la validité du modèle global est liée à la précision des données expérimentales et sur l'algorithme d'extrap-

lation. Comme la méthode d'extrapolation proposée par Jensen et al. n'est basée que sur la formulation de polynômes, et non sur des équations physiques, la qualité des résultats extrapolés n'est pas garantie.

Alors que les traitements de données de turbocompresseurs présentés dans la littérature ([58], [94], [5], [63], [79] sont similaires à l'approche de Jensen et al., d'autres modèles de turbocompresseurs ont été trouvés dans la littérature. Dans son mémoire de maîtrise [95], Mueller dérive un modèle de compresseur à partir du premier principe et utilise des données expérimentales afin de paramétriser son modèle. Il semble que cette méthode nécessite autant de paramètres d'ajustement que la méthode de Jensen et al. (9 au total) et ne résout pas la question de la précision à haute vitesse du compresseur. En outre, l'extrapolation vers la zone des faibles régimes de rotation produit des tendances contradictoires.

Le modèle de compresseur de Kolmanovsky détaillé dans [94] se base sur des fonctions d'apprentissage exponentielles, ce qui permet de réduire le nombre de paramètres d'ajustement à 6. Toutefois, l'extrapolation vers les valeurs à faible vitesse ne semblent pas satisfaisante.

Certains auteurs ont tenté d'utiliser des réseaux de neurones ([94], [43]) pour construire un modèle de compresseur. Ce type de modèles introduit un nombre élevé de paramètres de recalage (environ 40 d'après Moraal), ce qui entre en conflit avec le nombre de points d'apprentissages disponibles (entre 25 et 40) sur une cartographie de compresseur 'standard'. En outre, les modèles neuronaux ne sont pas adaptés à des problématiques d'extrapolation de données, et ce genre de modèle risque de produire des résultats erronés dans la zone d'extrapolation du modèle.

Cette étude bibliographique a montré que les méthodes d'extrapolations cartographiques n'incluent pas les équations physiques des turbomachines. Des formulations mathématiques sont déterminées à partir d'observations expérimentales et des paramètres sont identifiés par régression sur une base d'apprentissage. Il semble que la méthode développée par Jensen et al. fournit les résultats les plus satisfaisants parmi les traitements testés. Toutefois, une grande amélioration doit être réalisée en ce qui concerne l'extrapolation du rendement compresseur et turbine. La qualité de l'interpolation du rapport de pression compresseur à des vitesses élevées de rotation doit aussi être améliorée.

1.2 Détermination des cartographies des turbomachines par équations modèles

Les modèles analytiques des turbomachines sont utilisés afin de prédire leur performances. L'utilisation de tels modèles permet de créer des cartographies de performances des turbomachines à partir de modèles physiques plutôt que par essais. Le développement de ces modèles peut être divisé en deux parties :

- Dans un premier temps, les performances isentropiques (sans pertes) des turbomachines sont formulées à partir d'équations thermodynamiques.
- Dans un second temps, il est nécessaires de modéliser les pertes au seins des turbomachines. La combinaison de ces deux étapes permet de construire des cartographies de performances complètes.

Formulation thermodynamique des turbomachines :

La formulation de la variation d'enthalpie dans les turbomachines radiales sont développées et présentées dans les équations 4.8 à 4.11. On peut voir, à partir de ces équations que les performances du compresseur et de la turbine sont directement liés à la vitesse du turbocompresseur (via la vitesse tangentielle de pale U) et à la vitesse tangentielle du fluide V_θ . Ces vitesses sont calculées à partir de la résolution des équations aérodynamiques 0D-1D complètes écrites pour les turbomachines :

Obtention par modèles physiques des performances des turbomachines :

La première étape en vue de créer un modèle physique 0D-1D de turbocompresseur est de résoudre l'écoulement isentropique au sein d'une turbomachine. Ces équations sont la conservation de la masse, de l'énergie et du moment. Elles doivent être écrites dans le cas d'un repère en rotation. Le développement de ces équations dans le cas du turbocompresseur sont détaillées par Bozza [15]. Une fois ce 'débit idéal' calculé, il est nécessaire de tenir compte des pertes qui surviennent au sein de la turbomachine.

Les pertes sont des modèles basés sur des observations expérimentales, qui ont été largement acceptées au cours des dernières années. L'état de l'art de la modélisation des pertes aérodynamiques au sein des turbomachines est précisément décrit dans les papiers de Japikse [66] et Watson [134]. Les phénomènes physiques à prendre en compte lors de la modélisation complètes de turbomachines sont les suivants :

- Les pertes par cisaillement de la couche limite. Elles sont créées par le cisaillement de la couche limite visqueuse le long de la paroi. Certains modèles de pertes par frottement basés sur l'estimation des coefficient de frottement sont détaillés dans les documents par Watson [133], Ferguson [41] et Macek [82].
- Les pertes de flux secondaire. Le transport des particules de fluide à des niveaux différents de vitesse sous l'action de gradients de pression provoque le phénomène de vorticité. Une grande partie de l'énergie cinétique associée à ce processus est dissipée. Les modèles associés à ce type de pertes au sein de turbomachines radiales ont été mis au point par Dean et al. [68], [31] et Japikse et al. [65], [102].
- Les pertes par fuites. Ces pertes sont dues à des fuites au travers des jeux de fonctionnement et au travers des systèmes d'étanchéité. Un exemple des modèles de fuite est proposé par Descombes [33], [34].
- Les pertes par mélange. Ces pertes tiennent compte de la non-uniformité en termes de vitesse d'écoulement en aval de l'aubage. Un modèle de ce phénomène a été développé par Stewart [120].
- Les pertes par glissement. Même si le flux d'air est guidé par les lames, il y a un écart entre l'angle de sortie de l'écoulement et l'angle géométrique des pales de la turbomachine. Cette angle de déviation dépend du nombre de pales et de leur géométrie [106]. Le facteur de glissement exprime le ratio entre la vitesse tangentielle des pales et la vitesse d'écoulement tangentielle. Le facteur de glissement est habituellement calculé au moyen de formulations empiriques. Les formulations les plus couramment utilisées se trouvent dans les documents suivants : [136], [121], [46], [106].
- Pertes par frottement. Quand un disque est en rotation dans un fluide, un couple résistant est généré par la composante de cisaillement tangentielle entre le disque et le fluide. Ferguson a proposé une corrélation dans [41].
- Les pertes de débit sonique. Pour des débits fortement accélérés, le choc créé engendré une augmentation du niveau d'entropie.
- Certains auteurs [15], [96], [34] introduisent également une perte par désadaptation théorique, qui a été introduite par Spannake [119]. Selon Bozza, il est supposé que l'énergie cinétique associée à la composante normale à la paroi est complètement dissipée. Japikse [66] considère ce modèle comme une version simplifiée et moins physique des pertes de flux secondaires et précise que son utilisation est inutile si les modèles précédents sont correctement mis en œuvre.

Cette vue d'ensemble montre qu'au moins 6 modèles distincts de pertes doivent être mis en œuvre afin de construire un modèle physique de turbocompresseur. La construction de ces modèles nécessite beaucoup de données, notamment celles relatives à la géométrie du turbocompresseur. Lorsque de tels modèles sont correctement appliqués, il est possible d'obtenir une estimation à 10% près des performances des turbomachines (rapport de pression et rendement). Toutefois, dans la plupart des cas, la géométrie spécifique de la turbomachines est inconnue, et ces modèles ne peuvent pas être utilisés.

Une approche intéressante a été adoptée par Macek [82], [83]. Il a défini un modèle physique complet d'une

turbine radiale et défini les paramètres géométriques du turbocompresseur comme des paramètres à identifier. Ces paramètres sont ensuite déterminés par un algorithme d'optimisation alimenté par les données des cartographies, généralement fournies par les constructeurs des turbocompresseurs.

1.4 Transferts thermiques au sein des turbocompresseurs

La première analyse détaillée de l'impact des transferts thermiques sur les performances thermodynamiques des turbocompresseurs a été produite en 1981 par Rautenberg et al. [109], [110]. Au moyen d'essais, il a été montré que le compresseur et la turbine ne fonctionnent pas adiabatiquement. Une part non négligeable de la puissance thermique de la turbine est transférée vers le milieu ambiant, le carter central, le carter compresseur et les paliers. Ces transferts de chaleur impliquent une baisse de la température de sortie turbine, ainsi que l'augmentation de la température de sortie compresseur. Ces transferts thermiques modifient artificiellement les rendements isentropiques mesurés au banc pour le compresseur et la turbine. Cela signifie que la puissance réelle consommée par le compresseur sera différente de celle estimée par la mesure des températures amont et aval. Le même problème se produit à la turbine. Rautenberg et al. ont montré que les turbines peuvent avoir un rendement apparent supérieur à 1 dans des conditions spécifiques. Il en conclut que le rendement de la turbine mesuré sur un banc d'essai en conditions non-adiabatiques ne représente pas la performance aérodynamique de la turbomachine et ne devrait pas être utilisée pour calculer la puissance sur l'arbre.

Des observations similaires ont conduit à la création de correctifs appliqués au rendement des turbomachines. Ces correctifs sont déterminés à partir de comparaisons entre des essais en conditions adiabatiques et non-adiabatiques (Friberg et al. [48] et Frelin [47]). Toutefois, même si chaque modèle mis au point prend en compte le changement de rendement dû à l'échange de chaleur, il faut noter que se sont des modèles valables en conditions stabilisées. Afin de modéliser les transferts thermiques en transitoire, les auteurs ont introduit des modèles de conduction, convection et rayonnement basés sur des corrélations expérimentales.. Ces modèles impliquent l'introduction de coefficients d'échange thermique pour les phénomènes de conduction, convection et rayonnement.

Transferts de chaleur par conduction : Les transferts par conduction se produisent entre les carter turbine et compresseur, qui sont physiquement liés. La conduction se produit également à travers l'arbre. Des études numériques multidimensionnelles ([12], [13], [11], [26]) ont montré que le transfert de chaleur par conduction dans les turbocompresseurs est un phénomène essentiellement mono-dimensionnel. L'utilisation de la loi de Fourier (Eq. 4.19) combinée à des données numériques ou expérimentales en stabilisé permet d'identifier le coefficient thermique caractérisant la conduction pour un turbocompresseur spécifique.

Transferts de chaleur par convection : D'après des études par Shaaban [118], Cormerais [26], Westin [135], Bohn [12] et Salas [116], des transferts de chaleur par convection ont lieu dans les turbocompresseurs. Tout d'abord, il y a échange de chaleur par convection entre les carters et leurs flux respectifs (compresseur et turbine). Des transferts de chaleur par convection ont également lieu entre le carter du turbocompresseur et l'air ambiant. Les auteurs ont déterminé le coefficient d'échange par convection à partir de corrélations basées sur le nombre de Nusselt. Les principales expressions de corrélations du nombre de Nusselt dans les turbomachines se trouvent dans les papiers précédemment cités. Le nombre de Nusselt est un nombre sans dimension qui est une fonction du coefficient d'échange thermique, de la conductivité thermique du fluide et du diamètre du conduit. Sur la base de résultats expérimentaux, les auteurs ont construit une relation entre le nombre de Nusselt et d'autres paramètres sans dimension caractérisant l'écoulement, tels que le nombre de Reynolds et le nombre de Prandtl. Le principal avantage de la détermination du coefficient d'échange de chaleur au moyen de la corrélation du nombre de Nusselt est que le modèle mis au point prend en compte

les paramètres physiques. Le principal inconvénient est qu'il existe des écarts élevés entre les nombres de Nusselt calculés dans différentes études dans la littérature. Le principal exemple est fourni dans le cas d'une étude de Depcik [35], où les écarts entre différents modèles fournissent, sur la même application, des écarts jusqu'à 100 %.

Transfert de chaleur par rayonnement : Ce type de transfert de chaleur est modélisé ([71]) via l'équation de Stefan-Boltzmann, qui met en jeu l'émissivité du matériau. L'émissivité est une fonction du matériau, mais aussi de la température. les tables fournissant les valeurs d'émissivité pour les matériaux du turbocompresseur ainsi que leur évolution vis-à-vis de la température sont détaillées dans [71].

Afin d'identifier les coefficients de transfert de chaleur par convection, rayonnement et conduction, il est nécessaire de mesurer les transferts de chaleur survenant entre le compresseur, l'huile et la turbine. Ceci est réalisé au moyen d'un processus expérimental détaillé par Baar et al. [3], Shaaban [118] et Cormerais [26] dans leurs études respectives. Cette méthode expérimentale est basée sur la comparaison de mesures effectuées en conditions adiabatiques et non-adiabatiques. Dans le cas où le turbocompresseur opère en conditions isothermes et adiabatiques, la puissance du compresseur déterminée à partir des mesure de température est égale à la puissance prélevée sur l'arbre par le compresseur. Le même phénomène est observé à la turbine, car il n'y a pas d'échanges thermiques en conditions adiabatiques. Dans ces conditions, et pour un arbre tournant à vitesse constante, la différence entre la puissance du compresseur et la turbine est due aux pertes dans les palier hydrauliques. Par conséquent, les tests adiabatiques permettent de construire un modèle de pertes pour les paliers.

Lorsque le turbocompresseur est isolé du milieu extérieur (calorifugé), mais que des tests en conditions non-adiabatiques sont réalisés, il est possible d'identifier les échanges thermiques prenant place au sein du turbocompresseur. Pour cela, les 5 quantités suivantes doivent être déterminées :

- Puissance apparente du compresseur (mesurée via les température en amont et en aval du compresseur).
- Puissance réelle consommée par le compresseur.
- Puissance apparente de la turbine (mesurée via les température en amont et en aval de la turbine).
- Puissance réelle fournie par la turbine.
- Pertes par frottement dans le palier.

Les études de Cormerais [26] et Shaaban [118] ont montré que les échanges thermiques au compresseur ont lieu dans le collecteur en aval du rotor. Ainsi, les échanges thermiques au compresseur n'influent pas sur la puissance qu'il consomme pour comprimer les gaz. Par conséquent, la puissance consommée par le compresseur est déterminée à partir de essais adiabatiques, et la puissance apparente est mesurée par les températures en conditions non-adiabatiques. La différence entre ces deux valeurs est égale au transfert thermique qui ont lieu au compresseur.

La même hypothèse n'est pas valide du côté turbine. Afin de calculer la puissance fournie à l'arbre par la turbine, on la définit comme la somme des puissances consommées par le compresseurs et les frottements dans les paliers. Les frottements paliers sont déterminé via un modèle paramétrisé d'après les essais adiabatiques. La puissance apparente de la turbine est déterminée par les mesures de température en condition non-adiabatiques. La différence entre la puissance turbine apparente et celle sur l'arbre représentent les échanges thermiques à la turbine. Les équations explicitant ces calculs sont disponibles via les équations 4.22 à 4.24. Une fois les échanges de chaleur identifiés, certains auteurs ont montré que d'une manière efficace de construire un modèle d'échange de chaleur en transitoire de change est d'utiliser un méthode par résistances thermiques équivalentes. D'après Cormerais [26], il est possible de réduire le système turbocompresseur calorifugé en stabilisé à 3 résistances équivalentes (voir Fig. 4.11)

2 Présentation du banc d'essai

La campagne expérimentale sur le turbocompresseur au Laboratoire de Mécanique Energétique de l'Ecole Centrale de Nantes, où un banc d'essai turbocompresseur est développé et utilisé depuis 2002. Le principal intérêt de ce banc d'essai est qu'il permet de capturer le comportement du turbocompresseur sans avoir prendre en charge un moteur complet.

Le débit turbine est fourni au moyen de deux compresseurs industriels, qui permettent de fournir un débit jusqu'à $700 \text{ m}^3 \text{ h}^{-1}$ à une pression de 7 bar. L'air est chauffée par un réchauffeur électrique de 144 kW, qui permet d'atteindre une température d'entrée turbine de l'ordre de 800 K. La température d'entrée turbine est réglée par une boucle de régulation entre le réchauffeur d'air et un capteur de température situé à l'entrée de la turbine.

Le débit massique de la turbine est réglé par une vanne située en amont du réchauffeur. Une vanne est également située en aval du compresseur, afin de modifier son point de fonctionnement. Un circuit d'huile a été mis en place afin d'alimenter le palier du turbocompresseur. Le débit d'huile est régulé en termes de débit massique et de température. Ceci est réalisé via une vanne asservie et un échangeur de chaleur huile-eau. Les capteurs de débit massique se trouvent en amont du réchauffeur d'air de turbine et en amont du compresseur. Les conduits en amont et en aval du compresseur et la turbine sont calorifugés afin d'éviter les pertes de chaleur et les gradients de température. Dans cette étude, seuls les essais pour un turbocompresseur isolé ont été considérés. Un aperçu du banc est disponible sur la figure 5.1. Les caractéristiques détaillées des capteurs sont disponibles ci-dessous :

Type de capteur	Fabricant	Modèle	Echelle	Dispersions
Pression amont compresseur	Sensor technics	HCX piezo	0 – 1 bar	$\pm 0.1\% \text{ PE}$
Pression aval compresseur	Sensor technics	HCX piezo	0 – 2 bar	$\pm 0.1\% \text{ PE}$
Pression aval turbine	Sensor technics	HCX piezo	0 – 0.1 bar	$\pm 0.1\% \text{ FS}$
Pression amont turbine	Sensor technics	HCX piezo	0 – 5 bar	$\pm 0.1\% \text{ PE}$
Débit massique	Endress-Hauger	T-mass 65F	0 – 0.5 kg/s	$\pm 1.5\% \text{ VL}$
Débit huile	Bamo	MicroStream	45l/h	$\pm 2\% \text{ PE}$
Température turbine	-	1mm K thermocouple	173 – 900 K	$\pm 1\text{ K}$
Température compresseur	-	thermoresistive sensor	223 – 773 K	$\pm 0.6\text{ K}$
Vitesse turbocompresseur	Acam	Picoturn	-	$\pm 200 \text{ tr/min}$

3 Extrapolation des cartographies de turbocompresseur basée sur les lois physiques des turbomachines.

Il ressort de l'étude bibliographique que les méthodes existantes développées en vue d'extrapoler les cartographies de turbocompresseurs ont une faiblesse majeure quant à l'exactitude de l'extrapolation données. Toutefois, ces méthodes sont faciles à mettre en place et ne nécessitent pas la connaissance détaillée des paramètres géométrique des turbomachines.

A l'inverse, les modèles entièrement physiques prennent détaillent les phénomènes physiques de l'écoulement des turbomachines et sont donc robustes concernant l'extrapolation des données turbocompresseur. Cependant, ils sont très complexes à construire et impliquent une connaissance parfaite de la géométrie du turbocompresseur.

L'approche adoptée dans cette thèse a pour objectif de combiner les avantages des deux méthodes :

- L'utilisation de fonctions mathématiques à paramétrier permet de simplifier la construction du modèle.
- Le développement des équations des turbomachines peut offrir une validité physique pour procéder à

l'extrapolation des données.

Afin d'atteindre cet objectif, il a été décidé de réaménager les équations de base des turbomachines et d'identifier les développements potentiellement utilisables pour enrichir les fonctions mathématiques à paramétrier.

3.1 Courbes caractéristiques des turbomachines.

Il est possible de construire les courbes caractéristiques des turbomachines par le développement de leurs équations thermodynamiques. Un exemple d'un tel développement a été proposé par Pluviose concernant les turbomachines axiales [106]. Il a été proposé dans la thèse d'adapter ce développement au cas des turbomachines radiales :

Compresseur : On définit en premier lieu les notations adoptées, en se référant à la figure 4.4 : U est la vitesse tangentielle des pales, V est la vitesse absolue du fluide en sortie du rotor, W est cette même vitesse, mais exprimée dans le repère tournant lié au rotor. A partir de ces vitesses, on définit les triangles de vitesses caractéristique du compresseur centrifuge. Les indices '2' se réfèrent aux quantités en sorties du rotor, alors que les indices '1' concernent les quantités en entrée du rotor. Les angles β_1 et β_2 sont les angles géométriques des pales en entrée et en sortie du rotor. On rappelle à présent l'équation d'Euler, qui exprime le changement d'enthalpie h au travers du compresseur :

$$\Delta h_{comp} = U_2 V_{\theta 2} - U_1 V_{\theta 1}$$

Il est possible de construire les courbes caractéristiques des turbomachines en développant leurs équations thermodynamiques. Dans le cas des pompes (fluides incompressibles), il est possible d'exprimer des coefficients de similitude appelés coefficients de Rateau. Deux de ces coefficients sont adaptés au cas de fluides compressibles : le coefficient de débit δ et le coefficient de pouvoir manométrique μ_{th} . Un exemple de ce développement a été produit par Pluviose [106] pour les turbomachines axiales. Il est proposé ici d'adapter ce développement dans le cas de machines à flux radial. Dans le cas du compresseur, ces coefficients s'écrivent : $\delta = \frac{V_r 2}{U_2}$ and $\mu_{th} = \frac{U_2 V_{\theta 2} - U_1 V_{\theta 1}}{U_2^2}$. Le pouvoir manométrique est un paramètre adimensionnel relié à l'échange d'enthalpie à travers le compresseur. Le coefficient de débit exprime de manière adimensionnelle la vitesse du fluide en sortie du compresseur. Nous allons montrer qu'il est possible d'exprimer le pouvoir manométrique d'un compresseur radial comme une fonction linéaire du coefficient de débit. Le développement mathématique permettant d'accéder à cette relation linéaire est exprimé par les équations 6.2 à 6.4, qui sont redéveloppées ci-dessous.

A partir de l'équation d'Euler, on écrit :

$$U_2^2 \cdot \mu_{th} = \Delta h = U_2 V_{\theta 2} - U_1 V_{\theta 1}$$

Dans notre cas, on considère que le flux est irrotationnel en amont du compresseur, ce qui est cohérent avec les conditions réelles ($V_{\theta 1} = 0$). En utilisant le triangle des vitesses, on obtient que $V_{\theta 2} = U_2 - V_r 2 \cdot \cotan(\beta_2)$, ce qui permet d'aboutir aux expressions suivantes :

$$\begin{aligned} \Delta h &= U_2^2 - U_2 V_r 2 \cdot \cotan(\beta_2) \\ \frac{\Delta h}{U_2^2} &= 1 - \frac{V_r 2}{U_2} \cotan(\beta_2) \\ \mu_{th} &= 1 - \delta \cdot \cotan(\beta_2) \end{aligned}$$

On s'aperçoit que dans le système de coordonnées δ, μ_{th} , la courbe caractéristique du compresseur radial est une droite de pente négative, d'ordonnée à l'origine 1. La pente théorique de la droite ne dépend que de l'angle géométrique fixe β_2 . Cette évolution est tracée sur la figure 6.2.

Turbine : Dans le cas de la turbine, il est également possible d'exprimer le pouvoir manométrique comme une fonction linéaire du coefficient de débit. Le développement mathématique permettant d'accéder à cette relation linéaire est exprimé par les équations 6.6 à 6.7, qui sont redéveloppées ci-dessous. L'équation d'Euler dans le cas de la turbine est également rappelée. Les indices '3' se réfèrent à l'état en amont de la turbine, et les indices '4' concernent l'aval.

$$\Delta h_{turb} = U_4 V_{\theta 4} - U_3 V_{\theta 3}$$

Dans le cas de la turbine, le coefficient de débit et le pouvoir manométrique sont exprimés tels que : $\delta = \frac{V_{r3}}{U_3}$ and $\mu_{th} = \frac{U_4 V_{\theta 4} - U_3 V_{\theta 3}}{U_3^2}$. En développant l'équation d'Euler's equation et en considérant que l'écoulement est irrotationnel en aval de la turbine ($V_{\theta 4} = 0$), on obtient le développement suivant :

$$\begin{aligned}\Delta h &= -U_3^2 + U_3 V_{r3} \cotan(\beta_3) \\ \frac{\Delta h}{U_3^2} &= -1 + \frac{V_{r3}}{U_3} \cotan(\beta_3) \\ \mu_{th} &= -1 + \delta \cdot \cotan(\beta_3)\end{aligned}$$

La courbe caractéristique de la turbine radiale est une droite de pente positive d'ordonnée à l'origine -1. Comme dans le cas du compresseur, la droite est tracée dans le système de coordonnées δ, μ_{th} (Fig.6.3).

3.2 Transposition des droites caractéristiques dans les repères réduits des cartographies de turbocompresseurs.

D'après les développements précédents, il apparaît que l'expression de la variation d'enthalpie dans une turbomachine radiale dans un certain système de coordonnées permet d'identifier une variation linéaire. Il s'agit d'une propriété intéressante, car les expressions mathématiques sont adaptées aux traitements d'extrapolation. Il a été proposé dans la thèse de vérifier si cette propriété linéaire est conservée en utilisant les repères des cartographies de turbocompresseur. Afin de se conformer à la théorie des similitude, les données des cartographies sont généralement exprimées comme des fonctions d'un débit massique réduit. En utilisant l'expression du changement d'enthalpie au travers du compresseur et de la turbine, il a été démontré que l'enthalpie peut être exprimée comme une fonction linéaire du débit massique réduit. Ainsi, les cartographies turbocompresseurs peuvent être traitées afin de faire apparaître une relation linéaire entre le changement d'enthalpie aux travers des turbomachines et leur débit massique réduit. Les expressions correspondantes sont présentées en premier lieu pour le compresseur :

$$\frac{\Delta h}{U_2^2} = 1 - \frac{Q m_{redC}}{\rho_2 S_2 U_2} \cotan(\beta_2) \sqrt{\frac{T_{ref}}{T_{01}}} \frac{P_{01}}{P_{ref}}$$

Les tests de caractérisation des compresseurs sont réalisés pour des pression P_{01} et des température T_{01} amont constantes. De plus, l'angle des pales β_2 et la section de sortie du rotor S_2 sont constantes. Finalement, en considérant que l'écoulement est observé immédiatement après la sortie du rotor, on peut considérer que le fluide a été accéléré mais pas comprimé, car il n'a pas encore pénétré le collecteur aval

(Heywood [61]). Par conséquent, on considère que $\rho_2 = constante = \rho_1$. En introduisant le terme constant $K_C = \frac{\cotan(\beta_2) \sqrt{\frac{T_{ref}}{T_{01}}} \frac{P_{01}}{P_{ref}}}{\rho_2 S_2}$, on fait apparaître le caractère linéaire de l'expression obtenue :

$$\frac{\Delta h}{U_2^2} = 1 - \frac{Qm_{redC}}{U_2} K_C$$

Un développement équivalent a été obtenu dans le cas de la turbine :

$$\frac{\Delta h}{U_3^2} = -1 + \frac{Qm_{redT}}{\rho_3 S_3 U_3} \cotan(\beta_3) \sqrt{\frac{T_{ref}}{T_{03}}} \frac{P_{03}}{P_{ref}}$$

Dans le cas de la turbine, les tests de caractérisation sont pratiqués pour une température amont T_{03} constante, mais pour des pressions amont P_{03} différentes. Par conséquent, la densité du fluide en amont de l'écoulement varie d'un point de la cartographie à un autre, donc ρ_3 ne peut être considéré constant. Cependant, on peut développer l'expression du débit massique à la turbine pour identifier un terme constant :

$$\begin{aligned} \rho_3 &= \frac{P_{03}}{R T_{03}} \\ \rho_3 \frac{P_{ref}}{P_{03}} &= \frac{P_{ref}}{R T_{03}} \end{aligned}$$

On obtient au final :

$$\begin{aligned} \frac{\Delta h}{U_3^2} &= -1 + \frac{Qm_{redT}}{S_3 U_3} \cotan(\beta_3) \sqrt{\frac{T_{ref}}{T_{03}}} \frac{R T_{03}}{P_{ref}} \\ \frac{\Delta h}{U_3^2} &= -1 + \frac{Qm_{redT}}{S_3 U_3} \cotan(\beta_3) \frac{R \sqrt{T_{ref} T_{03}}}{P_{ref}} \end{aligned}$$

Comme T_{ref} , T_{03} et P_{ref} sont fixés à des valeurs constantes lors des essais, il est possible d'introduire un terme constant tel que : $K_T = \frac{R \cotan(\beta_3) \sqrt{T_{ref} T_{03}}}{S_3 P_{ref}}$.

$$\frac{\Delta h}{U_3^2} = -1 + \frac{Qm_{redT}}{U_3} K_T$$

Pour une vitesse de pale U_3 donnée, l'équation précédent permet d'obtenir une relation linéaire entre le changement d'enthalpie spécifique au travers de la turbine et son débit réduit.

Validation à partir de données expérimentales : Nous avons vu dans les sections précédentes qu'une relation linéaire pourrait être construit entre le changement d'enthalpie du fluide à travers les turbomachines et leur débit massique réduit. Afin de vérifier que cette relation est belle est bien vérifiée, des données cartographiques ont été traitées afin de faire apparaître cette relation linéaire. Le turbocompresseur considéré équipe un moteur diesel à injection directe de 1,9 litres de cylindrée. Les résultats de ce traitement sont visibles sur la figure 6.4, où il apparaît que les évolutions linéaires sont vérifiées. Le principal résultat de cette validation est que l'expression linéaire de la variation d'enthalpie spécifique pourrait être intégrée à une technique d'extrapolation de données. La complexité sera accrue dans le cas de la turbine. En effet, il apparaît que la géométrie variable requiert une discrétisation des données supplémentaires en fonction de la position VGT.

3.3 Développement d'une méthode d'extrapolation des cartographies de turbocompresseurs basée sur les lois physiques des turbomachines.

La section suivante se concentre sur le développement d'une méthode d'extrapolation des cartographies de turbocompresseurs, réutilisant les éléments de courbes caractéristiques précédemment développés.

Traitements compresseur : Afin de construire des cartographies compresseur, il est nécessaire de connaître, pour un débit masse donnée, les valeurs du changement d'enthalpie spécifique Δh et de l'enthalpie spécifique isentropique Δh_{is} au travers du compresseur. D'après l'équation 6.14, on sait que l'évolution de l'enthalpie spécifiques peut être déterminée à partir d'une relation linéaire. Ces tendances linéaires sont très pratiques pour l'extrapolation des données. Toutefois, nous n'avons aucune indication quant à la forme de l'évolution du changement d'enthalpie isentropique.

Il a précédemment été démontré que l'évolution du changement d'enthalpie Δh en fonction du débit massique est linéaire. Il est donc possible de déterminer un ensemble de paramètres a et b , tels que :

$$\Delta h = a(N_{turb}) Qm + b(N_{Turb})$$

Les coefficients a et b sont déterminées au moyen de la méthode des moindres carrés à partir des données cartographiques. D'après les développements des courbes caractéristiques, ils ne dépendent que de la vitesse du rotor N_{Turb} . Afin de calculer les valeurs de Δh pour les valeurs de faible régime, il est nécessaire d'extrapoler les valeurs des coefficients $a(N_{turb})$ et $b(N_{Turb})$. $b(N_{Turb})$ est l'ordonnée à l'origine de Δh pour chaque iso-vitesse. La valeur théorique de l'ordonnée à l'origine de Δh est U_C^2 . Par conséquent, on peut écrire que :

$$b(N_{turb}) \sim N_{turb}^2$$

En ce qui concerne la pente de l'évolution linéaire de Δh , il ressort des données des fournisseurs que $a(N_{Turb})$ tend à être constant en atteignant les faibles valeurs de régime de rotation. Par conséquent, les valeurs extrapolées de $a(N_{Turb})$ vers la région des faibles régimes atteindra une asymptote horizontale. On se référera à la figure 6.5 pour plus de précisions. Une fois que les valeurs de $a(N_{Turb})$ et de $b(N_{Turb})$ sont connues sur l'ensemble du champs d'opération du compresseur, Δh est entièrement déterminé.

Il est à présent nécessaire de déterminer le traitement pour Δh_{is} . Comme aucune information n'est disponible quant à la forme de Δh_{is} en fonction du débit massique corrigé, il a été décidé d'utiliser une méthode de corrélation mathématique ('curve fitting') afin d'apprendre l'évolution du changement d'enthalpie isentropique. On a vu durant l'étude bibliographique que Jensen et al. [69] ont mis au point une méthode d'extrapolation de champs compresseur intéressante. Cette méthode est basée sur la corrélation d'un paramètre sans dimension ψ , qui est le paramètre de tête du compresseur :

$$\psi = \frac{Cp.T_{amb} \left(\left(\frac{P_{01}}{P_{amb}} \right)^{\frac{\gamma-1}{\gamma}} - 1 \right)}{0.5 U_c^2} \quad \text{with} \quad U_c = \frac{\pi}{60} d_c \omega_t$$

De par sa définition, le paramètre de tête est directement lié à la variation d'enthalpie spécifique isentropique :

$$\Delta h_{is} = \left(\left(\frac{P_{02}}{P_{01}} \right)^{\frac{\gamma-1}{\gamma}} - 1 \right) Cp T_{01} = 0.5 \psi U_C^2$$

Par conséquent, la méthode de Jensen, est théoriquement adaptée pour déterminer Δh_{is} à partir de données cartographiques. Cependant, cette technique offre une précision médiocre pour les vitesses de rotation les plus élevées. Afin de corriger ce problème, une version modifiée de la méthode de Jensen a été mise en place : les données cartographiques du compresseur sont discrétisées en fonction de leur vitesse de rotation (Fig. 6.6). Une méthode d'apprentissage de Jensen est appliquée pour chaque zone discrétisée. Dans le cas où il existe n_n courbes iso-vitesse sur la cartographie, on définit n_N jeux de coefficients de Jensen à corrérer :

$$\psi_{zone_{1i}} = \frac{k_{1i} + k_{2i} \cdot M_{inl_i} + k_{3i} \cdot \phi + k_{4i} \cdot M_{inl_i} \cdot \phi}{k_{5i} + k_{6i} \cdot M_{inl_i} - \phi} \quad i = 1 : n_N$$

où ϕ est un paramètre de débit sans dimension et M_{inl} le nombre de Mach à l'entrée du compresseur. Les paramètres k sont appris par méthode des moindres carrés d'après les données cartographiques.

$$\phi = \frac{Q_m}{\rho_{amb} \cdot \frac{\pi}{4} \cdot D_c^2 \cdot U_c} \quad M_{inl} = \frac{U_c}{\sqrt{\gamma R t_{amb}}}$$

Il est à présent nécessaire de déterminer le traitement pour extrapoler Δh_{is} vers la zone des faibles régimes de rotation. En effet, Moraal et al. [94] ont montré que le traitement de Jensen permet de préserver, en apparence, une évolution correcte des courbes de ψ dans la zone des faibles vitesses, mais aucune équation ou observation physique ne permet de s'assurer de la validité des données extrapolées. Afin de corriger cette situation, une méthode itérative a été développée.

A partir des données expérimentales, il a été constaté que le rendement isentropique maximum du compresseur pour une vitesse de rotation donnée a une évolution quadratique en fonction de la vitesse de rotation de l'arbre. Cette tendance a été observée sur les compresseurs radiaux testés au cours de cette thèse. Un exemple de cette courbe et de son extrapolation est rapportée sur la Fig. 6.7. En partant de ce constat, il est possible de construire un schéma itératif afin d'assurer la validité physique de l'extrapolation de Δh_{is} :

1. Une première approximation de Δh_{is} est obtenue en utilisant le traitement discrétisé inspiré de Jensen. Les coefficients de la première courbe iso-vitesse ($k_{11} \rightarrow k_{61}$) sont utilisés dans la zone extrapolée.
2. En utilisant les valeurs extrapolées de $a(N_{Turb})$ et de $b(N_{Turb})$ dans la zone des faibles vitesses, la valeur de Δh est déterminée.
3. Connaissant Δh_{is} et Δh , il est possible de calculer le rendement isentropique correspondant : $\eta_C = \frac{\Delta h_{is}}{\Delta h}$. Le rendement par rapport au débit massique peut donc être construit dans la zone extrapolée.
4. Une fois ces évolutions construites, la valeur du rendement isentropique par iso-vitesse est calculé et comparé à la courbe quadratique 'rendement maximum fonction de la vitesse de rotation'. Si les résultats sont en accord, les valeurs de Δh_{is} sont considérées comme définitives. Dans le cas contraire, les valeurs de Δh_{is} sont modifiées jusqu'à ce que l'accord entre les rendements maximum et la courbe d'évolution théorique concorde. On se référera à la figure 6.7 pour plus de précisions.

Ce traitement assure la validité physique des données extrapolées à l'aide de la tendance du rendement maximal du compresseur. La spécificité de la méthode développée est qu'elle est basée sur la relation fondamentale entre Δh et Δh_{is} , permettant de faire apparaître le rendement : $\eta_C = \frac{\Delta h_{is}}{\Delta h}$. On note que les méthodes d'apprentissage trouvées dans la littérature utilisent deux traitements distincts, un pour la cartographie de rapports de pression et un pour la cartographie du rendement [94], [69], [95], [58]. Par conséquent, ces méthodes ne respectent pas nécessairement la définition du rendement isentropique.

Au final, le traitement proposé dans cette thèse suit la mise en œuvre suivante. Une fois que les valeurs de Δh et de Δh_{is} ont été calculés pour un débit massique corrigé, le rapport de pression et le rendement sont calculés de la manière suivante :

- Comme Δh_{is} est connu, le rapport de pression peut être directement calculé en utilisant la relation suivante : $\frac{P_{02}}{P_{01}} = (1 + \frac{\Delta h_{is}}{CpT_{01}})^{\frac{\gamma}{\gamma-1}}$.
- Le rendement isentropique est également obtenu : $\eta_C = \frac{\Delta h_{is}}{\Delta h}$. Contrairement aux méthodes d'interpolation / extrapolation de la littérature, le rendement est naturellement dérivé de la connaissance des changements d'enthalpie isentropique et non-isentropique.

Traitements turbine :

Afin de construire les cartographies de données turbine, les valeurs du changement d'enthalpie spécifique Δh et du changement d'enthalpie spécifique isentropique Δh_{is} doivent être connues pour un débit massique Qm_T donné. Comme dans le cas du compresseur, nous allons utiliser la relation linéaire entre Δh et le débit massique corrigé Qm_{redT} pour construire l'extrapolation.

Dans un premier temps, on s'intéresse à la détermination de Δh . Comme l'évolution de Δh en fonction du débit massique corrigée est linéaire (Eq. 6.23), il est donc possible de déterminer un ensemble de paramètres a et b , dépendant de la vitesse de rotation N_{turb} tels que :

$$\Delta h = a(N_{turb}) Qm_{redT} + b(N_{turb})$$

Dans le cas où le rotor ne tourne pas, la puissance capturée par la turbine est nulle. Par conséquent, l'évolution de Δh fonction de Qm_{redT} pour $N_{turb} = 0$ est une droite horizontale telle que : $\Delta h = 0$. Par conséquent, a et b sont extrapolés vers la zone des faibles vitesses de rotation de telle manière que $a(0) = 0$ et $b(0) = 0$. Il faut également noter que dans le cas où la turbine est à géométrie variable, plusieurs jeux de coefficients a et b devront être déterminés (un jeu par position VGT).

Afin de calculer l'évolution de $\Delta h_{is} = (1 - (\frac{P_{04}}{P_{03}})^{\frac{\gamma-1}{\gamma}}) Cp T_{03}$ en fonction du débit massique, il est nécessaire d'avoir une relation entre le taux de pression à travers la turbine $\frac{P_{04}}{P_{03}}$ et le débit massique corrigé Qm_{redT} . Une telle relation est fournie par la modélisation de la turbine comme un écoulement à travers un orifice. Jensen et al. [69] ont, entre autres, démontré qu'une telle approche est bien adaptée à la modélisation de l'écoulement au travers d'une turbine. En outre, ce modèle tend naturellement vers 0 lorsque le taux de pression atteint 1. Par conséquent, l'approche de Jensen sera directement ré-utilisée ici. Les paramètres k_i sont déterminées au moyen d'un algorithme des moindres carrés.

$$Qm_{redT} = A_t \sqrt{\frac{2\gamma}{\gamma-1} \left[\left(\frac{P_{04}}{P_{03}}\right)^{\frac{2}{\gamma}} - \left(\frac{P_{04}}{P_{03}}\right)^{\frac{\gamma+1}{\gamma}} \right]} \quad \frac{P_{04}}{P_{03}} < \frac{2}{\gamma+1}^{\frac{\gamma-1}{\gamma}}$$

$$Qm_{redT} = A_t \sqrt{\frac{2\gamma}{\gamma-1} \left[\left(\frac{2}{\gamma+1}\right)^{\frac{2}{\gamma}} - \left(\frac{2}{\gamma+1}\right)^{\frac{\gamma+1}{\gamma}} \right]} \quad \frac{P_{04}}{P_{03}} > \frac{2}{\gamma+1}^{\frac{\gamma-1}{\gamma}}$$

$$A_t = \frac{k_1 \cdot N_{turb} + k_2}{P_{it}} + k_3 \cdot N_{turb} + k_4$$

Une fois que la relation entre le rapport de pression et le débit massique ait été définie, il est possible d'exprimer l'évolution de Δh_{is} en fonction de Qm_{redT} . Contrairement au cas du compresseur, il n'est pas nécessaire d'introduire un traitement spécifique pour extrapolier Δh_{is} est de données vers les valeurs inférieures de régime de rotation. En effet, comme dit précédemment, le modèle d'écoulement au travers d'un orifice est basé sur une équation de la physique qui décrit bien le comportement de la turbine pour les faibles rapports de pression. Il est possible de synthétiser le traitement d'interpolation / extrapolation proposé pour la turbine de la façon suivante :

- Le rapport de pression fonction du débit massique est calculé directement en utilisant l'équation d'écoulement au travers d'un orifice.
- En connaissant le rapport de pression, le changement d'enthalpie spécifique isentropique est calculé : $\Delta h_{is} = (1 - (\frac{P_{04}}{P_{03}})^{\frac{\gamma-1}{\gamma}}) Cp T_{03}$.

- Δh est déterminé à partir des extrapolations linéaires. Enfin, le rendement isentropique est calculé : $\eta_T = \frac{\Delta h}{\Delta h_{is}}$.

3.4 Résultats et validation des modèles développés

Applications des traitements sur des données cartographiques : Les résultats du traitement effectué sur trois turbocompresseurs différents utilisés sur les applications suivantes sont présentés : (1) moteur diesel de 2,0 L de cylindrée, (2) moteur diesel de 1,5 L de cylindrée et (3) moteur essence de 1,2 L de cylindrée. Les données fournies par la cartographie (étoiles) se superposent sur les extrapolations des résultats de calcul (lignes pleines). L'extrapolation est effectuée de façon à couvrir l'intégralité des plages de fonctionnement en débit et rapport de pression.. Une extrapolation à basse vitesse de rotation est également effectuée pour évaluer la robustesse de la méthode d'extrapolation. Il faut noter que turbine (1) est à géométrie variable, toutefois, pour plus de commodité et vu que cela n'a aucune influence sur la méthode de calcul, seuls les résultats à ouverture 50% sont indiqués.

Les résultats de la méthode développée précédemment sont comparés aux résultats de la méthode de Jensen. Cette comparaison n'est pas effectuée pour le débit massique de turbine car c'est la méthode de Jensen qui est utilisée dans les deux cas . D'après les résultats de la Fig. 6.10 à Fig. 6.12, on peut remarquer une forte amélioration de la précision du traitement du rapport de pression. Dans le même temps, l'extrapolation du rendement du compresseur a également été améliorée (Fig. 6.13 to Fig. 6.15). On peut noter que la partie gauche des caractéristiques du compresseur extrapolées sont purement théoriques, car un phénomène de pompage survient généralement pour les faibles débits. Cependant, il est possible de coupler un modèle de pompage. Un exemple de cette combinaison est indiquée sur la Fig. 6.20. Concernant l'évolution des rendements turbine, on s'aperçoit que leur forme est plus en accord avec les courbes de rendement expérimentales relevées sur la figure ?? que le traitement proposé par Jensen et al.

Validation du processus d'extrapolation par rapport à des données expérimentales : Les figures 6.21 and 6.22 montrent la comparaison entre les données mesurées sur le banc d'essai turbocompresseur (décrit précédemment dans la thèse) et les résultats du modèle développé. Le banc d'essai turbocompresseur a permis de mesurer des point de fonctionnement aux faibles vitesses de rotation. Le modèle du compresseur est appliquées à des données compresseur supérieure à 90 krpm, le modèle de turbine est appliquée aux données de plus de 35 krpm. Par conséquent, la partie inférieure de la plage de fonctionnement est entièrement extrapolée. Les résultats sont présentés pour une température de 773 K à l'entrée de la turbine. On notera que le rendement de la turbine atteint des valeurs supérieures à 1 ; ce phénomène est dû au processus d'échange de chaleur et sera expliqué dans le chapitre consacré à la modélisation des échanges thermiques. On s'aperçoit que les résultats de l'extrapolation sont en bon accord avec les données expérimentales. Les valeurs calculées de rendement restent, sur la plupart des points, dans la zone de dispersion dû aux capteurs. Les résultats en termes de rapport de pression ou de débit massique sont également satisfaisants. Ces bons résultats obtenus en extrapolation montrent que les modèles développés sont précis et robustes. Néanmoins, il sera intéressant de tester notre approche sur d'autres turbocompresseurs que celui de l'étude.

4 Echanges thermiques au sein des turbocompresseurs

4.1 Calcul des échanges thermiques à partir de mesures

Le but de cette section est de détailler le processus et les équations mis en place afin d'identifier les échanges de chaleur se produisant au sein d'un turbocompresseur isolé, mais non adiabatique. L'étude sera basée sur les données obtenues à partir des mesures au banc d'essai précédemment présenté dans la thèse. Une attention particulière est accordée afin de distinguer la puissance effective sur l'arbre de la turbomachine \dot{W}_{sh} et la puissance apparente calculée via les mesures de température \dot{W} .

Turbocompresseur isolé en conditions non-adiabatiques : équations : Les acquisitions ont été réalisées dans des conditions stabilisées, la température d'entrée du compresseur a été fixée à 293 K, la température de l'huile a été réglée à 353K et la température d'entrée turbine a été régulée entre 373K et 873K ($T_T > T_O > T_C$). Dans ces conditions, les résultats des études expérimentales et numériques détaillées dans [12], [13], [11], [26] montrent que les transferts de chaleur peuvent être considérés comme unidimensionnels et que la chaleur est transférée de la turbine vers le compresseur (Q_C) et l'huile (Q_O) (voir Fig. 7.1). En outre, la puissance de l'arbre de turbine (\dot{W}_{Tsh}) est transférée vers le compresseur par l'intermédiaire de l'arbre (\dot{W}_{Csh}), même si des pertes par frottement se produisent au niveau des paliers (\dot{W}_F). Les pertes par frottement sont transformées en chaleur et donc le gain de puissance pour l'écoulement d'huile due aux échanges de chaleur et aux pertes par frottement est exprimé comme suit :

$$\dot{W}_O = \dot{W}_F + Q_O$$

Au moyen de l'équilibre des puissances sur l'arbre turbine à l'arbre est exprimée dans l'équation 7.2. Enfin, la conservation de l'énergie permet d'écrire l'équation d'échange de chaleur (Eq. 7.3).

$$\begin{aligned} -\dot{W}_{Tsh} &= \dot{W}_F + \dot{W}_{Csh} \\ -Q_T &= Q_C + Q_O \end{aligned}$$

Les puissances apparentes calculées au moyen de la mesure de température prennent en compte la puissance sur l'arbre et les transferts de chaleur :

$$\begin{aligned} \dot{W}_T &= Q_T + \dot{W}_{Tsh} \\ \dot{W}_C &= \dot{W}_{Csh} - Q_C \end{aligned}$$

Enfin, à partir du développement des équations précédentes, il est possible d'obtenir le système de 4 équations et 6 inconnues, qui doit être résolu afin de déterminer les échanges de chaleur. Les seules quantités connues sont les valeurs de \dot{W}_T et \dot{W}_C à partir des mesures. Il faut remarquer qu'une cinquième équation $Q_O = \dot{W}_F - \dot{W}_O$ pourrait être ajoutée au système, ce qui conduirait à un système de 5 équations et 6 inconnues. Toutefois, les incertitudes faites sur la température d'huile sont élevées, ce qui est dû au caractère biphasique (brouillard) huile/air) à la sortie du carter du turbocompresseur. Cette incertitude peut fortement impacter les résultats et par conséquent, la valeur de \dot{W}_O ne sera pas introduite dans les développements suivants.

$$\begin{aligned} Q_C &= \dot{W}_{Csh} - \dot{W}_C \\ Q_T &= \dot{W}_T - \dot{W}_{Tsh} \\ Q_O &= -Q_C - Q_T \\ \dot{W}_F &= -\dot{W}_{Tsh} - \dot{W}_{Csh} \end{aligned}$$

Ce système ne peut être résolu car il y a plus d'inconnues que d'équations disponibles. Afin d'obtenir suffisamment d'informations pour résoudre le système d'équations, les mesures des tests isolés adiabatiques doivent être introduits.

Turbocompresseur isolé et adiabatique : équations

Dans le cas adiabatique, il n'y a pas d'échange de chaleur au sein du turbocompresseur, donc :

$$Q_T = Q_C = Q_O = 0$$

A partir de ce constat, on obtient :

$$\begin{aligned}\dot{W}_O &= \dot{W}_F \\ \dot{W}_{Csh} &= \dot{W}_C \\ \dot{W}_{Tsh} &= \dot{W}_T \\ \dot{W}_F &= -\dot{W}_{Tsh} - \dot{W}_{Csh}\end{aligned}$$

Il apparaît que les mesures effectuées dans le cas adiabatique et isolé permettent d'obtenir directement les puissances à l'arbre de la turbomachine \dot{W}_{Csh} et \dot{W}_{Tsh} . Enfin, la puissance perdue aux roulements par frottement \dot{W}_F est directement calculée.

Combinaison des tests adiabatiques et non-adiabatiques : hypothèses et introduction des modèles :

Afin de calculer les transferts de chaleur qui surviennent dans le turbocompresseur, le processus expérimental détaillé par Baar et al. [3], Shaaban [118] et Cormerais [26] est utilisé. Ce processus est détaillé dans la section d'étude bibliographique. Elle s'appuie sur une étude comparative des puissances compresseur, turbine et du circuit d'huile entre les cas adiabatique et non-adiabatiques ($\dot{W}_{adia} \neq \dot{W}_{non-adia}$). Il est supposé que la capacité calorifique à pression constante C_p est constante à travers la turbomachine, par conséquent, les pouvoirs du compresseur et de la turbine sont calculées en utilisant les équations suivantes :

$$\begin{aligned}\dot{W}_C &= Qm_C C_{p,air} \Delta T_{comp} \\ \dot{W}_T &= Qm_T C_{p,air} \Delta T_{turb}\end{aligned}$$

Une hypothèse importante énoncée dans [3], [118] and [26], est que la puissance à l'arbre du compresseur \dot{W}_{Csh} n'est pas impactée par les échanges de chaleur. Cette hypothèse a été validée expérimentalement par Shaaban, qui a montré que les échanges de chaleur du compresseur en amont du rotor ne représentent que moins de 3% des échanges de chaleur pour le compresseur. En ré-introduisant cette hypothèse, \dot{W}_{Csh} est déterminé à partir des données du compresseur adiabatique et l'échange de chaleur au niveau du compresseur est calculé de la façon suivante :

$$\begin{aligned}\dot{W}_{Csh,non-adia} &= \dot{W}_{Csh,adia} \\ Q_C &= \dot{W}_{Csh,non-adia} - \dot{W}_C\end{aligned}$$

Les pertes de puissance par friction \dot{W}_F sont connues dans le cas adiabatique. Afin d'estimer cette quantité dans le cas non-adiabatique, il est nécessaire de construire un modèle de frottement des paliers. Le modèle de friction utilise une estimation basée sur la méthode de Petroff pour les paliers hydrodynamiques. Le modèle est calibré en utilisant les résultats des tests adiabatiques. Une fois que les puissances relatives au compresseur et aux pertes par frottement sont connus, il est possible de calculer la puissance à l'arbre de turbine au moyen de l'équilibre des puissances. Enfin, la connaissance de la puissance mécanique de la turbine combinée aux mesures en conditions non-adiabatiques permet de déduire les échanges thermiques à la turbine.

$$\begin{aligned}-\dot{W}_{Tsh,non-adia} &= \dot{W}_{Csh,non-adia} + \dot{W}_F \\ Q_T &= \dot{W}_{T,non-adia} - \dot{W}_{Tsh,non-adia}\end{aligned}$$

Modèle de frottement :

Dans le cas des tests isolés en conditions adiabatiques, on note une différence la puissance de l'arbre du compresseur \dot{W}_{Csh} et celle de l'arbre turbine \dot{W}_{Tsh} . Cette différence est dûe aux pertes survenant dans le système de palier. La première source de perte de puissance provient de l'écoulement visqueux dans les paliers. L'huile est soumise à des contraintes de cisaillement à cause de la rotation de l'arbre, créant ainsi un couple résistif : T_B . La deuxième source de perte de puissance sont causées par la bague empêchant le mouvement axial de l'arbre : les pressions appliquées sur les roues des turbomachines créent des efforts axiaux (F_C et F_T , voir Fig. 7.3). Le déplacement axial de l'arbre est limité par la butée axiale près de la roue de la turbine : une force de contact F_{ax_stp} est donc établie entre l'arbre du rotor et le carter du turbocompresseur. Comme l'arbre est en rotation, cette force de contact se traduira par un couple résistif : T_{ax_stp} . Par conséquent, les pertes de puissance par frottement sont divisées en deux sources de contribution : le frottement visqueux se produisant dans le palier et le frottement de contact dû à des efforts appliqués sur la butée axiale. Les contributions doivent être calculées afin de construire le modèle de friction : $\dot{W}_F = \dot{W}_{ax_stp} + \dot{W}_B$. On négligera dans l'étude les forces radiales appliquées sur l'arbre. Cette hypothèse est motivée par les faits suivants :

- L'arbre du rotor est équilibré dynamiquement.
- La masse du rotor est faible (<100 g).
- Comme le compresseur et les carters de turbine sont presque axisymétriques, les distributions de pression sur les roues sont censées être uniformes, de sorte que les forces qui en résultent ont une composante radiale négligeable.

Par conséquent, la formulation de la Petroff des pertes visqueuses sans effort radial sera utilisée. Le couple résistif et la perte de puissance déduits de ce couple sont exprimés dans l'équation suivante (μ est la viscosité de l'huile, R est le rayon de l'arbre du rotor, B_w la largeur du palier et B_R le jeu radial du palier).

$$\begin{aligned}T_B &= \frac{2\pi\mu N_{turb} R^2 B_w}{B_R} \\ \dot{W}_B &= \frac{2\pi\mu N_{turb}^2 R^2 B_w}{B_R}\end{aligned}$$

Le couple causé par la butée axiale et les pertes de puissance sont exprimées dans l'équation suivante (f est le coefficient de frottement entre l'arbre et la butée axiale, qui dépend de la viscosité de l'huile, de la vitesse de rotation et la force axiale, R_{ax_stp} est la longueur de contact entre l'arbre et la butée axiale).

$$\begin{aligned}T_{ax_stp} &= (F_T - F_C) f(\mu, N_{turb}, \Delta F) \frac{R_{ax_stp}}{2} N_{turb} \\ \dot{W}_{ax_stp} &= (F_T - F_C) f(\mu, N_{turb}, \Delta F) \frac{R_{ax_stp}}{2} N_{turb}^2\end{aligned}$$

Les modèles trouvés dans la littérature [118], [117], [26] ont montré qu'il est nécessaire de recaler le modèle de frottement développé afin d'obtenir un niveau de précision satisfaisant. de modèle 0D. Dans notre cas, nous avons combiné les expressions de \dot{W}_B and \dot{W}_{ax_stp} d'une façon qui permet l'introduction de deux coefficients de corrélation K_1 et K_2 . Un jeu unique de coefficients est trouvé en utilisant un algorithme de moindres carrés. La base d'apprentissage provient des tests pour le turbocompresseur isolé en conditions adiabatiques. Ces 2 coefficients inclus les paramètres géométriques du système (R, B_w, \dots) ainsi que les incertitudes du modèle. Les valeurs de K_1 et K_2 ne sont pas fournies ici pour des raisons de confidentialité.

$$\dot{W}_F = \mu N_{turb}^2 (k_1(F_T - F_C) + k_2)$$

La viscosité de l'huile est calculée selon la formule suivante pour une huile 15W40 entre 290K et 400K. La viscosité de l'huile est calculée en utilisant la valeur moyenne de la température de l'huile telle que définie par Shaaban [118].

$$\begin{aligned}\mu &= 220.87 \left(T_{oil_mean} \right)^{-2.0462} \\ T_{oil_mean} &= \frac{T_{oil_in} + T_{oil_out}}{2}\end{aligned}$$

Le résultat du modèle une fois corrélé par rapport aux résultats des tests adiabatiques est tracé sur la Fig. 7.4. Il apparaît que les pertes calculées sont en adéquation avec les résultats expérimentaux. Environ 95 % des points calculés présentent moins de 10 % d'erreur par rapport aux données expérimentales. Il est également nécessaire de vérifier le comportement du modèle en extrapolation. Les résultats de cette étude sont montré sur la figure 7.5, où la température de l'huile et la vitesse de rotation ont été augmentées. Les données extrapolées montrent que les tendances physiques sont respectés. On doit néanmoins garder à l'esprit que les calculs d'échanges thermiques dépendront fortement de ce modèle de la perte de puissance.

4.2 Résultats de mesure

Les résultats des mesures expérimentales réalisées pour cette thèse vont être détaillés dans cette section. Dans un premier temps, les cartographies compresseur et turbine seront construits afin de souligner l'impact de la température d'entrée turbine sur le rendement apparent mesuré et les débits. En second lieu, les échanges de chaleur identifiés pour la turbine, le compresseur et le circuit d'huile seront tracés et analysés.

Cartographies compresseur :

La figure 7.6 montre l'impact de la température d'entrée turbine sur les courbes de performance du compresseur. Il semble que l'évolution du rapport de pression par rapport au débit massique corrigé soit indépendant de la température d'entrée turbine. Cependant, le rendement est affecté par le changement de température à l'entrée de la turbine. On peut voir que plus la température d'entrée turbine est élevée, le rendement apparent du compresseur diminue. Étant donné que les caractéristiques pression contre débit sont indépendantes de la température, on écrit :

$$\begin{aligned}(1) \quad \left(\frac{N_{turb}}{\sqrt{T_{in}}} \right)_{Adia} &= \left(\frac{N_{turb}}{\sqrt{T_{in}}} \right)_{573K} = \left(\frac{N_{turb}}{\sqrt{T_{in}}} \right)_{773K} \\ (2) \quad \left(\frac{P_{out}}{P_{in}} \right)_{Adia} &= \left(\frac{P_{out}}{P_{in}} \right)_{573K} = \left(\frac{P_{out}}{P_{in}} \right)_{773K} \\ (3) \quad \left(Q_m \frac{\sqrt{T_{in}}}{P_{in}} \right)_{Adia} &= \left(Q_m \frac{\sqrt{T_{in}}}{P_{in}} \right)_{573K} = \left(Q_m \frac{\sqrt{T_{in}}}{P_{in}} \right)_{773K}\end{aligned}$$

La théorie des similitudes appliquée aux turbomachines (Annexe A, sinon voir le livre de Pluviose [106]), montre que ces trois égalités impliquent nécessairement l'égalité du nombre de Mach, du nombre de Reynolds ainsi que la conservation du triangle des vitesses au rotor. Cela signifie que le rendement aérodynamique du rotor est le même dans les 3 cas. Cependant, les résultats montrent une dépendance du rendement compresseur en fonction de la température d'entrée turbine. Ce phénomène est expliqué comme suit :

- L'écoulement au travers du rotor du compresseur a un rendement indépendant de la température d'entrée turbine. Ceci est démontré par la théorie de similitudes et la conservation des caractéristiques débit / rapport de pression.

- Il y a un transfert d'énergie thermique de la turbine vers le compresseur. Ce transfert cause une élévation de température du fluide en sortie du compresseur. Cette élévation de température impacte le rendement : $\eta_c = \frac{\left(\left(\frac{P_{02}}{P_{01}}\right)^{\frac{\gamma-1}{\gamma}} - 1\right)}{\frac{T_{02}}{T_{01}} - 1}$.
- Comme le rendement aérodynamique au travers du rotor est indépendant de la température entrée turbine, cela signifie que le transfert thermique est effectif après le rotor. Par conséquent, le transfert thermique au compresseur a lieu dans le collecteur, en aval du rotor. Cela confirme les observations trouvées dans la littérature.

Sur le tracé de gauche de la figure. 7.6, il apparaît que le rapport entre le rendement en conditions adiabatiques et non-adiabatiques est constant en fonction du débit massique du compresseur. En outre, la différence de rendement entre le cas adiabatique et non-adiabatique diminue quand la vitesse de rotation de l'arbre augmente, ce qui signifie que la puissance thermique transférée au compresseur a tendance à avoir une influence négligeable à grande vitesse de rotation. Ces observations sont confirmées sur la figure 7.7.

Cartographies turbine :

La figure 7.8 montre l'impact de la température d'entrée turbine sur les courbes caractéristiques de la turbine. Dans un premier temps, seuls les résultats pour une pleine ouverture de la géométrie turbine sont proposés. Comme dans le cas du compresseur, trois cas sont considérés : le cas adiabatique ainsi que les cas non-adiabatique avec une température d'entrée turbine de 573K et une température d'entrée turbine de 773K. D'après la théorie des similitude (Annexe A), pour une vitesse de rotation donnée, les caractéristiques de débit massique corrigé devraient être indépendantes de la température d'entrée turbine. Ce n'est pas le cas ici, car les courbes caractéristiques ne peuvent pas être exactement superposées. Cela est particulièrement visible aux vitesses de rotation les plus élevées : les courbes de débit massique pour les trois températures d'entrée turbine à 55000 tr / min sont distinctes, comme illustré sur la figure. 7.9. Cela signifie que contrairement au cas du compresseur, le triangle des vitesses n'est pas conservé lorsque la température d'entrée turbine est modifiée. Par conséquent, le rendement de la détente au travers du rotor turbine est fonction de la température d'entrée turbine. La puissance à l'arbre de la turbine \dot{W}_{Tsh} est donc également tributaire de cette température.

On note également que le rendement mesuré atteint des valeurs supérieures à 1. Un rendement supérieur à 1 est impossible à atteindre. C'est l'effet des transferts de chaleur à la turbine qui est perçu : comme de la chaleur est transférée vers le circuit d'huile l'huile et le compresseur, la température de sortie turbine sera plus faible que dans le cas adiabatique. En regardant l'équation de rendement de la turbine, il en découle

$$\text{une élévation du rendement apparent mesuré : } \eta_t = \frac{1 - \left(\frac{T_{04}}{T_{03}}\right)^{\frac{\gamma-1}{\gamma}}}{1 - \frac{P_{04}}{P_{03}}}.$$

Extrapolation des données de la cartographie compresseur en conditions adiabatiques

La figure 7.6 montre que les données compresseur en conditions adiabatiques ne couvrent qu'une plage de fonctionnement restreinte. Les caractéristiques adiabatiques du compresseur sont nécessaires pour déterminer les puissances relatives au compresseur et à la turbine. Afin d'étendre la plage de détermination des échanges thermiques, la cartographie adiabatique du compresseur a été extrapolée.. Comme le compresseur respecte la théorie de similitude, les courbes de taux de pression sont indépendantes de la température d'entrée turbine. Par conséquent, les courbes de pression du compresseur pour une température d'entrée turbine de 773K sont les mêmes qu'en conditions adiabatiques. En ce qui concerne l'extrapolation du rendement, cette approche ne peut pas être utilisée. Toutefois, la figure . 7.7 a montré que les ratios entre les rendements déterminés dans des conditions 'chaudes' et dans des conditions adiabatiques sont constants et tendent vers 1 lorsque

la vitesse arbre augmente. Par conséquent, il est possible de tracer une courbe d'évolution du ratio entre les rendements en conditions adiabatiques et non-adiabatique, dépendant de la vitesse de l'arbre. L'asymptote horizontale de cette courbe est de 1 lorsque la vitesse de l'arbre tend vers l'infini, ce qui permet une simple extrapolation de cette courbe (Fig. 7.10). Afin d'extrapoler le rendement du compresseur adiabatique, cette courbe est couplée aux valeurs de rendement en conditions non-adiabatiques.

Etude des paramètres influençant les transferts de chaleur

Les transferts de chaleur au sein du turbocompresseur lors des essais sur banc ont été identifiés à l'aide des équations et hypothèses précédemment développées et hypothèses. Dans cette section, on étudie les paramètres ayant une influence sur l'évolution des transferts thermiques. Les résultats pour une ouverture VGT de 100 % sont présentées ici (l'impact de la géométrie turbine sera étudiée plus tard dans la thèse). Il a été décidé de tracer sur la figure 7.11 les transferts de chaleur pour le compresseur, la turbine et l'huile dans le système de coordonnées du compresseur (débit contre rapport de pression). Le but de ce tracé est de permettre une comparaison directe entre chaque transfert de chaleur.

Sur cette figure, on voit que l'ordre de grandeur des transferts de chaleur dans le turbocompresseur est de 100 W. On note également que la puissance thermique évacuée par le débit d'huile est généralement supérieure à la puissance reçu par le compresseur. La puissance thermique évacuée par le débit d'huile est fortement dépendante de la vitesse de rotation de l'arbre. Il existe une forte corrélation entre les transferts thermiques compresseur et turbine, qui est dûe à l'établissement d'un équilibre thermique en conditions stabilisées. Les transferts de chaleur sont également tracés sur les figures 7.12 et 7.13. Ces graphes montrent l'évolution des transferts thermiques en regard des paramètres physiques des turbomachines (débit, rapport de pression et vitesse de rotation). Pour une fois dans la thèse, les valeurs de vitesse de l'arbre ne sont pas corrigées, ce qui permet une comparaison directe entre la turbine et le compresseur. Il est rappelé que les résultats présentés sont valables en stabilisé : les figures 7.12 et 7.13 sont liées. Chaque point de fonctionnement du compresseur tracé sur la figure 7.13 trouve une correspondance pour la turbine sur la figure 7.12. Cette correspondance est dûe à l'équilibre des puissances sur l'arbre (plus les pertes de frottement) entre le compresseur et la turbine dans des conditions stables. Un exemple de la correspondance entre les points de fonctionnement compresseur et turbine est indiquée dans l'annexe B.

Température d'entrée turbine :

La puissance thermique transférée de la turbine vers le compresseur et le circuit de lubrification est dépendante de la température d'entrée turbine. Pour une valeur de température entrée turbine T_{03} de 773K, la puissance thermique transférée à la turbine (respectivement au compresseur) est de 750W (resp. 250W), tandis qu'elle est de 400W (resp. 125W) pour $T_{03} = 573K$. Le rapport des transferts thermiques sur la puissance à l'arbre turbine $\frac{Q_T}{W_{tsh}}$ est également affecté par la variation de la température d'entrée : l'augmentation des pertes de chaleur à turbine Q_T est supérieure à l'augmentation de la puissance à l'arbre de la turbine. Le même phénomène est observé pour le compresseur.

Vitesse de rotation de l'arbre turbocompresseur :

Il apparaît que les puissances thermiques transférées les plus élevées sont atteintes pour les basses vitesses de rotation. On note qu'une augmentation de la vitesse du turbocompresseur de 70kRPM à 170kRPM implique une diminution du transfert thermique moyen de 750W à 350W pour une température d'entrée turbine T_{03} de 773K (400W à 100W quand $T_{03} = 573K$). Dans le cas du compresseur, les transferts

de chaleur moyens passent de 250W à 140W (125W à 30W quand $T_{03} = 573K$). En fait, aux faibles vitesses de rotation, la puissance thermique évacuée de la turbine représente jusqu'à 100 % de la puissance à l'arbre (50 % dans le cas du compresseur). Toutefois, les transferts de chaleur représentent moins de 5 % de la puissance à l'arbre pour les vitesses de rotations les plus élevées. Cela signifie que tandis que les transferts de chaleur ont un fort impact sur les performances du turbocompresseur à faible régime, ces transferts ont un impact négligeable aux vitesses de rotation élevées.

Débit massique :

Les transferts de chaleur liés au compresseur dépendent du débit massique. Néanmoins, on notera que le rapport entre la puissance thermique échangée et la puissance à l'arbre au compresseur $\frac{Q_C}{\dot{W}_{Csh}}$ est indépendant du débit massique (voir la figure 7.13).

La dépendance des échanges thermiques à la turbine vis-à-vis des rapports de pression (indirectement du débit massique) est visible sur la figure 7.12. La dépendance est difficile à établir, car la gamme de rapport de pression et de débit couverte pour chaque iso-vitesse est étroite. On note néanmoins que l'évolution tend à devenir horizontale pour les valeurs les plus élevées de régime de rotation.

Géométrie turbine VGT :

Dans son rapport de thèse, Shaaban [118] a montré que la position VGT n'a aucun impact sur les transferts de chaleur vers le compresseur. La même étude a été réalisée ici pour le compresseur et la turbine : la position VGT a été fixée à 20 % et les résultats sont comparés aux résultats obtenus pour une ouverture de 100 % (voir figures 7.14 et 7.15). Il en ressort que les transferts de chaleur ne sont pratiquement pas affectés par la position d'ouverture turbine (la variation reste inférieure à 10 %). Il est difficile de préciser si cette variation est due à une variation des transferts thermiques où à des dispersions introduites par le modèle de perte par frottement dans les paliers. Toutefois, comme la variation de la position VGT n'a qu'un impact mineur sur les transferts thermiques, la position

4.3 Modélisation des transferts thermiques

Maintenant que les transferts de chaleur ont été étudiés, il est proposé de modéliser, que se soit en stabilisé ou en transitoire, l'impact des transferts de chaleur sur les performances de la turbomachine. Un modèle simple serait d'utiliser les cartographies de données créées lors de l'étude transfert de chaleur. Toutefois, il a été vu que les transferts de chaleur ont été identifiés dans des conditions particulières :

- Vitesse de rotation de l'arbre stabilisée.
- Températures stabilisées en amont et en aval des turbomachines.
- Température en entrée de la turbine supérieure à la température de l'huile, elle-même plus élevée que la température d'entrée du compresseur.

En conditions réelles, ces conditions ne seront pas nécessairement vérifiées. Par conséquent, la réutilisation des transferts de chaleur identifiés précédemment ne fourniront pas de résultats valides. Toutefois, les transferts de chaleur identifiés peuvent être utilisés comme une base d'apprentissage combinée à un modèle de transfert de chaleur. Il a été vu dans la section étude bibliographique qu'un modèle pertinent est basé sur la détermination des coefficients d'échange thermique. Dans sa thèse, Cormerais [26] a développé une approche intéressante pour modéliser les transferts de chaleur dans les turbocompresseurs. Cette approche est fondée sur l'analogie entre les coefficients de transfert thermique et les résistances électriques. Considérant un environnement isolé

mono-dimensionnel soumis à une différence de température ΔT , le transfert de chaleur Q est créé. A partir de l'analogie électrique, la résistance équivalente R est associée :

$$R = \frac{\Delta T}{Q}$$

Plus précisément, les résistances thermiques dans le cas des transferts convectifs et dans le cas des transferts par conduction sont exprimées dans l'équation. S se réfère à la surface d'échange thermique, H est le coefficient d'échange convectif, λ est la conductivité thermique.

$$\begin{aligned} R_{conv} &= \frac{1}{hS} \\ R_{cond} &= \frac{e}{\lambda S} \end{aligned}$$

Comme détaillé dans l'étude bibliographique, on admet que les transferts de chaleur dans le turbocompresseur sont unidimensionnels. En outre, on introduit le modèle de résistance thermiques du turbocompresseur. Le turbocompresseur est divisé en trois parties : le compresseur, le carter central et la turbine. Des transferts de chaleur par convection se produisent entre les écoulements et les carters des turbomachines. Ensuite, des transferts par conduction ont lieu entre les turbomachines et le carter central. Le débit d'huile est également pris en compte par des transferts de chaleur par convection. Il est rappelé que les expériences au banc d'essai ont été effectuées en utilisant un turbocompresseur isolé, donc aucune perte de chaleur vers l'air ambiant n'est considérée. En utilisant l'analogie avec la théorie de l'électricité, les lois de Kirchhoff sont introduites, ce qui permet de réduire le système à seulement trois résistances thermiques (Fig. 4.11).

Le système d'équations régissant les transferts de chaleur est décrit ci-dessous, avec T_{int} la température théorique du point central, qui se trouve à l'interface des trois résistances thermiques équivalentes. T_T est la température d'entrée turbine et T_O la température de l'huile avant l'entrée dans le carter du turbocompresseur. T_C est la température de sortie du compresseur calculée en utilisant les cartographies en conditions adiabatiques. En effet, il a été vu que les échanges de chaleur au compresseur se produisent en aval du rotor.

$$\begin{aligned} Q_C &= \frac{T_{int}-T_C}{R_C} \\ Q_T &= \frac{T_{int}-T_T}{R_T} \\ Q_O &= \frac{T_{int}-T_O}{R_O} \\ -Q_T &= Q_C + Q_T \end{aligned}$$

La combinaison de ces quatre équations permet de déterminer une expression mathématique de T_{int} :

$$T_{int} = \frac{\frac{T_T}{R_T} + \frac{T_O}{R_O} + \frac{T_C}{R_C}}{\frac{1}{R_T} + \frac{1}{R_O} + \frac{1}{R_C}}$$

En utilisant cette expression, il est possible d'exprimer les transferts thermiques sans introduire la température virtuelle T_{int} :

$$\begin{aligned} Q_C &= \frac{1}{1 + \frac{R_C}{R_T} + \frac{R_C}{R_O}} \left(\frac{T_C}{-R_T - R_O} + \frac{T_O}{R_O} + \frac{T_T}{R_T} \right) \\ Q_T &= \frac{1}{1 + \frac{R_T}{R_C} + \frac{R_T}{R_O}} \left(\frac{T_T}{-R_C - R_O} + \frac{T_O}{R_O} + \frac{T_C}{R_C} \right) \\ Q_O &= \frac{1}{1 + \frac{R_O}{R_C} + \frac{R_O}{R_T}} \left(\frac{T_O}{-R_C - R_T} + \frac{T_T}{R_T} + \frac{T_C}{R_C} \right) \end{aligned}$$

Ces équations montrent que chaque résistance thermique et chaque température du système a un impact sur l'équilibre thermique global du turbocompresseur. Ce système d'équations a une infinité de solutions pour R_C , R_T et R_O , en fonction de la valeur de T_{int} . T_{int} est une température théorique, déterminée dans le carter central, à l'interface des flux de chaleur de la turbine, du compresseur et de l'huile. Dans ce travail, T_{int} a été définie de la manière suivante :

$$T_{int} = \frac{T_C + T_O + T_T}{3}$$

Cette formule sera utilisée pour déterminer les valeurs de T_{int} , qui sont introduites dans le système d'équation précédent. Cela permet de déterminer les valeurs des résistances thermiques. Afin de valider cette approche, les résistances seront déterminées pour $T_T=773\text{K}$. Le modèle ainsi paramétré rejouera en aveugle les essais à 573K . Si les résultats obtenus sont en accord avec les mesures, il en sera déduit que le modèle est satisfaisant.

Dépendance des résistances thermiques :

Afin de construire un modèle de résistance thermique du turbocompresseur, il est nécessaire d'exprimer les dépendances des résistance thermique en fonction des paramètres physiques des turbomachines. Deux méthodes différentes ont été envisagées pour exprimer la résistance thermique en fonction des caractéristiques de débit :

1 - *corrélation du nombre de Nusselt* : Cette approche est très répandue dans l'étude des échanges de chaleur se produisant dans les flux de conduits ou d'échangeurs de chaleur. Elle est basés sur des équations physiques et des corrélations expérimentales. Toutefois, il a été montré dans l'étude bibliographique que, même dans le cas des flux simples, les corrélations Nusselt montrent de grandes disparités d'un auteur à un autre (jusqu'à 100 % de la différence [35]). Dans notre cas d'étude, l'écoulement est très complexe, ce qui conduit à une difficulté accrue pour identifier une corrélation du nombre de Nusselt. Cela résulte, dans la littérature, à une adaptation au cas par cas des formulations de corrélation. Les formulations obtenues sont souvent très complexes et tendent à s'éloigner du cadre des formulations physiques.

2 - *Construction d'une cartographie des résistances* : L'étude des corrélations via le nombre de Nusselt a montré que les coefficients de transfert de chaleur sont généralement exprimés en fonction du nombre de Reynolds. Il a été vu dans le développement de la théorie de similitude (annexe A) que les cartographies du compresseur et de la turbine sont tracées dans des repères respectant cette théorie. La théorie de similitude appliquée aux turbomachines implique la conservation des quantités suivantes :

- Nombre de Reynolds.
- Nombre de Mach.
- Triangle de vitesses du rotor.

Cela signifie que chaque point de fonctionnement exprimé dans le système de coordonnées corrigées des turbomachines est spécifique d'une condition d'écoulement donnée (Reynolds, Mach, triangle des vitesses). Par conséquent, il semble valide de représenter les résistances thermiques calculées pour le compresseur et la turbine dans leur repères respectifs (rapport de pression contre débit massique). En effet, ces cartographies relient implicitement les résistances thermiques aux conditions d'écoulement. Les résultats obtenus sont fournis sur la figure 7.18. A partir de ces tracés, on peut voir que dans ce système de coordonnées, les résistances thermiques ne dépendent pas de la température d'entrée turbine.

Il a été vu précédemment que la plage de fonctionnement du compresseur est entièrement couverte par les tests effectués. Toutefois, ce n'est pas le cas de la turbine, pour laquelle la plage de fonctionnement couverte est étroite. Ceci est problématique en régime transitoire : l'équilibre des puissances sur l'arbre n'est pas respecté, ce qui conduit à l'augmentation ou la diminution de la vitesse de rotation de l'arbre. Dans ce cas, la turbine n'opère pas nécessairement au sein de la plage de fonctionnement couverte lors des essais en stabilisé. Afin de surmonter ce problème, on a identifié une dépendance de la résistance thermique à la turbine vis-à-vis du débit massique. Cette dépendance est linéaire et cette propriété est utilisée afin de procéder à l'extrapolation des données (voir la figure 7.18).

Les valeurs de la résistance thermique liée au circuit d'huile sont tracées sur la figure 7.19. Il apparaît que leurs valeurs dépendent de la vitesse de l'arbre et de la température d'entrée turbine. D'après [59], [90] and [77], ces paramètres ont un effet couplé sur l'écoulement au sein du palier :

- Le débit d'huile est directement liée à la vitesse de rotation de l'arbre du turbocompresseur.
- La viscosité de l'huile dépend de la température de l'huile. Les pertes par frottement et le flux de chaleur à la turbine modifient la température de l'huile dans le roulement, et par conséquent la viscosité de l'huile.
- Le changement de la viscosité de l'huile influe directement sur l'excentricité de l'arbre dans le roulement, et par conséquent, les caractéristiques de l'écoulement d'huile.
- Le changement des caractéristiques du débit d'huile a une forte influence sur l'échange de chaleur relatif au circuit d'huile.

Afin de construire un débit d'huile valide du modèle d'échange thermique, il est donc nécessaire de prendre en compte les paramètres suivants : l'excentricité de l'arbre dans le roulement, l'impact de la chaleur sur la viscosité de l'huile, le débit massique d'huile. Ces paramètres interagissent les uns avec les autres, et il est donc nécessaire d'avoir accès à une grande base de données expérimentales afin de corrélérer chaque sous-modèle [59]. Dans notre cas, les données disponibles sont insuffisantes pour construire un tel modèle. Néanmoins, la température d'huile étant régulée à 360 K, une valeur similaire aux conditions réelles sur moteur, on utilisera directement les valeurs de résistance thermique relevées lors de nos essais, en fonction du régime de rotation (voir figure 7.19). La principale limitation de cette approche est qu'elle n'est valable que pour des températures d'entrée turbine comprises entre 573 et 773 K. Des tests supplémentaires ont été prévus afin d'élargir la zone de validité du modèle, mais les résultats n'ont pas pu être inclus à temps dans cette étude.

Part III

Gas Exchange processes through Flow Restrictions

Chapter 8

Literature review

8.1 Pipe flow governing equations

The amount of fresh air induced into the cylinder is the main parameter to be taken into account when developing the engine control laws. Today, the complexification of the automotive engine air system via the introduction of the exhaust gas recirculation loops leads to higher needs in terms of aerodynamics models accuracy. It is intended to perform a literature review of the aerodynamical models applied to the engine airpath and to identify the approach which appears to be the most suitable for the development of control laws. The aerodynamics models dedicated to the engine modeling can be divided into three categories :

- The mean-value or lump models.
- The models based on a 1 dimensional discretization of the air system.
- The models based on a multi-dimensional discretization of the air system.

The common point between the three methods is that they are based on the same fundamental equations and assumptions : firstly, the fluid is modeled as a continuous medium, satisfying the compressible ideal gas hypothesis. A more detailed analysis of the air modeling is available in appendix E. In order to describe the evolution of the flow, three fundamental principles are applied : the mass conservation, the energy conservation and the momentum conservation. These equations are developed below. In order to keep the developments as understandable and as simple as possible, the considered case is a 1D pipe flow of a compressible gas. If the variation of the pipe section is gradual, the fluid properties are approximately uniform across any cross-section, and the flow is said to be quasi-one-dimensional.

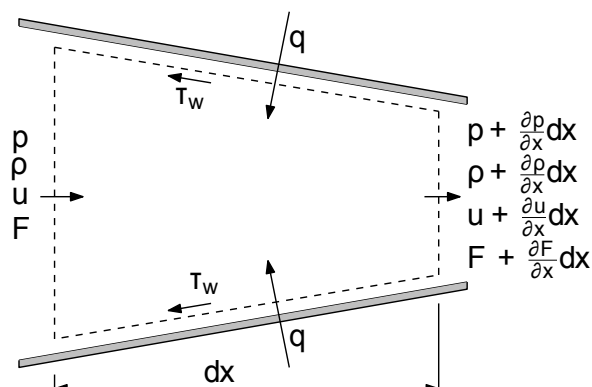


FIG. 8.1 – Control Surface for quasi-one-dimensional flow

On Fig. 8.1, an ideal compressible fluid at pressure p , of density ρ and of speed u runs through an infinitesimal length of a pipe of section F . The pipe is subject to heat exchanges q and to wall shear stress τ_w . Each parameter of the fluid undergoes a variation through the infinitesimal pipe length. These variations are governed by the three following conservation laws :

Mass flow rate equation

The rate of change of mass within the control volume is equal to the net mass flow rate through the element. After re-arrangement in a conservation law form :

$$\frac{\partial \rho}{\partial t} + \frac{\partial \rho u}{\partial x} + \frac{\rho u}{F} \frac{dF}{dx} = 0 \quad (8.1)$$

Momentum equation

The rate of change of momentum within the control volume is equal to the sum of forces applied on the control volume. In order to model the friction between the flow and the wall, a shear stress τ_w , opposed to the flow, is introduced. Expressing the shear stress in terms of the pipe wall friction f gives $\tau_w = \frac{1}{2}\rho u^2 f$. p_0 is the total pressure, which is linked to the static pressure by the following relationship : $p_0 = p + \frac{1}{2}\rho u^2$.

$$\frac{\partial \rho u}{\partial t} + \frac{\partial p_0}{\partial x} + \frac{\rho u^2}{F} \frac{dF}{dx} + \rho G = 0 \quad (8.2)$$

$$G = \frac{1}{2}u|u|f \frac{4}{D} \quad (8.3)$$

Energy equation

The energy equation is derived from the first law of thermodynamics applied to the control volume. Heat transfer per unit mass of gas q has been introduced to take into account the heat transfer between the pipe and the fluid. h_0 is the specific stagnation enthalpy of the fluid, which is linked to the specific enthalpy of the fluid by the following relationship : $h_0 = h + \frac{1}{2}u^2$. e_0 is the specific stagnation energy of the fluid, which is linked to the specific energy of the fluid by the following relationship : $e_0 = e + \frac{1}{2}u^2$.

$$\frac{\partial \rho e_0}{\partial t} + \frac{\partial \rho u h_0}{\partial x} + \frac{\rho u h_0}{F} \frac{dF}{dx} - \rho q = 0 \quad (8.4)$$

These equations dictate the behavior of a compressible non-viscous 1D flow and are referred as the Euler equations. Heat exchanges and wall friction are taken into account via sub-models, and can be directly included in the equations. Even though some pipe section-change terms have been introduced, high area discontinuities cannot be taken into account as the $\frac{dF}{dx}$ term will introduce numerical errors. It is also possible to take into account the transport of species, via the introduction of additional equations. In the case where N species are to be tracked, $N-1$ species continuity equations must be added to the Euler equations. $Y_j = \frac{m_j}{m}$ is the mass fraction of the control volume for the species j . This approach neglects the diffusion the chemical reaction within the flow.

$$\frac{\partial \rho Y_j}{\partial t} + \frac{\partial \rho u Y_j}{\partial x} + \frac{\rho u Y_j}{F} \frac{dF}{dx} - \rho q = 0, \quad j = 1..N-1 \quad (8.5)$$

8.2 Pipe flow governing equations resolution

8.2.1 Mean-value models

Mean-value models (MVM) have a complexity that provides a good basis for the control and observers design. They are indeed usually formulated as non-linear ordinary differential equations, which provides a model complexity suitable for the control laws development and which allows to run simulations faster than real-time. In the case of MVM applied to the engine, the three governing equations are modified in order to simplify their resolution : the heat exchange, the wall friction and the change of section terms are not considered anymore. The effect kinetic energy is neglected, which means that the speed is neglected : $u = 0$. This leads to the following simplifications : $h_0 = h$, $e_0 = e$ and $p_0 = p$. Neglecting the speed effect has also an impact on the derivative definition : considering a moving particulate of the fluid, its position at a given time t is provided by its abscissa (x). The particulate density (for example) is therefore expressed as : $\rho(x, t) = \rho(x(t), t)$. Therefore, the total derivation of the density is expressed as follows :

$$\frac{d\rho}{dt} = \frac{\partial\rho}{\partial t} + \frac{\partial\rho}{\partial x} \frac{dx}{dt} \quad (8.6)$$

In the case where the speed effect is neglected, one gets : $u = \frac{dx}{dt} = 0$, and the total derivation is consequently equal to the partial derivation : $\frac{d\rho}{dt} = \frac{\partial\rho}{\partial t}$. This means that neglecting the speed effect allows to use some non-linear ordinary differential equations rather than the original partial differential equations. Consequently, the new system of equation will be less complex and less computationally expensive to resolve. Introducing the volume of the isolated system ($V = dx F$) allows to express the mass of the gas within the isolated system : $m = \rho V$. Coupling the previous developments to the mass flow rate expression ($Qm = \rho u F$) leads to the following system of equations, where $U_{int} = m C_v T$ is the internal energy of the control volume :

$$\frac{dm}{dt} + \frac{dQm}{dx} = 0 \quad (8.7)$$

$$\frac{dQm}{dt} + \frac{dpF}{dx} = 0 \quad (8.8)$$

$$\frac{dU_{int}}{dt} + \frac{dQmh}{dx} = 0 \quad (8.9)$$

This system of equation is based on a quasi-one-dimensional hypothesis, and therefore cannot take into account the discontinuities encountered in the engines : throttles, filters, valves, turbomachines. Therefore, the general modeling methodology applied is to divide the system into components and then defining boundaries and interactions using physical and thermodynamical equations. The components are arranged according to a scheme where control volumes are placed in series with flow restrictions (throttle, filters etc). An example is shown on Fig. 8.2. At each of the two boundaries of a control volume, there is a boundary condition which models the behavior of the corresponding flow restriction. The corresponding models will be developed later in this literature review. The accuracy of the global engine model will be extremely dependent upon the accuracy of the boundary conditions, as they impose the transport of mass and energy.

The mean value engine modeling is now a widely used approach, which allows an efficient development of the engine control laws and the associated observers. Some example of mean-value model building and of the development of the associated sub-models can be found in the following papers by Talon [122], [123], Guzzella [57] et van Nieuwstadt [129]. Even though these papers illustrate that the mean-value approach applied to the engine airpath can provide good results, it appears that neglecting the speed effect is a strong limitation, which has an impact on the results quality :

- The pressure wave effects cannot be taken into account. This can be an issue as the flow within the engine air system is widely impacted by the pressure waves caused by the valves opening/closure.
- Some error is systematically made, as the total quantities are assumed to be equal to the static quantities. Therefore, some non-negligible errors are made when the actual system flow speeds are high.
- Neglecting the fluid particulate speed does not allow to take into account the transport of the species. This point is particularly an issue when it is intended to deal with the EGR modeling. Indeed, it is necessary to take into account the transport of the exhaust gas towards the admission circuit.

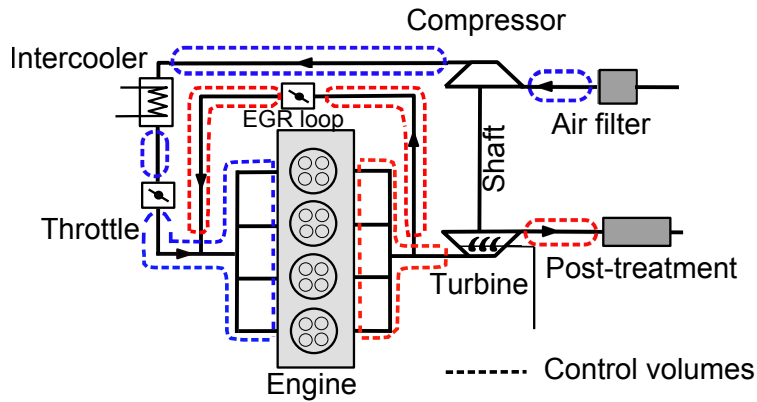


FIG. 8.2 – Example of equivalent-volumes discretization of a turbocharged engine with an high pressure EGR loop.

8.2.2 1-D spatial discretization schemes

The mean-value models introduced a simplification of the governing equations in order to solve them. However, it is generally not possible to get analytical solutions for the non-simplified set of equations 8.1, 8.2 and 8.4. Consequently, numerical techniques had to be developed. These techniques are based on the formulation of the governing equations as a system of hyperbolic equations [139]. Governing equations (8.1), (8.2), (8.4) can be rewritten in a conservative vectorial formulation Eq. (8.10). $W = [\rho, \rho u, \rho e_0]^T$ is the state vector of conservatives variables : mass, momentum and total energy. $F_{vec}(W) = [\rho u, \rho u^2 + p, \rho u h_0]^T$ is the flux vector. Vector $C(W)$ is the correction vector. It takes into account section variation, pipe wall friction and wall heat transfer.

$$\frac{\partial W}{\partial t} + \frac{\partial F_{vec}(W)}{\partial x} + C(W) = 0 \quad (8.10)$$

$$C(W) = \begin{bmatrix} \rho u \\ \rho u^2 + p \\ \rho u h_0 \end{bmatrix} \frac{d(\ln F)}{dx} + \begin{bmatrix} 0 \\ \rho G \\ -\rho q \end{bmatrix} \quad (8.11)$$

In the case where $C(W)=0$ (homentropic flow), it is possible to identify the conservation of three characteristics along the flow [139], [76]. The first developments of this method are from Riemann [112]. This is referred as the Method of Characteristics (MOC) ; its basics developments are shown in appendix C. The MOC allows to solve directly the homentropic governing equations. Additional developments allow to develop the MOC in the case of non-homentropic flows [139]. However, the MOC is a non-conservative scheme and therefore cannot deal with the shock wave phenomenon. Additional work by Rankine [108] and Hugoniot [64] allowed to introduce the shock and the surface discontinuity relationships into the MOC. Taking into

account the shocks phenomenon is crucial, as this phenomenon occurs frequently in flows, especially in the case of engine air system. The MOC was first solved using graphical methods, but work on the theory of numerical methods by von Neumann, Courant, Friedrichs, Richtmeyer and Lax [130], [131], [28], [29], [73] allowed to define the main stability, convergence and accuracy criteria of the finite difference schemes applied to aerodynamics. The method of characteristics is a first-order accuracy scheme, and therefore tends to diffuse the solutions at discontinuities. Additionally, as it does not naturally take into account the discontinuity phenomenon, a specific treatment (Rankine-Hugoniot relationships) needs to be implemented.

Nevertheless, the MOC allowed to develop the basis and the theory which have been used to develop shock-capturing schemes and higher-order spatial accuracy schemes. One of the most widespread numerical scheme is due to Lax and Wendroff [74], who developed a second-order spatial accuracy, shock capturing scheme. This numerical scheme inspired numerous variants (MacCormack [80], Rubin/Burstein [114] and Lerat/Peyret). Lerat and Peyret [75] have defined the W_β^α classification for these schemes (see appendix D). The main drawback of these schemes is that they are naturally oscillating through discontinuities. The development of flux limiters allowed to get rid of these oscillations. These flux limiters reduce locally the contribution of the second-order accuracy terms in the region of steep gradients. Therefore, the solution has a local reduced accuracy, but do not oscillate. These schemes have been developed based on an original work by Godunov [51], which solved the Euler's equation by resolving local Riemann (shock tube) problems. Godunov's scheme did not produce oscillations at discontinuities, but was only a first-order accurate scheme and required high computational time. Additional work by van Leer [126], [127], [128], Roe [113] and Harten [60] lead to the definition of the monotonicity and of the Total Variation Diminishing (TVD) criteria which allowed the development of high-resolution shock capturing schemes based on the approximated Riemann solvers. The two-steps Lax-Wendroff and McCormack schemes coupled to TVD schemes are today very commonly used in the engine simulation field. The Lax-Wendroff + TVD scheme has been compared to the MOC on some engine modeling applications [97], [78], [144]. It appears that the LW-TVD scheme provides significant improvement of the solutions accuracy, mainly at mid-high rotational speeds, which correspond to the higher frequencies of the pulses.

The Conservation Element- Solution Element (CE-SE) numerical scheme developed by Chang et al. [20], [21] has also been successfully tested in the case of engine applications. According to Onorati[98], this method provides a slight accuracy improvement compared to LW+TVD, while reducing the calculation time by approximately 20%. Finite element methods have also been introduced, leading however to an unacceptable calculation time as these methods are based on Riemann solvers [98].

The 1-dimensional simulation of engine pipe flow allows to take into account the pressure waves of the IC engines. The associated numerical schemes allow simple shock-capturing and the transport of the species. These numerical schemes have been tested in many application cases and it therefore can be said that such schemes have reached a matured level, with enough feedback to be qualified as accurate and reliable. Nevertheless, these numerical schemes are based on the Euler equations, which embedded the hypothesis of quasi one-dimensional flow. Therefore, as in the case of the previously developed control volume models, the boundary conditions applied to the pipe will have a strong impact on the final solution. Additionally, it will be seen later in this literature review that the numerical interaction between the pipe numerical scheme and the boundary can still be an issue. Finally, the 1d spacial discretized scheme generally run 30 to 100 times longer than real time, which can be an issue when developing control laws, as many simulations need to be run in order to optimize the control laws.

8.2.3 multi-D spatial discretization schemes

In order to get rid of the limiting quasi one-dimensional hypothesis, it is possible to express the governing equations in a multi-dimensional formulation (2 or 3 spacial dimensions). It is possible to include directly the viscous effect of the fluid : the Navier-Stokes equations are developed below, for the three dimensional case (x, y, z) , in the absence of body forces and external heat transfers :

$$\frac{\partial W}{\partial t} + \frac{\partial F(W)}{\partial x} + \frac{\partial G(W)}{\partial y} + \frac{\partial H(W)}{\partial z} = 0 \quad (8.12)$$

$$W = \begin{bmatrix} \rho \\ \rho u \\ \rho v \\ \rho w \\ \rho e_0 \end{bmatrix} \quad F_{vec}(W) = \begin{bmatrix} \rho u \\ \rho u^2 + p - \tau_{xx} \\ \rho uv - \tau_{xy} \\ \rho uw - \tau_{xz} \\ \rho uh_0 - u\tau_{xx} - v\tau_{xy} - w\tau_{xz} + q_x \end{bmatrix} \quad (8.13)$$

$$G_{vec}(W) = \begin{bmatrix} \rho v \\ \rho uv - \tau_{xy} \\ \rho v^2 + p - \tau_{yy} \\ \rho uw - \tau_{yz} \\ \rho vh_0 - u\tau_{xx} - v\tau_{xy} - w\tau_{xz} + q_y \end{bmatrix} \quad H_{vec}(W) = \begin{bmatrix} \rho w \\ \rho uw - \tau_{xz} \\ \rho vw - \tau_{yz} \\ \rho w^2 + p - \tau_{zz} \\ \rho wh_0 - u\tau_{xx} - v\tau_{xy} - w\tau_{xz} + q_z \end{bmatrix} \quad (8.14)$$

$\tau_{i,j}$ are the components of the viscous stress tensor. The viscous shear stress is due to the fluid viscosity and the difference of the flow speed along each direction. The components of the viscous stress tensor are expressed as :

$$\begin{aligned} \tau_{xx} &= \frac{2}{3}\mu \left(2\frac{\partial u}{\partial x} - \frac{\partial v}{\partial y} - \frac{\partial w}{\partial z} \right) & \tau_{yy} &= \frac{2}{3}\mu \left(2\frac{\partial v}{\partial y} - \frac{\partial u}{\partial x} - \frac{\partial w}{\partial z} \right) \\ \tau_{zz} &= \frac{2}{3}\mu \left(2\frac{\partial w}{\partial z} - \frac{\partial u}{\partial x} - \frac{\partial v}{\partial y} \right) & \tau_{xy} &= \mu \left(\frac{\partial u}{\partial y} + \frac{\partial v}{\partial x} \right) \\ \tau_{xz} &= \mu \left(\frac{\partial w}{\partial x} + \frac{\partial u}{\partial z} \right) & \tau_{yz} &= \mu \left(\frac{\partial w}{\partial y} + \frac{\partial v}{\partial z} \right) \end{aligned} \quad (8.15)$$

This system of equations can be solved using the same numerical techniques as developed for the 1-D case, but expressed in a multi-dimensional formulation. The main advantage of this approach is that it is possible to model the part of the engine air system which do not comply with the quasi one-dimensional flow hypothesis (i.e. the plenum, sudden area changes...). However, it appears that some major difficulties are encountered when developing multi-dimensional CFD codes :

- The boundary layer (near-wall flow) is complex to take into account and will potentially require dedicated numerical treatments [45].
- The flow in the engine air system is often turbulent (i.e. at the valve), and specific turbulence models need to be implemented [142], [143], [37], [125].
- The multi-dimensional computation require a meshing of the considered volumes. This step can be very long to achieve, as the quality of the mesh has a strong impact on the final results.
- The modeling of some components such as the valve will require a moving mesh, which has strong impact on the calculation time and the result accuracy.
- The calculation time tends to be large (1000 to 10000 times longer than real time), therefore not applicable to the control laws development.

In order to reduce the calculation time, multi-dimensional CFD calculations have been used in some interesting approaches which allowed to combine the advantages of the 1-D and of the multi-D numerical schemes. It is indeed possible to simulate the engine air system using 1-D methods and to use the multi-dimensional only where it is necessary. The commercial engine simulation code Gt-power [54] allows to

perform such hybrid simulations. Several papers have highlighted the advantages of this method in terms of accuracy and calculation time : Sinclair [115], Bozza [14] and Onorati [100] have illustrated this method advantages in the case of the engine global operation. A lot of work on the after-treatment systems and their radiated noise has been performed using 1D-multiD models (Onorati [99], [100], Montenegro [91], [92], Peters [103]) with significant improvement of the pressure waves estimation within these complex geometries. The coupling of 1D pipe systems to a 3D cylinder flow and combustion has also been successfully performed by Macek et al. [84], [85].

Even though these methods are interesting, the reduction of the calculation time does not appear to be sufficient to deal with the development of control laws. Additionally, when comparative studies are performed in these papers, it appears that the 1D calculation results stay in good agreement with the experimental results, even though the accuracy is decreased compared to 1D-multiD methods.

Pipe flow governing equations and associated numerical schemes : main points

- The governing equations of the pipe flow are based on the conservation of mass, energy and momentum. Additional hypotheses or spacial developments allow to create three categories for the modeling of pipe flows : 1- the mean-value models, 2- the 1d-spacial discretization schemes and 3- the multi-dimensional discretization schemes.
- The mean-value models are an excellent basis for the real-time modeling of the engine dedicated to the development of control-laws or observers. However, they are very restrictive regarding the pressure waves and the species advection impact on the engine behavior. Such phenomena are crucial for controlling low-pressure EGR loops. Additionally, the transfers of mass and energy are integrally imposed by the boundary conditions.
- The 1D spatial discretization schemes have undergone many developments in the last 40 years, which allowed to reach stratifying level of accuracy when applied to the ICE. However, theses numerical schemes are still extremely dependent upon the boundary conditions which are applied.
- Multi-dimensional aerodynamic resolution schemes allow to deal with non-quasi-dimensional flows. They are consequently less dependent on the boundary conditions, as flow restrictions such as plenums and post-treatment devices have been successfully modeled via these techniques. 1-D / multi-D hybrid numerical schemes have also been developed, allowing to combine the accuracy of the multi-dimensional accuracy to the calculation time of the one-dimensional methods. However, even in this case, the calculation times remain too high to deal with the development of the engine control laws.
- Finally, the most adequate modeling techniques in order to develop the engine control / command devices remain the mean-value and one-dimensional numerical schemes. However, these methods require the development of dedicated boundary conditions to be representative of the real engine behavior. Additionally, the calculation time of the 1D simulations remain in the average 100 times higher than real time, and specific attention should be paid to reduce as much as possible the associated computational time.

8.3 ICE boundary conditions

It has been seen that the boundary conditions play a major role in the simulation of the ICE air systems, as they dictate the mass and the energy flows. From the literature review, it appears that the MOC is a cornerstone of the establishment of the boundary conditions. Indeed, it allows, via a flux of information, to link the boundary to the pipe flow. This section dedicated to the aerodynamical boundary conditions of the ICE engines will be divided into two parts : At first, the derivation of the MOC in order to comply with the

1D boundary conditions requirements will be detailed. Secondly, the main hypotheses and equations of the boundary conditions will be introduced.

8.3.1 The MOC applied to boundary conditions

The boundary condition is placed at one end of the calculation region (in our case, the discretized 1D pipe flow). It is necessary to distinguish the inflow case from the outflow case. In the inflow case, the flow comes from the outside environment into the pipe. In the outflow case, the flow exits the pipe to the outside environment.

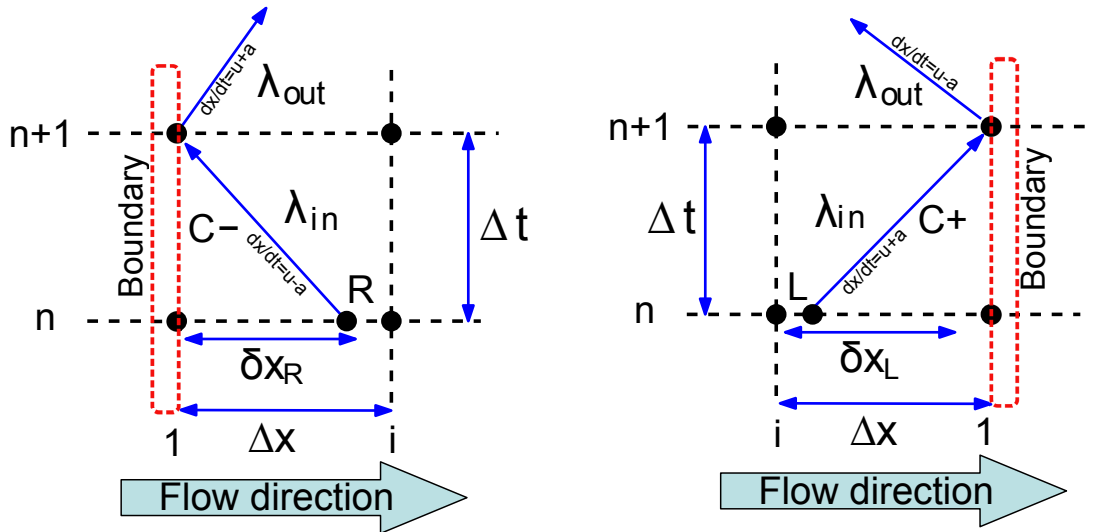


FIG. 8.3 – Representation of the homentropic characteristics : Inflow (left) and Outflow (right).

In this subsection, application of the method of characteristics to inflow valve boundary condition is reminded. Benson's notation will be used [5], as seen on Fig. 8.3. $C-$ (resp. $C+$) is the characteristic line incoming to the boundary in the inflow case (resp. outflow). λ_{in} is the Riemann variable incident to the boundary, and λ_{out} is the reflected Riemann variable at boundary. 1 is the spatial index of the node where the boundary conditions are solved. i is the spatial index of the node in the pipe which is the closest to the boundary condition node 1 .

In the case of boundary conditions, the homentropic flow assumption means that : 1- gas located in the boundary node of the pipe is always at the same entropy level than the outside environment gas. 2- There is no entropy creation through the boundary. These ideals conditions are almost never honored on a real flow, thus an entropy correction for non-homentropic flow is needed and will be introduced.

Homentropic inflow boundary condition

If the flow is assumed to be homentropic, one can use the incident characteristic conservation along $C-$:

$$\lambda_{in} = a_1^{n+1} - \frac{\gamma - 1}{2} u_1^{n+1} = a_R^n - \frac{\gamma - 1}{2} u_R^n \quad (8.16)$$

The thermodynamic state of the gas located at mesh R is determined by interpolation with the Courant, Isaacson, Rees (CIR) method [29], [139] between nodes (1) and (i) at step time (n) :

$$\frac{\delta x_R}{\Delta x} = \frac{-[u_1^n - a_1^n]}{\frac{\Delta x}{\Delta t} + (u_i^n - u_1^n) - (a_i^n - a_1^n)} \quad (8.17)$$

$$u_R^n = u_1^n + \frac{\delta x_R}{\Delta x} (u_i^n - u_1^n) \quad (8.18)$$

$$a_R^n = a_1^n + \frac{\delta x_R}{\Delta x} (a_i^n - a_1^n) \quad (8.19)$$

Homentropic outflow boundary condition

The same development can be applied to the outflow case : the incident characteristic conservation along $C+$ is used.

$$\lambda_{in} = a_1^{n+1} + \frac{\gamma - 1}{2} u_1^{n+1} = a_L^n + \frac{\gamma - 1}{2} u_L^n \quad (8.20)$$

The CIR method is then used to determine the state of the gas located at mesh L :

$$\frac{\delta x_L}{\Delta x} = \frac{[u_1^n + a_1^n]}{\frac{\Delta x}{\Delta t} + (u_1^n - u_i^n) + (a_1^n - a_i^n)} \quad (8.21)$$

$$u_L^n = u_1^n - \frac{\delta x_L}{\Delta x} (u_1^n - u_i^n) \quad (8.22)$$

$$a_L^n = a_1^n - \frac{\delta x_L}{\Delta x} (a_1^n - a_i^n) \quad (8.23)$$

Entropy correction for non homentropic flow

In the case where the evolution of the flow at the boundary is non-homentropic, the MOC developed under this assumption must be modified to take into account the change of entropy of the gas. This method has been introduced by Benson [5]. Its development is similar in the case of inflow or outflow. Figures 8.4 displays Benson's notation for an entropy correction algorithm : a_A is the 'entropy' level of gas at pressure p , with sound speed a . a_A is determined by an isentropic contraction from p to the reference pressure p_{ref} . A is the non dimensional speed of sound $\frac{a}{a_{ref}}$ and A_A the non dimensional entropy level $\frac{a_A}{a_{ref}}$. a_{ref} is a, arbitrary reference state, sometimes taken as the outside gas conditions.

On Fig. 8.4, one considers that the incident Riemann variable λ_{in} travels on the incident characteristic from time step n (point P) to time step $n + 1$ (point P'). In the case where there is some entropy creation between point P and point P', the Riemann variable is not invariant anymore. Therefore, it is necessary to make the distinction between the Riemann variable at time step n and the Riemann variable at time step $n + 1$. $\lambda_{in,c}$ is the Riemann variable at time step $n + 1$ and includes the change of entropy, while $\lambda_{in,n}$ is the Riemann variable at time step n :

$$\lambda_{in,c} = \lambda_{in,n} + \delta(\lambda_{in}) \quad (8.24)$$

Determining the entropy level a_A of the gas via an isentropic contraction from a reference state gives (Figure 8.4) :

$$\left(\frac{p}{p_{ref}} \right)^{\frac{2\gamma}{\gamma-1}} = \frac{a}{a_A} = \frac{A}{A_A} \quad (8.25)$$

$$\frac{\rho}{\rho_A} = \left(\frac{p}{p_{ref}} \right)^{\frac{1}{\gamma}} \quad (8.26)$$

Differentiation and re-arrangement of Eq. (8.25) and Eq. (8.26) gives :

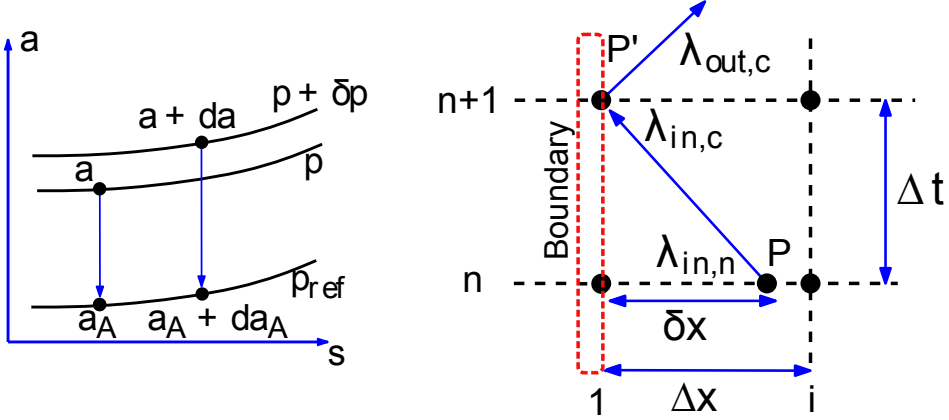


FIG. 8.4 – Benson entropy level definition (left). Non-homentropic Riemann variable definition (right).

$$\frac{d\rho}{\rho} = \frac{d\rho_A}{\rho_A} + \frac{1}{\gamma} \frac{dp}{p} \quad (8.27)$$

$$\frac{dp}{p} = \frac{2\gamma}{\gamma - 1} \left[\frac{da}{a} - \frac{da_A}{a_A} \right] \quad (8.28)$$

Along the $C-$ characteristic line, without section change, heat transfers and wall friction, rearrangement of governing equations (8.1), (8.2), (8.4) gives :

$$\frac{dp}{\rho a} - du = 0 \quad (8.29)$$

Re-arrangement of Eq. (8.27), Eq. (8.28) and Eq. (8.29) gives :

$$dA - A \frac{dA_A}{A_A} - \frac{\gamma - 1}{2} dU = 0 \quad (8.30)$$

This last equation can be rewritten :

$$d\lambda = A \frac{dA_A}{A_A} \quad (8.31)$$

Eq. (8.31) gives the change of Riemann variable along its characteristic line due to a change of entropy level. Eq. (8.31) will be used as keystone for entropy correction at boundary, as depicted in Fig. 8.4. The entropy level at mesh P' differs from the entropy level of gas entering the boundary. $\lambda_{in,n}$ is the Riemann variable, A_{An} is the non dimensional entropy level at mesh P . These two quantities are known at a given step time. $\lambda_{in,c}$ is the corrected Riemann Variable, A_{Ac} is the corrected non dimensional entropy level and $A_{P'}$ is the non dimensional speed of sound at mesh P' , when inflow entropy gradient is taken into account. These three quantities are unknown, and have to be determined by an iterative process based on Eq. (8.31). With this notations Eq. (8.31) becomes :

$$d\lambda \simeq \lambda_{in,c} - \lambda_{in,n} = A_{P'} \frac{A_{Ac} - A_{An}}{A_{Ac}} \quad (8.32)$$

During the iterative process proposed by Benson [5], the value of $\lambda_{in,n}$ and A_{An} are maintained constant. At first iterative step , the initial value of $\lambda_{in,c}$ is taken as $\lambda_{in,n}$ and $A_{P'}$ is computed with the value of the

previous time step. $\lambda_{in,c}$ is then used by the boundary condition to determine thermodynamic state at pipe entering. Then new values of A_{Ac} and $A_{P'}$ are computed. Then a new step begins : $\lambda_{in,c}$ is computed :

$$\lambda_{in,c} = \lambda_{in,n} + A_{P'} \frac{A_{Ac} - A_{An}}{A_{Ac}} \quad (8.33)$$

The new value of $\lambda_{in,c}$ is used by boundary condition to determine the corrected thermodynamic state at pipe entering, and new values of A_{Ac} and $A_{P'}$ are computed, etc. The processus stops when $\lambda_{in,c}$ is within the desired tolerance.

Benson's entropy correction iterative scheme

It has been seen that the entropy correction of the MOC requires an iterative scheme, due to the occurrence between $\lambda_{in,c}$ and A_{Ac} . This iterative scheme is generally not detailed in the literature paper, and one must go back to the original formulation by Benson [4] to find explicitly the development of the iterative process to converge Eq.8.33. This is an iterative loop based on the entropy level A_{Ac} .

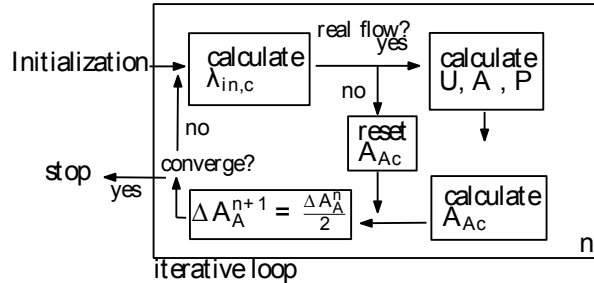


FIG. 8.5 – Schematic representation of Benson's MOC iterative scheme

At each step of the convergence loop, the entropy level is re-evaluated using : $A_{Ac}^{n+1} = A_{Ac}^n + \Delta A_A^n$. ΔA_A is initialized at the following value : $\frac{A_c - A_{Ais}}{2}$ where A_c and A_{Ais} are respectively the sound speed value and the isentropic entropy level of the outside gas. Once A_{Ac} is calculated, λ_{inc} is known and this allows to calculate U, A and subsequently P. The convergence of the iterative loop is governed by the term ΔA_A^n . At each time step, it is arbitrarily divided by two. Therefore, there is no adaptation of the convergence term regarding the error. This is the reason why the convergence loop can provide unreal flow conditions. In this case, the calculation loop is re-initialized, excepting the convergence term ΔA_A^n which is divided by two. In other words, the convergence term is initialized to a high value (high convergence speed), and if this provides unreal flow condition, the convergence term is decreased (lower convergence speed) and the convergence loop is re-initialized.

Therefore, it appears that the convergence scheme applied to the MOC is not optimal in terms of convergence speed. Indeed, in the case where unreal flow condition is met too often, the convergence term will be drastically decreased, which leads to long iteration time. After having implemented Benson's numerical scheme to model an exhaust valve, Brejaud [10] identified some cases where the algorithm did not allow to converge. Theoretically, implementing a more competitive iterative scheme, such as the Newton-Raphson algorithm, would improve the convergence speed, but such an approach has never been found in the literature review performed here.

MOC applied to boundary conditions : main points

- The MOC is widely used to deal with the boundary conditions problem, as it allows to transport some information between the 1-D discretized pipe schemes and the boundary condition.
- The initial developments of the method of characteristics have been achieved under the assumption of homentropic flow. This hypothesis is almost never satisfied under real conditions, which led to the derivation of this method for non-homentropic flows.
- Benson managed to produce a mathematically rigorous approach to deal with the non-homentropicity of the MOC. The main drawback of his approach is that it implies the resolution of an iterative loop. Benson proposed an iterative loop which is far from being optimal in terms of calculation time.
- Well-known convergence techniques (i.e. Newton-Raphson) are widely used today to converge iterative numerical schemes. However, no paper has been found to introduce such techniques to solve the entropy correction loop.

8.3.2 Boundary conditions equations and hypotheses

Three conditions are required to compute the flow variables (pressure, density, speed) at the boundary. The previously developed MOC allows to get one incident condition from the inside of the pipe. It is necessary to get two other conditions to solve the boundary problem. Generally, the boundary conditions are based on the Euler governing equations adapted to the steady-flow model. Additionally, the heat exchange and wall friction terms are removed. This leads to the following system of equations, where Eq. 8.34 is the mass conservation, Eq. 8.35 is the energy conservation and Eq. 8.36 is the momentum conservation. These equations express the conservation between state 1 and state 2 :

$$\rho_1 u_1 F_1 = \rho_2 u_2 F_2 \quad (8.34)$$

$$a_1^2 + \frac{\gamma - 1}{2} u_1^2 = a_2^2 + \frac{\gamma - 1}{2} u_2^2 \quad (8.35)$$

$$(p_1 + \rho_1 u_1^2) F_1 = (p_2 + \rho_2 u_2^2) F_2 \quad (8.36)$$

In this section, the main equations and hypotheses introduced to solve the boundary conditions found in the ICE will be introduced. However, the equations won't be developed, as they can be easily found in the referenced papers, and as most of the boundary equations will be re-developed later in the manuscript. For now, the following notation is introduced : [mass_{1/2}, energy_{1/2}, momentum_{1/2}] must be understood as a system of steady-flow equations (mass , energy and momentum conservation) written between nodes 1 and 2.

1- Open-end

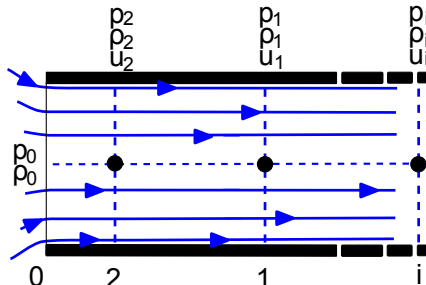


FIG. 8.6 – Schematic representation of the open-end inflow boundary condition

The inflow and outflow open-end boundary conditions are generally processed in a very similar way. A schematic representation of this kind of boundary condition is shown on Fig. 8.6 in the case of inflow. The outflow case would be represented in a similar way, but with the flow exiting the pipe. The index 1 represents the node where the boundary condition is solved. Index i is the node of the discretized pipe closest to the boundary condition. Index 2 represent a virtual node which is sometimes considered by some authors to allow the boundary equations resolution.

Most of times, a steady flow assumption is introduced and leads to a simple boundary condition for the open-end inflow : as long as the flow is subsonic, the pressures at the entry of the pipe and in the external region are equal ($p_0 = p_1$). This constant pressure condition is added to the conservation of energy between the stagnation state 0 and the boundary condition state 1. Along with the incident characteristic, this leads to the following system of 3 equations which allows to solve the boundary problem : [$p_0 = p_1$, $\text{energy}_{0/1}$, MOC]. The developments of this boundary condition are detailed in [5] or in [139]. The application of this boundary condition has been validated and provides satisfying results, even when compared to multi-D schemes [125], and without introducing any corrective term. Additional accuracy has been recently provided to this boundary condition by considering a 'lag' time in the establishment of the flow at the boundary by the mean of a Fourier analysis [105].

Some authors [17], [81], [72], [19] considered that the $p_0 = p_1$ assumption is not realistic, given that some recirculation vortexes can be seen at the entry or the exit of the pipe for the open-end boundaries. This phenomenon is referred as 'vena contracta'. In order to get rid of the constant pressure assumption, a virtual node 2 is introduced in order to solve the boundary equations. Now, these are 6 unknown quantities which must be determined (pressure, speed and density at the 2 nodes). The following equations are introduced : between the exterior of the pipe 0 and the node 2, the isentropic relationship and the energy conservation are introduced. The conservation of mass, energy and momentum is then written between the nodes 1 and 2. Finally, the MOC provides the last equation. This leads to the following system of equation : [$\text{isentropic}_{0/2}$, $\text{energy}_{0/2}$, $\text{mass}_{1/2}$, $\text{energy}_{1/2}$, $\text{momentum}_{1/2}$, MOC]. This method, when directly used, provides results which are not in good agreement with measurements. It is necessary to correct the results by the mean of experimental corrective coefficients, which are applied on the mass conservation equation written between nodes 1 and 2. This coefficient simulates the loss of flow area due to the vena contracta. To conclude, both methods achieve satisfying results. Nevertheless, the first method is more simple and does not require the determination of corrective experimental coefficients.

2- Inflow partially open-end

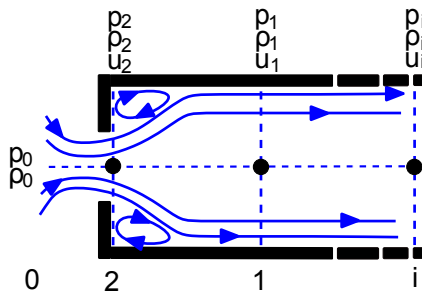


FIG. 8.7 – Schematic representation of the partially open-end inflow boundary condition

In this subsection, equations and assumptions from the literature partially open-end inflow models are developed. These models are also used to model the engine inflow valves. The control volume is shown on figure 8.7 : the gas enters the pipe as a jet of cross-sectional area F_2 . It then expands to occupy the full bore at plane 1. The isolated system is located between planes 1 and 2. There are 6 unknown quantities (pressure, density, velocity at 1 and 2), so six relations are needed. The distinction is made between the subsonic case

and the sonic case :

Subsonic case

Two main models have been developed in the case of a flow entering a pipe via a partially open-end : a constant pressure model and a sudden-enlargement model. The fundamental work which allowed is due to Jenny [67], and most of his work is detailed in [5] and in [139]. The theoretical basis of both models is very similar : they are based on the isentropic flow assumption and on the energy conservation between node 2 and the exterior 0. The conservation of mass and energy is used between nodes 2 and 1. The MOC provides a fifth equation. This is a last equation which differentiates the two models :

- Constant pressure model : In this case, the pressure is assumed to be the same at nodes 1 and 2. Therefore, the system of equations which allows to solve the boundary problem is the following one : [*isentropic*_{0/2}, *energy*_{0/2}, *mass*_{1/2}, *energy*_{1/2}, $p_1 = p_2$, *MOC*]
- Sudden enlargement model : For this model, the momentum conservation is written between state at 2 and state at 1. Therefore, the system of equations which allows to solve the boundary problem is the following one : [*isentropic*_{0/2}, *energy*_{0/2}, *mass*_{1/2}, *energy*_{1/2}, *momentum*_{1/2}, *MOC*]

It is interesting to develop the momentum conservation between the nodes 1 and 2. Indeed, at node 1, the flow is assumed to run in the full section of the pipe F_1 . However, the flow runs in a reduced section at 2, such that $F_2 < F_1$. The static pressure p_2 is assumed to be applied on the complete pipe section F_1 . Therefore, the momentum equation between 1 and 2 leads to :

$$\begin{aligned} p_2 F_1 + \rho_2 u_2^2 F_2 &= (p_1 + \rho_1 u_1^2) F_1 \\ (p_2 - p_1) F_1 &= F_1 \rho_1 u_1^2 + F_2 \rho_2 u_2^2 \end{aligned} \quad (8.37)$$

Sonic case

When the pressure ratio across the partially open-end is increased, sonic flow can occur at state 2. In this case, the sonic flow definition is used and this allows to write that $M_2 = \frac{u_2}{a_2} = 1$. This relationship provides an additional equation to the 6 equations from the subsonic case. It is necessary to remove one relation from the subsonic case in order to get 6 relations. Consequently, the constant pressure equation or the momentum equation are removed from the previous system of equations. They are indeed based on some restrictive assumptions. This leads to the following 6 conditions : [*isentropic*_{0/2}, *energy*_{0/2}, *mass*_{1/2}, *energy*_{1/2}, $M_2 = 1$, *MOC*]. This model will be referred as the sonic throat approach model.

An other method to model the sonic inflow from a partially open-end has also been introduced by Demoulin [32]. The flow is modeled as a sonic nozzle : a shock of section F_S such that $F_2 < F_S < F_1$ occurs. This models introduces 13 unknown quantities : the gas state a node 1, at node 2, upstream the shock, downstream the shock and the shock position. The development of the sonic nozzle approach is available in Demoulin's paper, or in any aerodynamical basics book.

Models comparison

It would be interesting to compare the results provided by the previously-developed models to study the impact of the introduced equations and hypotheses on the final result. The main available comparison of the models direct application is from Benson [5], who developed the partially open-end equations in order to plot quasistatic performance data maps. The data maps show the evolution of the sound speed a_1 vs. particle speeds u_1 . These data maps are plotted for each model in order to illustrate the results difference. However, the plots provided by Benson are not totally valid. Indeed, it has been seen in the previous developments that the MOC is systematically introduced as one of the 6 conditions to solve the boundary problem. The

correction of entropy can only be developed when the boundary is linked to the pipe, therefore Benson used the homentropic MOC to develop the boundary data maps. Benson uses this approach in order to provide a graphical representation of the equations, but states that this approach is not physically valid, as an equation such that the momentum conservation introduces an increase of entropy though the valve, and is therefore not compatible with the homentropic MOC. Therefore, this development cannot be used to provide a rigorous quasistatic comparison of the inflow partially open-end models under non-homentropic conditions.

Experimental correction

Many papers focus on the development of the discharge coefficient approach [140], [141], [7], [8], [9], [19], [49]. In this case, the results of the numerical boundary condition are corrected by an experimental coefficient which is applied on the mass flow rate equation. The mass flow rate provided by the model is compared to an experimental flow rate and the ratio is stored into a data map.

$$(\rho_1 u_1 F_1)_{model} = Cd (\rho_1 u_1 F_1)_{expe} \quad (8.38)$$

Therefore, the 'raw' results from the equations and hypotheses introduced in the models are hidden behind the discharge coefficient. This approach is widely used, as it allows to get accurate results. However, it requires that a physical engine exists in order to measure the Cd .

3- Outflow partially open-end

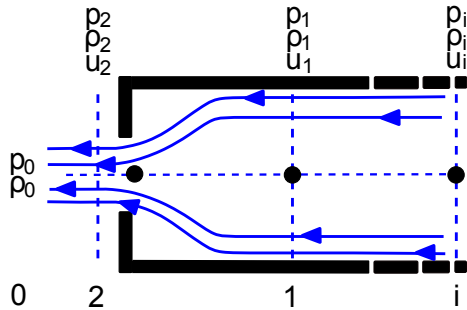


FIG. 8.8 – Schematic representation of the partially open-end outflow boundary condition

In this subsection, equations and assumptions from the literature partially open-end outflow models are developed. These models are also used to model the engine exhaust valves. The control volume is shown on figure 8.8 : the gas exits the pipe as a jet of cross-sectional area F_2 . One should notice that unlike in the inflow case, plane 2 is located outside of the pipe. The isolated system is located between planes 1 and 2. There are 6 unknown quantities (pressure, density, velocity at 1 and 2), so six relations are needed. In this case again, the distinction is made between the subsonic case and the sonic case :

Subsonic case

In the case of a subsonic outflow through a partially open-end, the following model is commonly introduced [5], [139]. The conservations of mass and energy are expressed between 1 and 2, and the flow is considered to expand isentropically between those two points. As long as the flow is subsonic, the static pressure at point 2 is assumed to be equal to the ambient pressure 0. These 4 equations are completed by the speed of sound expression ($a^2 = \frac{\gamma p}{\rho}$) and the MOC. Finally, the following system of equations is considered to solve the boundary problem : [$\text{isentropic}_{1/2}$, $\text{mass}_{1/2}$, $\text{energy}_{1/2}$, $p_2 = p_0$, $a^2 = \frac{\gamma p}{\rho}$, MOC].

Sonic case

When sonic flow occurs at the throat, the sonic relation is introduced : $M_2 = \frac{u_2}{a_2} = 1$. In the same time, the constant pressure assumption ($p_2 = p_0$) is not valid anymore, as the flow is choked at 2. Finally, the equations involved in the boundary problem resolution becomes : [isentropic_{1/2}, mass_{1/2}, energy_{1/2}, $M_2 = 1$, $a^2 = \frac{\gamma p}{\rho}$, MOC].

As in the inflow case, this system of equation is generally coupled to an experimental coefficient correction (C_d) approach.

4- Intra-pipe sudden area change

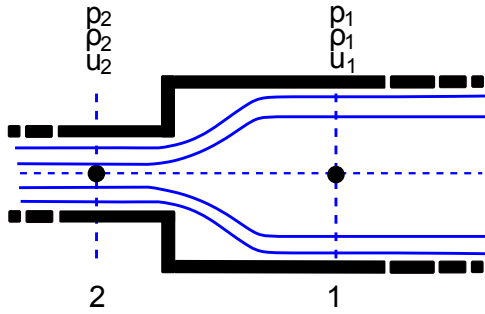


FIG. 8.9 – Schematic representation of an intra pipe sudden area change

This kind of boundary conditions occurs within a pipe (not at its extremity). Depending on the flow direction, a sudden area change can be either a sudden enlargement or a sudden contraction. In the case of a sudden enlargement, the same system of equations as in the inflow partially open-end is considered. In the case of a sudden contraction, the same system of equations as in the outflow partially open-end is used. The main difference between these intra-pipe cases and the boundary conditions at the exit/entry of the pipe is that the MOC must be solved twice : upstream and downstream the sudden area change.

5- Throttles, filters...

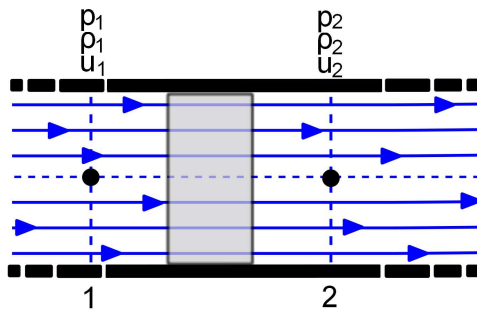


FIG. 8.10 – Schematic representation of an intra pipe pressure drop device

Components such as throttles, carburettors, recirculation valves, filters are generally modeled via an adiabatic pressure loss. The device is assumed to produce a static pressure loss Δp [139]. This pressure loss is generally expressed using a pressure loss coefficient f_C :

$$\Delta p = f_C \frac{\rho_1 u_1^2}{2} \quad (8.39)$$

The coefficient f_C is determined from test bench experiments and is stored in a data map. It is generally expressed as a function of the upstream Mach or Reynolds number. In the case of throttles or exhaust gas

recirculation, it is possible to include the angle of opening of these devices into the data mapping. This produces 'standard' data maps which can be re-used from an application to another one [19].

6- Pipe junctions

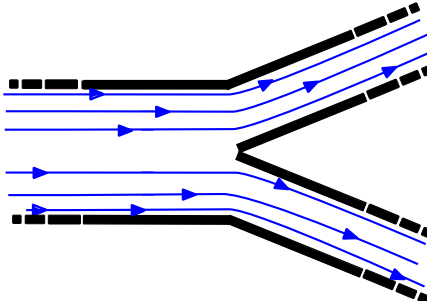


FIG. 8.11 – Example of pipe junction : 'Y' type

Such flow arrangements are commonly found in the engine exhaust systems. The flow is highly multi-dimensional when running through these devices, therefore their modeling is based on pressure loss coefficients data maps. The data maps have been built including the geometrical parameters of the duct junctions (number of pipes, incidence angles). Therefore, such data maps can be used independently of the considered application. Examples of data maps creation and correlation are extensively detailed in [139] and in [19].

Boundary conditions equations and hypotheses : main points

- The aerodynamical governing equations can be derived under the quasistatic assumption. This allows to build the equations system introduced to solve the boundary condition problem. These equations are used along with the MOC.
- The boundary equations are generally correlated from experiments using corrective coefficients data maps. These corrective coefficients can be divided into two categories : 1- The discharge coefficients C_d , which are applied on the mass conservation equation. 2- the pressure loss coefficients f_C , which dictate a loss of static pressure on the momentum equation.
- From the literature papers review, it appears that the models based on the f_C data maps (throttles, pipe junctions...) can be used as a component model library, and be used on any application. Indeed, these models include the geometrical properties of the component, which allows a good re-usability to the model.
- On the other hand, the model using the C_d coefficients, mostly the engine poppet valves, need to be re-mapped for each application. Indeed, the induction/exhaust ducts and the valve geometry change from an application to another. In order to measure the C_d associated to an engine valve, it is necessary to have the engine at disposal and to use it on a steady-flow test bench.

8.4 Gas exchange processes : proposed thesis developments

It has been seen in the literature review that the aerodynamics models and their associated boundary conditions have been extensively developed. The most adequate modeling techniques in order to develop the engine control remain the mean-value and one-dimensional numerical schemes. They allow to reach a satisfying degree of accuracy for the standard engine models. However, two limitations have been found in the case where these models are applied to the control laws development :

- In the case where a one-dimensional scheme is used, it appears that the boundary condition resolution schemes are not optimized in terms of calculation efficiency. For example, it has been shown that the entropy correction loop proposed by Benson is not optimal in terms of calculation time.
- Most of the boundary conditions models rely on an experimental correction, such as the discharge coefficients C_d . This correction is a strong limitation to the model-based approach, more particularly in the case of non-conventional engines. Indeed, in the case of innovative engine architectures, such as pneumatic hybridization systems ([62], [36]), the valve system does not have standard characteristics. Therefore, performing engine tuning and control laws developments before having a first prototype will likely introduce critical errors in the estimation of the airflow.

From these observations, it has been decided to investigate these two points :

- **Reduction of the need of discharge coefficients** : The goal is to get 'generic' flow restriction models in the case where no flow bench data are available. Such models should take into account the geometry of the restriction. Even though the complexity of the flows through the restrictions won't allow to get totally rid of the experimental corrective coefficients, it should be reminded that the required accuracy is generally decreased when dealing with the development of control laws. In order to build and to identify these models, it will be intended to include as much physics as possible in the construction of the models and to avoid the introduction of non-physical assumption, such as the isentropicity. Existing flow restriction models and proposed models will be compared to experimental measurements in order to identify the models providing the best accuracy without the introduction of discharge coefficients.
- **Optimized schemes for the resolution of the non-homentropic boundaries** : It is intended to optimize the iterative loops introduced in order to solve the inflow/outflow boundary problem. It has been seen that the convergence loop introduced by Benson [5] is not optimal, as its convergence term is fixed and re-initialized in the case where unrealistic flow conditions are calculated. In order to speed up the resolution process, a Newton-Raphson algorithm will be implemented.

Structure of the 'Gas Exchange processes through flow restrictions' part : A one-dimensional boundary condition will be considered as the composition of two complementary parts :

1. the physical equations which are introduced in order to build the model. These equations can also be used in order to build the mean-value boundary conditions.
2. the iterative scheme which is used to solve the local problem of the boundary. This scheme can also be considered as the 'interface' between the boundary model and the inpipe numerical scheme. Such schemes are not required to deal with the mean-value models, but they are necessary in order to solve the boundary problem in the case of the one-dimensional schemes.

This structure is shown on Fig. 8.4. The physical equations associated to the flow restriction boundaries will be developed in the chapter 11. These equations dictate the behavior of the flow at the restriction, therefore they are directly linked to the introduction, or not, of the experimental coefficients. It is intended

to identify the equation sets which will allow to reduce the requirement of such corrective factors. The iterative schemes dedicated to the resolution of the boundary problem will be developed in chapter 10. These numerical schemes have a strong impact on the calculation speed, and new developments will be introduced in order to improve the convergence speed. Finally, the equations developments will be combined to the proposed iterative schemes, and the calculation results will be compared to experimental measurements in chapter 12. It is intended to control :

1. the accuracy of the developed flow restriction models without introducing any discharge coefficient.
2. the convergence ability and robustness of the proposed iterative schemes.

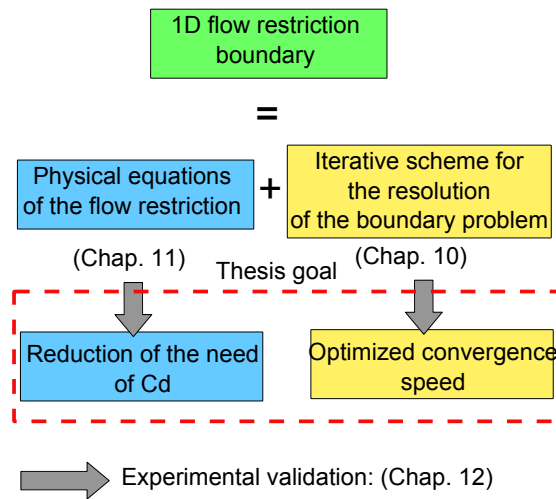


FIG. 8.12 – Chartflow of the 'Gas Exchange processes through Flow Restrictions' part.

Chapter 9

Experimental apparatus

The experimental campaign regarding the study of flow through restrictions has been performed at the Institut Prisme. The steady flow benches have been developed during this thesis, while the transient cylinder experiment was already available from previous studies.

9.1 Cylinder head steady flow bench

A global view of the cylinder head steady flow bench is shown on Fig. 9.1. A cylinder head from a 2.0l diesel Renault engine has been mounted on a 3-way flow bench. It is possible to plug the compressed air source at the plenum 1, at the plenum 2 or at the cylinder. It is therefore possible to re-create the following flow configurations :

- Flow from the cylinder to the plenum 1.
- Flow from the cylinder to the plenum 2.
- Flow from the plenum 1 to the cylinder.
- Flow from the plenum 2 to the cylinder.

It is possible to unmount the plenums in order to reduce the losses : for example, in the case where an exhaust flow is created (cylinder to plenum 2), the plenum 2 is unmounted in order to get ambient pressure applied at the duct exit.

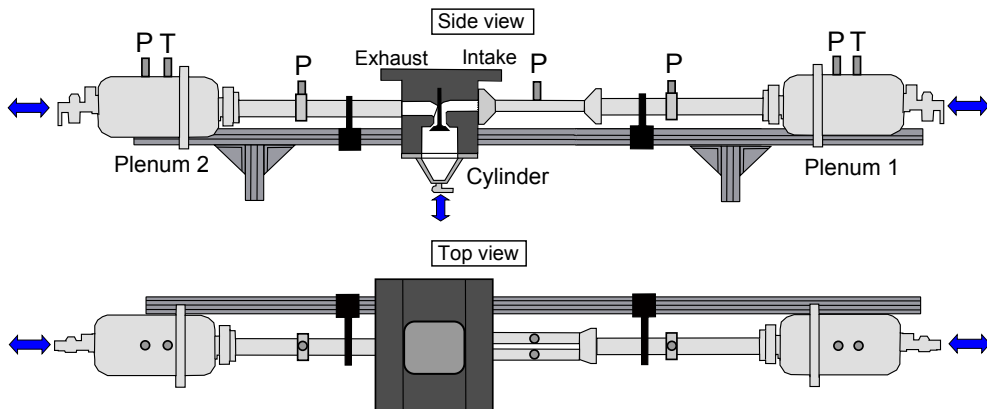


FIG. 9.1 – Cylinder head steady flow bench.

The disposition of the pressure and the temperature probes are shown on Fig. 9.1. The mass flow rate is measured upstream of the flow bench. When the piping geometry allowed to do it, a special disposition has been adopted in order to measure the pressure. This system is shown on the left plot of the Fig. 9.2 :

a 'belt' is created in order to avoid that any local multi-dimensional effect affects the measurement of the static pressure. The engine mounted on the bench has 4 valves; on the real application, each intake valve has a dedicated ducting system to improve the swirl creation. In order to mount this cylinder head on the bench, a specific adaptation has therefore been required (Fig. 9.2, right plot)

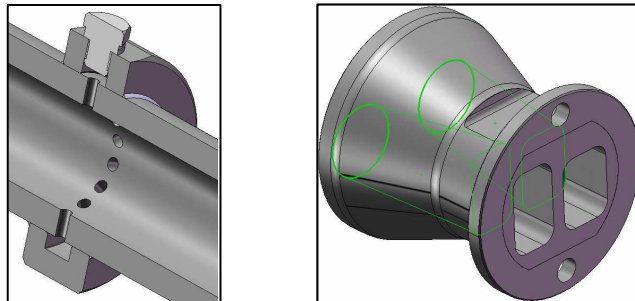


FIG. 9.2 – Left : System for the pressure measurement. Right : Interface between the pipe system and the intake side of the cylinder head.

Finally, each valve can be actuated independently by the mean of a fine pitch roller (1 turn = 0.1 mm lift). The valve lifts are acquired by a dial gauge system. The corresponding valve flow sections have been determined by the mean of CAD tools. However, no dimensions are provided here, due to confidentiality reasons.

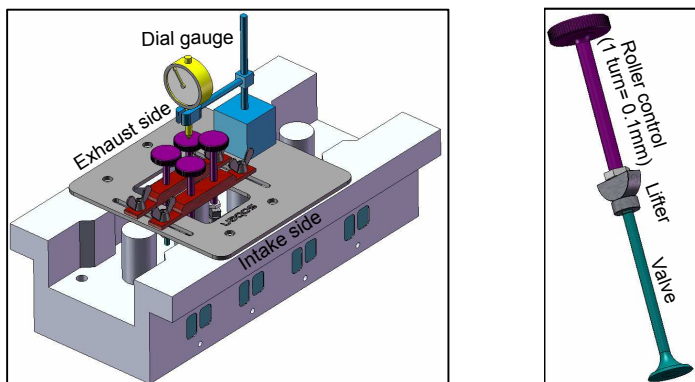


FIG. 9.3 – Cylinder head steady flow bench.

The complete list of sensors used on this bench is detailed in the following table :

Sensor type	Manufacturer	Model	Scale	Dispersion
Absolute pressure	Rosemount	3051 CA 4	0-10 bar	$\pm 0.055\% \text{ FS}$
Differential pressure	Rosemount	3051 CD 4	0-10 bar	$\pm 0.055\% \text{ FS}$
Mass flow rate	EPI	8600 MPNH	0-0.02 kg/s	$\pm 0.01\% \text{ FS}$
Temperature	LabFacility	Pt100	223-773K	$\pm 0.6 \text{ K}$

9.2 Diaphragm steady flow bench

A global view of the diaphragm steady flow bench is shown on Fig. 9.4. Diaphragms of diameter 1mm to 21.5mm can be placed on the flow to create a flow restriction. The upstream and downstream pipes inner diameter is 21.5mm. When a flow is established, the static pressure upstream and downstream the restriction

are measured. As in the cylinder head flow bench case, the pressure probes have been designed using a 'belt' in order to avoid any local multi-dimensional effect. The flow meter is controlled, which allows to assign a mass flow rate value from a computer.

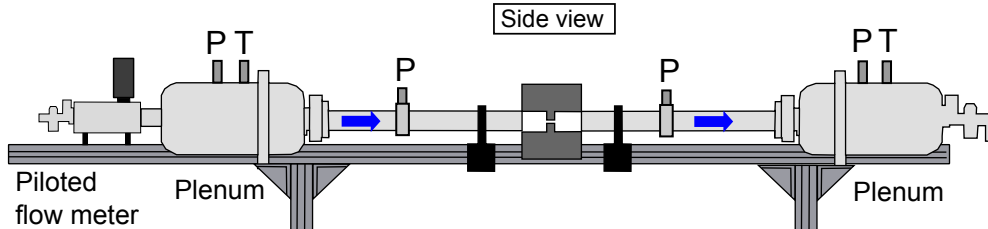


FIG. 9.4 – Diaphragm steady flow bench.

This bench was first intended to study low mass flow rates values in subsonic conditions. Therefore, the flow meter has been chosen to have a narrow full scale and the differential pressure probes have a full scale of 1 bar. It will be seen in the following of the document that these characteristics will limit the validation of some boundary models. Consequently, an adaptation of the hardware of the bench has been planned in order to reach higher mass flow rates values and to deal with sonic flow cases. However, this could not be performed in time to be included in this manuscript. The sensors used on the bench during this thesis are described in the following table :

Sensor type	Manufacturer	Model	Scale	Dispersion
Absolute pressure	Rosemount	3051 CA 4	0-5 bar	$\pm 0.055\% \text{ FS}$
Differential pressure	Rosemount	3051 CD 4	0-1 bar	$\pm 0.055\% \text{ FS}$
Mass flow rate	Brooks	5851S	0-100 nl/min	$\pm 0.2\% \text{ FS}$
Temperature	LabFacility	Pt100	223-773K	$\pm 0.6 \text{ K}$

9.3 Cylinder transient flow bench

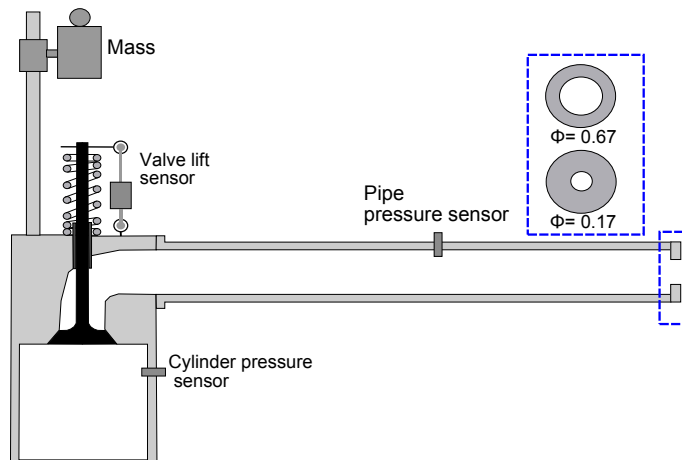


FIG. 9.5 – Cylinder transient flow bench.

Experiments have been performed on a valve gas dynamics test bench displayed on Figure 9.5. A cylinder is connected to a 5.552 meter long pipe. The cylinder has a volume of 6 liters. It is pressurized at a desired level. A falling mass opens the valve, thus a pressure wave is generated. The effective lift of the

valve is measured by a linear resistive sensor. Static pressure is measured in the cylinder and along the pipe. The pipe pressure sensor is located at 3.20 meters from the valve. The unusual length of the pipe has been selected to acquire the generated pressure wave from its creation to its extinction without being disturbed by the reflections at pipe boundaries. Diaphragms have been placed at the exit of the pipe in order to validate sudden restriction models. The sensors used on the bench are described in the following table :

Sensor type	Manufacturer	Model	Scale	Dispersion
Pipe pressure	Bosch	0-261-230-049	0-2.5 bar	-
Cylinder pressure	Kistler	4045A5	0-10 bar	-
Valve lift	Gefran	P212A25	-	-

No CAD geometry was available to determine the flow cross-sections. Consequently, geometric parameters of the valve are used to calculate the effective area of the valve port F_v as a function of the lift L_v , using the method proposed by Heywood [61]. F_s is the inner seat hydraulic diameter, then if $\frac{L_v}{F_s} < 0.124$, then F_v is defined by Eq. (9.1). If $\frac{L_v}{F_s} \geq 0.124$, F_v is defined by Eq.(9.2). F_h is the valve head diameter, w is the seat width and β is the seat angle.

$$F_v = \pi L_v \cos \beta \left(F_h - 2w + \frac{L_v}{2} \sin 2\beta \right) \quad (9.1)$$

$$F_v = \pi(F_h - w)\sqrt{(L_v - w \tan \beta) + w^2} \quad (9.2)$$

Valve hydraulic diameter	$\phi 30$ mm
Valve seat width	2 mm
Valve seat angle	40°
Pipe hydraulic diameter	$\phi 29$ mm
Cylinder volume	6 L

9.4 Numerical steady flow bench

Multi-dimensional simulations have been performed in order to visualize the evolutions of the flow and to access to quantities which could not be measured on experimental test benches. Simulations have been ran under Fluent 6.0.12. Only 2D axi-symmetrical simulations have been performed. Two geometries have been considered :

- A sudden enlargement port linking a pipe to a stagnation state (Fig. 9.6, left plot). The results from these simulations will be compared directly to the results from restriction models developed in this thesis. In the outflow case (flow from 1 to 0), the sudden restriction geometry has been modified to create a nozzle of angle α , with $\alpha \in [\frac{\pi}{4}; \frac{\pi}{2}]$.
- An axi-symmetrical poppet valve (Fig. 9.6, right plot). Even though such devices are not axi-symmetrical due to the bend of the intake/exhaust pipes on real applications, this configuration is used only to validate some flow hypotheses. The results from these simulations will not be compared to the results from restriction models developed in this thesis

In order to create a stagnation flow condition, the section F_0 is chosen such that for any value of F_2 , $\frac{F_2}{F_0} < 0.02$. Under these conditions, the values of $\frac{u_0}{a_0}$ never exceed 10^{-3} , which is a good approximation of a stagnation state. The air has been defined as a compressible ideal gas, with a standard Sutherland viscosity

law. The steady implicit 2D axi-symmetrical segregated solver has been used to solve Navier Stokes equations with a $k - \epsilon$ turbulence model. Selected discretization is a first order upwind scheme. Total pressure from 1 bar to 10 bar with no inlet speed have been imposed as inlet condition, while 1 bar static pressures has been imposed at the outflow. Inflow condition is either applied to plane 0 or 1, in order to create inflow or outflow conditions. Numerical measurements have been performed on three different planes : at the stagnation state plane 0, at the throat 2 and in the pipe 1. The length of the pipe has been defined as 30 times the equivalent diameter at 2 in order to let the flow reach its recovery plane. This allows to have an homogeneous flow for the numerical acquisition at plane 1.

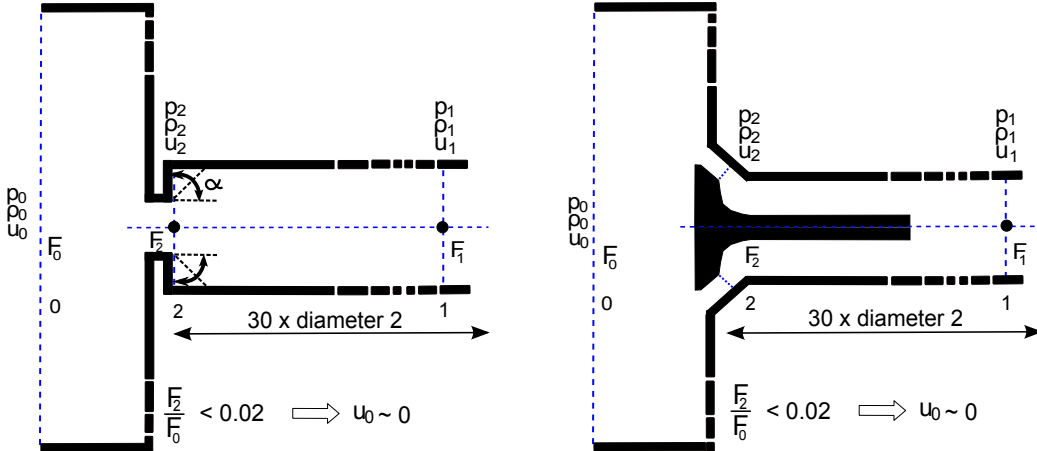


FIG. 9.6 – Considered geometries for the CFD simulation of partially open-ends (left) and poppet valves (right)

The convergence criterion the under-relaxation factors and the mesh quality parameter which have been used for running the CFD simulations are shown in the following table :

Mesh skewness	< 1e-2
Energy convergence criterion	1e-7
Other values convergence criterion	1e-5
Pressure under-relaxation factor	0.3
Density under-relaxation factor	1
Body forces under-relaxation factor	1
Momentum under-relaxation factor	0.7
$k-\epsilon$ under-relaxation factor	0.8
Turb. viscosity under-relaxation factor	1
Energy under-relaxation factor	1

Chapter 10

Optimized MOC-based iterative schemes for the resolution of the non-homentropic boundary conditions

In this chapter, the implementation of optimized convergence loops on the non-homentropic inflow/outflow boundary conditions will be developed. In a first part, the entropy correction loop of the inflow boundaries will be derived to use a Newton-Raphson algorithm to converge towards the final solution. In a second part, it will be seen that no numerical scheme is available in the literature to deal with non-homentropic outflow boundaries. Therefore, an iterative scheme allowing to deal with the increase of entropy through an outflow valve will be developed. This loop will also be combined to a Newton-Raphson algorithm.

Newton-Raphson convergence algorithm is a quadratic convergence speed scheme. It allows to minimize the value of a function by using its derivative in order to adapt its convergence factor. This algorithm is described as follows :

A function f of the variable x_1 is considered. It is assumed that an interval $[a; b]$ exists such that for $x_1 \in [a; b]$, $f(x_1) = 0$ is verified once. Under these conditions, it is possible to build an iterative scheme allowing to converge the function f to a value of x_1 which allows to get $f(x_1) = 0$. In the following developments, it is the it^{th} step of the Newton-Raphson iterative scheme. Introducing $f'(x_1) = \frac{df(x_1)}{dx_1}$, the Newton-Raphson algorithm expresses the successive values of x_1 which will allow to achieve $f(x_1) \simeq 0$:

$$x_1^{it+1} = x_1^{it} - \frac{f(x_1^{it})}{f'(x_1^{it})} \quad (10.1)$$

Note : It is important to make the distinction between 'n' and 'it'. 'n' is the time step of the global pipe numerical scheme, while 'it' is the iterative step of the boundary condition resolution scheme : at each time step 'n', an iterative loop ($it=1 \dots$) is run until convergence at the boundary condition in order to solve the local problem of the boundary.

10.1 Expression of the Newton-Raphson algorithm for the entropy correction loop

In order to improve the readability of the following developments, the main equations and notations introduced by Benson are reminded here. The MOC resolution scheme is based on the Euler's equations (mass, energy and momentum conservation) expressed in the homentropic formulation. However, exhaust valve flow does not respect this homentropic assumption, and the MOC has to be modified to take into

account the difference of entropy across the valve. Figures 10.1 displays Benson's notation for defining the entropy level of a state : a_A is the 'entropy' level of gas at pressure p , with sound speed a . a_A is determined by an isentropic contraction from p to the reference pressure p_{ref} . A is the non dimensional speed of sound $\frac{a}{a_{ref}}$ and A_A the non dimensional entropy level $\frac{a_A}{a_{ref}}$. Eq.10.2 shows the relationship introduced by Benson in order to calculate the entropy level a_A of a state at pressure p and speed of sound a regarding a reference pressure p_{ref} .

$$\left(\frac{p}{p_{ref}}\right)^{\frac{\gamma-1}{2\gamma}} = \frac{a}{a_A} = \frac{A}{A_A} \quad (10.2)$$

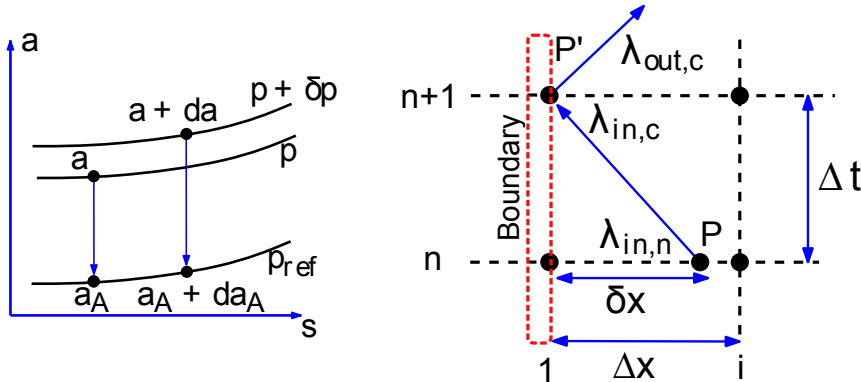


FIG. 10.1 – Benson entropy level definition (left). Non-homentropic Riemann variable definition (right).

$\lambda_{in,n}$ is the Riemann variable on the incident characteristic, which is calculated from the previous calculation time step n , interpolated between abscissae 1 and i at point P : $\lambda_{in,n} = A_P \pm \frac{\gamma-1}{2} U_P$. $\lambda_{in,c}$ refers to the boundary condition at time step $n+1$ at the abscissa 1 (point P') : $\lambda_{in,c} = A_{P'} \pm \frac{\gamma-1}{2} U_{P'}$. In the case of homentropic flow, $\lambda_{in,n}$ and $\lambda_{in,c}$ are directly linked and this allows to solve directly the boundary condition problem. In the non-homentropic case, $\lambda_{in,n} \neq \lambda_{in,c}$. Benson expresses a new equilibrium relation (Eq.10.3) between $\lambda_{in,n}$ and $\lambda_{in,c}$ by introducing the terms expressing the non isentropicity of the flow (see the literature review for more details) . A_{An} is the non dimensional entropy level at mesh P , A_{Ac} is the corrected non dimensional entropy level at P' and $A_{P'}$ is non dimensional speed of sound at P' .

$$\lambda_{in,c} = \lambda_{in,n} + A_{P'} \frac{A_{Ac} - A_{An}}{A_{Ac}} \quad (10.3)$$

As A_{Ac} and $A_{P'}$ are values referring to the time step $n+1$, Eq.10.3 must be solved using an iterative process. Even though this equation expresses the entropy correction in the inflow and outflow cases, it will be seen that the subsequent developments will differ. Consequently, the inflow and outflow cases are handled separately.

10.2 Inflow case

In this case, the entropy level difference between the incident characteristic and the flow from state 2 (Fig. 10.2) has two sources : Firstly, depending on the thermodynamical conditions, it is possible that the flow entering the pipe is at a different entropy level than the gas in the pipe. Secondly, the equations introduced to model the boundary will generate an increase of entropy. On real applications, this increase of entropy is due to the flow irreversibilities, such as the recirculation vortexes or any other shear stress phenomena

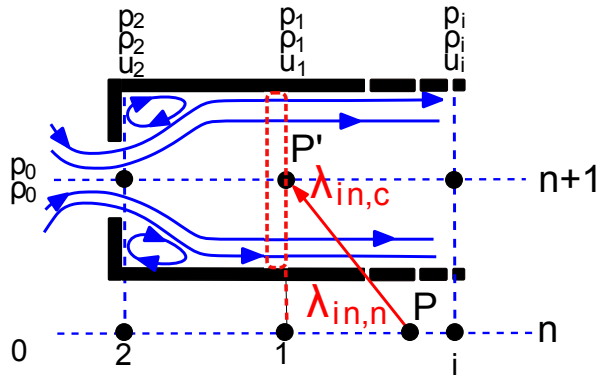


FIG. 10.2 – Non-homentropic Riemann variable definition for the valve inflow case.

linked to the boundary layer evolution. Therefore, the correction of entropy is impacted by the choice of the boundary model.

Now, in order to apply a Newton-Raphson algorithm to the MOC, it is necessary to introduce a function to minimize. Eq. 10.3 is rewritten, which allows to define the function f to minimize as :

$$f = \lambda_{in,c} - \left(\lambda_{in,n} + A_{P'} \frac{A_{Ac} - A_{An}}{A_{Ac}} \right) \quad (10.4)$$

This function is dependent upon the following variables $A_{P'}$, A_{Ac} and $\lambda_{in,c}$. These variables are based on some linear combinations of the following variables : p , u , a . There is consequently a large choice of variables available in order to build the Newton-Raphson algorithm. As we have no choice criterion for now, we are going to use the same variable as chosen by Benson when he built his algorithm : $\lambda_{in,c}$.

10.2.1 Newton-Raphson algorithm built using $\lambda_{in,c}$ as the convergence variable

Given this choice of variable, the Newton-Raphson iterative loop is written as follow :

$$\lambda_{in,c}^{it+1} = \lambda_{in,c}^{it} - \frac{f(\lambda_{in,c})^{it}}{f'(\lambda_{in,c})^{it}} \quad (10.5)$$

At a given iterative step it , the values of $\lambda_{in,c}$ and of $f(\lambda_{in,c})$ are known. It is however necessary to calculate the value of $f'(\lambda_{in,c}) = \frac{df(\lambda_{in,c})}{d\lambda_{in,c}}$, which is the derivative value of the function f regarding the Riemann variable $\lambda_{in,c}$.

$$f'(\lambda_{in,c}) = \lambda'_{in,c} - \lambda'_{in,n} - \left(A_{P'} \left(1 - \frac{A_{An}}{A_{Ac}} \right) \right)' \quad (10.6)$$

$$f'(\lambda_{in,c}) = 1 - \frac{dA_{P'}}{d\lambda_{in,c}} \left(1 - \frac{A_{An}}{A_{Ac}} \right) + A_{P'} \left(\frac{A_{An} \frac{dA_{Ac}}{d\lambda_{in,c}}}{A_{Ac}^2} \right) \quad (10.7)$$

After development, it appears in Eq.10.7 that $f'(\lambda_{in,c})$ introduces the following derivative functions : $\frac{dA_{P'}}{d\lambda_{in,c}}$ and $\frac{dA_{Ac}}{d\lambda_{in,c}}$. When developing $\frac{dA_{Ac}}{d\lambda_{in,c}}$ it comes :

$$\frac{dA_{Ac}}{d\lambda_{in,c}} = \frac{dA_{P'}}{d\lambda_{in,c}} P^{\frac{\gamma-1}{2\gamma}} + A_{P'} \frac{\gamma-1}{2\gamma} \frac{dP}{d\lambda_{in,c}} P^{-\frac{\gamma-1}{2\gamma}} \quad (10.8)$$

In Eq.10.8, one sees that the derivative of the pressure ratio regarding the Riemann variable $\frac{dP}{d\lambda_{in,c}}$ is introduced. From Benson's work, we know that in the subsonic case :

$$P = \left[\frac{1}{2C} \left(\phi \sqrt{\phi^2 + 4C} - \phi^2 \right) \right] \quad (10.9)$$

where :

$$C = \frac{\frac{\gamma-1}{2}U^2}{\left(1 - \frac{\gamma-1}{2}U^2 \right)^2} \quad (10.10)$$

$$U = \frac{\lambda_{outc} - \lambda_{inc}}{(\gamma - 1)A_C} \quad (10.11)$$

$$\lambda_{outc} = \left(\frac{3-\gamma}{\gamma+1} \right) \lambda_{inc} + \frac{2}{\gamma+1} \sqrt{(\gamma^2-1)A_c^2 + 2(1-\gamma)\lambda_{inc}^2} \quad (10.12)$$

In order to express P (note : $P = \frac{p}{p_{ref}}$) as a function of λ_{inc} , it is necessary to combine Eq.10.10, Eq.10.11, Eq.10.12 and to incorporate them into Eq.10.9. This provides a quite complex expression. When trying to derive this expression regarding λ_{inc} , an analytical formulation could not be expressed.

In order to overcome this issue, it is necessary to build a discretized data map of P regarding λ_{inc} . In the literature review, it has been seen that such thing cannot be performed using Benson's technique [5], as he systematically introduces the homentropic assumption. A data map building-process had to be defined to create the data maps associated to the inflow valve boundary equations without introducing the homentropic assumption. This process is described in the Chapter 11.

Once such data maps are available, it is possible to express any variable with respect to another one, and without having to introduce complicated analytical formulations. The data map of P as a function of λ_{inc} is shown on Fig.10.3. This figure has been plotted using Benson's partially open-end subsonic inflow equations under constant pressure assumption combined to the sonic throat model equations. In order to plot this figure, the stagnation state as been defined as the reference state : $p_{ref} = p_0$, $a_{ref} = a_0$. Therefore, P represents the pressure ratio across the valve $\frac{p}{p_0}$. For a given point, it is possible to calculate the numerical derivative of P regarding λ_{inc} , using numerical derivation : $\frac{dP}{d\lambda_{inc}} = \frac{P_{i+1}-P_i}{\lambda_{inc}(i+1)-\lambda_{inc}(i)}$, where i are the abscissa indexes of the data map. This method provides satisfying results in most cases. However, the developed iterative algorithm systematically fails to converge for low valve opening ratios. This is a problematic behavior, as valves work systematically in this operating range at valve opening or closure.

When looking at Fig.10.3, it appears that the curves tend to become vertical when reaching the lowest valve opening ratio values ($\phi \Rightarrow 0$). ϕ is the valve opening ratio, which in reference to Fig. 10.2 would lead to the following definition : $\phi = \frac{F_2}{F_1}$. For the low valve opening ratio operating range, the almost vertical slopes mean that $\frac{dP}{d\lambda_{inc}}$ will reach high values ($> 10^{15}$ on some points). This has two impacts on the Newton-Raphson scheme :

- The large values of P' will lead to large values of $f'(\lambda_{in,c})$. Consequently, this will produce extremely low values for the Newton-Raphson convergence term $\frac{f(\lambda_{in,c})^{it}}{f'(\lambda_{in,c})^{it}}$ ($< 10^{-16}$ on some points). Therefore, the convergence time will be extensively increased.
- The numerical differential scheme produces large errors in the case of very steep slopes. These errors, once introduced into the Newton-Raphson scheme, do not allow the algorithm to converge

10.2.2 Newton-Raphson algorithm built using P as the convergence variable

In the last subsection, it has been shown that implementing a Newton-Raphson using $\lambda_{in,c}$ as the convergence variable does not provide satisfying results. The natural causality of the MOC is as it follows : $\lambda_{in} \rightarrow (U, A, P, A_A)$. Indeed, in any case, the Riemann variable λ_{in} is the starting point of the determination of the

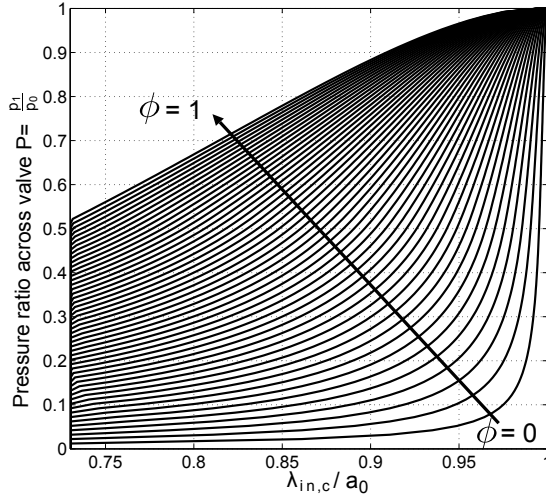


FIG. 10.3 – Data map of the pressure ratio expressed as a function of $\lambda_{in,c}$, covering the entire valve opening ratio ϕ range (0 to 1). The stagnation state has been used as the reference state : $p_{ref} = p_0$, $a_{ref} = a_0$

non-dimensional particle speed and of the non-dimensional speed of sound, which are subsequently used to calculate the pressure ratio and the entropy level at the valve boundary.

In this subsection, it is proposed to introduce the pressure ratio across the valve as the convergence variable. It will be shown that the main advantage of this causality is that it allows to avoid the infinite slopes when developing the Newton-Raphson expression.

In the same way as in the previous section, the starting point of the work is the result provided by Benson (Eq.10.13) which will provide the function f to be minimized by the Newton-Raphson algorithm (Eq.10.14).

$$\lambda_{in,c} = \lambda_{in,n} + A_{P'} \frac{A_{Ac} - A_{An}}{A_{Ac}} \quad (10.13)$$

$$f = \lambda_{in,c} - \left(\lambda_{in,n} + A_{P'} \frac{A_{Ac} - A_{An}}{A_{Ac}} \right) \quad (10.14)$$

As the pressure ratio is now the 'entry' point of the model, it is the pressure ratio which will be updated at each iterative step (Eq.10.15).

$$P^{it+1} = P^{it} - \frac{f(P)^{it}}{f'(P)^{it}} \quad (10.15)$$

The function f and its derivative f' must now be expressed regarding the pressure ratio. At a given iterative step it , P and $f(P)$ are known. Now, $f'(P)$ must be expressed :

$$f'(P) = \frac{d\lambda_{in,c}}{dP} - \frac{dA_{P'}}{dP} \left(1 - \frac{A_{An}}{A_{Ac}} \right) + A_{P'} \left(\frac{A_{An} \frac{dA_{Ac}}{dP}}{A_{Ac}^2} \right) \quad (10.16)$$

with :

$$\frac{dA_{Ac}}{dP} = \frac{dA_{P'}}{dP} P^{\frac{\gamma-1}{2\gamma}} + A_{P'} \frac{d \left(P^{\frac{\gamma-1}{2\gamma}} \right)}{dP} \quad (10.17)$$

As $\frac{d\lambda_{inc}}{dP}$ can be expressed as a function of $\frac{dA_{P'}}{dP}$, there are now two derivative functions introduced to build the Newton-Raphson algorithm : $\frac{d\left(P^{\frac{\gamma-1}{2\gamma}}\right)}{dP}$ and $\frac{dA_{P'}}{dP}$. The first one can be analytically expressed, while the second one requires the use of a data map to be numerically calculated. $P^{\frac{\gamma-1}{2\gamma}}$ vs. P and $A_{P'}$ vs. P are plotted on Fig.10.4. From this figure, it appears that for $P > 0.05$, the curves slopes are moderate, never tending towards infinity. Pressure ratios lower than 0.05 are almost never encountered on automotive engine applications. Consequently, the choice of P as the Newton-Raphson convergence variable allows to build a robust iterative scheme in order to solve the entropy correction loop.

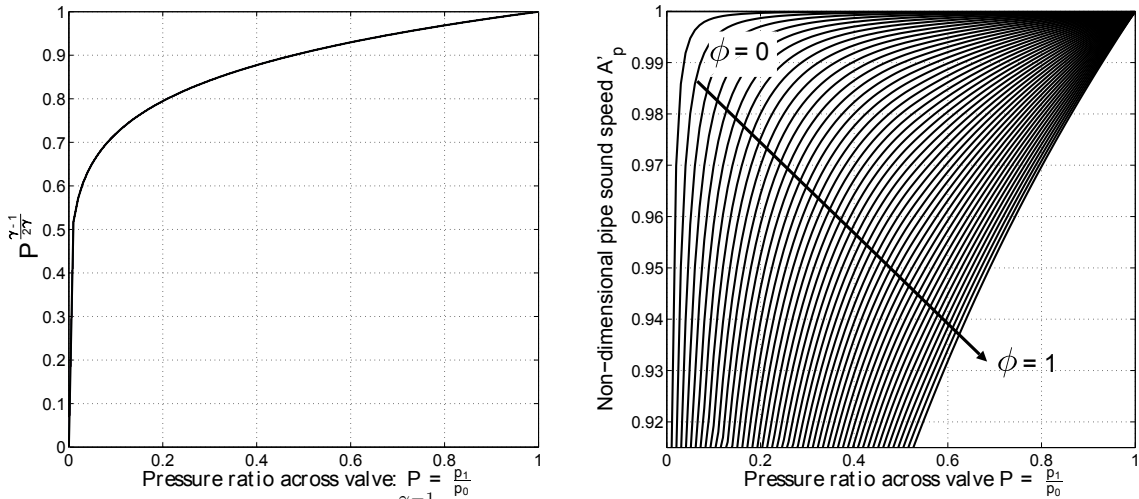


FIG. 10.4 – Left : Evolution of $P^{\frac{\gamma-1}{2\gamma}}$ with respect to P . Right : Data map of the pressure ratio expressed as a function of λ_{inc} , covering the entire valve opening ratio ϕ range (0 to 1). The stagnation state has been used as the reference state : $p_{ref} = p_0$, $a_{ref} = a_0$.

Note regarding the data maps

In the previous developments, the subsonic parts of the data maps have been defined using Benson's constant pressure subsonic inflow model. The sonic parts have been built using the sonic throat model. In the case where other models are used, it is necessary to build the data maps associated to these models equations, as they will produce different $A_{P'}$ vs. P evolutions. It is also reminded that the process used to build the non-homentropic data maps of the valve models is detailed in Chapter 11.

10.2.3 Implementation of the proposed entropy correction loop resolution : inflow case

It is now proposed to detail the implementation of the introduced inflow iterative loop (see Fig. 10.5). It is considered that the time step n has been completed, which means that any state is known within the pipe or at its boundary. In order to perform the calculation at time step $n + 1$, a numerical scheme (for example Lax-Wendroff) is used to calculate the states of the nodes inside the pipe. Now, it is necessary to calculate the state at the inflow boundary : one wants to calculate the state at point P' using the incident characteristic coming from the point P (see Fig. 10.2).

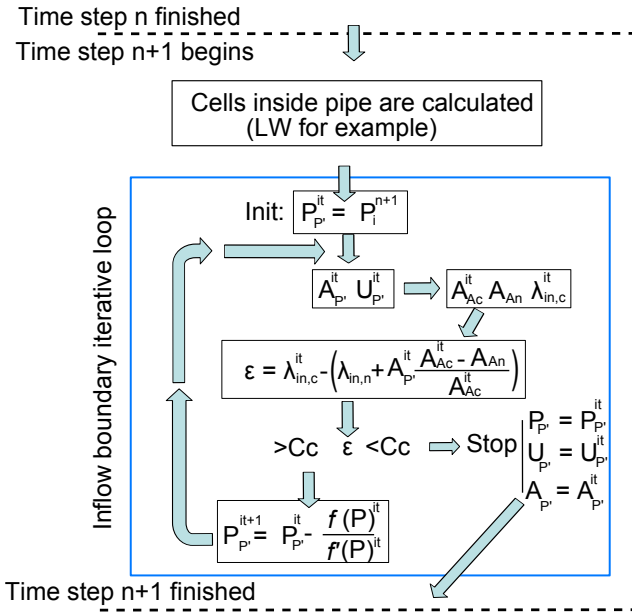


FIG. 10.5 – Chartflow of the proposed inflow entropy correction loop.

In order to achieve this calculation, the entropy correction loop using the pressure ratio-based Newton-Raphson scheme is used. In the following developments, upper case variables are used. These variables are non-dimensional, with respect to the state outside the pipe : $A_x = \frac{a_x}{a_0}$, $U_x = \frac{u_x}{a_0}$ and $P_x = \frac{p_x}{a_0}$.

1. The loop is initialized by taking $P_{P'}^{it} = P_i^{n+1}$, which means that the pressure at the boundary is initialized at the value of the pressure of the closest node inside the pipe.
2. The temporary value of $P_{P'}^{it}$ is used as the input of the datemap of the inflow model, which allows to get the value of $U_{P'}^{it}$ (these datamaps are built in the next chapter, see Fig.11.4 or Fig. 11.12). The value of $A_{P'}^{it}$ is calculated using the conservation of energy ($1 = A^2 + \frac{\gamma-1}{2}U^2$).
3. Knowing $P_{P'}^{it}$, $U_{P'}^{it}$ and $A_{P'}^{it}$ allows to calculate A_{Ac}^{it} and $\lambda_{in,c}^{it}$. These quantities combined to $\lambda_{in,n}$ and A_{An} allow to calculate the difference $\epsilon = \lambda_{in,c}^{it} - \left(\lambda_{in,n} + A_{P'}^{it} \frac{A_{Ac}^{it} - A_{An}}{A_{Ac}^{it}} \right)$.
4. In the case where ϵ is smaller than the convergence criterion C_C , the solution is converged, and the time step $n + 1$ is finished. If $\epsilon > C_C$, the value of $P_{P'}^{it}$ is updated using the Newton-Raphson relationship (Eq. 10.15). It is reminded that the value of $f'(P)$ is calculated using the datemap of A vs P which allow to perform the numerical value of $\frac{dA_{P'}}{dP}$ and $\frac{d\lambda_{in,c}}{dP}$. The loop is performed until convergence is achieved.

10.3 Outflow case

In this section, one considers a flow exiting a pipe through a partially open-end. Using Benson's notation, the incident Riemann variable $\lambda_{in,n}$ is transmitted to the boundary on C+ : $u + a$. $\lambda_{in,c}$ represents the Riemann variable at the boundary, which takes account of the entropy change between the pipe node P and the boundary node 1. In order to solve the boundary problem, it is possible to neglect locally the entropy increase due to the wall friction model and to the heat exchanges model between i and 1. As the spacial discretization is assumed to be small, this simplification has a negligible impact on the final result.

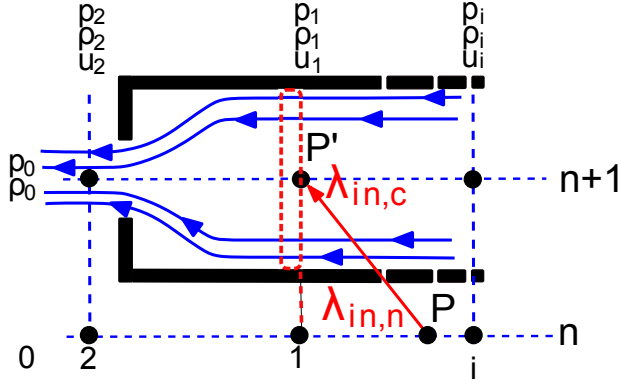


FIG. 10.6 – Non-homentropic Riemann variable definition for the valve outflow case.

Additionally, the pipe section at i and 1 are equal. Consequently, in reference to figure 10.6, one can write that :

$$\lambda_{in,c} = \lambda_{in,n} \quad (10.18)$$

$$A_{P'} + \frac{\gamma - 1}{2} U_{P'} = A_P + \frac{\gamma - 1}{2} U_P \quad (10.19)$$

This means that $\lambda_{in,c}$ is directly known using the CIR method at the point P (see Fig. 10.6). Nevertheless, the increase of entropy due to the outflow valve model equations between 1 and 2 must be taken into account. In order to achieve this it is necessary to build an iterative scheme. In fact, Benson [5] has shown that this iterative process is required even in the case where the flow is fully isentropic between 1 and 2. This is illustrated in the following of the section.

10.3.1 Isentropic outflow boundary resolution

The homentropic outflow valve boundary has been introduced in the literature review chapter under the outflow partially open-end reference. It has been seen that the introduced system of equations is the following one in the case of subsonic flow : [isentropic_{1/2}, mass_{1/2}, energy_{1/2}, $p_2 = p_0$, $a^2 = \frac{2p}{\rho}$, MOC]. In order to solve this fully homentropic boundary condition, Benson [5] proposes the following method : the energy (Eq. 10.20), isentropic Eq. (10.21) and mass (Eq. 10.22) equations are combined in order to produce the equivalent equation 10.23, where $\phi = \frac{F_2}{F_1}$:

$$a_1^2 + \frac{\gamma - 1}{2} u_1^2 = a_2^2 + \frac{\gamma - 1}{2} u_2^2 \quad (10.20)$$

$$\frac{a_2}{a_1} = \left(\frac{p_1}{p_2} \right)^{\frac{\gamma-1}{2\gamma}} \quad (10.21)$$

$$\rho_1 u_1 F_1 = \rho_2 u_2 F_2 \quad (10.22)$$

$$\frac{u_1}{a_2} = \sqrt{\frac{\frac{2}{\gamma-1} \left[\left(\frac{a_1}{a_2} \right)^2 - 1 \right]}{\frac{1}{\phi^2} \left(\frac{a_1}{a_2} \right)^{\frac{4}{\gamma-1}} - 1}} \quad (10.23)$$

Introducing $A^* = \frac{a_1}{a_2}$ and after development, Benson introduces Eq. 10.24 which must be solved in order to solve the previous system of equations. Once A^* has been calculated and as a_{ref} is arbitrarily fixed, it is subsequently possible to calculate u_1 and p_1 . However, Eq. 10.24 must be solved using an iterative

scheme. Benson introduced a method based on dichotomy, however, it is possible and without any difficulty to introduce a Newton-Raphson based on A as the convergence variable.

$$f(A) = \left(A^{\frac{4}{\gamma-1}} - \phi^2 \right) (\lambda_{in,c} - A)^2 - \frac{\gamma-1}{2} (A^2 - 1) \phi^2 = 0 \quad (10.24)$$

In the case of sonic flow, the sonic throttle equation is introduced ($\frac{u_2}{a_2} = 1$), and a similar development as previously shown leads to Eq. 10.25, which must be solved using an iterative scheme. In the case of sonic flow, the ratio $\frac{a_1}{a_2}$ is constant for a given value of ϕ and this ratio must be known in order to determine the other quantities. This ratio of sound speed is referred as the critical sound speed ratio $\left(\frac{a_1}{a_2}\right)_{cr}$ when the flow becomes sonic at throat.

$$f\left(\frac{a_1}{a_2}\right)_{cr} = \phi^2 - \left[\frac{\gamma+1}{\gamma-1} - \left(\frac{2}{\gamma-1} \right) \left(\frac{a_1}{a_2} \right)_{cr}^2 \right] \left(\frac{a_1}{a_2} \right)_{cr}^{\frac{4}{\gamma-1}} = 0 \quad (10.25)$$

10.3.2 Non-isentropic outflow boundary resolution

From the literature review, it appears that in the case of the outflow valve boundary condition, the only developed model found in the literature relies on an isentropic flow assumption between 1 and 2 (see section 8.3.2). This model is necessarily combined to a discharge coefficient C_d , as the isentropic flow assumption is no realistic. In an attempt to reduce the need of such an experimental correction, some non-isentropic outflow valve models have been developed in this thesis. Such models are developed and detailed in the next chapter (Chap. 11). These models introduce the resolution of the momentum conservation equation expressed between states 1 and 2 :

$$(p_1 + \rho_1 u_1^2) F_1 = (p_2 + \rho_2 u_2^2) F_2 - (p_1 + \Psi \rho_1 u_1^2)(F_1 - F_2) \quad (10.26)$$

Eq. 10.26 replaces the isentropic flow equation in the system of equations 10.20 to 10.22. Consequently, it is not possible to derive Eq. 10.23 and 10.24 anymore. In order to overcome this issue, a polytropic approach has been developed. The goal of this method is to keep the formulation of the non-isentropic model resolution scheme as close as possible to Benson's isentropic formulation, as it allows to keep the developments simple and easy to solve.

Polytropic formulation of the non-isentropic outflow boundary

It has been seen that the outflow resolution scheme from the literature is based on an isentropic flow assumption. It is proposed to develop a non-isentropic outflow resolution scheme based on a polytropic formulation. In the case where the flow is not isentropic between 1 and 2, one gets :

$$\frac{a_2}{a_1} \neq \left(\frac{p_1}{p_2} \right)^{\frac{\gamma-1}{2\gamma}} \quad (10.27)$$

However, it is possible to identify a polytropic exponent κ such that :

$$\frac{a_2}{a_1} = \left(\frac{p_1}{p_2} \right)^{\frac{\kappa-1}{2\kappa}} \quad (10.28)$$

It is possible to calculate the value of κ and to plot its evolution on a data map :

$$\kappa = \frac{-1}{2 \log(\frac{a_1}{a_2}) / \log \frac{p_1}{p_2} - 1} \quad (10.29)$$

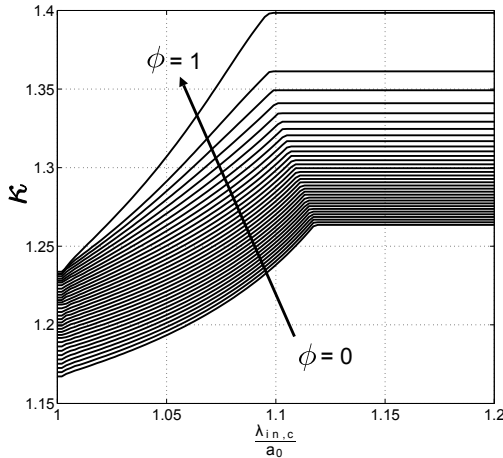


FIG. 10.7 – Polytropic coefficient evolution with respect to the incident Riemann variable. The curves have been built using Eq.10.26 with $\Psi = 1$.

On Fig. 10.7, κ is plotted with respect to $\frac{\lambda_{in}}{a_0}$ where a_0 is the total sound speed upstream of the restriction (Eq. 10.30). The corresponding outflow valve model has been built using the momentum equation 10.26 with $\Psi = 1$.

$$a_0^2 = a_1^2 + \frac{\gamma - 1}{2} u_1^2 = a_2^2 + \frac{\gamma - 1}{2} u_2^2 \quad (10.30)$$

It is reminded that in the case of an isentropic process of a perfect gas, $\kappa = 1.40$. In this case, the deviation from 1.40 expresses an increase of the entropy level due to the irreversibilities taken into account by the momentum equation resolution. Once the flow becomes sonic at throat, the evolution of $\frac{a_1}{a_2}$ with respect to $\frac{p_1}{p_2}$ is constant, therefore the corresponding polytropic coefficient remains constant in the sonic operating range. Now, it is possible to develop the system of equations Eq.10.31, Eq.10.32 and Eq.10.33. The combination of these equations allows to develop Eq. 10.34.

$$a_1^2 + \frac{\gamma - 1}{2} u_1^2 = a_2^2 + \frac{\gamma - 1}{2} u_2^2 \quad (10.31)$$

$$\frac{a_2}{a_1} = \left(\frac{p_1}{p_2}\right)^{\frac{\kappa-1}{2\kappa}} \quad (10.32)$$

$$\rho_1 u_1 F_1 = \rho_2 u_2 F_2 \quad (10.33)$$

$$\frac{u_1}{a_2} = \sqrt{\frac{\frac{2}{\gamma-1} \left[\left(\frac{a_1}{a_2}\right)^2 - 1 \right]}{\frac{1}{\phi^2} \left(\frac{a_1}{a_2}\right)^{\frac{4}{\kappa-1}} - 1}} \quad (10.34)$$

As in the homentropic case, Eq. 10.34 is developed and this allows to get Eq. 10.35 which must be solved in order to solve the subsonic non-homentropic outflow valve boundary problem :

$$f(A) = \left(A^{\frac{4}{\kappa-1}} - \phi^2\right) (\lambda_{in,c} - A)^2 - \frac{\gamma - 1}{2} \left(A^2 - 1\right) \phi^2 = 0 \quad (10.35)$$

In the case of sonic flow at throat ($\frac{u_2}{a_2}$), the following equation is derived :

$$f\left(\frac{a_1}{a_2}\right)_{cr} = \phi^2 - \left[\frac{\gamma + 1}{\gamma - 1} - \left(\frac{2}{\gamma - 1}\right) \left(\frac{a_1}{a_2}\right)_{cr}^2\right] \left(\frac{a_1}{a_2}\right)_{cr}^{\frac{4}{\kappa-1}} = 0 \quad (10.36)$$

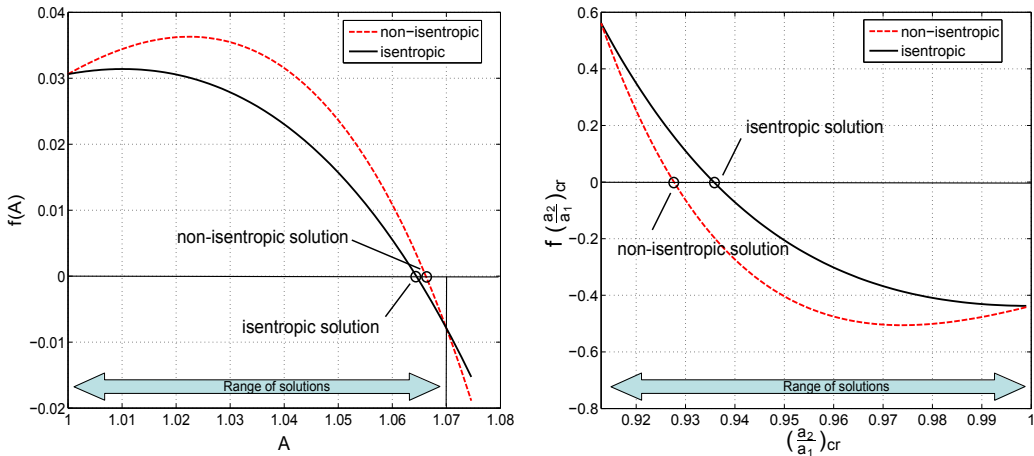


FIG. 10.8 – Solutions of Eq. 10.35 (left) and Eq. 10.36 (right) for $\lambda_{in,c} = 1.07$ and $\phi = 0.75$, in the isentropic and non-isentropic cases. The non-isentropic curves have been built using the polytropic expression of Eq.10.26 with $\Psi = 1$.

An example of the evolution of $f(A)$ and $f(\frac{a_1}{a_2})_{cr}$ are shown on Fig. 10.8 in the isentropic and the non-isentropic cases. From this plot, it appears that the introduction of the entropy change across the valve modifies the value of A (resp. $(\frac{a_1}{a_2})_{cr}$ for which $f(A) = 0$ (resp. $f(\frac{a_1}{a_2})_{cr} = 0$). The introduction of the non-isentropicity is performed by the mean of the polytropic coefficient κ .

10.3.3 Creation of the datemap of κ :

In order to simplify the resolution of the overall problem, it is interesting to express κ by the means of a datemap. Such datemap is built using the following process :

1. A non-homentropic model is chosen for the outflow restriction. Such models are developed in the next chapter, for example a non-homentropic partially open-end (see section 11.2), a nozzle (see subsection 11.2) or a valve (see subsection 11.4.2).
2. Calculation techniques are provided in the next chapter in order to calculate the complete solution range of the following 6 quantities : p_1, p_2, a_1, a_2, u_1 and u_2 . For example, in the case of the outflow partially open-end, the method provided in section 11.2.1 allows to build the solution for the 6 quantities.
3. Once these quantities are known, equation 10.29 : $\kappa = \frac{-1}{2 \log(\frac{a_1}{a_2})/\log \frac{p_1}{p_2} - 1}$ is used in order to calculate κ .

10.3.4 Implementation of the proposed iterative loop : outflow case

The developed method allows to solve the outflow valve boundary problem in the non-homentropic case. The change of entropy level between 1 and 2 is taken into account via a polytropic formulation. It is proposed in this section to detail the implementation of the proposed non-homentropic outflow iterative loop.

It is considered that the polytropic coefficient κ is stored into a datemap with respect to $\frac{\lambda_{in,c}}{a_0}$, with a_0 the total speed sound upstream of the restriction. One considers that the time step n has been completed, which means that any state is known within the pipe or at its boundary. In order to perform the calculation at time step $n + 1$, a numerical scheme (for example Lax-Wendroff) is used to calculate the states of the nodes inside the pipe. Now, it is necessary to calculate the state at the outflow boundary : the goal is to determine the state at point P' using the incident characteristic coming from the point P (see Fig. 10.6). In

the following developments, upper case variables are used. These variables are non-dimensional, with respect to the state upstream of the restriction : $A_x = \frac{a_x}{a_0}$, $U_x = \frac{u_x}{a_0}$ and $P_x = \frac{p_x}{a_0}$, with a_0 the total sound speed (Eq. 10.30).

Subsonic case :

- From Benson's work [5], it appears that the solution of $f(A) = 0$ will lie between 1 and $\lambda_{in,c}$. Therefore, the sound speed ratio $A_{P'}^{it}$ is initialized as follows : $A_{P'}^{it} = \frac{1+\lambda_{in,c}}{2}$.
- Using the energy conservation ($1 = A^2 + \frac{\gamma-1}{2} U^2$), it is possible to determine the value of $U_{P'}^{it}$.
- In the outflow case, it has been seen (see Eq. 10.18) that $\lambda_{in,c}$ is directly known from the point P using the CIR method. As $\lambda_{in,c}$, $A_{P'}^{it}$ and $U_{P'}^{it}$ are known, the following relationship : $\frac{\lambda_{in,c}}{a_0} = A_{P'}^{it} + \frac{\gamma-1}{2} U_{P'}^{it}$ allows to determine the value of a_0 .
- $\frac{\lambda_{in,c}}{a_0}$ is then calculated and used as the input of the datamap of κ vs. $\frac{\lambda_{in,c}}{a_0}$ (see Fig. 10.7), which allows to get the value of the polytropic coefficient.
- Now that κ^{it} , $A_{P'}^{it}$ and $\lambda_{in,c}$ are known the value of $f(A)$ can be calculated. In the case where $f(A) < C_C$, the solution is converged (C_C is the convergence criterion). In the case where $f(A) > C_C$, the Newton-Raphson algorithm is introduced in order to update the value of $A_{P'}^{it}$. The loop is run until the solution is converged.

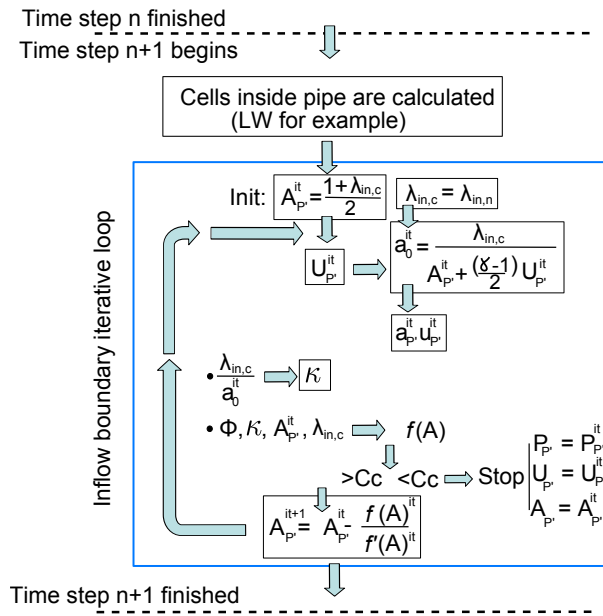


FIG. 10.9 – Chartflow of the proposed outflow iterative loop. Subsonic case.

Sonic case :

- Using Benson's work ([5]), the solution of $f(\frac{a_{P'}}{a_2})_{cr} = 0$ is initialized as follows : $(\frac{a_{P'}}{a_2})_{cr}^{it=1} = 1 + \sqrt{\frac{2}{\gamma+1}}$
- It has been seen that the polytropic coefficient κ is constant in the sonic flow operating range. Therefore, in the sonic case, the value of the flow area ratio ϕ leads directly to the value of κ .
- $f(\frac{a_{P'}}{a_2})_{cr}$ is calculated. In the case where $f(\frac{a_{P'}}{a_2})_{cr} > C_C$, the Newton-Raphson algorithm is introduced in order to update the value of $(\frac{a_{P'}}{a_2})_{cr}$. The loop is run until the solution is converged.

4. Finally, by introducing the value of $\lambda_{in,c}$ the value of $A_{P'}$, $U_{P'}$ and $P_{P'}$ are determined.

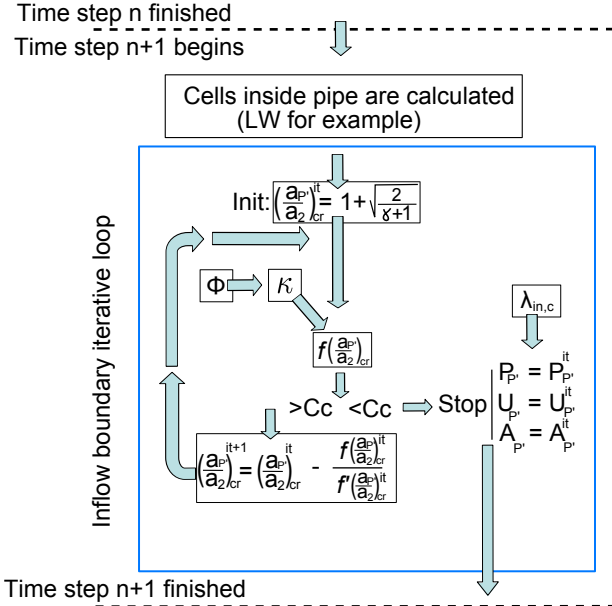


FIG. 10.10 – Chartflow of the proposed outflow iterative loop. Sonic case.

10.4 Convergence criterion choice

The iterative scheme developed for the inflow and outflow boundary resolution allow to converge towards the solution within a chosen tolerance. This tolerance is referred as the convergence criterion C_C , which is defined by the user. The lower the convergence criterion, the slower the calculation. However, low values of C_C provide better accuracy to the numerical scheme. From various numerical tests, it appeared that defining $C_C = 10^{-5}$ allows to provide good accuracy while allowing quick convergence thanks to the Newton-Raphson algorithm. In fact, when values higher than 10^{-5} are imposed to the convergence criterion, spurious oscillations can occur at the boundary (Fig. 10.11).

The case shown on Fig. 10.11 is detailed : a rarefaction wave is incident to the partially open-end boundary. Therefore, when the wave reaches the boundary, some back flow from the stagnation state occurs. In this case, it is necessary to detect the direction of the flow. This is performed by using the sign of $(\lambda_{in} - 1)$ ([5], [139]). Consequently, the convergence error due to the iterative scheme has two consequences on the global simulation :

- At first, the convergence error leads to error made on the calculation of the flow quantities (pressure, density, particle speed...).
- Secondly, these errors have an impact on the calculation of λ_{in} . Now, λ_{in} is used as a detection criterion of the flow direction. Therefore, in the case where high values of convergence criterion are used, misdetection of the flow direction may occur. In this case, this leads to the creation of spurious oscillations.

This phenomenon is clearly illustrated on Fig.10.11 : the reduction of the convergence criterion is directly correlated to the reduction of the spurious oscillations at the boundary node.

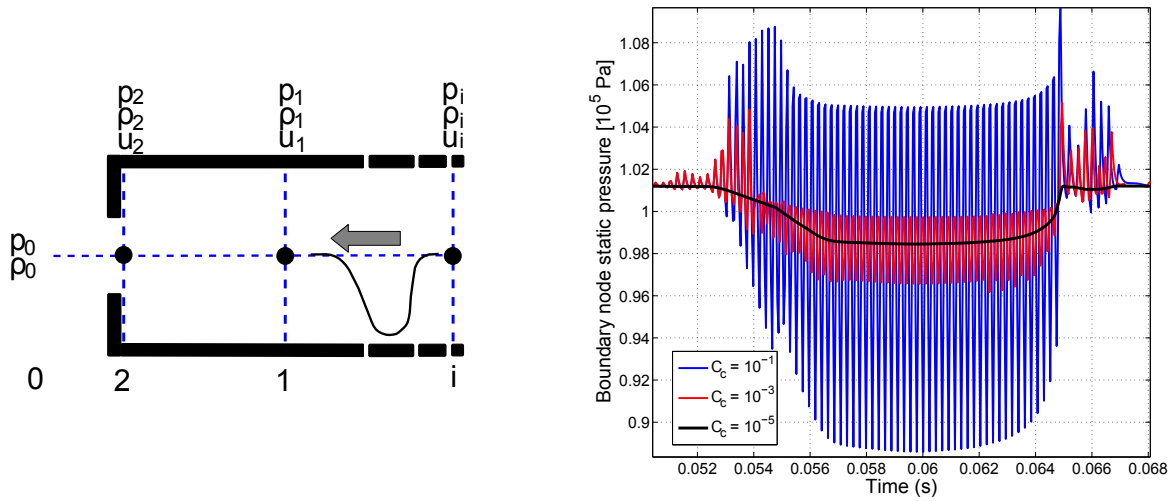


FIG. 10.11 – Illustration of the impact of the convergence criterion value C_C on the creation of spurious oscillations at boundary. Left : The considered case is a rarefaction wave incident on a partially open-end. Right : Calculated static pressure at the boundary node for various values of C_C .

10.5 Convergence speed

The main goal of the implementation of the Newton-Raphson algorithm was to reduce the computational requirements. In order to analyze the gains of the Newton-Raphson algorithm compared to the original Benson convergence scheme, a comparative study has been performed. A valve opening-closure cycle has been performed in order to simulate an intake flow (outflow valve boundary model) or an exhaust flow (inflow valve boundary model). During the simulation, the number of iteration required by the iterative scheme is stored. Typical results from this study are shown on Fig. 10.12.

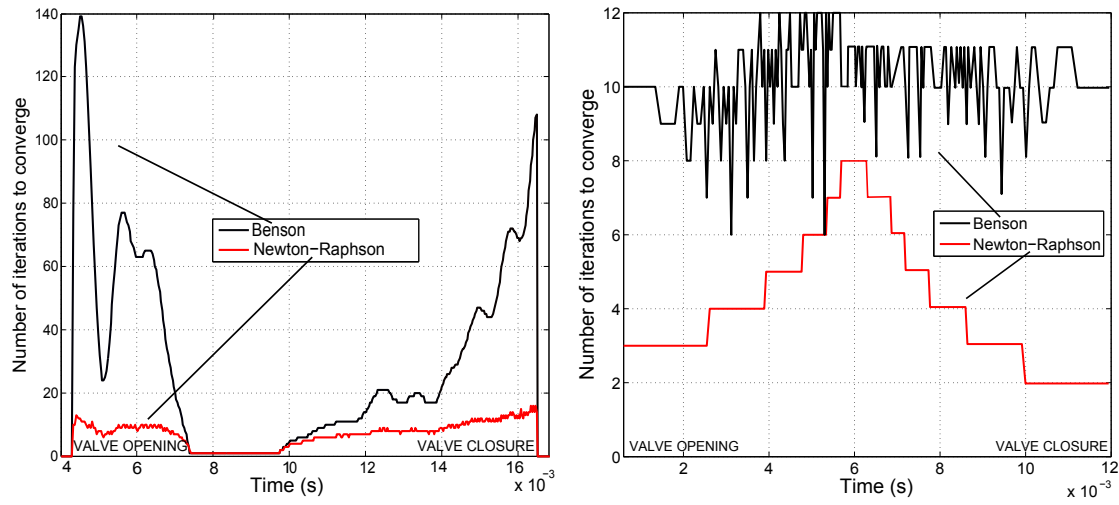


FIG. 10.12 – Comparison of the number of iterations required by the studied convergence schemes. Subsonic test case with pressure ratio = 1.55. Convergence criterion : $C_c = 10^{-5}$. Left : Inflow valve model results. Right : Outflow valve model results.

The following observations have been made :

- Inflow valve : The implementation of the Newton-Raphson algorithm on the entropy correction loop

allows to decrease by a factor 4-5 (on the average) the number of iterations required to converge towards the solution. This factor has been observed both in subsonic and sonic cases. On the average, for one single exhaust cycle, this allows to reduce the number of iterations from ~ 20000 (Benson) to 4500 (present work with Newton-Raphson), for a convergence criterion of 10^{-5} .

- Outflow valve : In this case, the gain is lower, as the number of iteration is reduced by a factor 1.5 on the average. In fact, it should be noticed that the main goal of the outflow valve boundary resolution work in this thesis was to deal with non-homentropic valve models.

Optimized iterative scheme for the MOC entropy correction loop : main points

Inflow valve :

- In the inflow valve case, the entropy correction loop has been derived and a Newton-Raphson iterative scheme has been implemented.
- It has been seen that the Newton-Raphson developments lead to derivative formulations which cannot be solved analytically. In order to overcome this issue, the data maps corresponding to the inflow valve equations are used to express the evolution the inflow valve model quantities. This allows to use numerical derivation to develop the Newton-Raphson algorithm.
- The choice of the convergence variable is crucial, as some variables will lead to the introduction of infinite slopes, which will introduce errors into the numerical derivation and won't allow the Newton-Raphson scheme to converge.
- The average number of iterations required to converge to the final inflow valve solution has been reduced by a factor 4-5. For a single exhaust cycle, this allows to reduce the number of iterations from ~ 20000 (Benson) to ~ 4500 (present work with Newton-Raphson), for a convergence criterion of 10^{-5} .

Outflow valve :

- In the outflow valve case, even when the entropy change across the valve is taken into account, it is possible to write that $\lambda_{in,c} = \lambda_{in,n}$. Therefore, even though an iterative scheme is imperatively required to solve the outflow boundary problem, this is not an entropy correction loop strictly speaking.
- The main limitation identified in the literature review is that the outflow valve boundary was only solved in the homentropic case. The main outcome of the present work is that a mathematical formulation has been developed in order to solve non-homentropic outflow valve problems.
- This formulation is based on the introduction of a polytropic expression of the entropy change across the valve. This allows to keep the same formulation as in the homentropic case. Consequently, the overall resolution process is kept as simple as possible.
- Additionally, a Newton-Raphson algorithm has been implemented on this formulation. Nevertheless, even though some gains have been observed, they are much smaller than in the inflow valve case.

Chapter 11

Non-isentropic boundary condition models : data maps building and new developments

In this section, it is intended to :

1. Specify the process introduced in order to build the non-isentropic datamaps associated to the boundary models. It has been seen in the previous chapter that the implementation of the Newton-Raphson algorithm on the boundary resolution scheme relies on data maps in order to perform numerical derivation. For each model introduced in this chapter, the resolution process adopted to produce the corresponding non-homentropic data maps will be briefly described and the corresponding data maps analyzed.
2. Introduce new boundary condition models. It has been seen in the literature review that most of the aerodynamical models of the engine airpath rely on some experimental corrections. It is proposed to build models based on the complete Euler's equations set in order to get more physical results without having to introduce experimental correction.

The synthesis of the models developed in this section is shown on table 11. In the case of the inflow models, it appears that no new development is proposed for the partially open-end restrictions (POE). In fact, it has been seen that the models from the literature are based on the complete Euler's equations set, completed by some hypotheses based on experimental observations. Therefore, it is only intended to detail the process introduced in order to build their non-homentropic datamaps (section 11.1). However, new developments are proposed in the case of the poppet valve models. Such devices are usually modeled using the same models as the POE, but associated to experimental correction terms. The proposed inflow poppet valve model relies on an assembly of non-homentropic sub-models in order to take into account the valve geometry (subsection 11.4.1).

In the case of the outflow restrictions, the models from the literature are based on the assumption that the flow is isentropic through the restriction. As this assumption is not representative of the real flow conditions, such models are systematically corrected using experimental corrections. In this section, it is proposed to develop non-isentropic models for the outflow restrictions. In the case of the partially open-ends, a method in order to solve the complete Euler's equations will be detailed (section 11.2, Eq.11.33 to 11.43) . This model will be extended to the case of an outflow nozzle, by modifying the terms of the momentum conservation equation (section 11.2, Eq.11.44 to 11.45). An assembly of sub-models will also be proposed in order to model an outflow poppet valve (subsection 11.4.2).

Finally, it will be shown that the existing and the developed boundary restriction models can be combined in order to solve the flow upstream and downstream a diaphragm without introducing the isentropicity assumption (section 11.3).

Flow direction	Boundary condition	Literature model	Proposed model in thesis
Inflow	POE (subsonic)	Sudden enlargement	-
		Cst pressure	-
	POE (sonic)	Sonic throat	-
		Matched nozzle	-
	Poppet valve	Sudd. enlargement + exp. corr	Sub-models assembly
Outflow	POE	Isentropic + exp. corr.	Euler's equations resolution
	Nozzle	-	Euler's equations resolution + momentum eq. modification
	Poppet valve	Isentropic + exp. corr	Sub-models assembly
Inpipe	Diaphragm	Isentropic + exp. corr.	Inflow+Outflow models assembly

TAB. 11.1 – Synthesis of the boundary condition models developed in this section.

Note : In the case of the POE inflow, distinction is made between the subsonic and sonic flows, as they involve different models. This is not the case in the outflow case, as the sonic flow is just an extension of the subsonic case.

11.1 Inflow restriction models : Partially open-ends (POE)

In this section, equations and assumptions from literature inflow valve models are re-developed in order to build non-homentropic data maps. Indeed, it has been seen in the literature review that Benson [5] managed to build $\frac{u}{a_{ref}}$ vs. $\frac{a}{a_{ref}}$ data maps of valve models, but under homentropic flow assumption. It is necessary to build data maps without introducing the homentropic flow assumption, as it is not representative of the models equations sets.

The control volume is reminded on figure 11.1 : the gas enters the pipe as a jet of cross-sectional area $F_2 = F_t$. It then expands to occupy the full bore at plane 1. The isolated system is located between planes 1 and 2. It should be noticed that on real systems, a distance of around 20 times the diameter of the flow restriction is required to get rid of non-homogeneous effects and pressure recovery. In the following developments, it is considered that the flow become homogeneous immediately after the restriction, at plane 1.

There are 6 unknown quantities (pressure, density , velocity at 1 and 2), so six equations are needed. These equations are reminded here and the process adopted to build non-homentropic data maps is described in the following developments. The upper case variables are the non-dimensional variables with respect to a reference state. The mathematical expressions developed below have been obtained using the stagnation state 0 as the reference state. Therefore, $A = \frac{a}{a_0}$, $U = \frac{u}{a_0}$ and $P = \frac{p}{p_0}$. The first equation is provided by the isentropic contraction assumption between the exterior and throat :

$$P_2 = A_2^{\frac{2\gamma}{\gamma-1}} \quad (11.1)$$

The second equation is given by the conservation of total energy between exterior and throat :

$$A_2^2 + \frac{\gamma-1}{2} U_2^2 = 1 \quad (11.2)$$

Third and fourth equations are respectively given by the conservation of total energy and of the mass between the throat and the pipe entry :

$$A_1^2 + \frac{\gamma-1}{2} U_1^2 = A_2^2 + \frac{\gamma-1}{2} U_2^2 \quad (11.3)$$

$$\rho_1 U_1 = \phi \times \rho_2 U_2 \quad (11.4)$$

In the subsonic case, a fifth equation is added by considering either the resolution of the momentum equation between 1 and 2 or by introducing a constant pressure assumption ($p_1 = p_2$). In the sonic case, the fifth equation is provided by the sonic throat equation ($u_2 = a_2$). A sixth equation is required to solve the set of equations. Benson introduced the MOC relations ($\lambda_{in} = A - \frac{\gamma-1}{2}U$) in order to solve the system. However, this leads to the implicit introduction of an isentropic process, and the final data map is not representative of the equations used to build the model. In order to overcome this issue, the following approach has been adopted :

1. When the flow is subsonic, the throat non-dimensional speed $\frac{u_2}{a_0}$ is imposed. If the flow is sonic at the throat, the pipe non dimensional speed $\frac{u_1}{a_0}$ is imposed.
2. Using the set of equations chosen to build the model, the five other quantities are determined.
3. By varying $\frac{u_2}{a_0}$ or $\frac{u_1}{a_0}$ within their physical range, the entire valve operating range is covered.
4. As the 6 quantities are known at each operating point of the valve, it is possible to build a complete data-map.

The inflow restriction models are now developed in order to build their characteristics data maps :

11.1.1 Subsonic case : non-homentropic data maps building

In order to create the data-map, one imposes a subsonic solution at the throat. From the energy equation :

$$U_2 \in [0; \sqrt{\frac{\gamma+1}{2}}] \quad (11.5)$$

This relation is used along with Eq. 11.1, 11.2, 11.3, 11.4. At this point, one last equation is needed to close the system. Here appears the different assumptions yielding to the two families of subsonic inflow valve models found in the literature : the constant pressure model [5] [139] and the momentum equation model [5] [72] [32].

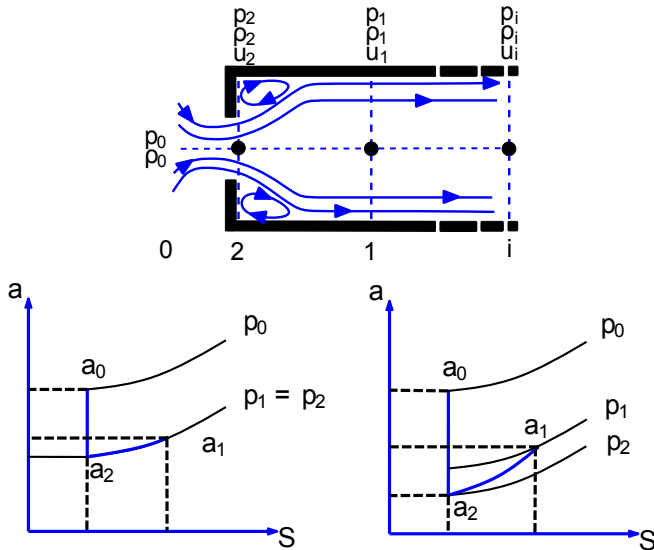


FIG. 11.1 – Subsonic inflow valve models sound speed vs. entropy evolution - constant pressure model (left) - momentum conservation (right)

Subsonic constant pressure model :

With this assumption, the gas is supposed to expand adiabatically, but irreversibly at constant pressure between valve throat and pipe entering. This assumption will be applied only for a subsonic flow at throat.

$$P_1 = P_2 \quad (11.6)$$

Rearrangement of equations (11.1), (11.2), (11.3), (11.4), (11.6) leads to equation (11.7).

$$\frac{U_1}{1 - U_1^2} = -\frac{\phi}{A_2} \times \sqrt{\frac{2}{\gamma - 1} \left[\frac{1}{A_2^2} - 1 \right]} \quad (11.7)$$

This equation is solved and it is possible to create a data map using the following process :

1. Non dimensional speed at throat U_2 is chosen. A_2 is determined using Eq. (11.2).
2. Knowing A_2 , Eq. (11.7) is numerically solved in order to get U_1 . A_1 is calculated using the energy equation (11.3).
3. Using the isentropic evolution between the cylinder and the throat and the constant pressure assumption allows to determine $P_1 = \frac{p_1}{p_0}$ and $P_2 = \frac{p_2}{p_0}$.

Subsonic momentum resolution model (sudden enlargement model)

With this assumption, valid for a subsonic flow, the momentum equation between throat and pipe entering will be used to close the equation set :

$$\begin{aligned} & \rho_2 F_2 u_2^2 - \rho_1 F_1 u_1^2 \\ & + p_1 F_1 - p_2 F_2 - \int_2^1 p \frac{dF}{dx} dx = 0 \end{aligned} \quad (11.8)$$

In order to solve the integral $\int_2^1 p \frac{dF}{dx} dx$, Benson introduces the sudden enlargement assumption. It states that the pressure p_2 is uniform in the plane 2 and that it is applied to a section of the pipe area F_1 . Furthermore, the jet area in 2 is equal to the valve throat area : $F_2 = F_t$. This leads to the equation (11.9), which can be rewritten as in equation (11.10). Then a rearrangement of equations (8.18), (8.19), (11.3), (11.4), (11.10) leads to equation (11.11).

$$\phi \rho_2 u_2^2 - \rho_1 u_1^2 + (p_1 - p_2) = 0 \quad (11.9)$$

$$\frac{p_1}{p_2} = \frac{1 + \gamma \phi \left(\frac{u_2}{a_2} \right)^2}{1 + \gamma \left(\frac{u_1}{a_1} \right)^2} \quad (11.10)$$

$$U_1^2 - \frac{2}{\gamma + 1} \left[\frac{1}{\phi} \frac{A_2^2}{U_2} + \gamma U_2 \right] U_1 + \frac{2}{\gamma + 1} = 0 \quad (11.11)$$

Equation (11.11) is solved and it is possible create a data map using the following process :

1. Non dimensional speed at throat U_2 is chosen. A_2 is determined using Eq. (11.2).
2. Knowing A_2 , Eq. (11.11) is numerically solved in order to get U_1 . A_1 is calculated using the energy relation Eq. (11.3).
3. Using the isentropic evolution between the cylinder and the throat and equation (11.10) allows to determine $P_1 = \frac{p_1}{p_0}$ and $P_2 = \frac{p_2}{p_0}$.

11.1.2 Sonic case : non-homentropic data maps building

In the sonic case, the flow at the throat is sonic ($\frac{u_2}{a_2} = 1$), and this is the pipe flow speed u_1 which is imposed in order to build the data maps. From the literature study, two models can be derived in order to model the sonic inflow restriction model : one simply based on the sonic throat equation, and another one modeling the flow as a matched nozzle.

Sonic throat model

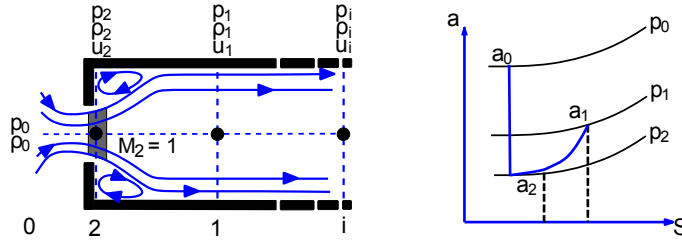


FIG. 11.2 – Sonic throat model : sound speed vs. flow entropy evolution

This model is directly derived as follows : Eq. 11.1, 11.2, 11.3, 11.4 are still introduced. U_1 is imposed (Eq. 11.12). U_{1cr} is the value of U_1 when the flow is just becoming sonic at throat. The introduction of the sonic throat expression (Eq. 11.13) provides a sixth equation, and the equations set is therefore complete.

$$U_1 \in [U_{1cr}; \sqrt{\frac{\gamma+1}{2}}] \quad (11.12)$$

$$U_2 = A_2 \quad (11.13)$$

Now, Eq. 11.13 and 11.2 give :

$$U_2 = A_2 = \sqrt{\frac{2}{\gamma+1}} \quad (11.14)$$

Rearrangement of equations (11.14) and (11.4) gives :

$$\frac{p_1}{p_1} = \frac{\phi}{\sqrt{\frac{2}{\gamma+1}}} \times \frac{A_1^2}{U_1} \quad (11.15)$$

Rearrangement of equations (11.1), (11.3), (11.15) gives :

$$\frac{p_1}{p_0} = \phi \times \frac{1 - \frac{\gamma-1}{2}(U_1)^2}{U_1} \times \left(\frac{2}{\gamma+1}\right)^{\frac{\gamma+1}{2(\gamma-1)}} \quad (11.16)$$

It is possible to solve the previous system of equations using the following process :

1. U_1 being imposed, equation (11.3) leads to A_1 , while equation (11.16) allows to determine $P_1 = \frac{p_1}{p_0}$. Now, the state is fully determined at plane 1.
2. As U_2 is known for a sonic flow, equation (11.4) allows to calculate ρ_2 .
3. Finally equation (11.1) leads to P_2 .

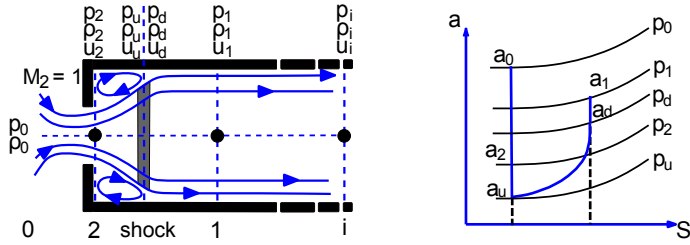


FIG. 11.3 – Matched nozzle model : sound speed vs. flow entropy evolution

Matched nozzle model

In this model, one assumes that the flow behaves as in the matched nozzle theory : a shock occurs at a section F_s such that $F_t < F_s < F_1$. One introduces the shock area ratio : $\phi_S = \frac{F_t}{F_s}$ such that $\phi < \phi_S < 1$. The associated system of equations is quite complex, as there are 13 unknown quantities. Twelve of them are pressure, density and velocity at plane (2), upstream the shock (u), downstream the shock (d) and at the pipe (1). The last unknown quantity is the area of the adaption shock F_S . The first 3 equations are provided using the isentropic contraction and energy conservation between the cylinder and plane 2 Eq. (11.17), Eq. (11.18) and sonic flow at the throat Eq. (11.19) :

$$P_2 = A_2^{\frac{2\gamma}{\gamma-1}} \quad (11.17)$$

$$A_2^2 + \frac{\gamma-1}{2} U_2^2 = 1 \quad (11.18)$$

$$U_2 = A_2 \quad (11.19)$$

Isentropic relaxation Eq. (11.20), total energy conservation Eq. (11.21) and mass conservation Eq. (11.22) between plane 2 and upstream of the shock are used.

$$\frac{P_u}{P_2} = \left(\frac{A_u}{A_2} \right)^{\frac{2\gamma}{\gamma-1}} \quad (11.20)$$

$$A_u^2 + \frac{\gamma-1}{2} U_u^2 = A_2^2 + \frac{\gamma-1}{2} U_2^2 = 1 \quad (11.21)$$

$$\rho_u U_u = \rho_2 U_2 \phi_S \quad (11.22)$$

A re-arrangement of equations (11.20), (11.21), (11.22) leads to :

$$\left[\frac{\sqrt{1 - \left(\frac{\gamma-1}{2} \right) U_u^2}}{A_2} \right]^{\frac{2}{\gamma-1}} = \phi_S \times \frac{U_2}{U_u} \quad (11.23)$$

Evolution across the adaptation shock is determined using total energy conservation Eq. (11.24), mass conservation Eq. (11.25) and momentum conservation Eq. (11.26) :

$$A_d^2 + \frac{\gamma-1}{2} U_d^2 = A_u^2 + \frac{\gamma-1}{2} U_u^2 = 1 \quad (11.24)$$

$$\rho_d U_d = \rho_u U_u \quad (11.25)$$

$$p_d - p_u = \rho_u u_u^2 - \rho_d u_d^2 \quad (11.26)$$

Re-Arrangements of Eq. (11.24), (11.25), (11.26) leads to the two following equations :

$$U_d^2 - \left(\frac{2}{\gamma + 1} \right) \left[\frac{A_u^2}{U_u} + \gamma U_u \right] U_d + \frac{2}{\gamma + 1} = 0 \quad (11.27)$$

$$\frac{p_d}{p_u} = 1 + \frac{2\gamma}{\gamma + 1} (M_u^2 - 1) \quad (11.28)$$

Finally, the last equation system is determined writing isentropic contraction Eq. (11.29), total energy conservation Eq. (11.30), mass conservation Eq. (11.31) between downstream of the shock and the pipe at 1 :

$$\frac{P_1}{P_d} = \left(\frac{A_1}{A_d} \right)^{\frac{2\gamma}{\gamma-1}} \quad (11.29)$$

$$A_1^2 + \frac{\gamma - 1}{2} U_1^2 = A_d^2 + \frac{\gamma - 1}{2} U_d^2 \quad (11.30)$$

$$\rho_1 U_1 = \rho_d U_d \frac{\phi}{\phi_S} \quad (11.31)$$

Re-Arrangement of Eq. (11.29), (11.30), (11.31) leads to :

$$\left[\frac{\sqrt{1 - \left(\frac{\gamma-1}{2} \right) U_1^2}}{A_d} \right]^{\frac{2}{\gamma-1}} = \frac{\phi}{\phi_S} \times \frac{U_d}{U_1} \quad (11.32)$$

It is possible to solve the previous system of equations and to create a data map using the following process :

1. ϕ_S is chosen. As the flow at throat is sonic, A_2 and U_2 are determined.
2. Using these values into Eq. (11.23) allows to calculate U_u . A_u is also known using energy conservation.
3. U_u and A_u are introduced in Eq. (11.27), which is solved to get U_d . A_d is calculated using energy conservation.
4. U_1 is calculated by Eq. (11.32). Using energy conservation leads to A_1 .
5. Using equations (11.29), (11.28), (11.20) and (11.17) allows to calculate any pressure ratio along the system.

11.1.3 Non-homentropic inflow boundary data maps : direct analysis

Using the previous developments, the characteristic data maps of the inflow restriction models are plotted on Fig. 11.4. This plot allows to make the comparison between each inflow boundary model. Results are shown in terms of non-dimensional flow speed at the boundary node 1. This quantity is directly linked to the mass flow rate running through the restriction. Results are also provided for several values of the opening ratio $\frac{F_2}{F_1}$.

In the sonic case, the flow evolutions provided by the two models are totally different : the flow modeled by the matched nozzle approach provides a constant non-dimensional speed in the sonic region. This flow velocity evolution is generally not found at boundaries such as valves. On the other hand, the flow modeled using the sonic throat approach provides an increase of the non-dimensional flow speed when the pressure ratio decreases. Horizontal evolution is reached once the sonic flow state has been established within the pipe itself. Such an evolution is representative of the inflow valve behavior [88].

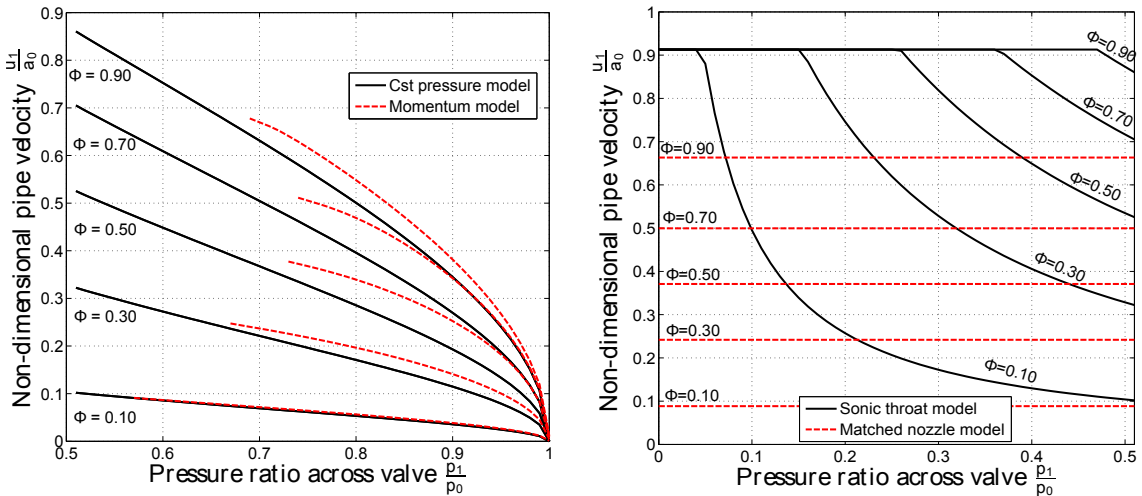


FIG. 11.4 – Steady flow results comparison between boundary restriction models : subsonic case (left) and sonic case (right).

In the subsonic case, it appears that the momentum resolution model systematically produces higher non-dimensional speed values than for the constant pressure model. Additionally, the sonic flow limit occurs for higher pressure ratio values. This is due to the 'pressure drop' effect which is a consequence of the momentum equation resolution. The resolution of the momentum under the sudden enlargement assumption provides pressures such that $p_2 < p_1$. This provides a 'pressure recovery' behavior between 2 and 1. In the case of the constant pressure model, the following condition is imposed : $p_2 = p_1$.

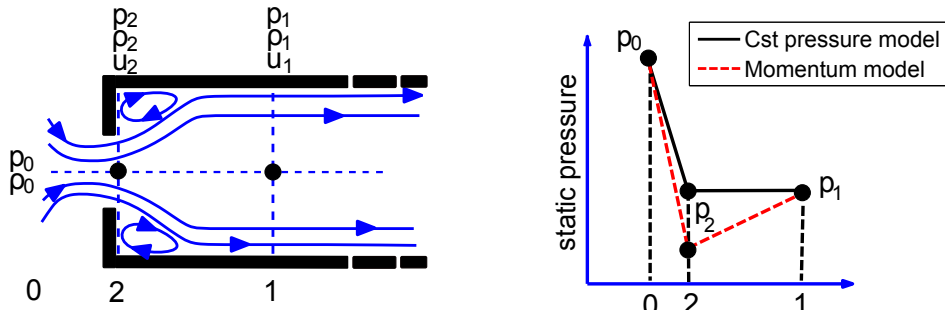


FIG. 11.5 – Spacial evolution of the static pressure for the subsonic inflow restriction models.

This provides the pressure evolutions shown on Fig. 11.5. The pressure ratio $\frac{p_2}{p_0}$, which is actually 'seen' by the restriction, is lower than the 'global' pressure ratio $\frac{p_1}{p_2}$ when the momentum equation is used. Consequently, for a given global pressure ratio $\frac{p_1}{p_0}$, the model using the momentum equation will provide higher velocity values.

11.2 Outflow restriction models : POE and nozzle.

In this section, a non-homentropic outflow restriction boundary will be developed. The only outflow restriction model found in the literature is based on an isentropic flow assumption and is systematically combined to an experimental coefficient correction approach. In order to reduce the need of such a correction, the resolution of the momentum equation instead of the isentropic equation is developed.

In order to solve the momentum conservation equation, the pressure distribution inside the pipe is non-

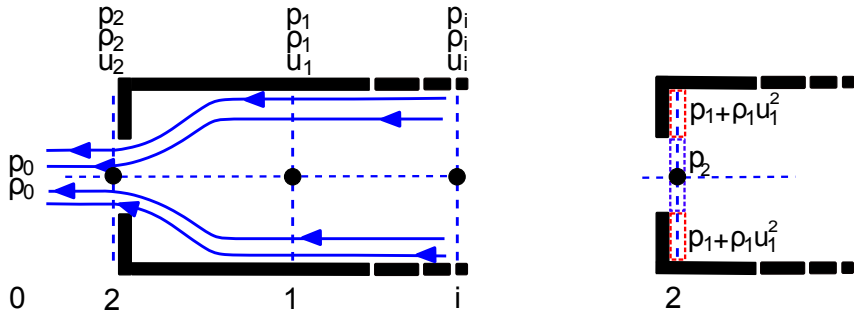


FIG. 11.6 – Subsonic outflow valve model considered system (left) and pressure distribution used to solve the momentum conservation (right)

uniform : at the throat, the static pressure is assumed to be equal to the pressure p_2 . However, the pressure applied on the wall is set as the total pressure from the upstream state 1. This approach is valid under a sudden restriction assumption and leads to the following momentum conservation equation :

$$(p_1 + \rho_1 u_1^2) F_1 = (p_2 + \rho_2 u_2^2) F_2 - (p_1 + \rho_1 u_1^2)(F_1 - F_2) \quad (11.33)$$

This equation can be re-written in the following formulation, with $\phi = \frac{F_2}{F_1}$

$$\frac{p_2}{p_1} = \frac{(2 - \phi) + \gamma \frac{u_1^2}{a_1^2} (2 - \phi)}{1 + \gamma \phi \frac{u_2^2}{a_2^2}} \quad (11.34)$$

Eq. 11.34 is introduced in the equation sets to solve both subsonic and sonic cases and to build the corresponding data maps. The equations set is provided by the conservation of total energy between exterior and throat (Eq. 11.35) and the conservation of total energy and of the mass between the throat and the pipe entry (Eq. 11.36 and 11.37) :

$$A_2^2 + \frac{\gamma - 1}{2} U_2^2 = 1 \quad (11.35)$$

$$A_1^2 + \frac{\gamma - 1}{2} U_1^2 = A_2^2 + \frac{\gamma - 1}{2} U_2^2 \quad (11.36)$$

$$\rho_1 U_1 = \phi \times \rho_2 U_2 \quad (11.37)$$

Using equations 11.34 to 11.37 allows to develop a mathematical formulation helpful to solve the systems of equations. The development of this formulation has been inspired by a development from Benson [5] in the inflow case. It is adapted here to deal with the outflow momentum resolution :

Equation 11.37 can be rewritten such that :

$$\frac{p_1}{p_2} = \phi \left(\frac{u_2}{u_1} \right) \left(\frac{a_1}{a_2} \right)^2 \quad (11.38)$$

Combining Eq. 11.34 and 11.38 allows to obtain the following equation :

$$\frac{(2 - \phi)}{\phi} + \gamma \frac{u_2^2}{a_2^2} = \frac{u_2}{u_1} \left(\frac{a_1}{a_2} \right)^2 + \gamma (2 - \phi) \frac{u_1}{a_2} \frac{u_2}{a_2} \quad (11.39)$$

Now, we introduce the total sound speed of the flow :

$$a_{tot}^2 = a_1^2 + \frac{\gamma - 1}{2} u_1^2 = a_2^2 + \frac{\gamma - 1}{2} u_2^2 \quad (11.40)$$

which can be re-written :

$$\left(\frac{a_1}{a_2}\right)^2 = \left(\frac{a_{tot}}{a_2}\right)^2 - \frac{\gamma - 1}{2} \left(\frac{u_1}{a_2}\right)^2 \quad (11.41)$$

Introducing Eq. 11.41 into Eq. 11.38 leads to :

$$\frac{(2 - \phi)}{\phi} + \gamma \frac{u_2^2}{a_2^2} = \frac{u_2}{u_1} \left[\left(\frac{a_{tot}}{a_2}\right)^2 - \frac{\gamma - 1}{2} \left(\frac{u_1}{a_2}\right)^2 \right] + \gamma(2 - \phi) \frac{u_1 u_2}{a_2 a_2} \quad (11.42)$$

Finally, multiplying Eq. 11.42 by $\left(\frac{2}{\gamma+1}\right) \left[\left(\frac{a_2}{a_{tot}}\right)^2 \frac{u_1}{u_2}\right]$ allows to get a second order polynomial expression of $\frac{u_1}{a_{tot}}$:

$$\left(\frac{\gamma - 1}{\gamma + 1} - \frac{2\gamma}{\gamma + 1}(2 - \phi)\right) \left(\frac{u_1}{a_{tot}}\right)^2 + \frac{2}{\gamma + 1} \left(\frac{(2 - \phi)}{\phi} \left(\frac{a_2}{a_{tot}}\right)^2 \frac{a_{tot}}{u_2} + \gamma \frac{u_2}{a_{tot}}\right) \frac{u_1}{a_{tot}} - \frac{2}{\gamma + 1} = 0 \quad (11.43)$$

Taking into account outflow simple geometries : the outflow nozzle

It is possible to modify the outflow momentum equation in order to take into account simple outflow geometries. It has been previously assumed that when the outflow geometry is a sudden flow contraction, the total upstream pressure is applied on the pipe wall at the exit of the pipe. In the case where the outflow geometry is a nozzle of a given angle, the dynamic pressure term $\rho_1 u_1^2$ which is applied on the wall at the exit of the pipe is modified by a corrective term Ψ . This term is directly linked to the outflow restriction geometry : if the nozzle angle is of 45° , it is assumed that 50% of the dynamic pressure is effectively applied on the wall, and that 50% of the dynamic pressure of the flow is deflected, which leads to $\Psi = 0.5$. The variation of the corrective factor with the nozzle angle is plotted on Fig. 11.7. This leads to the modified momentum equation 11.44 :

$$(p_1 + \rho_1 u_1^2) F_1 = (p_2 + \rho_2 u_2^2) F_2 - (p_1 + \Psi \rho_1 u_1^2)(F_1 - F_2) \quad (11.44)$$

The same developments as performed previously lead to the following equation, which is the equivalent of Eq. 11.43 :

$$\left(\frac{\gamma - 1}{\gamma + 1} - \frac{2\gamma}{\gamma + 1}(1 + \Psi(1 - \phi))\right) \left(\frac{u_1}{a_{tot}}\right)^2 + \frac{2}{\gamma + 1} \left(\frac{(2 - \phi)}{\phi} \left(\frac{a_2}{a_{tot}}\right)^2 \frac{a_{tot}}{u_2} + \gamma \frac{u_2}{a_{tot}}\right) \frac{u_1}{a_{tot}} - \frac{2}{\gamma + 1} = 0 \quad (11.45)$$

11.2.1 Subsonic outflow restriction boundary with momentum conservation : POE and nozzle data map building

In order to create the data-map, a subsonic solution is imposed at the throat :

$$U_2 \in [0; \sqrt{\frac{\gamma + 1}{2}}] \quad (11.46)$$

Additionally, the last equation, valid when the flow is subsonic, is provided by assuming that the static pressure at 2 is equal to the stagnation pressure p_0 :

$$p_2 = p_0 \quad (11.47)$$

Once U_2 is imposed, it is possible to calculate the other variables using the following process :

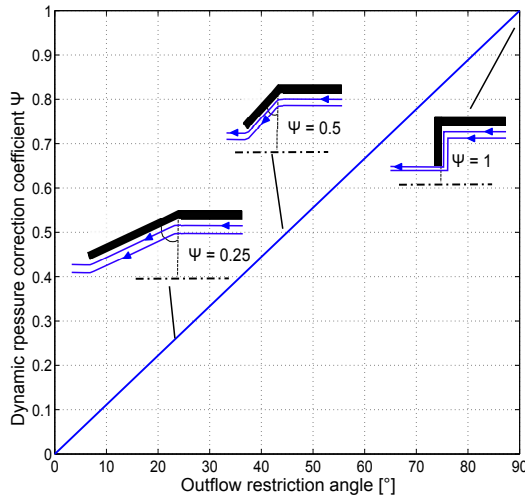


FIG. 11.7 – Evolution of Ψ with respect to the outflow angle.

1. Non dimensional speed at throat U_2 is chosen. A_2 is determined using Eq. (11.35).
2. Knowing A_2 , U_2 and ϕ , Eq. (11.43) (or Eq. (11.45)) is numerically solved in order to get U_1 . A_1 is calculated using the energy relation Eq. (11.36).
3. Using the constant pressure assumption between the throat and the stagnation state, p_2 is determined. Finally, Eq. 11.34 allows to calculate p_1 .

11.2.2 Sonic outflow restriction boundary with momentum conservation : POE and nozzle data map building

In the case where the flow is sonic at throat, one gets :

$$U_2 = A_2 = cst \quad (11.48)$$

When looking at Eq. 11.43, it appears that when U_2 , A_2 and ϕ are fixed, the solution of U_1 is a constant. Consequently, the value of A_1 is also a constant. Therefore, it appears that the system solution does not evolve once the flow is sonic at throat. Consequently, the data map in the sonic case is easily obtained :

1. The flow is sonic at throat, so : $A_2 = U_2 = \sqrt{\frac{2}{\gamma+1}}$.
2. The corresponding value of U_1 is determined using Eq. 11.43 (or Eq. 11.45). A_1 is calculated using the energy conservation equation.
3. The pressure ratio $\frac{p_1}{p_0}$ is varying between 0 and $(\frac{p_1}{p_0})_{cr}$. $(\frac{p_1}{p_0})_{cr}$ is the value of the pressure ratio value when the flow just becomes sonic at throat.

11.2.3 Non-homentropic outflow boundary data maps : direct analysis

Using the previous developments, the characteristic data maps of the outflow restriction models are plotted on Fig. 11.8. This plot compares the inflow boundary models : on the left plot, the isentropic model from the literature is compared to the model using the momentum equation with $\Psi = 1$. The right plot shows the results of the momentum model with $\Psi = 1$ and $\Psi = 0.5$. The results are shown in terms of non-dimensional flow speed at the boundary node 1. This quantity is directly linked to the mass flow rate running through the restriction. The results are also provided for several values of the opening ratio $\phi = \frac{F_2}{F_1}$.

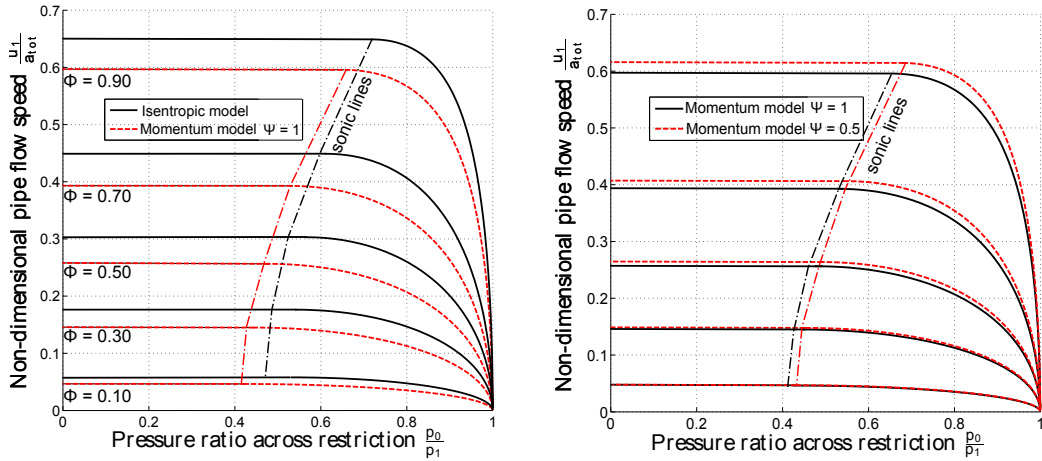


FIG. 11.8 – Steady flow results comparison between outflow boundary restriction models.

Left plot analysis : the curves show that the non-dimensional flow velocities are systematically higher in the case of the isentropic assumption than when the momentum equation is used. Additionally, the sonic flow limit occurs for higher pressure ratio values in the isentropic case. As the isentropic evolution neglects any loss occurring through the restriction, it produces higher velocities than when some losses are introduced via the momentum equation. Finally, the sonic flow blockage is visible on this plot, as the flow velocity evolution becomes horizontal in the sonic operating range.

Right plot analysis : the calculations performed with $\Psi = 0.5$ provide higher non-dimensional velocity values than when $\Psi = 1$, which means that the corrective factor applied on the dynamic pressure provides the correct trend to the flow evolution. Indeed, placing a nozzle at the exit of a pipe instead of a sudden contraction will increase the flow velocity. The impact of Ψ is clearly visible for the higher values of ψ . This is explained by the fact that the corrected dynamic pressure term $\Psi \rho_1 u_1^2$ is directly linked to the pipe flow velocity, which reaches higher values for the high values of the section ratio ψ .

11.3 Complete non-homentropic flow resolution upstream and downstream a diaphragm

In the previous model developments, some isentropic hypotheses are still introduced in order to simplify the resolution of the systems of equations. In the following section, a method in order to model the complete flow behavior upstream and downstream a flow restriction without introducing an isentropic simplification will be described. One considers the flow restriction shown on Fig. 11.9 : the flow comes from an upstream pipe of section F_3 . The gas runs through a flow restriction of section F_2 , and then goes in a downstream pipe of section F_1 . The following section ratios are introduced : $\phi_1 = \frac{F_2}{F_1}$ and $\phi_3 = \frac{F_2}{F_3}$. In order to model the flow evolution between 3 and 1, this restriction will be considered as the combination of a sudden restriction and a sudden enlargement.

One assumes that the flow is established and that this provides a non-dimensional flow velocity $U_2 = \frac{u_2}{a_{tot}}$ at the restriction throat. a_{tot} is the total sound speed of the flow :

$$a_{tot}^2 = a_1^2 + \frac{\gamma - 1}{2} u_1^2 = a_2^2 + \frac{\gamma - 1}{2} u_2^2 = a_3^2 + \frac{\gamma - 1}{2} u_3^2 \quad (11.49)$$

Knowing U_2 , it is possible to solve the flow problem between 2 and 1 by introducing the equations of the sudden enlargement inflow restriction boundary model : [energy_{1/2}, mass_{1/2}, momentum_{1/2}]. Using the developments described in subsection 11.1.1, this leads to the following equations in the subsonic case :

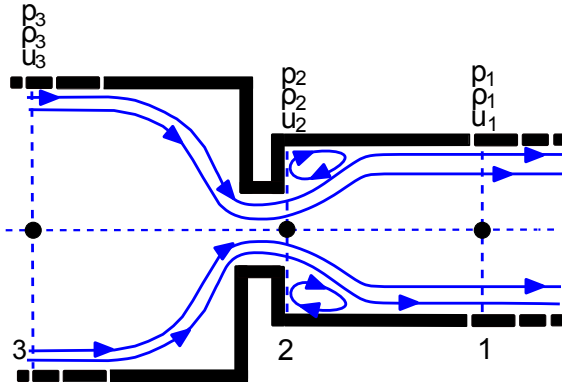


FIG. 11.9 – Considered system for the upstream/downtream restriction non-homentropic flow resolution.

$$U_1^2 - \frac{2}{\gamma + 1} \left[\frac{1}{\phi_1} \frac{A_2^2}{U_2} + \gamma U_2 \right] U_1 + \frac{2}{\gamma + 1} = 0 \quad (11.50)$$

$$\frac{p_1}{p_2} = \frac{1 + \gamma \phi_1 \left(\frac{u_2}{a_2} \right)^2}{1 + \gamma \left(\frac{u_1}{a_1} \right)^2} \quad (11.51)$$

The equations are solved using the same process as previously shown in the thesis, which allows to know U_2 , A_2 , U_1 , A_1 and $\frac{p_1}{p_2}$.

Now, it is necessary to solve the problem between 3 and 2. In order to do this, the equations of the sudden restriction model are introduced : [energy_{3/2}, mass_{3/2}, momentum_{3/2}]. Using the developments described in section 11.2, this leads to the following equations in the subsonic case :

$$\left(\frac{\gamma - 1}{\gamma + 1} - \frac{2\gamma}{\gamma + 1} (2 - \phi_3) \right) (U_3)^2 + \frac{2}{\gamma + 1} \left(\frac{1}{\phi_3} \frac{A_2^2}{U_2} + \gamma U_2 \right) U_3 - \frac{2}{\gamma + 1} = 0 \quad (11.52)$$

$$\frac{p_3}{p_2} = \phi_3 \left(\frac{U_2}{U_3} \right) \left(\frac{A_3}{A_2} \right)^2 \quad (11.53)$$

The equations are solved, which allows to get : U_3 , A_3 and $\frac{p_3}{p_2}$. By combining the results of the flow between 3 and 2 to the results obtained for the flow between 2 and 1, the global problem is solved. It should be noticed that the complete problem is solved without introducing any isentropic flow assumption. The sonic flow case is processed similarly as the subsonic case, but with the adequate sonic flow equations from subsections 11.1.1 and 11.2. An example of the flow evolution is shown on Fig. 11.10. In order to differentiate the impact of the upstream and downstream parts of the restriction on the global solution, the following study is performed : at first, the value of ϕ_3 is fixed at 0.50, and the downstream area ratio ϕ_1 is varying between 0.25 and 0.75. In a second time, ϕ_1 is fixed at 0.50 and the upstream area ratio ϕ_3 is varying between 0.25 and 0.75. This provides the following cases :

Case	ϕ_3	ϕ_1
1	0.50	0.25
2	0.50	0.50
3	0.50	0.75
4	0.25	0.50
5	0.75	0.50

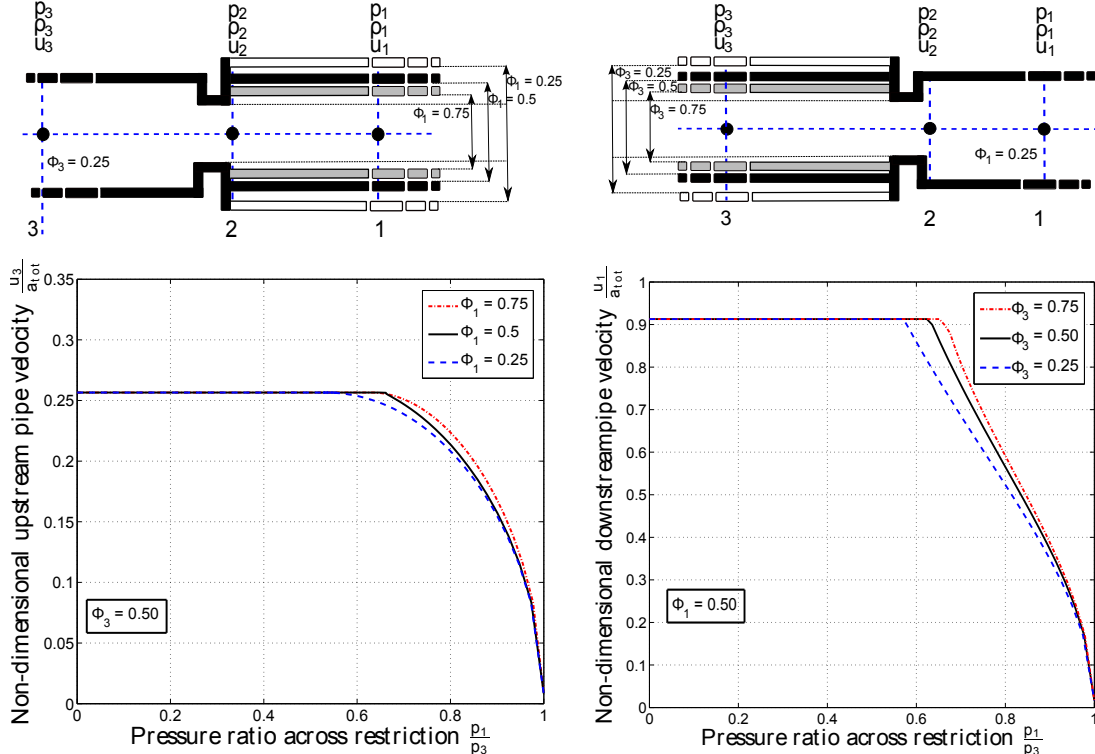


FIG. 11.10 – Left : impact of the downstream geometry ϕ_1 on the upstream non-dimensional flow velocity. Right : impact of the upstream geometry ϕ_3 on the downstream flow velocity.

On the left plot of Fig. 11.10, the evolution of the upstream velocity U_3 is plotted for three values of downstream pipe area ratio ϕ_1 . It appears that the higher value of ϕ_1 , the higher value of U_3 . It is reminded that $\phi_1 = \frac{F_2}{F_1}$. Therefore, at high values of ϕ_1 , the downstream sudden enlargement is lower : the flow is less affected by the restriction, leading to higher speed velocity values. On the right plot of Fig. 11.10, this is the downstream velocity U_1 which is plotted for three values of upstream pipe area ratio ϕ_3 . In this case again, it appears that the higher value of ϕ_3 , the higher value of U_1 . Consequently, lower sudden area restrictions allows to reach higher flow velocities.

It is concluded that this complete restriction modeling based on the resolution of the steady-flow Euler's equations mass, energy and momentum conservation) allows to take into account the effect of the flow upstream and downstream the restriction. This model will be validated experimentally in the next chapter.

11.4 Poppet valve boundary condition

In the following section, the models of the poppet outflow/inflow valves will be detailed. In the literature papers, poppet valves are usually modeled using the inflow/outflow sudden area change models coupled to an experimental correction. In reality, poppet valve flows are different from the sudden enlargement or

restriction flows. It has been intended in this section to take into account of the changes of flow section when exhaust or intake flows occur through a poppet valve. It will be seen that they are composed of an assembly of sub-models previously developed. The developed models have been inspired by observations made from the CFD calculation results. Typical flow structures for an axi-symmetrical poppet valve are shown on Fig. 11.11. This figure allows to introduce the planes which are used to develop the models : plane 0 is placed at the stagnation condition, 2 is the valve throat, which is defined as the minimum cross-section of the flow and 1 is placed within the pipe linked to the valve boundary. Plane 3 is the plane perpendicular to the flow at throat which provides the maximum flow cross-section between the valve and the wall outside of the pipe. L_t is the distance between planes 2 and 3, L_3 is the radial length of the flow section F_3 and L_2 the radial length of the flow section F_2 .

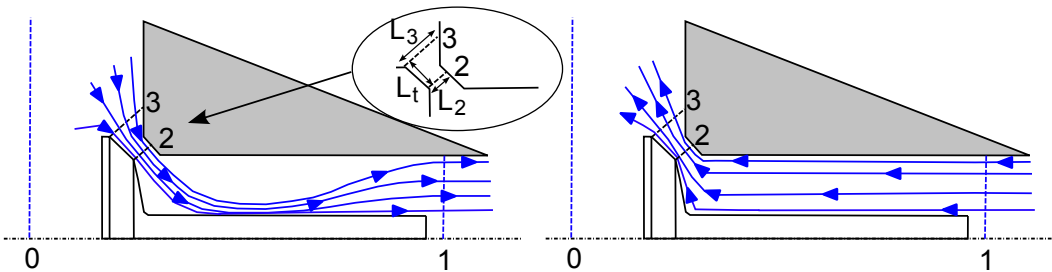


FIG. 11.11 – Example of axi-symmetrical poppet valve flow structures in the inflow (left plot) and outflow (right plot) cases. Poppet valve models associated planes are also plotted.

11.4.1 Inflow poppet valve

In the case of the inflow poppet valve, the flow is established between the stagnation state 0 and the pipe 1. This type of flow occurs during an exhaust cycle from a cylinder to the exhaust ducts. Steady-flow CFD calculations have been performed to validate some hypotheses which are introduced in order to build the inflow model. From these CFD observations, it appears that :

1. under subsonic conditions, the static pressure is almost constant between the throat and the pipe : $p_2 \simeq p_1$.
2. the flow can be assumed to be isentropic between 0 and 3.

Consequently, the following model assembly has been used to build the inflow poppet valve model :

- An isentropic flow assumption is used between 0 and 3.
- The complete steady-flow Euler's equations set (mass, energy, momentum) is used between 3 and 2. This local sub-model is similar to the non-homentropic model developed for the outflow restriction model in the previous section. The associated momentum model also uses a dynamic pressure corrective Ψ . In this case, Ψ is calculated as follows : $\Psi = \frac{1}{90} \text{atan}\left(\frac{L_3 - L_2}{L_t}\right)$.
- In the subsonic case, the inflow constant pressure model is used between the valve throat 2 and the pipe 1. In the case where sonic flow occurs, the inflow sonic throat model is applied.

11.4.2 Outflow poppet valve

In the case of the outflow poppet valve, the flow is established between the pipe 1 and the stagnation state 0. This type of flow occurs during an intake cycle from the intake piping to the cylinder. As in the inflow case, steady-flow CFD calculations have been performed to validate some hypotheses. From these CFD observations, it appears that :

1. under subsonic conditions, the static pressure at plane 3 is equal to the downstream pressure $p_3 = p_0$.
2. the static pressure at the valve throat p_2 is lower than the static pressure p_3 .

Consequently, the following model assembly has been used to build the outflow poppet valve model :

- The complete steady-flow Euler's equations set (mass, energy, momentum) is used between 1 and 2. This the same model as developed for the non-homentropic outflow restriction model. The model is applied with $\Psi = 1$.
- The inflow sudden enlargement model is solved between 2 and 3. It is reminded that this model from the literature has been developed to solve inflow restriction models. It is based on the complete Euler's equations sets and takes into account the pressure recovery phenomenon (Fig. 11.5). Therefore, this model satisfies the fact that $p_2 < p_3$.
- Finally, the static pressure p_3 is set as equal to p_0 .

In the sonic case, the creation of the datemap is different : the sonic state at the valve throat allows to get the values of U_2 and A_2 . From the equation 11.45, this leads to a fixed value for U_1 and A_1 . The pressure ratio $\frac{p_0}{p_1}$ varies between its critical value (when the flow becomes sonic) and 0.

It is concluded that the poppet valve inflow/outflow models have been built using an assembly of more simple boundary models, which have been previously developed in this thesis. The choice of these models has been dictated by flow observations from the 2-D axi-symmetrical poppet valve CFD calculations which have been performed.

11.4.3 Poppet valve inflow/outflow data maps : direct analysis

An example of the characteristic data maps of the inflow/outflow poppet valve models is shown on Fig. 11.12 and 11.13. These data maps have been built using the geometry of the valves from the cylinder test bench experiment.

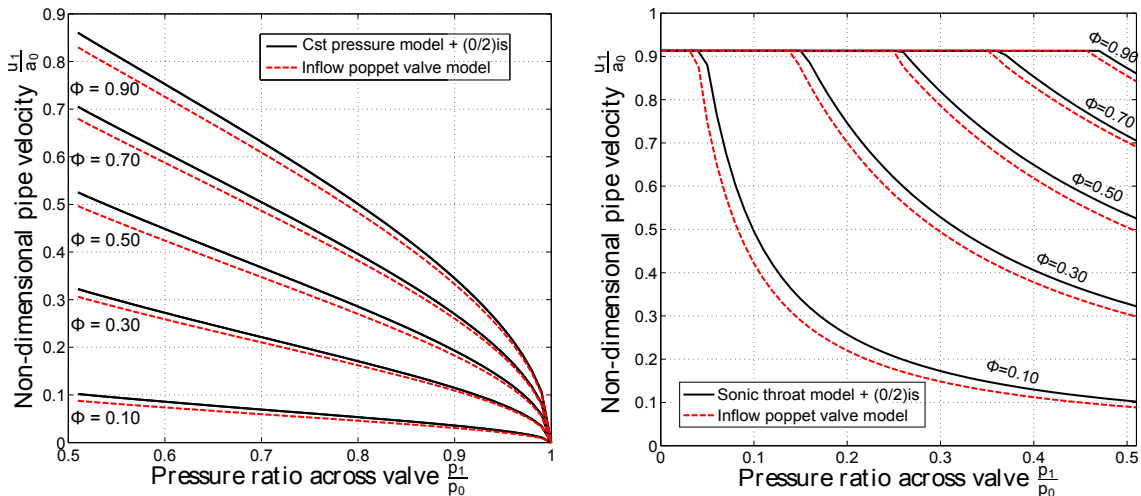


FIG. 11.12 – Steady flow results comparison between the standard inflow models and the inflow poppet valve model : subsonic case (left) and sonic case (right).

In the inflow case, the poppet valve model is compared to the inflow constant pressure model, as the inflow poppet valve model is a modified version of this model. The poppet valve model provides lower flow velocity values, in both subsonic and sonic case. This is explained by the fact that the flow between 3 and 2 is modeled non-homentropically, while the constant pressure model is fully isentropic upstream the throat.

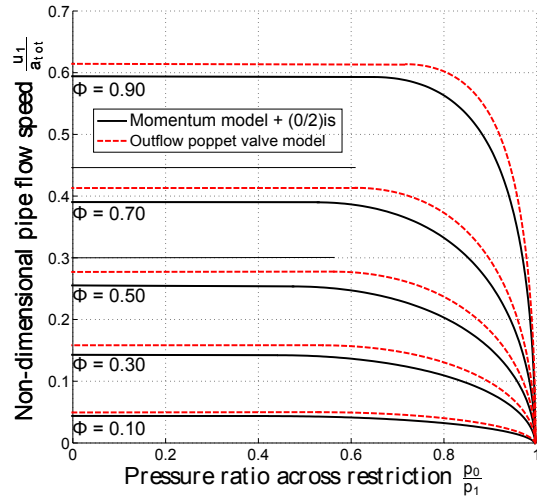


FIG. 11.13 – Steady flow results comparison between outflow boundary restriction model and the outflow poppet valve model.

In the outflow case, the poppet valve model is compared to the outflow non-homentropic model using the momentum conservation resolution and $p_2 = p_0$. The poppet valve model provides higher flow velocity values, in both subsonic and sonic case. This is due to the static pressure recovery phenomenon taking place between 2 and 3. This leads to $p_2 < p_0$ and consequently leads to higher flow velocities when solving the Euler's equations between 1 and 2.

It is concluded that assembling flow restriction boundary models has allowed to build the model of a more complex flow evolution. It appears that the combination of models is simple to perform, and that it has an effect on the final results. The poppet valve inflow/outflow models will be validated with respect to experimental data in the following of the thesis.

Inflow / outflow restriction models : main points

- The equations of the inflow/outflow boundary conditions have been derived in order to build their characteristic data maps. These data maps can be used to compare directly the non-homentropic behavior of the boundary models. Additionally, these data maps are used in order to perform numerical differentiation during the Newton-Raphson entropy correction process.
- In the case of the subsonic inflow restrictions, it has been seen that the constant pressure model provides lower non-dimensional speed values than the model using the momentum conservation equation. Additionally, the sonic throat model seems to provide reasonable results, which is not the case of the matched nozzle model. An important point to notice is that any inflow restriction model introduces an isentropic relationship between the stagnation state and the restriction throat.
- The momentum conservation has been included in the equations set of the outflow boundary condition. The momentum equation allows to take into account the losses due to the change of section at the pipe exit. Consequently, this model provides lower flow velocity values than the isentropic model, which consider that no loss is occurring within the flow.
- The inflow and outflow models based on the momentum equation resolution have been combined in order to solve the upstream and the downstream flow of a restriction without introducing any isentropic flow assumption.
- CFD calculations results have been analyzed in order to build innovative poppet valve models based on the assembly of several boundary conditions sub-models.
- It is possible to sum-up the inflow/outflow boundary conditions from the literature and the ones developed in this thesis as follows ;
 - Inflow restriction : Subsonic constant pressure model, subsonic momentum resolution model, sonic throat model and sonic matched nozzle model.
 - Outflow restriction : Isentropic throat model and momentum resolution model.
 - Complete flow resolution upstream and downstream a restriction using the steady-flow Euler's equations.
 - Poppet valve inflow/outflow boundary models.

Chapter 12

Inflow / outflow restriction models : numerical and experimental validation

In order to identify which sets of equations provide the best accuracy, the boundary model results will be compared to CFD computational results and to experimental measurements. The boundary flow equations are developed under a steady-flow assumption. In order to investigate the validity of a boundary equations system, it is therefore interesting to compare the boundary results to steady-flow test bench results. This provides the direct performance of the equations and the associated hypotheses. However, as the engine flow is essentially non-steady, additional transient tests will be performed in order to validate the performance and the accuracy of the boundary equations coupled to their iterative schemes.

12.1 Partially open-end CFD results vs. boundary models data maps comparison

In this section, the results from the 2D axi-symmetrical calculations are compared to the boundary models data-maps previously developed. The inflow and outflow cases are introduced. The considered systems for the axi-symmetrical model simulated under Fluent are shown on Fig. 12.1.

- in the inflow case, the pressure and the temperature are imposed at the boundary 0. In order to create a stagnation flow condition, the section F_0 is chosen such that for any value of F_2 , $\frac{F_2}{F_0} < 0.02$. Under these conditions, the values of $\frac{u_0}{a_0}$ never exceed 10^{-3} , which is a good approximation of a stagnation state. Then, the gas from the stagnation state 0 enters the pipe through the partially open-end of area F_2 . The gas then expands to occupy the full pipe cross-section area F_1 .
- in the outflow case, the gas flow exits the pipe of section F_1 through a partially open-end of area F_2 to reach the exterior stagnation state ext . In this case again, the section F_{ext} is chosen such that in any case, $\frac{u_{ext}}{a_{ext}} < 10^{-3}$. The generator state 0 is imposed within the pipe.

It should be noticed that the considered geometries have exactly the same configurations as the isolated systems considered to build the models of the boundaries. The only difference comes from the position of the plane 1 : in the boundary development assumptions, it is stated that the pressure recovery is instantaneous. In reality, it takes some distance (usually 20 times the diameter of the flow restriction) to achieve the pressure recovery.

The considered geometries are very simple, and are therefore not representative of the complex flows occurring within the poppet valves. However, this study will allow to verify whether the equations and hypotheses introduced in the previous developments are valid or not. Additionally, poppet valve flows are extremely complex to simulate under CFD codes, as the effect of the boundary-layer is predominant and very difficult

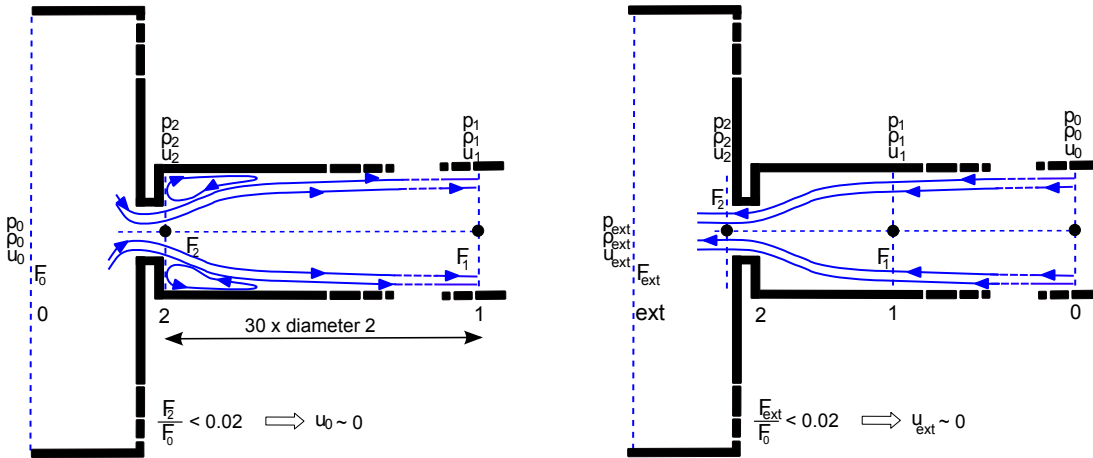


FIG. 12.1 – Considered geometries for the CFD simulation of partially open-ends : inflow (left) and outflow (right).

to model accurately. CFD is not the main subject of this thesis, consequently only 'simple' flows will be modeled in the following developments.

12.1.1 Inflow case

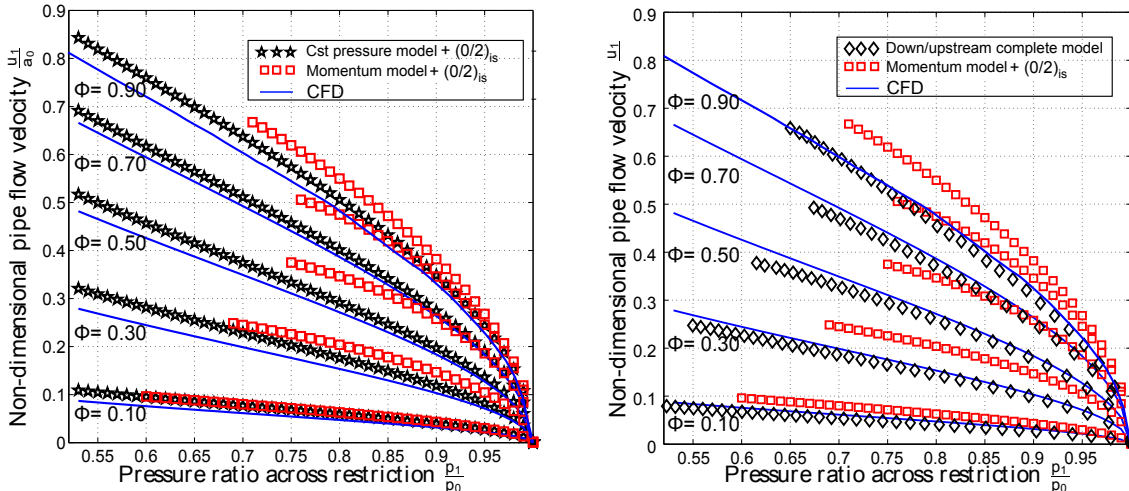


FIG. 12.2 – Steady subsonic flow results comparison between CFD and models.

In the subsonic case, the following boundary models have been compared to the CFD results :

- the inflow constant pressure model ($p_2 = p_1$). This model uses an isentropic assumption between the stagnation state 0 and the throat 2.
- the inflow momentum resolution model. This model also uses an isentropic assumption between the stagnation state 0 and the throat 2.
- the complete upstream/donwstream restriction flow model, which is fully non-isentropic. The upstream area ratio ϕ has been set to 0.02 to respect the geometry used in the CFD model. The downstream area ratio is modified between 0.10 and 0.90, as for the other boundary models.

The Fig. 12.2 shows that the momentum model used with the isentropic throat assumption systematically over-estimates the non-dimensional pipe flow velocity. The constant pressure model provides results in relative

good agreement with the CFD results, even though it also uses the isentropic throat assumption. The good behavior of this model is surprising, as the CFD results clearly show that there is a pressure drop and then a static pressure recovery between 2 and 1 (see Fig 12.3). In fact, the constant pressure assumption overestimates the downstream entropy creation, which compensates the upstream isentropic evolution effect. The upstream/downstream model provides the most accurate results when compared to the CFD results. It is interesting to notice that this model is very close to the momentum model : the only difference is that the isentropic throat assumption is replaced by the resolution of the mass, energy and momentum conservation between 0 and 2. Consequently, it appears that the rigorous resolution of the steady-flow Euler's equations provide satisfying results. The main reason is that no simplification hypothesis is introduced. Even though these good results have been obtained on a simple geometry, it is interesting to notice that good degree of accuracy can be achieved when modeling multi-dimensional flow with the complete set of 1D equations.

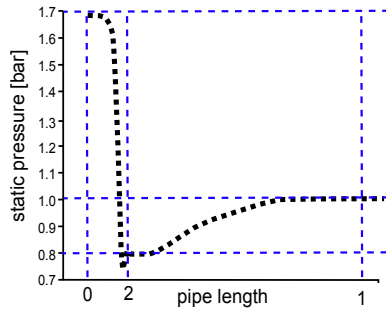


FIG. 12.3 – Example of the static pressure evolution from the inflow partially open-end CFD results.

In the sonic case, the following boundary models have been compared to the CFD results :

- the inflow sonic throat model. This model uses an isentropic assumption between the stagnation state 0 and the throat 2.
- the inflow sonic matched nozzle model. This model uses an isentropic assumption between the stagnation state 0 and the throat 2.
- the complete upstream/donwstream restriction flow model, which is fully non-isentropic. The downstream part of the flow is solved using the sonic throat approach, while the complete steady-flow Euler's equations set is solved upstream the throat.

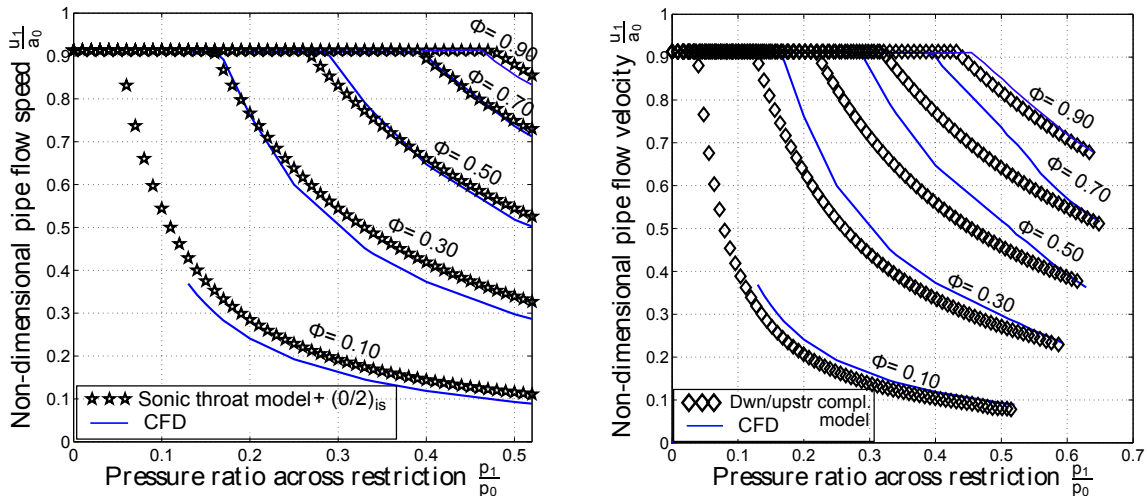


FIG. 12.4 – Steady sonic flow results comparison between CFD and the boundary models.

It appears on the left plot of Fig. 12.4 that the sonic throat approach provides good results, as excellent agreement is achieved when comparing the results of the model to the CFD results. On the right plot, the results of the complete downstream/upstream model are plotted. Even though the trends seem to be respected, the results provided by this model are less representative of the CFD results. Indeed, even though the accuracy is excellent when the flow just becomes sonic, the full non-homentropic model tends to underestimate the flow velocity when the pressure ratio is decreasing. This phenomenon has been explicated by looking at the sonic flow structure from the CFD calculations (Fig. 12.5). The CFD results allowed to show that the sonic throat model is not entirely valid : it is assumed that the flow is sonic at the exit of the throat (plane 2). In fact, it appears from the CFD calculations that the flow is sonic in the throat, and that the flow is supersonic at plane 2. Therefore, the flow speed at 2 is underestimated, and this consequently leads to an underestimation of the downstream flow velocity U_1 . The sonic flow results can be explained as follows :

- When the upstream flow is assumed to be isentropic, the downstream flow velocity underestimation is partially corrected by the neglecting the upstream losses.
- When the upstream flow is solved using the momentum equation, nothing corrects the underestimation of the downstream flow velocity.

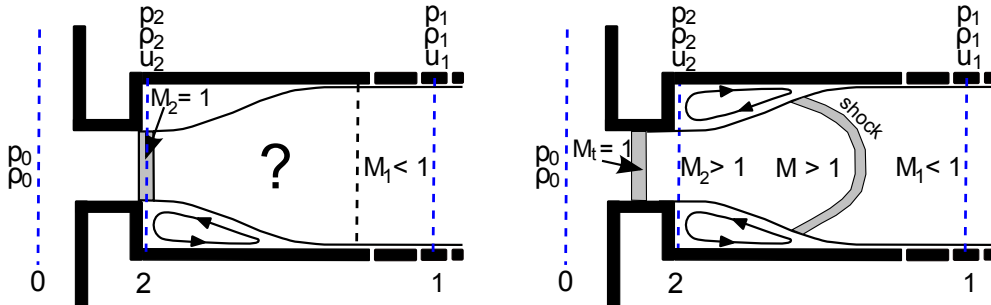


FIG. 12.5 – Left : sonic flow structure from the sonic throat assumption. Right : sonic flow structure from CFD observations

Finally, Fig. 12.6 shows the results provided by the model based on the matched nozzle theory. This model provides poor results accuracy, and is therefore inappropriate to the modeling of sonic inflows through restrictions.

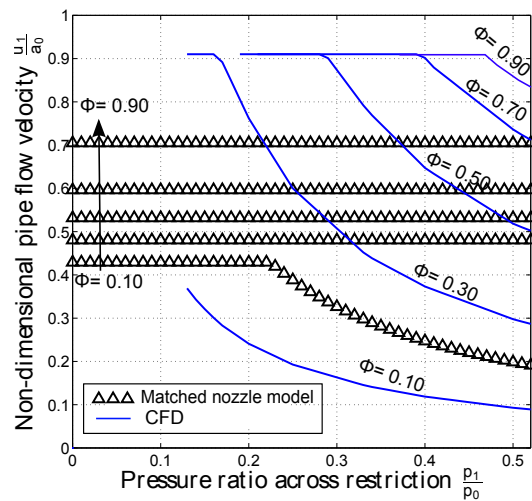


FIG. 12.6 – Steady sonic flow results comparison between CFD and the matched nozzle model.

12.1.2 Outflow case

In the outflow case, two configurations have been tested :

- An outflow restriction using a sudden contraction geometry. The results from the CFD calculations have been compared to the isentropic outflow model from the literature and to the momentum resolution model developed in this thesis with $\Psi = 1$.
- An outflow restriction using a 45° nozzle geometry. The results from the CFD calculations have been compared to the isentropic outflow model from the literature and to the momentum resolution model developed in this thesis with $\Psi = 0.5$.

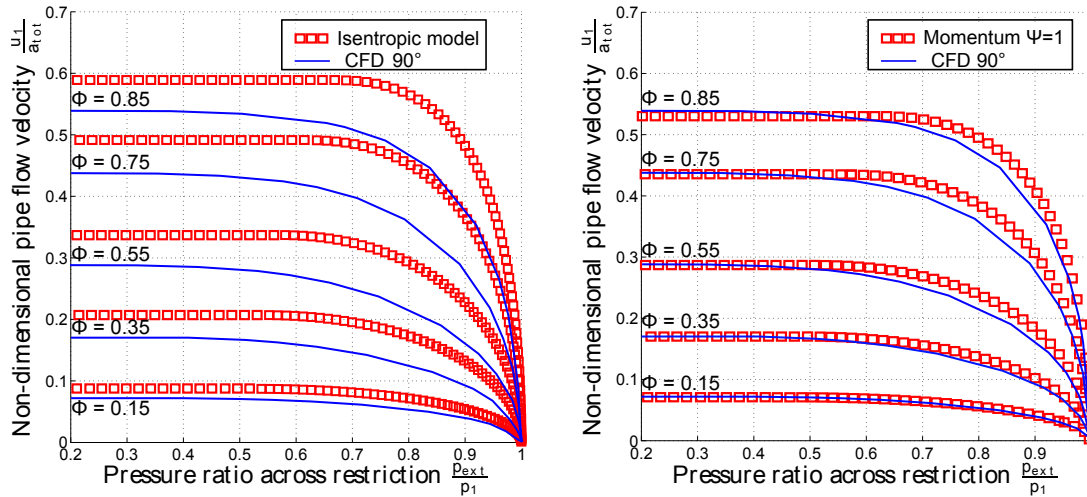


FIG. 12.7 – Steady subsonic outflow results for an outflow sudden restriction. Left : Comparison between the CFD calculation and the isentropic model. Right : Comparison between the CFD calculation and the momentum resolution model with $\Psi = 1$.

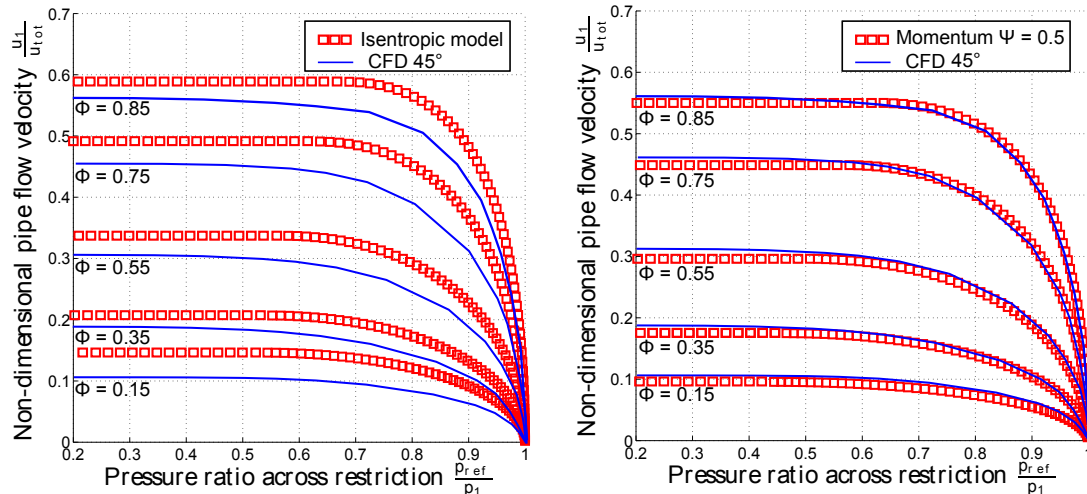


FIG. 12.8 – Steady subsonic for a 45° outflow nozzle. Left : Comparison between the CFD calculation and the isentropic model. Right : Comparison between the CFD calculation and the momentum resolution model with $\Psi = 0.5$.

The first thing which can be noticed is that the 45° nozzle geometry provides higher flow velocities than the sudden restriction. However, in both cases, the isentropic model from the literature overestimates the non-dimensional flow velocity. Such model therefore requires the use of an experimental coefficient. The

momentum model results are in good agreement with the CFD results, even though the flow velocity is slightly overestimated in the sudden restriction case. The interesting point is that the momentum corrector Ψ takes well into account the change of geometry of the outflow restriction. Consequently, it is concluded that the momentum resolution allows to take into account the simple outflow geometries without introducing any discharge coefficient.

12.2 Experimental validation of the boundary models

12.2.1 Steady flow validation

In this subsection, the results provided by the boundary models are compared to the measurements performed on the steady-flow test benches :

- Inflow restriction boundary models will be compared to the cylinder head bench measurements with flow going from the cylinder to the pipe (exhaust).
- Outflow restriction boundary models will be compared to the cylinder head bench measurements with flow going from the pipe to the cylinder (intake).
- A combination of the inflow / outflow models will be compared to the intra-pipe diaphragm bench measurements.

From the description of the test benches in Chapter 9, it appears that other flow restrictions than the valves or the diaphragm are found within the pipe systems of the experiments. In order to validate the behavior of the developed boundaries, it is therefore necessary to dissociate the effect of the studied flow restrictions from the effect of the others. In order to achieve this, the following method has been adopted :

- 1 The test benches have been modeled using a 1D spatial discretization scheme (Lax-Wendroff TVD) coupled to the boundary conditions described in the literature review chapter.
- 2 The studied flow restrictions (valves, diaphragm) have been physically removed from the test bench. The corresponding restrictions models have also been removed from the test benches models. Some tests have been performed without these restrictions in order to correlate the experimental benches and their respective models without the studied flow restrictions.
- 3 Finally, the studied flow restrictions have been re-introduced on the test bench and in the model, and the measurements and calculations of the comparative study have been launched.

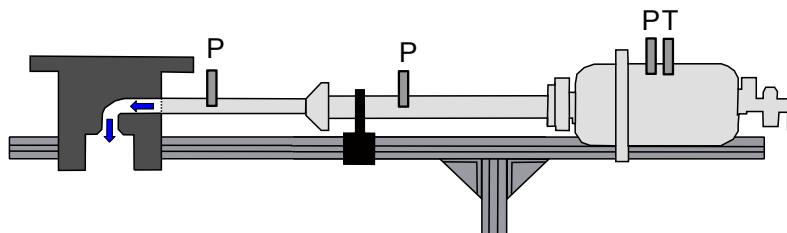


FIG. 12.9 – Non-studied flow restriction correlation : experimental setup in the case of the cylinder head flow bench.

An example of the experimental setup is provided on Fig. 12.9. The poppet valve has been removed and the orifice of the valve stem has been obstructed. The flow is established and the static pressure are measured upstream and downstream each flow restriction of the flow bench. The model is then correlated using these data : the model is assumed to be correct when for a given mass flow rate, the static pressure decrease at each flow restriction is correlated within 0.1%.

Inflow poppet valve model : experimental validation

The considered system for the validation of the inflow valve boundary is reminded on Fig. 12.10 : the gas at stagnation state 0 is entering the pipe through the flow area F_2 of the poppet valve. F_2 is the minimum measured area between the cylinder and the downstream pipe. Its value varies with the valve lift evolution [61]. The boundary node 1 has a cross-sectional area equal to the pipe section minus the valve stem section : $F_1 = F_{\text{pipe}} - F_{\text{stem}}$.

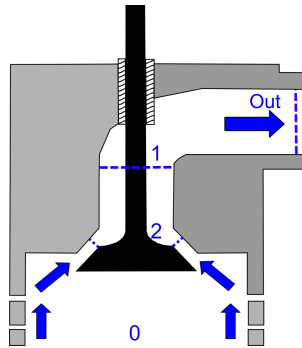


FIG. 12.10 – Considered system for the inflow valve boundary validation.

The considered cross-sectional areas have been determined by the mean of CAD tools. Their values are not detailed here due to confidentiality reasons. The results of the models results vs. measurements are shown on Fig.12.11 for valve lifts varying from 1 to 10mm. The flow section ratios ϕ could not be indicated on the plots due to confidentiality reasons, however it is indicated that $\phi = 1$ for a valve lift of 6mm. This explains why the results for the 6 and 10mm valve lifts are superimposed.

One sees that under steady flow conditions, the inflow poppet valve model provides results in good agreement with the experimental measurements. Sonic flow conditions were not reached for the higher values of valve lift, due to the air compressor limitations. However, it should be notified that the same phenomenon occurs on a real engine.

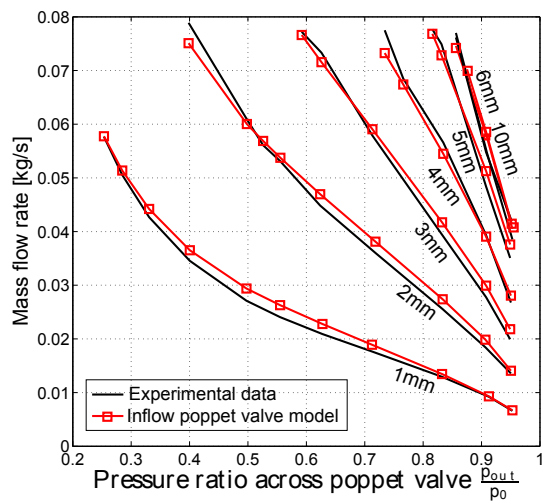


FIG. 12.11 – Inflow poppet valve model results compared to flow bench data.

Outflow poppet valve model : experimental validation

The considered system for the validation of the inflow valve boundary is reminded on Fig. 12.12 : the gas at the entry of the pipe (plane *Upst*) reaches the plane 1, just before exiting the pipe through the valve throat 2. The downstream flow goes through the cylinder which is at ambient pressure, as the cylinder bottom is wide opened. F_2 is the minimum measured area between the cylinder and the downstream pipe. Its value varies with the valve lift evolution [61].

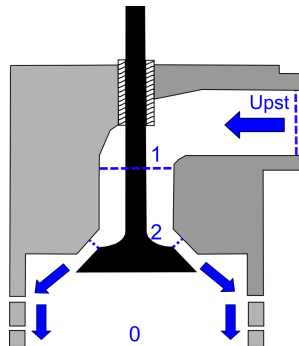


FIG. 12.12 – Considered system for the inflow valve boundary validation.

As in the inflow case, the considered cross-sectional areas have been determined by the mean of CAD tools. Their values are not detailed here due to confidentiality reasons. The results of the models results vs. measurements are shown on Fig.12.13 for valve lifts varying from 1 to 10mm. The flow section ratios ϕ could not be indicated on the plots due to confidentiality reasons.

Under steady flow conditions, the outflow poppet valve model provides results in good agreement with the experimental measurements. As in the inflow case, sonic flow conditions were not reached for the higher values of valve lift, due to the air compressor limitations. However, sonic flow almost never occur during the intake cycle on real engines. The mass flow rates in the inflow and outflow cases have the same order of value. Nevertheless, the mass flow rates are slightly higher in the case of the outflow. This evolution is well take into account by the valve models.

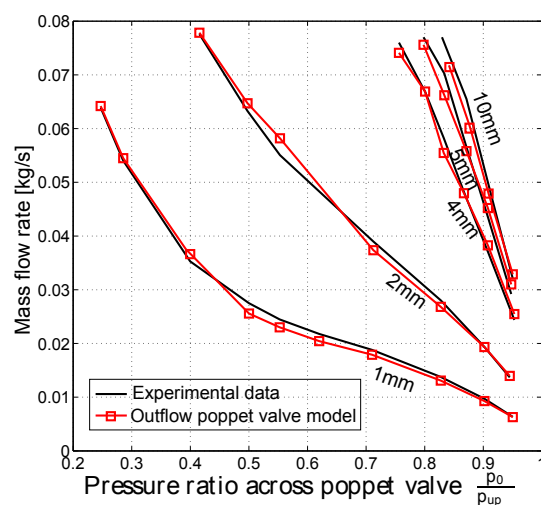


FIG. 12.13 – Outflow poppet valve model results compared to flow bench data.

Complete upstream/downstream restriction model : experimental validation

The considered system for the validation of the complete upstream/downstream restriction boundary is reminded on Fig. 12.14 : the gas at the entry of the pipe (plane *Upst*) enters the downstream pipe through the diaphragm restriction 2. The section 1 is located such that the static pressure recovery has occurred. The diaphragm configuration provides the following flow section ratios : $\frac{F_2}{F_{upst}} = \frac{F_2}{F_1}$.

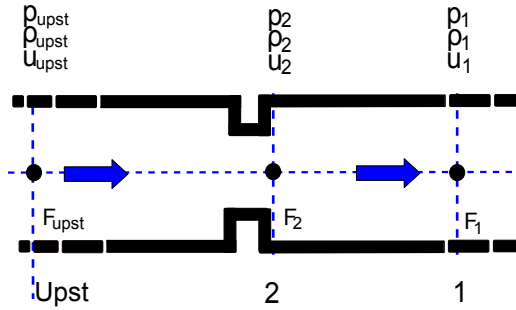


FIG. 12.14 – Considered system for the complete upstream/downstream restriction model validation with respect to a diaphragm ($\frac{F_2}{F_{upst}} = \frac{F_2}{F_1}$).

It is reminded that due to hardware limitations, the experiments could only be achieved for low mass flow rates values and for subsonic flow configurations. Further explanations are available in Chapter 9. Experimental data extrapolations have been performed using CFD calculations results. The experimental data and their numerical extensions are compared to the complete upstream/downstream restriction model results on Fig. 12.15.

It appears that the developed model provides results in good agreement with the experimental test bench measurements. The flow bench allowed to reach very low values of area ratios (up to 0.02), and it is a good point that the complete restriction model allows to deal with such extreme configurations. However, the validation of this model cannot be complete, as it is only valid for area ratios lower than 0.20 and for the subsonic case. Test bench hardware transformations have been planned in order to extend the measurement range, but they could not be achieved before the end of this thesis.

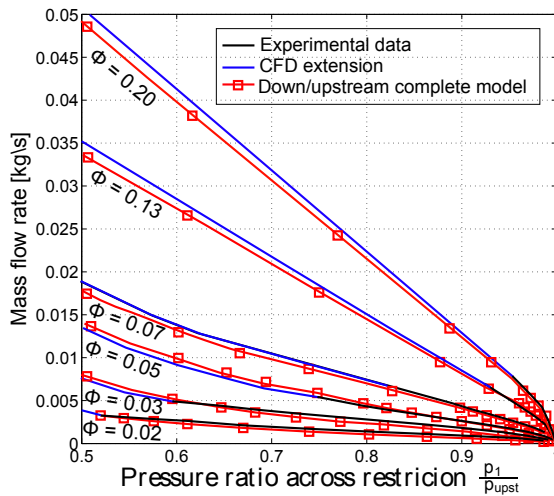


FIG. 12.15 – Complete upstream/downstream restriction model results compared to the diaphragm flow bench data.

12.2.2 Transient flow validation

In this subsection, the flow restriction model coupled to their iterative resolution schemes are tested under transient conditions, without introducing any discharge coefficient. It is reminded that the transient test bench is composed of :

- a cylinder which can be pressurized. In this study, 2 cylinder pressures will be considered : 1.80 and 4 bars. This allows to create both subsonic and sonic conditions at the valve throat.
- a poppet valve which is activated.
- a downstream pipe. A diaphragm is placed at the exit of the downstream pipe. This creates a sudden area change at the interface of the pipe and the outside environment (stagnation state). Two diaphragms have been used : the first one creates a cross-section change ratio of 0.67. The second one creates a cross-section change ratio of 0.17. It is reminded that the section change ratio ϕ is defined as follows : $\phi = \frac{F_{diaph}}{F_{pipe}}$.

These experimental configurations will allow to validate the following models :

- The inflow poppet valve (see section 11.4.2) model between the cylinder and the downstream pipe. Both subsonic and sonic flow configurations will be tested.
- The inflow/outflow partially open-end models at the interface between the pipe exit and the outside conditions. The tested outflow model is the non-homentropic outflow model (see section 11.2) through a restriction. As the considered geometry at the exit of the pipe is a diaphragm restriction (angle of 90°), the momentum equation of this model is written with $\Psi = 1$ (see Fig. 11.7). In the inflow case, the inflow sudden enlargement model from the literature is used (see section 11.1). There is some backflow occurring at the exit of the pipe when the pressure wave from the cylinder exhaust reaches the end of the pipe.

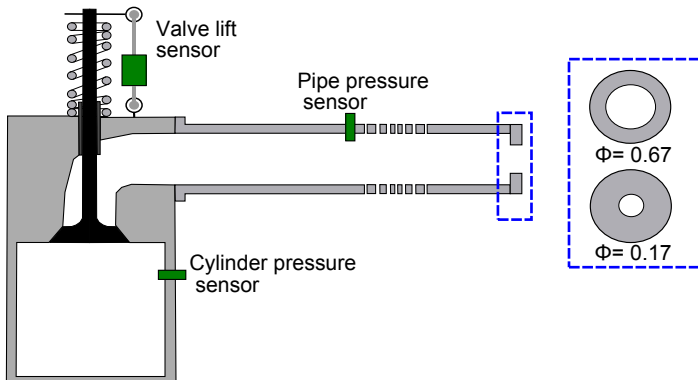


FIG. 12.16 – Considered system for the transient restriction models validation.

The flow restriction boundaries are 'plugged' to a Lax-Wendroff + TVD 1D numerical scheme. The parameters of the spatial and time discretization chosen for the Lax-Wendroff algorithm are shown in table 12.1. The cylinder is considered as a volume ($u=0$) and its pressure and temperature are calculated using the conservation of mass and energy.

The results of this study are plotted on figures 12.17 to 12.20. Each figure shows the valve lift evolution which has been measured on the test bench and which is re-created in the simulation. The only valve model parameter is the valve geometry, which is detailed in Chapter 9. The cylinder pressure evolution is also plotted. Finally, the pressure signal measured by the pipe pressure sensor is plotted. It allows to see the pressure waves evolutions within the pipe. Incident and rarefaction waves are indexed using letters from *a* to *f*. Pressure wave *a* is the incident wave due to the valve opening. Pressure wave *b* is due to the incident wave reflection at the pipe exit. Pressure waves *d* and *e* are due to the reflection on the closed valve, while

Designation	Value
Space increment Δx [m]	2e-2
Time increment Δt [s]	20e-6
Wall friction coefficient f	0.005
Number of meshes	365
Number of time steps	5000

TAB. 12.1 – Lax-Wendroff simulation parameters.

pressure waves d and f are their reflection at the exit of the pipe. Now, the accuracy of the simulation with respect to the experimental measurements is being discussed.

Inflow valve model : The accuracy of the inflow valve model is validated by analyzing the pressure wave a and the cylinder pressure drop. It appears that in both subsonic and sonic cases, the pressure drop in the cylinder is accurately modeled. The fact that the pressure drop in the cylinder is correct means that the mass flow rate is correctly estimated at the valve throat, without introducing any discharge coefficient. The plotted pressure waves a show that the valve model allows to provide accurate incident wave, in terms of pressure amplitude and of travel timing. This means that the particle velocity u and the sound speed a of the wave are accurately modeled. Therefore, it is concluded that the inflow valve model provides excellent accuracy in terms of mass flow rate estimation and of pressure wave characteristics using the sole valve geometry as model parameter.

Non-homentropic inflow / outflow partially open-end model : In order to validate the behavior of the sudden restriction at the exit of the pipe, the pressure wave b is analyzed. It is also interesting to study the evolution of pressure waves d and f , but one must keep in mind that the results of these two pressure waves are impacted by the reflection at the closed valve (pressure waves c and e). It appears from the results plots that in any considered case, the pressure wave b is accurately modeled, in terms of pressure amplitude and of transport timing. The $\phi = 0.67$ diaphragm provides a reflected rarefaction wave, while the $\phi = 0.17$ provides a reflected pressure wave. This phenomenon is well taken into account by the restriction model. However, the pressure waves d and f are less accurately modeled than reflected wave b . The following parameters have an influence on the pressure wave transmission and can be at the source of the error made on the estimation of pressure waves d and f :

- According to Piscaglia [105] the fact that the boundary conditions are developed under the steady-flow assumption introduces an error on the estimation of the reflected waves at the pipe boundaries. It is consequently necessary to take into account a lag time in the flow establishment at the exit of the pipe.
- The results plots show that the waves error begins to grow for the pressure wave c , which is reflected on the closed valve. The closed valve is modeled as a simple closed end (a 90° angle wall). In reality, the closed valve geometry is more complex, and the simplification made to model the closed valve may introduce some errors on the reflected pressure wave estimation.

Even though the study of these two parameters could not be included in this thesis due to lack of time, the provided results stay in good agreement with the experimental results, without introducing any experimental corrective coefficient. On the opposite, the outflow partially open-end model from the literature produces errors when it is not used with a discharge coefficient. An example of a result provided by the literature model is shown on Fig. 12.21. It is reminded that the model from the literature is based on an isentropic flow assumption. It appears that the literature model produces high errors on the reflected waves estimation. A discharge coefficient of 0.85 would be necessary to correct the behavior of this model, while the non-homentropic sudden restriction model developed in this thesis provides excellent accuracy without introducing a corrective factor.

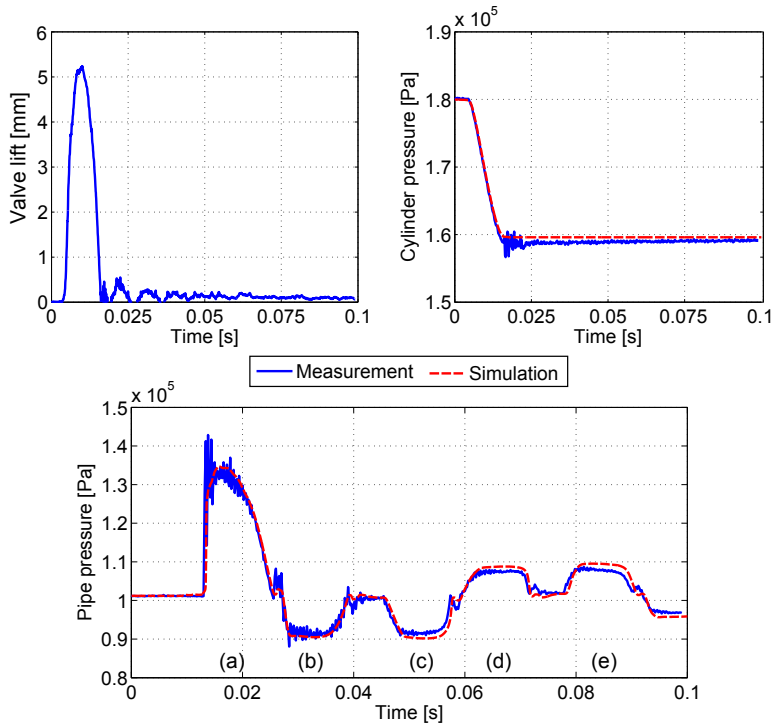


FIG. 12.17 – Comparison between the simulation and experimental results in the subsonic case ($P_{cyl} = 1.8$ bar) and a diaphragm / pipe section ratio ϕ of 0.67.

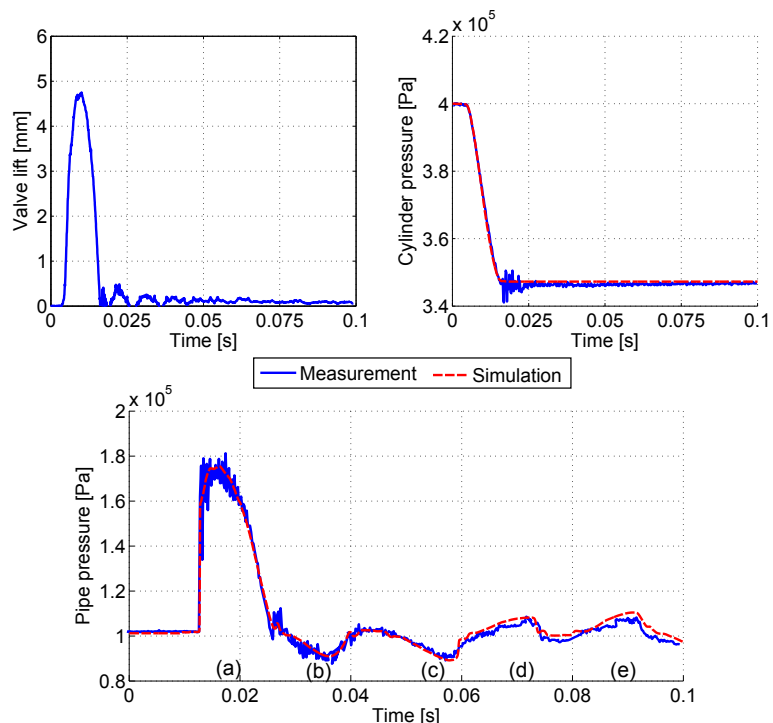


FIG. 12.18 – Comparison between the simulation and experimental results in the sonic case ($P_{cyl} = 4$ bar) and a diaphragm / pipe section ratio ϕ of 0.67.

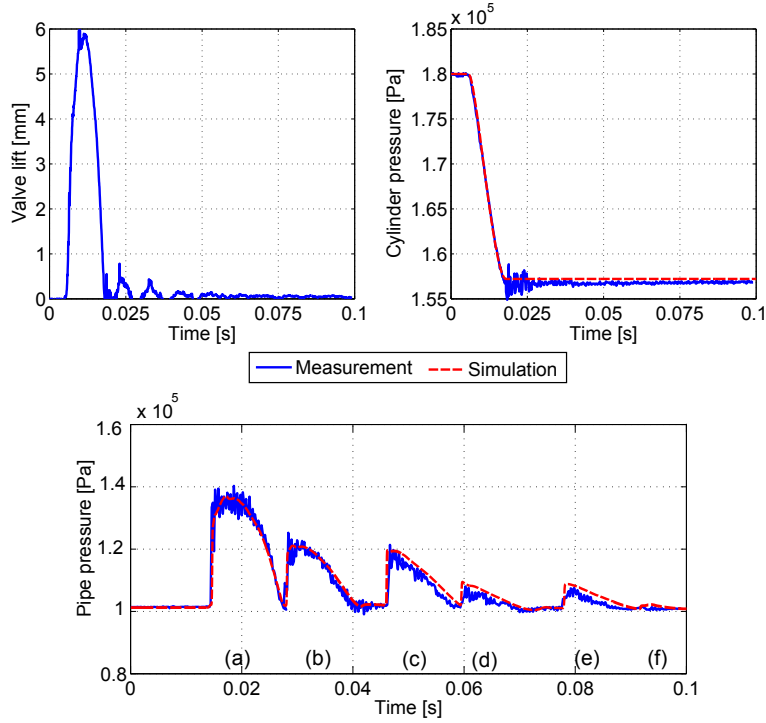


FIG. 12.19 – Comparison between the simulation and experimental results in the subsonic case ($P_{cyl} = 1.8$ bar) and a diaphragm / pipe section ratio ϕ of 0.17.

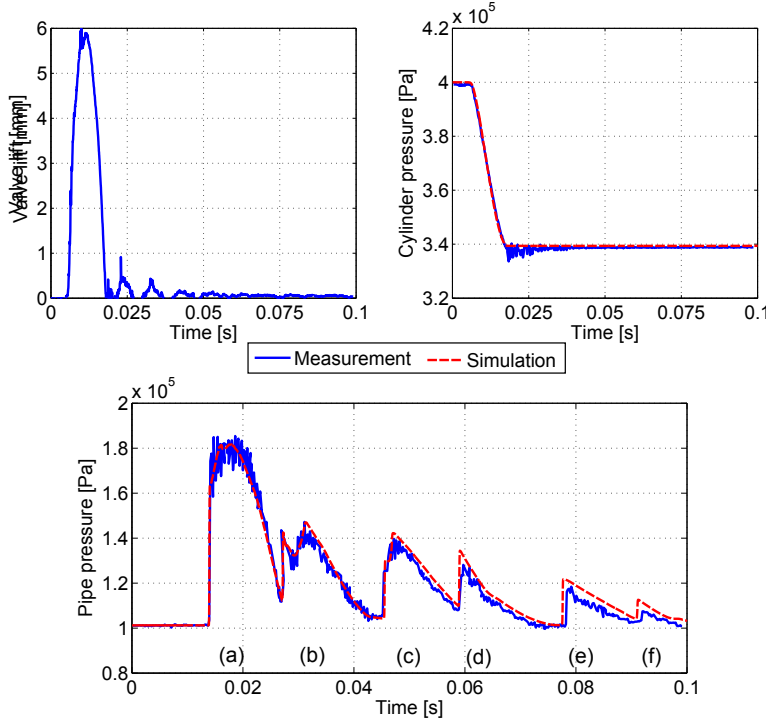


FIG. 12.20 – Comparison between the simulation and experimental results in the sonic case ($P_{cyl} = 4$ bar) and a diaphragm / pipe section ratio ϕ of 0.17.

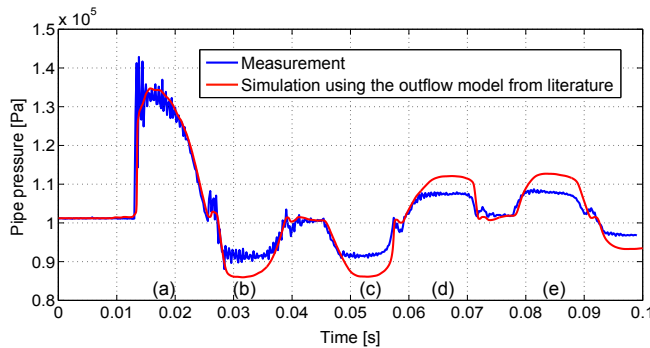


FIG. 12.21 – Comparison between the results of the simulation using the outflow model from the literature ($C_d=1$) and the experimental results in the sonic case ($P_{cyl} = 1.8$ bar) and for a diaphragm / pipe section ratio ϕ of 0.67.

It is concluded that the inflow valve model and the non-homentropic sudden area change models developed in this thesis provide results in good agreement with the transient experimental data. The most important point is that no discharge coefficient has been applied on the flow restriction models : the non-isentropicity of the models takes naturally into account the irreversibility of the flow. The only input parameter of the model is the geometrical cross-section ratio ϕ of the restriction.

Numerical and experimental validation of the boundary models : main points

- The boundary models have been compared to numerical and experimental measurements under steady and transient flow conditions. This study has allowed to ensure the validity of the developed model equations and their associated hypotheses.
- In the subsonic inflow case (subsection 12.1.1), it appears that the isentropic flow assumption upstream the restriction leads to an overestimation of the flow velocity when the momentum equation is solved downstream the restriction. The constant pressure assumption downstream the restriction artificially increases the entropy level, which allows to get results in good agreement with the experimental results. However, the best accuracy has been achieved by solving the complete Euler's equations set upstream and downstream the flow restriction (Fig. 12.2).
- In the sonic inflow case, it has been seen that the sonic throat assumption is not entirely representative of the CFD results observations. When the complete flow is solved upstream and downstream the restriction, the flow velocity is underestimated. However, the isentropic flow assumption upstream of the restriction allows to correct this behavior (Fig. 12.4).
- In the outflow case, the resolution of the momentum equation allows to get excellent agreement between the model results and the measurements. It also allows to take in to account simple geometry variations of the restriction (Fig. 12.8).
- The inflow and outflow poppet valve models have been successfully tested under steady flow conditions. The agreement of the model results with the experimental results is satisfying, without introducing any discharge coefficient (Fig. 12.11 and 12.13). The complete upstream/downstream flow resolution model has also been validated regarding experimental steady flow bench. The results are in good agreement with the measurements, even though the validation has only been carried out for low mass flow rates values and in the subsonic case.
- Finally the inflow valve boundary and the inflow/outflow sudden restriction models have been tested under transient flow conditions. It appears that the models provide excellent results in terms of mass flow rate, pressure and thermodynamical characteristics estimation.

Conclusions of the work performed on the gas exchange processes through flow restrictions

This part of the thesis has been dedicated to the modeling of the flow through the restrictions of the automotive duct systems. The work has been divided into two main parts : in a first part, the numerical schemes introduced to solve the boundary problem have been developed in order to improve the convergence speed of the introduced iterative loops. In a second time, the equations sets which create the aerodynamical behaviors of the flow restrictions have been introduced. The main goal has been to reduced the requirement of the discharge coefficients by avoiding to introduce non-realistic hypotheses.

Optimized MOC-based iterative schemes for the resolution of the non-homentropic boundaries :

The entropy correction loop has been developed and the convergence scheme from the literature (Benson [5]) analyzed. It has been seen that this scheme is not optimal in terms of convergence scheme. Consequently, a Newton-Raphson iterative scheme implementation has been proposed. The Newton-Raphson developments lead to derivative formulations which cannot be solved analytically. In order to overcome this issue, the data maps corresponding to the inflow restriction equations are used to express the evolution the inflow valve model quantities. This allows to use numerical derivation to develop the Newton-Raphson algorithm. The study has shown that the choice of the convergence variable is crucial, as some variables will lead to the introduction of infinite slopes, which will introduce errors into the numerical derivation and won't allow the Newton-Raphson scheme to converge. The pressure ratio across the restriction has been identified as the variable which allows to provide a satisfying range of stability. The implementation of the Newton-Raphson scheme allows to reduce the average number of iterations by a factor 4-5.

In the outflow valve case, even though an iterative scheme is required to solve the outflow boundary problem, it has been shown that this is not an entropy correction loop strictly speaking. From the literature review, it appeared that the outflow valve boundary was only solved in the homentropic case. The main outcome of the present work is that a mathematical formulation has been developed in order to solve non-homentropic outflow valve problems. This formulation is based on the introduction of a polytropic expression of the entropy change across the valve. This allows to keep the same formulation as in the homentropic case. Additionally, a Newton-Raphson algorithm has been implemented on this formulation. Nevertheless, even though some gains have been observed, they are much smaller than in the inflow valve case.

Inflow / outflow restriction models : new developments and validation :

The boundary conditions from the literature have been developed and analyzed. It has been shown that these boundary models are generally based on an isentropic flow assumption, which simplifies the boundary problem resolution. However, this hypothesis is generally not verified experimentally and the models consequently require an experimental correction to provide accurate results. The isentropic relationship generally replaces the momentum conservation resolution. In order to improve the accuracy of the models without having to introduce a corrective coefficient, the momentum conservation equation has been re-introduced in the boundary equations systems. Additionally, the possibility to assemble the simple inflow/outflow boundary models to build more complex boundaries such as poppet valves or diaphragms has been demonstrated. The developed models have been compared to CFD results and to experimental measurements. In almost any case, the developed models using the complete Euler's equations set provided a strong improvement of the accuracy, using the geometry of the flow restriction as the only input parameter (no correction). The validation has been performed for steady flows and transient flows.

The CFD calculations have taken a special place in this study. Indeed, it has been decided to keep the CFD simulations as simple as possible : only simple geometries have been considered in order to compare CFD results directly to boundary models. In the case of more complex geometries, such as the poppet valves, the CFD simulations have only been used to validate some flows structure hypotheses. Such approach has proved in this thesis to be reliable and efficient.

Résumé : Echanges gazeux au travers des restrictions des MCI

1 Etude bibliographique

1.1 Equations régissant les écoulements de fluides compressibles

La quantité d'air frais admise dans le cylindre est un des principaux paramètres à prendre en compte lors de l'élaboration des lois de contrôle moteur. Aujourd'hui, la complexification du système d'air des moteurs automobiles, notamment due à l'introduction de système de recirculation de gaz d'échappement (EGR), entraîne une hausse des besoins en termes de précision des modèles aérodynamiques. Il est proposé dans cette partie d'effectuer une étude bibliographique des modèles aérodynamiques appliqués au système d'air du moteur. L'objectif est de déterminer l'approche qui semble être la plus appropriée pour le développement de lois de commande. Les modèles aérodynamiques dédiés à la modélisation du moteur peuvent être divisés en trois catégories :

- Les modèles moyens.
- Les modèles basés sur une discrétisation spatiale 1D du système d'air.
- Les modèles basés sur une discrétisation multi-dimensionnelle du système d'air.

Le point commun entre les trois méthodes est qu'elles sont basées sur les mêmes équations fondamentales et hypothèses : d'une part, le fluide est modélisé comme un milieu continu, satisfaisant l'hypothèse de gaz compressible idéal. Une analyse plus détaillée de la modélisation de l'air est disponible en annexe E. Pour décrire l'évolution des écoulements, trois principes fondamentaux sont appliqués : la conservation de la masse, la conservation de l'énergie et la conservation du moment. Ces équations sont développées ci-dessous. Afin de maintenir les développements aussi compréhensibles et aussi simples que possible, le cas considéré est un écoulement 1D d'un gaz compressible. Si la variation de la section du conduit est progressive, les propriétés des fluides sont uniformes dans toute la section transversale, et l'écoulement est dit quasi-unidimensionnel. Sur la figure 8.1, un fluide idéal compressible à la pression p , de densité ρ et à la vitesse u traverse une longueur infinitésimale d'une conduite de section F . Le conduit est soumis à des échanges de chaleur avec l'extérieur q et au cisaillement τ_ω . Chaque paramètre du fluide subit une variation dans la longueur infinité-simale. Ces variations sont régies par les lois de conservation suivantes :

Equation de conservation du débit :

$$\frac{\partial \rho}{\partial t} + \frac{\partial \rho u}{\partial x} + \frac{\rho u}{F} \frac{dF}{dx} = 0$$

Equation de conservation du moment :

$$\frac{\partial \rho u}{\partial t} + \frac{\partial p_0}{\partial x} + \frac{\rho u^2}{F} \frac{dF}{dx} + \rho G = 0$$

$$G = \frac{1}{2}u|u|f \frac{4}{D}$$

Afin de modéliser les frottements entre le fluide et les parois, on introduit une contrainte de cisaillement τ_w , opposée à l'écoulement du fluide. En exprimant cette contrainte comme une fonction d'un coefficient de frottement théorique f , on obtient : $\tau_w = \frac{1}{2}\rho u^2 f$. p_0 est la pression totale, liée à la pression statique par l'expression suivante : $p_0 = p + \frac{1}{2}u^2$.

Equation de conservation de l'énergie

$$\frac{\partial \rho e_0}{\partial t} + \frac{\partial \rho u h_0}{\partial x} + \frac{\rho u h_0}{F} \frac{dF}{dx} - \rho q = 0$$

Ces équations dictent le comportement d'un écoulement compressible non visqueux mono-dimensionnel, sont désignées comme les équations d'Euler 1D. Les échanges de chaleur et de frottement sur le mur sont pris en compte par l'intermédiaire des sous-modèles, et peuvent être directement inclus dans les équations. Même si certains termes relatifs au changement de section du conduit sont introduits, des discontinuités de section trop importantes ne peuvent pas être prises en compte. En effet le terme $\frac{dF}{dx}$ introduit des erreurs numériques lorsqu'il devient trop important. Il est également possible de prendre en compte le transport des espèces, via l'introduction d'équations supplémentaires (voir le livre de Winterbone [139]).

1.2 Méthodes de résolutions des équations modèles

On passe à présent en revue les méthodes de résolution permettant de résoudre les équations précédemment introduites.

Modèles moyens : Les modèles moyens ont une complexité compatible avec le développement de lois de commandes et d'observateurs. Ils sont généralement formulés à partir d'équations différentielles ordinaires, qui permettent des temps de calcul plus rapides que le temps réel. Dans notre cas, les trois équations du système sont modifiées afin de simplifier leur résolution : les échanges de chaleur, les frottements et les changements de section de ne sont plus considérés. L'effet de l'énergie cinétique est négligé : $u = 0$. Cela conduit aux simplifications suivantes : $h_0 = h$, $e_0 = e$ and $p_0 = p$. Négliger l'effet de vitesse a aussi un impact sur la définition des dérivées : Considérons un déplacement d'une particules du fluide. Sa position à un moment donné t est fournie par son abscisse (x). La densité associée à la particule (par exemple) est donc exprimée sous la forme : $\rho(x, t) = \rho(x(t), t)$. Par conséquent, le calcul total de la densité se décompose comme suit :

$$\frac{d\rho}{dt} = \frac{\partial \rho}{\partial t} + \frac{\partial \rho}{\partial x} \frac{dx}{dt}$$

Dans le cas où l'effet de la vitesse est négligé, on obtient : $u = \frac{dx}{dt} = 0$, et la dérivée totale est donc équivalente à la dérivée partielle : $\frac{d}{dt} = \frac{\partial}{\partial t}$. Cela signifie que négliger la vitesse permet de construire des équations différentielles ordinaires plutôt que des équations aux dérivées partielles. Par conséquent, le nouveau système d'équations sera moins complexe et moins coûteux en termes de temps de calcul.
On introduit le volume du système isolé ($V = dx F$) qui permet d'exprimer la masse du gaz à l'intérieur de ce système : $m = \rho V$. On aboutit au système d'équations suivant, où $U = m C_v T$ est l'énergie interne du volume de contrôle et $Qm = \rho u F$ le débit massique de l'écoulement :

$$\begin{aligned} \frac{dm}{dt} + \frac{dQm}{dx} &= 0 \\ \frac{dQm}{dt} + \frac{dQm}{dx} &= 0 \\ \frac{dU}{dt} + \frac{dQmh}{dx} &= 0 \end{aligned}$$

Ce système d'équation est basé sur une hypothèse d'écoulement mono-dimensionnel, et ne prend donc pas en compte les discontinuités rencontrées dans les moteurs : volets papillons, filtres, soupapes, turbocompresseurs. Par conséquent, la méthode générale est de diviser en volumes de contrôle (où le système précédent est résolu), séparés par les discontinuités (qui nécessitent un traitement particulier). Ces discontinuités sont les conditions limites des volumes de contrôle, et une implémentation spécifique des équations physiques doit être introduite. La précision du modèle moteur global sera extrêmement dépendante des conditions aux limites, car elles dictent le transport de masse et d'énergie.

La modélisation moyenne du moteur est une approche largement utilisée, qui permet un développement efficace des lois de contrôle moteur et des observateurs associés. Quelques exemples de construction de ces modèles peuvent être trouvés dans les documents suivants par Talon [122], [123], Guzzella [57] et van Nieuwstadt [129]. Même si ces auteurs montrent que l'approche par modèle moyen appliquée au système d'air moteur peut donner de bons résultats, négliger la vitesse est une contrainte forte, qui a un impact sur la qualité des résultats :

- Les effets des ondes de pression ne sont pas pris en compte. Or, le débit dans le système d'air du moteur est largement affecté par les ondes de pression générées par l'ouverture / fermeture des soupapes.
- Une erreur est systématiquement introduite en considérant que quantités totales sont égales aux quantités statiques. Par conséquent, certaines erreurs non négligeables sont commises lorsque des vitesses élevées de fluide sont atteintes.
- Négliger la vitesse ne permet pas de prendre en compte le transport de l'espèce. Ce point est problématique lorsqu'on aborder la modélisation des boucles EGR. En effet, il est nécessaire de prendre en compte le transport des gaz d'échappement vers le circuit d'admission.

Schémas numériques à discréétisation spatiale 1D : Les modèles moyens introduisent une simplification des équations afin de les résoudre. Si on désire résoudre sans simplification les équations de conservation, il est nécessaire d'introduire des méthodes de résolutions numériques adaptées. Ces techniques sont basées sur la formulation d'un système d'équations hyperboliques. Le système d'équation peut être réécrit sous une formulation vectorielle conservative. $W = [\rho, \rho u, \rho e_0]^T$ est le vecteur d'état des variables conservatives : la masse, le moment et l'énergie totale. $F(W) = [\rho u, \rho u^2 + p, \rho u h_0]^T$ est le vecteur flux. Le vecteur $C(W)$ est le vecteur des termes correctifs correction. Il prend en compte la variation de section, le frottement à la paroi et le transfert de chaleur.

$$\frac{\partial W}{\partial t} + \frac{\partial F(W)}{\partial x} + C(W) = 0$$

$$C(W) = \begin{bmatrix} \rho u \\ \rho u^2 + p \\ \rho u h_0 \end{bmatrix} \frac{d(\ln F)}{dx} + \begin{bmatrix} 0 \\ \rho G \\ -\rho q \end{bmatrix}$$

Dans le cas où $C(W) = 0$ (écoulement homentropique), il est possible d'identifier la conservation de trois caractéristiques [139], [76]. Les premiers développements de cette méthode sont de Riemann [112]. C'est ce qu'on appelle la méthode des caractéristiques (MDC) ; ses développements de base sont indiquées dans l'annexe C. La MDC permet de résoudre directement les équations régissant un écoulement homentropique. Des développements supplémentaires permettent de développer la MDC dans le cas d'écoulements non-homentropiques (Winterbone [139]). Toutefois, la MDC est un schéma non-conservatif et ne prend pas en compte les chocs. Des travaux supplémentaires par Rankine [108], Hugoniot [64] ont permis d'introduire la prise en compte des chocs et des discontinuités de surface dans la méthode des caractéristiques. La prise en compte du phénomène de choc est essentiel, car ce phénomène se produit fréquemment dans les écoulements, en particulier dans le cas du système d'air du moteur. En premier lieu, la méthode des caractéristiques a été résolue en utilisant des méthodes graphiques, mais les travaux sur la théorie des méthodes numériques

par von Neumann, Courant, Friedrichs, Lax et Richtmeyer [130], [131], [28], [29], [73] ont permis de définir les critères de stabilité, de convergence et de précision d'une approche par différences finies appliquée à la résolution des systèmes d'équations en aérodynamique. Le principal inconvénient de la MDC est qu'il s'agit d'un schéma précis au premier ordre, qui tend donc à diffuser les solutions au passage des discontinuités. En outre, comme il ne prend pas naturellement en compte ces phénomènes de discontinuité, un traitement spécifique (les relations de Rankine-Hugoniot) doit être mis en œuvre.

Néanmoins, la MDC a permis de définir la base et la théorie qui ont été utilisées pour développer des schémas numériques d'ordre de précision supérieur et capturant naturellement les phénomènes de choc et de discontinuité de contact. L'un des schémas numériques les plus répandus est dû à Lax et Wendroff [74], qui ont développé un schéma précis au second ordre, capturant les chocs. Ce schéma numérique a inspiré de nombreuses variantes (MacCormack [80], Rubin-Burstein [114], Lerat-Peyret [75]. Lerat et Peyret ont défini la classe de schéma W_β^α qui permet de regrouper ces schémas numériques sous une même théorie de développement (voir l'Annexe D).

Le principal inconvénient de ces systèmes est qu'ils sont naturellement oscillants au travers des discontinuités. Le développement de limiteurs de flux a permis de se débarrasser de ces oscillations. Ces limiteurs de flux réduisent localement (dans les zones de forte discontinuité) la contribution des termes de précision du second ordre. Par conséquent, la solution a une précision locale réduite, mais n'oscille pas. Ces schémas ont été élaborés à partir d'un développement original par Godounov [51], qui a résolu l'équation d'Euler via la résolution du problème de Riemann (tube à choc). Le schéma numérique de Godounov ne produit pas d'oscillations aux discontinuités, mais n'est précis qu'au premier ordre précis et nécessite un temps de calcul élevé. D'autres travaux par Van Leer [126], [127], [128], Roe [113] et Harten [60] ont conduit à la définition des critères de monotonie et de 'Total Variation Diminution' (TVD). Ces critères ont permis le développement de schémas numériques de haute précision capturant naturellement les chocs. L'adoption d'une résolution approchée du problème de Riemann a permis de réduire le temps de calcul requis. Les schémas numériques type W_β^α couplés à des traitements TVD sont aujourd'hui très couramment utilisés dans le domaine de la simulation moteur. Un comparatif des performances d'un schéma lax-Wendroff + TVD a été comparé à la méthode des caractéristiques sur certaines applications de modélisation moteur (Onorati [97], Liu [78], Zhang [144]). Il apparaît que le schéma LW-TVD apporte une amélioration significative de la précision des solutions, surtout aux régimes de rotation moteur les plus élevés.

Le développement le plus récent concernant la simulation 1D des écoulements au sein des moteurs à combustion interne est le schéma 'Conservation Element- Solution Element'(CE-SE) développé par Chang et al. [20], [21]. Ce schéma a été testé avec succès dans le cas d'applications de moteurs. Selon Onorati [98], cette méthode constitue une amélioration en termes de précision par rapport à un schéma type LW + TVD, tout en réduisant les temps de calcul d'environ 20%. Les méthodes par éléments finis ont également été introduites, mais ces dernières introduisent un temps de calcul inacceptable, car ces méthodes sont basées sur les solveurs de Riemann [98].

Il est conclu que la simulation mono-dimensionnelle des écoulements aérodynamiques internes du moteur permet de prendre en compte les ondes de pression ainsi que les phénomènes de choc. Les schémas numériques associés permettent également de suivre l'advection des espèces chimiques. Ces schémas numériques ont été testés dans de nombreuses applications et ont donc atteint un niveau de maturité leur conférant précision et robustesse. Néanmoins, ces schémas numériques sont basés sur les équations d'Euler, qui sont basées sur l'hypothèse d'écoulement quasi-unidimensionnel. Par conséquent, il est nécessaire d'introduire des conditions aux limites pour prendre en compte les restrictions. Comme dans le cas des modèles moyens, ces conditions aux limites ont une forte incidence sur la solution finale. En outre, l'interaction entre le conduit discréte et ses conditions peut être problématique à mettre en place (ce sera vu plus loin dans cette étude). Enfin, les schémas numériques discréteisés requièrent généralement un temps de calcul généralement 30 à 100

fois supérieur au temps réel. Ce temps de calcul peut être problématique lors de l'élaboration des lois de commande, lorsque de nombreuses simulations doivent être exécutées.

Schémas numériques à discrétisation spatiale multi-dimensionnelle : Il est possible d'exprimer les équations qui régissent les écoulements aérodynamiques compressibles dans une formulation multi-dimensionnelle (2 ou 3 dimensions spatiales). Dans ce cas, les effets visqueux du fluide sont également inclus. Les équations de Navier-Stokes sont développées dans le corps de thèse à l'équation 8.12, pour le cas tridimensionnel (x, y, z), en l'absence des forces de gravité et des échanges de chaleur avec l'extérieur. Ce système d'équations peut être résolu en utilisant les mêmes techniques numériques mises au point pour le cas 1-D, mais exprimées dans une formulation multi-dimensionnelle. Le principal avantage de cette approche est qu'il est possible de modéliser correctement les composants du système d'air des moteurs qui ne sont pas conformes avec l'hypothèse d'écoulement quasi-dimensionnel (le plenum, les changements brusques de section ...). Toutefois, d'autres difficultés apparaissent lors du développement des codes numériques multi-dimensionnels :

- La couche limite (l'écoulement à proximité de la paroi) est complexe à prendre en compte et requiert des traitements numériques spécifiques [45].
- L'écoulement dans le système d'air du moteur est souvent turbulent (notamment aux soupapes), et des algorithmes spécifiques doivent être mis en œuvre (voir les papiers de Yakhot [142], [143], Durbin [37] et Thornhill [125]).
- Le calcul multi-dimensionnel requiert un maillage de la géométrie considérée. Cette étape peut être longue à réaliser, car la qualité du maillage a une forte incidence sur le résultat final.
- Dans le cas de certains éléments tels que la soupape, il est nécessaire d'adopter un maillage mobile, qui a une incidence forte sur le temps de calcul et la précision du résultat.
- Le temps de calcul temps est plus long que pour les autres méthodes (1000 à 100000 fois plus long que le temps réel). Ce problème rend l'utilisation des méthodes multi-dimensionnelles incompatibles avec le développement et la mise au point des lois de contrôle moteur

1.3 Conditions limites des Moteurs à Combustion Interne (MCI)

Il a été constaté que les conditions aux limites jouent un rôle majeur dans la simulation des systèmes d'air des moteurs à combustion interne. Cette section consacrée aux conditions limites aérodynamiques des moteurs sera divisée en deux parties : Premièrement, l'adaptation de la Méthode Des Caractéristiques (MDC) pour construire les conditions aux limites 1D seront détaillées. Deuxièmement, les principales hypothèses et les équations des conditions aux limites seront introduites.

La MDC appliquée à la construction des conditions aux limites : Les conditions limites sont placées à une extrémité du domaine de calcul (dans notre cas, l'écoulement dans les conduites discrétisées 1D). Il est nécessaire de distinguer les cas où l'écoulement est entrant ou sortant du domaine de calcul.

Dans ce paragraphe, l'application de la méthode des caractéristiques à un écoulement entrant à la souape est rappelé. La notation introduite par Benson [5] sera utilisée, comme on le voit sur la figure 8.3. $C-$ (resp. $C+$) est la caractéristique entrante à la condition limite (resp. sortante). λ_{in} est la variable de Riemann incidente à la condition limite, et λ_{out} est la variable de Riemann réfléchie. 1 est l'indice spatial du nœud où la condition limite est résolue. i est l'indice spatial du nœud à l'intérieur du domaine de calcul le plus proche de la condition limite.

Dans le cas des conditions aux limites, l'hypothèse de flux homentropique signifie que : 1 - les gaz situés dans le nœud à la condition limite sont toujours au même niveau d'entropie que l'environnement extérieur. 2

- Il n'y a pas de création d'entropie au passage de la condition limite. Ces hypothèses idéales ne sont presque jamais honorées pour un écoulement réel. Par conséquent, un algorithme de correction d'entropie doit être implémenté dans le cas d'écoulements non-homentropiques.

Cas homentropique : écoulement entrant : On se référera à la figure 8.3. Dans le cas où l'écoulement est supposé être homentropique, on utilise la conservation de la caractéristique incidente le long de $C-$:

$$\lambda_{in} = a_1^{n+1} - \frac{\gamma-1}{2} u_1^{n+1} = a_R^n - \frac{\gamma-1}{2} u_R^n$$

L'état thermodynamique du gaz se trouvant à la maille R est déterminé par interpolation avec la méthode développée par Courant, Isaacson, Rees (CIR) [29], [139]. Cette interpolation est effectuée entre les noeuds (1) et (i) au temps (n) (voir les équations 8.17 à 8.19).

Cas homentropique : écoulement sortant : Une relation similaire peut être développée dans le cas d'un écoulement sortant : la conservation le long de la caractéristique incidente $C+$ est utilisée.

$$\lambda_{in} = a_1^{n+1} + \frac{\gamma-1}{2} u_1^{n+1} = a_L^n + \frac{\gamma-1}{2} u_L^n$$

La méthode CIR est ensuite utilisée pour déterminer l'état du gaz se trouvant au noeud L (voir les équations 8.21 à 8.23).

Correction d'entropie pour un écoulement non homentropique : Dans le cas où l'écoulement à la frontière est non-homentropique, la MDC développée sous hypothèse d'homentropicité doit être modifiée afin de prendre en compte le changement du niveau d'entropie. La méthode de correction d'entropie, introduite par Benson [5] permet de modifier la MDC en ce sens. Les notations de Benson sont introduites sur la figure 8.4 : a_A est le niveau d'entropie du gaz à la pression p , avec la vitesse du son a . a_A est déterminée par une détente isentropique de p à la pression de référence p_{ref} . A est la vitesse du son non dimensionnelle $\frac{a}{a_{ref}}$ et A_A le niveau d'entropie adimensionné : $\frac{a_A}{a_{ref}}$. a_{ref} est l'état de référence, arbitrairement choisi.

Sur la figure 8.4, on considère que la variable de Riemann incidente λ_{in} se déplace sur la caractéristique incidente à partir du temps n (point P) vers le temps $n+1$ (point P'). Dans le cas où il y a création d'entropie entre le point P et le point P' , la variable de Riemann n'est pas invariante. Par conséquent, il est nécessaire de faire la distinction entre la variable de Riemann au moment n et la variable de Riemann au moment $n+1$. $\lambda_{in,c}$ est la variable de Riemann au pas de temps $n+1$ et prend en compte le changement du niveau d'entropie. $\lambda_{in,n}$ est la variable de Riemann initiale au pas de temps n :

$$\lambda_{in,c} = \lambda_{in,n} + \delta(\lambda_{in})$$

Les équations 8.25 à 8.32 du corps de thèse sont le développement d'une expression permettant d'exprimer le changement du niveau d'entropie ($d\lambda$) le long d'une caractéristique incidente à la condition limite. On obtient comme expression finale :

$$d\lambda \simeq \lambda_{in,c} - \lambda_{in,n} = A_{P'} \frac{A_{Ac} - A_{An}}{A_{Ac}}$$

D'après la figure 8.4, le niveau d'entropie en P' est différent de celui au point P. $\lambda_{in,n}$ est la variable de Riemann incidente et A_{An} est le niveau d'entropie adimensionné au point P. Ces deux quantités sont connues via la méthode CIR. $\lambda_{in,c}$ est la variable de Riemann corrigée, A_{Ac} est le niveau d'entropie adimensionné et $A_{P'}$ est la vitesse du son adimensionnée en P' . Ces trois quantités prennent en compte le changement de niveau d'entropie et doivent être déterminées. Etant donné que le changement d'entropie $d\lambda$, que l'on cherche à déterminer, dépend de ces 3 quantités inconnues, il est nécessaire de résoudre l'équation précédente via un processus itératif. Un tel processus a été proposé par Benson [5].

Processus itératif de correction d'entropie : méthode de Benson. On a vu que la correction d'entropie appliquée à la MDC exige une résolution itérative, en raison de l'occurrence entre $\lambda_{in,c}$, A_{Ac} et $A_{P'}$. Benson a introduit une boucle de convergence, qui est schématisée sur la figure 8.5. Cette boucle itérative est basée sur le niveau d'entropie A_{Ac} .

A chaque pas de la boucle itérative, le niveau d'entropie est ré-évalué à l'aide de la formulation suivante : $A_{Ac}^{n+1} = A_{Ac}^n + \Delta A_A^n$. A_{Ac} est initialisé à la valeur suivante : $\frac{A_c - A_{Ais}}{2}$ où A_c et A_{Ais} sont respectivement la valeur de la vitesse du son et le niveau d'entropie du gaz à l'extérieur. Une fois que A_{Ac} est calculé, $\lambda_{in,c}$ est également connu, ce qui permet de calculer U, A, puis P. La convergence de la boucle itérative est régie par le terme ΔA_A^n . A chaque pas de temps, il est arbitrairement divisé par deux. Par conséquent, il n'y a pas d'adaptation du terme de convergence par rapport à l'erreur. C'est la raison pour laquelle cette boucle de convergence peut fournir des conditions d'écoulement irréelles. Dans ce cas, la boucle de calcul est ré-initialisée, à l'exception du terme convergence ΔA_A^n qui est divisé par deux. Pour résumer la méthode de Benson, on initialise le terme de convergence à une valeur élevée (vitesse de convergence haute). Si cette convergence aboutit à des résultats irréels, le terme de convergence est diminué (vitesse de convergence plus faible) et la boucle de convergence est ré-initialisée.

Par conséquent, il apparaît que le ce schéma itératif appliqué à la convergence de la MDC n'est pas optimal en termes de vitesse de convergence. En effet, dans le cas où des conditions d'écoulement irréelles sont rencontrées trop souvent, le terme de convergence sera considérablement diminué, ce qui mène à des temps de convergence longs. De plus, après avoir mis en œuvre le schéma numérique proposé par Benson pour modéliser une soupape d'échappement, Brejaud [10] a relevé certains cas où l'algorithme ne parvient pas à converger. Théoriquement, la mise en œuvre d'un algorithme de convergence optimisé, comme l'algorithme de Newton-Raphson, permettrait d'améliorer la vitesse de convergence, mais une telle approche n'a jamais été trouvée dans la revue de la littérature réalisée.

Equations et hypothèses introduites pour la construction des conditions limites : Trois quantités sont requises pour calculer les variables de l'écoulement (pression, densité, vitesse) à la frontière. La MDC couplée à la correction d'entropie permet d'obtenir une condition incidente provenant de l'intérieur du domaine de calcul. Il est nécessaire d'obtenir deux autres quantités pour résoudre le problème à la condition limite. En règle générale, les conditions aux limites sont basées sur les équations d'Euler adaptées au cas d'écoulement stationnaire. En outre, les échanges de chaleur et le frottement pariétal ne sont pas pris en compte. Cela conduit au système d'équations suivant, qui expriment la conservation de la masse, de l'énergie et du moment entre l'état 1 et état 2 :

$$\begin{aligned}\rho_1 u_1 F_1 &= \rho_2 u_2 F_2 \\ a_1^2 + \frac{\gamma-1}{2} u_1^2 &= a_2^2 + \frac{\gamma-1}{2} u_2^2 \\ (p_1 + \rho_1 u_1^2) F_1 &= (p_2 + \rho_2 u_2^2) F_2\end{aligned}$$

Dans cette section, les principales équations et hypothèses introduites dans les papiers de la littérature pour résoudre les conditions aux limites seront introduites. La notation suivante est introduite : l'expression [$mass_{1/2}$, $energy_{1/2}$, $momentum_{1/2}$] doit être comprise comme le système d'équations bilan de l'écoulement suivant : (masse, énergie et moment), écrit entre les noeuds 1 et 2 .

1 - Section pleine ouverte : Les conditions limites d'écoulement entrant ou sortant via une pleine section sont généralement traitées de façons très similaires. Une représentation schématique de ce type de condition limite est indiquée sur la figure 8.6, dans le cas d'un écoulement entrant. L'indice 1 représente la maille où la condition limite est résolue. L'indice i est lié au noeud du domaine de calcul adjacent à la condition limite. L'indice 2 représente un noeud virtuel, qui est parfois introduit par certains auteurs pour permettre la résolution des équations aux limites.

La plupart du temps, l'hypothèse quasi-statique est introduite et conduit à une condition à la limite simple pour l'écoulement : tant que l'écoulement est subsonique, la pression à l'extrémité de la conduite est égale à la pression extérieure ($p_0 = p_1$). Cette condition de pression constante est ajoutée à la conservation de l'énergie entre l'état 0 la condition limite 1. On utilise également la caractéristique incidente, ce qui conduit au système suivant de 3 équations suivant [$p_0 = p_1$, $energy_{0/1}$, MDC]. Les détails de cette condition aux limites sont détaillés dans [5] ou dans [139]. L'application de cette condition limite a été validée et fournit des résultats satisfaisants.

2 - Ecoulement entrant : Section partiellement ouverte : Dans ce cas, le gaz provenant de l'extérieur du conduit pénètre dans le conduit par une restriction (Fig. 8.7). Ces modèles sont également utilisés pour modéliser les soupapes du moteur. Le gaz entre dans le conduit par une restriction, ce qui produit un jet de section F_2 . Il s'élargit ensuite pour occuper la section complète du conduit en 1. Le système isolé est situé entre les plans 1 et 2. Il y a 6 inconnues (pression, densité et vitesse en 1 et 2), donc six équations sont nécessaires. La distinction est faite entre le cas subsonique et le cas sonique :

Cas subsonique : Deux modèles principaux ont été développés dans le cas d'un écoulement entrant par une section partiellement ouverte : un modèle à pression constante et un modèle à élargissement brusque. Le travail fondamental de ces modèles est dû à Jenny [67], son travail étant détaillé dans [5] et dans [139]. Le fondement théorique de ces deux modèles est très similaire : ils sont fondés sur l'hypothèse d'écoulement isentropique et sur la conservation de l'énergie entre le nœud 2 et l'extérieur 0. La conservation de la masse et de l'énergie sont utilisées entre les noeuds 2 et 1. La MDC fournit une cinquième équation. La dernière équation différencie les deux modèles :

- Modèle à pression constante : Dans ce cas, la pression est supposée être la même au niveau des noeuds 1 et 2 (dans le conduit et au col). Par conséquent, le système d'équations qui permet de résoudre le problème aux limites est le suivant : [$isentropic_{0/2}$, $energy_{0/2}$, $mass_{1/2}$, $energy_{1/2}$, $p_1 = p_2$, MOC].
- Modèle à élargissement brusque : Pour ce modèle, la conservation du moment est écrite entre l'état 2 et l'état 1. Le système d'équations qui permet de résoudre le problème est le suivant : [$isentropic_{0/2}$, $energy_{0/2}$, $mass_{1/2}$, $energy_{1/2}$, $momentum_{1/2}$, MOC].

Il est intéressant de développer la conservation du moment entre les nœuds 1 et 2. En effet, l'écoulement pénètre dans le conduit via une veine de vitesse de section F_2 réduite, telle que $F_2 < F_1$. Néanmoins, la pression statique P_2 est appliquée sur la section complète F_1 en aval du col : c'est l'hypothèse d'élargissement brusque. Par conséquent, l'équation de conservation du moment entre 1 et 2 conduit à :

$$(p_2 - p_1)F_1 = F_1\rho_1u_1^2 + F_2\rho_2u_2^2$$

Cas sonique : Lorsque le rapport de pression est augmenté, un écoulement sonique a lieu au col. Dans ce cas, l'équation de col sonique est utilisée, ce qui permet d'écrire que $M_2 = \frac{u_2}{a_2} = 1$. Cette relation fournit une équation supplémentaire : on obtient sept équations disponibles, pour 6 inconnues. On supprime une relation, et c'est soit l'équation de pression constante, soit de conservation du moment qui sont supprimées. Elles sont en effet basées sur des hypothèses restrictives. Ceci conduit aux 6 relations suivantes : [$isentropic_{0/2}$, $energy_{0/2}$, $mass_{1/2}$, $energy_{1/2}$, $M_2 = 1$, MOC].

Correction expérimentale : De nombreux documents traitent du développement de coefficients de correction de débit [140], [141], [7], [8], [9], [19], [49]. Dans ce cas, les résultats de la condition aux limites numériques sont corrigés par un coefficient expérimental qui est appliqué sur l'équation de débit massique. Le débit massique fourni directement par le modèle est comparé à un débit expérimental et le ratio est stocké dans une cartographie de correction.

$$(\rho_1 u_1 F_1)_{model} = Cd (\rho_1 u_1 F_1)_{exp}$$

Cette approche est largement utilisée, car elle permet d'obtenir des résultats précis. Toutefois, elle exige que le moteur existe physiquement, afin de mesurer expérimentalement les valeurs des correctifs.

3 - Ecoulement sortant : Section partiellement ouverte : Le domaine de contrôle est indiqué sur la figure 8.8, où l'on voit le gaz sort du conduit sous la forme d'un jet de section F_2 . Contrairement au cas de l'écoulement entrant, le plan 2 est situé à l'extérieur du conduit. Le système isolé est situé entre les plans 1 et 2. Il y a 6 inconnues (pression, densité et vitesse en 1 et 2), donc six relations sont nécessaires. La distinction est faite entre les cas subsonique et sonique :

Cas subsonique : Dans le cas d'un écoulement subsonique sortant par une ouverture partielle, le modèle suivant est communément présenté [5], [139]. Les relations de conservation de la masse et de l'énergie sont exprimées entre 1 et 2, et l'écoulement est supposé isentropique entre ces deux points. Tant que l'écoulement est subsonique, la pression statique au point 2 est supposée être égale à la pression extérieure P_0 . Ces 4 équations sont complétées par l'expression de la vitesse du son : ($a^2 = \frac{\gamma p}{\rho}$) et de la MDC. Finalement, on obtient le système d'équations suivant : [$isentropic_{1/2}$, $mass_{1/2}$, $energy_{1/2}$, $p_2 = p_0$, $a^2 = \frac{\gamma p}{\rho}$, MOC].

Cas sonique : Lorsque l'écoulement devient sonique au col, la relation de blocage sonique est introduite : $M_2 = \frac{u_2}{a_2} = 1$. Dans le même temps, l'hypothèse de pression constante n'est plus valable, puisque l'écoulement est sonique au col. Au final, on obtient le système d'équations suivant : [$isentropic_{1/2}$, $mass_{1/2}$, $energy_{1/2}$, $M_2 = 1$, $a^2 = \frac{\gamma p}{\rho}$, MOC].

Comme dans le cas de l'écoulement entrant, le système d'équation est généralement couplé à une correction par coefficient expérimental.

4 - Changement de section brusque à l'intérieur du conduit : Ce type de conditions aux limites se produit lorsque de conduits de diamètres différents sont liés directement. Selon la direction de l'écoulement, un changement de section brusque peut être soit un élargissement soit une contraction. Dans le cas d'un élargissement brusque, le même système d'équations que dans le cas d'un écoulement entrant par une section partielle est utilisé. Dans le cas d'une contraction brusque, c'est le système d'équations relatif à l'écoulement sortant par une restriction qui est utilisé. La principale différence entre le cas 'intra-conduit' et les conditions aux limites à la sortie ou l'entrée du conduit concerne la résolution de la méthode des caractéristiques. Dans le cas 'intra-conduit', elle doit être résolue en amont et en aval du changement de section.

5 - Vannes papillons, filtres Les composants tels que les vannes, les carburateurs, ou les filtres sont généralement modélisés par une perte de pression adiabatique. Cette perte de pression est généralement exprimée en utilisant un coefficient de perte de pression déterminé expérimentalement :

$$\Delta p = f_C \frac{\rho_1 u_1^2}{2}$$

Le coefficient F_C est déterminé à partir de tests au banc d'essai et est stocké dans une cartographie de données. Il est généralement exprimé en fonction du nombre de Mach ou nombre de Reynolds de l'écoulement. Dans le cas des vannes, il est possible d'inclure l'angle d'ouverture de ces dispositifs en entrée de la cartographie.

6 - Raccords de conduits : Ces restrictions sont trouvées fréquemment lors de la modélisation de collecteurs d'échappement. Les écoulements sont fortement multi-dimensionnels au passage de ces dispositifs

et par conséquent, leur modélisation est basée sur des coefficients de perte de charge expérimentaux. De nombreuses cartographies regroupant ces coefficients sont disponibles dans la littérature (par exemple dans [139] ou dans [19]). Elles incluent les paramètres géométriques des raccords, ce qui rend leur utilisation générique.

Echanges Gazeux : problématique de thèse

Il a été observé dans l'étude bibliographique que les modèles aérodynamiques des moteurs à combustion interne et de leurs conditions limites associées ont été largement développés. Ils permettent aujourd'hui d'atteindre un degré satisfaisant de précision. Cependant, deux limitations ont été identifiées en vue du développement et de la mise au point de lois de contrôle moteur innovantes :

- Les boucles EGR haute et basse pression sont devenues des composants 'standards'. Pour contrôler ce type de système, il est nécessaire de prendre en compte le transport des espèces dès les étapes de conception du projet. Cela implique l'utilisation de schémas numériques 1D, ce qui a un impact négatif sur le temps de calcul. La réduction du temps de calcul des schémas numériques est par conséquent un axe de recherche crucial. Or, il semble que la boucle de résolution de la méthode des caractéristiques n'est pas optimale en terme de vitesse de convergence.
- L'étude des performances théoriques d'un moteur avant la construction d'un premier prototype physique (approche de développement par modèle) est intéressant en termes de réduction de coût et de temps de développement. Néanmoins, ce type de développement requiert une précision accrue des modèles, car aucun correctif expérimental n'est alors disponible.. Par exemple, dans le cas d'architectures moteur novatrices, telles que les systèmes d'hybridation pneumatique ([62], [36], les systèmes de soupapes n'ont pas les caractéristiques standard, et une cartographie des coefficients de débit C_d d'un moteur existant ne peut donc être ré-utilisée.

A partir de ces observations, il a été décidé d'orienter le travail sur deux axes principaux :

- **Réduction de la nécessité de coefficients expérimentaux de correction :** L'objectif est d'identifier les systèmes d'équations des conditions limites qui offrent la meilleure précision sans introduire de coefficient correctif expérimental. Dans le cas d'un écoulement entrant via une section partiellement ouverte, les modèles introduits dans l'étude bibliographique seront comparés à des résultats d'essais. On identifie ainsi les équations offrant la meilleure précision sans l'introduction d'un coefficient expérimental. Dans le cas d'un écoulement sortant via une section partiellement ouverte, l'étude bibliographique n'a révélé qu'un seul modèle disponible, basé sur une hypothèse d'écoulement isentropique. Par conséquent, de nouveaux systèmes d'équations, non-isentropiques, seront développés. Les résultats de ces nouveaux modèles seront comparés aux résultats expérimentaux, sans introduire de coefficient de décharge. L'objectif est d'obtenir un modèle 'générique' dans le cas où aucune donnée provenant d'un banc expérimental n'est disponible. Même si la complexité des écoulements, notamment aux soupapes, ne permettra pas de se passer complètement de coefficients expérimentaux, il faut rappeler que la précision requise est généralement diminuée lorsqu'il s'agit de modèles dédiés au développement de lois de commande.
- **Boucle de résolution optimisée pour la résolution des conditions limites non-homentropiques :** On a vu que la boucle de convergence proposée par Benson [5] n'est pas optimale, car son terme de convergence est fixe et ré-initialisé dans le cas où les conditions d'écoulement calculées sont irréelles. Afin d'accélérer le processus de résolution, l'algorithme de Newton-Raphson sera introduit.

2 Bancs expérimentaux

La campagne expérimentale concernant l'étude des restrictions a été réalisée à l'Institut Prisme. Les bancs expérimentaux recréant des conditions d'écoulement stabilisées ont été développées durant cette thèse, alors que les bancs d'écoulements transitoires provenaient d'études précédentes.

Soufflerie culasse

Une vue globale du système est disponible sur la Fig. 9.1. Une culasse provenant d'un moteur Renault (2.0l diesel) a été monté sur un banc de soufflerie 3 voies. Il est possible de créer les configurations d'écoulements stabilisés suivants :

- Écoulement du cylindre vers le plenum 1.
- Écoulement du cylindre vers le plenum 2.
- Écoulement du plenum 1 vers le cylindre.
- Écoulement du plenum 2 vers le cylindre.

Chacune des soupapes peut être actionnée indépendamment via un système de vis (pas : 1 tour = 0.1 mm de levée). Les levées soupape sont acquises via des comparateurs. Les sections géométriques correspondant aux ouvertures soupapes ont été déterminées au moyen d'outils CAO. Ces dimensions ne sont pas fournies dans ce manuscrit dû à des restrictions de confidentialité. La liste complète des capteurs montés sur l'expérience est disponible ci-dessous :

Capteur	Fabricant	Modèle	Echelle	Dispersion
Absolute pressure	Rosemount	3051 CA 4	0-10 bar	$\pm 0.055\% \text{ PE}$
Differential pressure	Rosemount	3051 CD 4	0-10 bar	$\pm 0.055\% \text{ PE}$
Mass flow rate	EPI	8600 MPNH	0-0.02 kg/s	$\pm 0.01\% \text{ PE}$
Temperature	LabFacility	Pt100	223-773K	$\pm 0.6 \text{ K}$

Soufflerie diaphragme

Une vue globale de la soufflerie diaphragme est disponible sur la Fig. 9.4. Des diaphragmes d'un diamètre de passage 1mm à 21.5mm peuvent être placés dans l'écoulement pour créer une restriction. Les conduits en amont et en aval de la restriction sont de diamètre intérieur 21.5mm. Les pressions statiques en amont et en aval sont mesurées. Le débitmètre est asservi, ce qui permet d'assigner les valeurs de débit massique directement d'un ordinateur de commande. Le banc a été créé dans le but d'étudier les écoulements subsoniques aux faibles valeurs de rapport de pression. Ces caractéristiques se sont révélées limitantes pour le cadre de notre étude, et une adaptation du banc est prévue pour couvrir une plus grande plage d'écoulements. Néanmoins, ces modifications n'ont pas pu être effectuées durant la thèse, et la configuration du banc durant la thèse a été la suivante :

Capteur	Fabricant	Modèle	Echelle	Dispersion
Absolute pressure	Rosemount	3051 CA 4	0-5 bar	$\pm 0.055\% \text{ PE}$
Differential pressure	Rosemount	3051 CD 4	0-1 bar	$\pm 0.055\% \text{ PE}$
Mass flow rate	Brooks	5851S	0-100 nl/min	$\pm 0.2\% \text{ PE}$
Temperature	LabFacility	Pt100	223-773K	$\pm 0.6 \text{ K}$

Soufflerie culasse transitoire

Des tests concernant des écoulements transitoires ont été effectués sur un banc de soufflerie culasse dynamique (Fig. 9.5). Un cylindre est connecté à un conduit de 5.5m de long. Le cylindre a un volume de 6

litres et peut être pressurisé jusqu'à 10 bars. Un cycle d'ouverture/fermeture soupape est créé, ce qui produit une onde de pression d'échappement. La levée de la soupape est mesurée par un capteur résistif. La pression est mesurée tout au long du conduit. La longueur du conduit a été dimensionnée afin d'éviter de perturber les mesures par les réflexions aux limites du conduit. Des diaphragmes ont été placés à la sortie du conduit pour valider les modèles de restrictions brusques. Les caractéristiques des capteurs montés sur le banc sont disponibles dans la table suivante :

Sensor type	Manufacturer	Model	Scale	Dispersion
Pipe pressure	Bosch	0-261-230-049	0-2.5 bar	-
Cylinder pressure	Kistler	4045A5	0-10 bar	-
Valve lift	Gefran	P212A25	-	-

'Soufflerie' numérique

Des simulations multi-dimensionnelles ont été réalisées afin de visualiser les écoulements et d'accéder à des quantités non-mesurables sur banc expérimental. Les simulations ont été réalisées sous Fluent 6.0.12. Seuls des cas axi-symétriques 2D ont été réalisés. Les géométrie suivantes ont été considérées :

- Un élargissement brusque reliant un conduit à un volume (Fig. 9.6, gauche). Dans certains cas (écoulement de 1 vers 0), la géométrie d'élargissement brusque a été modifiée afin de créer un cône d'angle α , avec $\alpha \in [\frac{\pi}{4}; \frac{\pi}{2}]$.
- Une soupape axi-symétrique (Fig. 9.6, droite). Cette configuration simplifiée d'écoulement aux soupapes a été utilisée afin de valider certaines hypothèses d'écoulement.

Afin de créer les conditions de volume (vitesse nulle), la section F_0 is chosen de telle manière que pour n'importe quelle valeur de F_2 , $\frac{F_2}{F_0} < 0.02$. Sous ces conditions, la valeur de $\frac{u_0}{a_0}$ n'excède jamais 10^{-3} . L'air a été défini comme un gaz compressible idéal utilisant une loi de viscosité Sutherland standard. Le solveur 'steady 2D axi-symmetrical segregated solver' a été utilisé afin de résoudre les équations de Naviers-Stokes couplées à un modèle $k - \epsilon$ de turbulence. Une pression totale 1 à 10 bar avec vitesse nulle a été imposée comme condition d'entrée, alors qu'une pression statique de 1 bar a été imposée comme condition de sortie du domaine de calcul. La longueur du conduit a été définie comme 30 fois le diamètre équivalent de la restriction étudiée. Le but est d'éviter les phénomènes de non-uniformité rencontré dans le sillage des discontinuités. Les paramètres suivants ont été considéré lors de l'étude :

Mesh skewness	< 1e-2
Energy convergence criterion	1e-7
Other values convergence criterion	1e-5
Pressure under-relaxation factor	0.3
Density under-relaxation factor	1
Body forces under-relaxation factor	1
Momentum under-relaxation factor	0.7
$k-\epsilon$ under-relaxation factor	0.8
Turb. viscosity under-relaxation factor	1
Energy under-relaxation factor	1

3 Boucles itératives optimisées pour la résolution de la MDC dans le cas de conditions limites non-homentropiques.

Dans une première partie, la boucle de correction d'entropie sera modifiée afin d'utiliser un algorithme de Newton-Raphson pour converger vers la solution finale. Dans une deuxième partie, il sera montré qu'aucun schéma numérique n'est disponible dans la littérature pour faire face aux conditions limites d'écoulement sortant non-homentropiques. Par conséquent, un schéma itératif permettant de traiter l'augmentation du niveau sera élaboré. Cette boucle sera également associée à un algorithme de Newton-Raphson pour la convergence.

L'algorithme de convergence de Newton-Raphson permet de minimiser la valeur d'une fonction à l'aide de sa dérivée en vue d'adapter son facteur de convergence. Cet algorithme est décrit comme suit : Une fonction f de la variable x_1 est considérée. On suppose l'existence d'un intervalle $[a, b]$ tel que pour $x_1 \in [a; b]$, l'égalité $f(x_1) = 0$ est vérifiée. Dans ces conditions, il est possible de construire un schéma itératif permettant de faire converger la fonction f vers une valeur de x_1 qui vérifie $f(x_1) = 0$. Dans les développements suivants, it est la $it^{i\text{ème}}$ étape du schéma itératif. En introduisant la fonction dérivée $f'(x_1) = \frac{df(x_1)}{dx_1}$, l'algorithme de Newton-Raphson exprime les valeurs successives de x_1 qui permettent d'atteindre $f(x_1) \simeq 0$:

$$x_1^{it+1} = x_1^{it} - \frac{f(x_1^{it})}{f'(x_1^{it})}$$

Note : Il est important de faire la distinction entre les indices 'n' and 'it'. Les indices 'n' représentent le pas de temps du schéma de résolution du conduit (par exemple le pas de temps du schéma Lax-Wendroff), alors que les indices 'it' concernent le pas itératif du schéma de résolution propre à la condition limite. A chaque pas de temps 'n' du schéma global, une boucle de résolution itérative ($it=1 \dots$) est lancée pour résoudre le problème local de condition limite.

3.1 Fonction à minimiser dans le cas de la correction d'entropie

On rappelle que Benson [5] a exprimé la modification de la caractéristique incidente à la condition limite due à un changement de niveau d'entropie :

$$\lambda_{in,c} = \lambda_{in,n} + A_P \frac{A_{Ac} - A_{An}}{A_{Ac}}$$

A partir de cette équation, on définit les fonctions à minimiser par un algorithme de Newton-Raphson pour les cases d'écoulement entrant ou sortant :

3.2 Cas d'un écoulement entrant dans le domaine de calcul

Dans ce cas, la différence de niveau d'entropie entre la caractéristique incidente et l'écoulement au col de la restriction 2 (voir la figure 10.2) a deux origines : en premier lieu, en fonction des conditions thermodynamiques, il est possible que le gaz à l'extérieur du conduit se trouve à un niveau d'entropie différent du gaz à l'intérieur du conduit. En second lieu, les équations des modèles de restriction présentés vont générer une augmentation du niveau d'entropie. Sur des applications réelles, cette augmentation de l'entropie est due à l'irréversibilité de l'écoulement, comme les phénomènes de recirculation ou de cisaillement dans la couche limite. Par conséquent, la correction d'entropie est affectée par le choix du modèle à la condition limite, car ceux-ci ne génèrent pas tous la même création d'entropie.

En vue d'appliquer l'algorithme de Newton-Raphson à la MDC, il est nécessaire d'introduire une fonction à minimiser. La fonction d'entropie introduite par Benson est modifiée afin de créer une fonction qui à minimiser f :

$$f = \lambda_{in,c} - \left(\lambda_{in,n} + A_{P'} \frac{A_{Ac} - A_{An}}{A_{Ac}} \right)$$

Cette fonction dépend des variables suivantes $A_{P'}$, A_{Ac} et $\lambda_{in,c}$. Ces variables sont basées sur des combinaisons linéaires des variables suivantes : p , u , a . Il existe donc un large choix de variables disponibles afin de construire l'algorithme de Newton-Raphson. Comme nous n'avons aucun critère de choix pour l'instant, nous allons utiliser la même variable choisie par Benson pour construire son algorithme, qui est $\lambda_{in,c}$:

Algorithme de Newton-Raphson construit en utilisant $\lambda_{in,c}$ comme variable de convergence : Compte tenu de ce choix de variable, la boucle itérative de Newton-Raphson est écrite comme suit :

$$\lambda_{in,c}^{it+1} = \lambda_{in,c}^{it} - \frac{f(\lambda_{in,c})^{it}}{f'(\lambda_{in,c})^{it}}$$

Il est nécessaire de calculer la dérivée de la fonction à minimiser. Dans notre cas on obtient :

$$f'(\lambda_{in,c}) = \lambda'_{in,c} - \lambda'_{in,n} - \left(A_{P'} \left(1 - \frac{A_{An}}{A_{Ac}} \right) \right)'$$

$$f'(\lambda_{in,c}) = 1 - \frac{dA_{P'}}{d\lambda_{in,c}} \left(1 - \frac{A_{An}}{A_{Ac}} \right) + A_{P'} \left(\frac{\frac{dA_{Ac}}{d\lambda_{in,c}}}{A_{Ac}^2} \right)$$

Le développement de $\frac{dA_{Ac}}{d\lambda_{in,c}}$ permet d'obtenir l'expression suivante :

$$\frac{dA_{Ac}}{d\lambda_{in,c}} = \frac{dA_{P'}}{d\lambda_{in,c}} P^{\frac{\gamma-1}{2\gamma}} + A_{P'} \frac{\gamma-1}{2\gamma} \frac{dP}{d\lambda_{in,c}} P^{-\frac{\gamma-1}{2\gamma}}$$

Les développements inclus dans le corps de thèse (Eq. 10.9 à 10.12) montrent que la dérivée $\frac{dP}{d\lambda_{in,c}}$ introduit des expressions qui nécessitent l'utilisation de méthode de dérivation numérique plutôt qu'analytique. Ainsi, on construit la cartographie de l'évolution de P en fonction de $\lambda_{in,c}$ et la dérivée est obtenue d'après l'expression suivante : $\frac{dP}{d\lambda_{inc}} = \frac{P_{i+1} - P_i}{\lambda_{inc}(i+1) - \lambda_{inc}(i)}$, où i est l'indice en abscisse de la cartographie. Une fois que ces quantités sont calculées, l'algorithme de Newton-Raphson est opérationnel. Dans la majorité des cas, on obtient une convergence satisfaisante. Néanmoins, on note une divergence de l'algorithme sur des points de fonctionnement où la section d'entrée est faible et le rapport de pression élevé entre l'extérieur et l'intérieur du tube. Ces conditions sont représentatives d'un cas de début d'admission sur un moteur, et il est donc nécessaire d'identifier la cause de ces divergences.

En regardant l'évolution de P par rapport à $\lambda_{in,c}$, on note que ces points de fonctionnements concordent avec une zone où les pentes tendent vers l'infini (Fig. 10.3, $\phi = 0$: section d'entrée fermée, $\phi = 1$ section d'entrée pleine ouverte). Sur certains points, les valeurs calculées de $\frac{dP}{d\lambda_{in,c}}$ atteignent la valeur de 10^{15} . Cela a deux effets sur l'algorithme de Newton-Raphson :

- Les valeurs élevées de P' conduisent à des valeurs élevées de $f'(\lambda_{in,c})$. Par conséquent, le terme de convergence correspondant $\frac{f(\lambda_{in,c})^{it}}{f'(\lambda_{in,c})^{it}}$ ($< 10^{-16}$ sur certains points) prendra des valeurs très faibles. .
- La dérivation numérique produit des erreurs importantes dans le cas de pentes très raides. Ces erreurs, une fois introduites dans l'algorithme de Newton-Raphson, empêchent la convergence de l'algorithme.

Algorithme de Newton-Raphson construit en utilisant P comme variable de convergence : Dans le dernier paragraphe, il a été démontré que la mise en œuvre de l'algorithme de Newton-Raphson appliqué à la boucle d'entropie en utilisant $\lambda_{in,c}$ comme variable de convergence ne fournit pas de résultats satisfaisants. Dans ce paragraphe, il est proposé d'utiliser le rapport de pression P au travers de la condition limite comme variable de convergence. Le principal avantage de cette causalité est qu'il permet d'éviter les pentes infinies causant la divergence de l'algorithme de Newton-Raphson.

On définit la fonction f à minimiser par l'algorithme de Newton-Raphson :

$$f = \lambda_{in,c} - \left(\lambda_{in,n} + A_{P'} \frac{A_{Ac} - A_{An}}{A_{Ac}} \right)$$

Comme le rapport de pression est défini comme la variable de convergence, c'est donc P qui est mis à jour à chaque étape de l'itération :

$$P^{it+1} = P^{it} - \frac{f(P)^{it}}{f'(P)^{it}}$$

La fonction dérivée f' doit maintenant être exprimée par rapport à la variable de convergence P . À un pas de l'itération n donné, $f'(P)$ est exprimée comme suit :

$$f'(P) = \frac{d\lambda_{inc}}{dP} - \frac{dA_{P'}}{dP} \left(1 - \frac{A_{An}}{A_{Ac}} \right) + A_{P'} \left(\frac{A_{An} \frac{dA_{Ac}}{dP}}{A_{Ac}^2} \right)$$

avec :

$$\frac{dA_{Ac}}{dP} = \frac{dA_{P'}}{dP} P^{\frac{\gamma-1}{2\gamma}} + A_{P'} \frac{d\left(P^{\frac{\gamma-1}{2\gamma}}\right)}{dP}$$

Comme $\frac{d\lambda_{inc}}{dP}$ peut être exprimée comme une fonction de $\frac{dA_{P'}}{dP}$, il y a donc deux fonctions dérivées à calculer pour construire l'algorithme de Newton-Raphson : $\frac{d\left(P^{\frac{\gamma-1}{2\gamma}}\right)}{dP}$ and $\frac{dA_{P'}}{dP}$. La première peut être exprimé analytiquement, alors que la seconde nécessite l'utilisation d'une cartographie pour être calculée numériquement. Les évolutions de $P^{\frac{\gamma-1}{2\gamma}}$ et de $A_{P'}$ par rapport à P sont tracées sur la figure 10.4. Il apparaît que $P > 0,05$, les pentes des courbes sont modérées, ne tendant jamais vers l'infini. Des rapports de pression inférieurs à 0,05 ne sont pas rencontrés sur les chaînes d'air de moteurs automobiles. Par conséquent, le choix de P comme variable de convergence de Newton-Raphson permet de construire un système itératif robuste afin de résoudre la boucle de correction d'entropie.

3.3 Cas d'un écoulement sortant du domaine de calcul

Dans cette section, on considère un écoulement sortant d'un conduit au travers d'une section partiellement ouverte. En utilisant la notation de Benson, la variable incidente de Riemann $\lambda_{in,n}$ est transportée sur C+ : $u + a$. $\lambda_{in,c}$ représente la variable de Riemann à la limite, qui tient compte de la variation d'entropie entre le nœud à l'intérieur du conduit P et du nœud à la frontière 1. Afin de résoudre le problème de condition limite, il est possible de négliger localement l'accroissement d'entropie dû au frottement pariétal et aux échanges de chaleur entre les nœuds i et 1. Comme la discrétisation spatiale est supposée fine, cette simplification a un impact négligeable sur le résultat final. En outre, la section du conduit entre i et 1 est constante. Par conséquent, on écrit que :

$$\lambda_{in,c} = \lambda_{in,n}$$

Néanmoins, l'augmentation du niveau d'entropie due à singularité de sortie entre 1 et 2 doit être prise en compte. Il en résulte la nécessité de construire un schéma itératif. En fait, Benson [5] a montré que ce processus itératif est nécessaire même dans le cas où l'écoulement est entièrement isentropique entre 1 et 2. Ceci est illustré dans le développement suivant :

Résolution d'un écoulement sortant isentropique :

Le modèle associé à un écoulement sortant d'un conduit au travers d'une section partiellement ouverte sous hypothèse d'isentropicité a été présenté dans l'étude bibliographique. Il est rappelé que le système d'équations mis en place est le suivant dans le cas d'un écoulement subsonique : [isentropic_{1/2}, mass_{1/2}, energy_{1/2}, p₂ =

$p_0, a^2 = \frac{\gamma p}{\rho}, MOC]$. Afin de résoudre cette condition limite homentropique, Benson propose la méthode suivante : les équations de conservation de l'énergie (Eq. 10.20), de la masse (Eq. 10.22) et l'hypothèse d'isentropicité Eq. (10.21) sont combinées afin de construire la relation suivante : où $\phi = \frac{F_2}{F_1}$ et $A = \frac{a_1}{a_{ref}}$:

$$f(A) = \left(A^{\frac{4}{\gamma-1}} - \phi^2 \right) (\lambda_{in,c} - A)^2 - \frac{\gamma-1}{2} (A^2 - 1) \phi^2 = 0$$

La résolution de l'équation précédente permet d'obtenir la valeur de a_1 (a_{ref} étant fixé). Il est ensuite possible de calculer les valeurs de u_1 et p_1 en utilisant les autres équations du système. Cependant, il est nécessaire d'introduire un processus itératif pour résoudre cette équation. Benson a proposé basée sur la dichotomie pour la résolution itérative, néanmoins il est possible d'introduire un algorithme de Newton-Raphson basée sur A comme variable de convergence.

Dans le cas d'un écoulement sonique, l'équation de col sonique est introduite ($\frac{u_2}{a_2} = 1$). Dans le cas d'un écoulement sonique, le rapport $\frac{a_1}{a_2}$ est constant pour une ouverture de section de sortie donnée (ϕ). Ce ratio est appelé rapport de vitesses du son critique $\left(\frac{a_1}{a_2}\right)_{cr}$ lorsque l'écoulement devient sonique au col. Il est nécessaire de calculer cette quantité pour résoudre le problème de condition limite dans le cas sonique. Un développement similaire au cas subsonique produit la relation suivante, qui doit être résolue en utilisant un processus itératif :

$$f\left(\frac{a_1}{a_2}\right)_{cr} = \phi^2 - \left[\frac{\gamma+1}{\gamma-1} - \left(\frac{2}{\gamma-1} \right) \left(\frac{a_1}{a_2} \right)_{cr}^2 \right] \left(\frac{a_1}{a_2} \right)_{cr}^{\frac{4}{\gamma-1}} = 0$$

Résolution d'un écoulement sortant non-isentropique :

D'après l'étude bibliographique, il apparaît que dans le cas de la condition limite d'un écoulement sortant, le seul modèle développé dans la littérature est basé sur l'hypothèse d'écoulement isentropique entre 1 et 2. Ce modèle est nécessairement associé à un coefficient de décharge C_d . D'autres modèles d'écoulements sortants, mais non-isentropiques seront introduits plus loin dans la thèse. Ces modèles utilisent l'équation de conservation du moment, sous hypothèse d'élargissement brusque, exprimée entre les états 1 et 2 :

$$(p_1 + \rho_1 u_1^2) F_1 = (p_2 + \rho_2 u_2^2) F_2 - (p_1 + \rho_1 u_1^2)(F_1 - F_2)$$

Cette équation remplace l'hypothèse d'écoulement isentropique dans le système d'équations régissant la condition limite d'écoulement sortant. Par conséquent, il n'est plus possible de dériver les deux équations introduites dans le paragraphe précédent. Afin de résoudre le problème de condition limite dans le cas d'un écoulement sortant non-isentropique, une approche polytropique a été développée. L'objectif de cette méthode est de conserver la formulation développée pour le cas isentropique, dans un souci de conserver une résolution simple.

Dans le cas d'un écoulement non-isentropique entre 1 et 2, on a l'inégalité suivante :

$$\frac{a_2}{a_1} \neq \left(\frac{p_1}{p_2} \right)^{\frac{\gamma-1}{2\gamma}}$$

Toutefois, il est possible d'identifier un exposant polytropique κ tel que :

$$\frac{a_2}{a_1} = \left(\frac{p_1}{p_2} \right)^{\frac{\kappa-1}{2\kappa}}$$

Il est possible d'exprimer κ et de tracer son évolution sur une cartographie en utilisant la relation suivante :

$$\kappa = \frac{-1}{2 \log\left(\frac{a_1}{a_2}\right)/\log\frac{p_1}{p_2} - 1}$$

L'évolution de κ est tracée sur la figure 10.7. On rappelle que dans le cas d'un processus isentropique d'un gaz parfait, $\kappa = 1,40$. Dans ce cas, l'écart par rapport à 1,40 exprime une augmentation du niveau d'entropie due à l'irréversibilité prise en compte par la résolution de l'équation du moment. Une fois que l'écoulement devient sonique au col, l'évolution de $\frac{a_1}{a_2}$ par rapport à $\frac{p_1}{p_2}$ est constante, donc le coefficient polytropique correspondant reste constant dans la plage d'écoulement sonique.

En utilisant la relation polytropique, il est possible de développer les relations suivantes, similaires au cas isentropique :

$$f(A) = \left(A^{\frac{4}{\kappa-1}} - \phi^2 \right) (\lambda_{in,c} - A)^2 - \frac{\gamma-1}{2} (A^2 - 1) \phi^2 = 0$$

$$f\left(\frac{a_1}{a_2}\right)_{cr} = \phi^2 - \left[\frac{\gamma+1}{\gamma-1} - \left(\frac{2}{\gamma-1} \right) \left(\frac{a_1}{a_2} \right)_{cr}^2 \right] \left(\frac{a_1}{a_2} \right)_{cr}^{\frac{4}{\kappa-1}} = 0$$

Ainsi, tout en conservant le formalisme du cas isentropique, on inclut la non-isentropicité du modèle en utilisant une formulation d'évolution polytropique. Pour un modèle donné, une cartographie du coefficient polytropique κ est créée puis utilisée pour résoudre le problème :

- Les valeurs de κ sont stockées dans une cartographie et exprimées par rapport à $\frac{\lambda_{in,c}}{a_{ref}}$, où a_{ref} est une vitesse du son de référence arbitrairement choisie. arbitrarily defined.
- $\lambda_{in,c}$ est connue, car dans le cas d'écoulement sortant, on écrit sous certaines hypothèses : $\lambda_{in,n} = \lambda_{in,c}$.
- Connaissant $\lambda_{in,c}$, la valeur de κ est lue dans la cartographie.
- Finalement, on utilise un schéma itératif pour résoudre l'équation, comme dans le cas subsonique.

3.4 Choix du critère de convergence

Le schéma itératif développé pour la résolution des conditions limites entrantes ou sortantes permettent de converger vers la solution du problème. Néanmoins, il est nécessaire de définir un critère de convergence, qui va définir le seuil de précision en dessous duquel le calcul itératif est stoppé et la solution considérée comme convergée. Plus la valeur du critère de convergence défini est faible, plus la solution sera précise mais plus le temps de convergence sera long. A partir de tests numériques, il est apparu que définir la valeur du critère de convergence C_C à 10^{-5} fournit un compromis satisfaisant entre précision et temps de calcul lorsque l'algorithme de Newton-Raphson est utilisé. Il est apparu que pour des valeurs de critère de convergence supérieures à 10^{-5} , des oscillations parasites peuvent apparaître (voir la figure 10.11).

Sur cette figure, une onde de raréfaction incidente à la condition limite partiellement ouverte se déplace. Le gaz à l'intérieur du conduit, à l'origine au repos, évolue lorsque l'onde atteint la limite. Un phénomène de 'backflow' apparaît, c'est à dire qu'un écoulement entrant se crée momentanément à la frontière, dû à l'arrivée de l'onde de dépression. Il est alors nécessaire de détecter le sens de l'écoulement. Ceci est réalisé en utilisant le signe de $(\lambda_{in} - 1)$ ([5], [139]). Par conséquent, l'erreur due à la convergence du schéma itératif a deux conséquences sur le résultat global :

- Dans un premier temps, l'erreur de convergence a un impact sur le calcul des quantités relatives à l'écoulement (pression, densité, vitesse des particules ...).
- En second lieu, ces erreurs ont un impact sur le calcul de λ_{in} . On a vu que la valeur de λ_{in} est utilisée comme un critère de détection du sens de l'écoulement. Par conséquent, dans le cas où des valeurs élevées du critère de convergence sont utilisées, il est possible d'obtenir une mauvaise estimation du sens de l'écoulement. Dans ce cas, des oscillations parasites apparaissent.

3.5 Vitesse de convergence

L'objectif principal de l'introduction de l'algorithme de Newton-Raphson dans les boucles de résolution des conditions limites était de réduire le temps de calcul. Afin d'analyser les gains de l'algorithme de Newton-Raphson par rapport au schéma proposé par Benson, une étude comparative a été effectuée. Un cycle d'ouverture-fermeture d'une soupape est réalisé afin de simuler soit un débit entrant dans un conduit (cycle d'échappement) ou sortant d'un conduit (cycle d'admission) au travers d'une soupape. Pendant la simulation, le nombre d'itérations nécessaires pour converger vers la solution a été stocké. Les résultats de cette étude sont présentés sur la figure 10.12. Les observations suivantes sont rapportées :

- Ecoulement entrant : La mise en œuvre de l'algorithme de Newton-Raphson sur la boucle de correction d'entropie permet de diminuer d'un facteur de 4-5 (en moyenne) le nombre d'itérations nécessaires pour converger vers la solution. Ce facteur a été observé dans les cas subsoniques et soniques. En moyenne, pour un seul cycle d'échappement, le nombre d'itérations es réduit, passant de ~ 20000 (Benson) à 4500 (développement proposé utilisant l'algorithme de Newton-Raphson), lorsqu'un critère de convergence de 10^{-5} est utilisé.
- Ecoulement sortant : Dans ce cas, le gain observé est plus faible, car le nombre d'itérations requis n'est réduit que par un facteur de 1,5 en moyenne. On rappelle néanmoins que l'objectif principal du travail relatif à l'écoulement sortant est la prise en compte de la non-isentropicité du problème.

4 Modèles non-isentropiques associés aux conditions limites : construction des cartographies et nouveaux développements.

Les schémas numériques dédiés à la résolution des limites non-homéentropiques ont été introduits. Ces schémas permettent de résoudre numériquement les équations de l'écoulement aux conditions limites. Ces équations déterminent la modélisation du comportement de l'écoulement aux limites et sont donc directement liées à la précision des résultats. Plusieurs modèles d'écoulement ont été développés dans l'étude bibliographique. Il est proposé dans la thèse de redévelopper ces équations afin de préciser le processus de construction des cartographies qui sont utilisées dans les boucles de résolution. Il est également proposé de développer de nouveaux modèles, notamment dans le cas d'écoulement sortant d'un conduit. Le but est d'introduire des conditions limites non isentropiques plus physiques. Enfin, il sera montré que les modèles de conditions limites 'basiques' développées ou existantes peuvent être combinées afin de créer des conditions aux limites de systèmes plus complexes.

4.1 Modèles non-isentropiques de restrictions : Cas des écoulements entrant dans le conduit

Dans cette section, les équations et hypothèses des modèles de la littérature dans le cas des écoulements entrant dans un conduit via une ouverture partielle sont re-développés. Le but est de construire des cartographies non-homéentropiques. En effet, il a été observé dans l'étude bibliographique que Benson [5] réussi à construire de telles cartographies, mais sous hypothèse homéentropique. Il est nécessaire de construire des cartographies sans introduire l'hypothèse d'écoulement homéentropique, car elle n'est pas représentative des systèmes d'équations utilisés. Dans le corps de thèse, les modèles suivants sont re-développés dans le cas d'un écoulement entrant : modèle subsonique sous hypothèse de pression constante, modèle subsonique sous hypothèse d'élargissement brusque, modèle sonique avec écoulement choqué au col et modèle sonique de tuyère isentropique.

Le système isolé est rappelé sur la figure 11.1 : le gaz pénètre dans le conduit sous la forme d'un jet de section

$F_2 = F_t$. Il s'élargit ensuite pour occuper la section complète du conduit au niveau du plan 1. Le système isolé est situé entre les plans 1 et 2. Dans les développements suivants, il est considéré que l'écoulement devient homogène immédiatement après la restriction, au niveau du plan 1.

Il y a 6 inconnues à déterminer (pression, densité et vitesse en 1 et en 2), donc six équations sont nécessaires. Ces équations sont rappelées ici et la procédure adoptée pour construire des cartographies non-homentropiques est décrite. Les variables en majuscules sont les variables adimensionnées par rapport à un état de référence. Les expressions mathématiques développées dans cette section ont été obtenues en utilisant l'état de stagnation 0 comme état de référence. Par conséquent, on obtient $A = \frac{a}{a_0}$, $U = \frac{u}{a_0}$ and $P = \frac{p}{p_0}$. Tous les modèles d'écoulement entrant au travers d'une section partiellement ouverte trouvés dans la littérature se fondent sur les 4 équations suivantes : une évolution isentropique entre l'état 0 et le col 2, la conservation de l'énergie entre l'état 0 et le col 2, la conservation de l'énergie entre le col 2 et l'état 1 dans le conduit et la conservation de la masse entre le col 2 et l'état 1 dans le conduit :

$$\begin{aligned} P_2 &= A_2^{\frac{2\gamma}{\gamma-1}} \\ A_2^2 + \frac{\gamma-1}{2} U_2^2 &= 1 \\ A_1^2 + \frac{\gamma-1}{2} U_1^2 &= A_2^2 + \frac{\gamma-1}{2} U_2^2 \\ \rho_1 U_1 &= \phi \times \rho_2 U_2 \end{aligned}$$

Dans le cas subsonique, une cinquième équation est ajoutée en considérant soit la résolution de l'équation de quantité de mouvement sous hypothèse d'élargissement brusque entre 1 et 2 : $\phi \rho_2 u_2^2 - \rho_1 u_1^2 + (p_1 - p_2) = 0$, soit en considérant une hypothèse de pression constante entre le col et le conduit : $p_1 = p_2$. Une sixième équation est donc nécessaire pour boucler le système. Afin de construire une cartographie des solutions du système, on n'utilise pas la méthode des caractéristiques sous hypothèse homentropique $\lambda_{in} = A - \frac{\gamma-1}{2} U$ (comme le fait Benson), mais on impose un des paramètres afin de balayer l'ensemble des solutions admises par le système. Dans le cas subsonique, on impose la vitesse au col telle que :

$$U_2 \in [0; \sqrt{\frac{\gamma+1}{2}}]$$

Dans le cas sonique, l'équation d'écoulement choqué au col apparaît naturellement : $\frac{u_2}{a_2} = 1$. Il n'est donc plus nécessaire de considérer la résolution de l'équation du moment entre les états 2 et 1 ou d'introduire une hypothèse de pression constante. Par contre, c'est désormais la vitesse en 1 qui est imposée, car la vitesse en 2 est imposée par l'écoulement sonique au col. U_{1cr} est la valeur de la vitesse en 1 lorsque l'écoulement devient sonique.

$$U_1 \in [U_{1cr}; \sqrt{\frac{\gamma+1}{2}}[$$

Il existe un deuxième modèle sonique développé par Demoulin [32], qui considère l'écoulement sonique entrant comme une tuyère. Néanmoins, il sera vu que ce modèle fournit des résultats non-physiques et n'est donc pas détaillé plus en détails ici.

On peut à présent résumer le processus de construction des cartographies non-homentropiques de la façon suivante :

1. Les modèles de conditions limites permettent l'introduction de 5 relations alors qu'il y a 6 inconnues à déterminer.
2. Afin de préserver le caractère non-homentropique des systèmes d'équations introduits, on impose soit la vitesse au col (cas subsonique), soit la vitesse dans le conduit (cas sonique). Ce paramètre est balayé afin de couvrir l'ensemble des solutions admises par les systèmes d'équations.

3. Une fois que le paramètre de vitesse est imposé, il est possible de déterminer les autres quantités en résolvant le système d'équations.
4. Lorsque les 6 quantités sont connues à chaque point de fonctionnement de la restriction, il est possible de construire une cartographie complète.

Analyse des cartographies : Les cartographies des modèles précédemment développés sont tracés sur la figure 11.4. Ce sont les vitesses adimensionnées dans le conduit $\frac{u_1}{a_0}$ qui sont tracées. Cette quantité est directement liée au débit massique passant au travers de la restriction. Les résultats sont fournis pour plusieurs rapports de section $\frac{F_2}{F_1}$. On compare à présent les résultats fournis par les différents modèles :

Dans le cas subsonique, on note que le modèle basé sur la résolution de l'équation du moment produit systématiquement des vitesses d'écoulement supérieures au modèle basé sur l'hypothèse de pression constante. De plus, on voit que la limite sonique est différente : elle arrive pour des rapports de pression $\frac{p_1}{p_0}$ supérieurs dans le cas de l'équation du moment. Ces phénomènes sont dûs à la chute de pression statique qui a lieu en aval du col lorsque l'équation du moment est résolue ($p_2 < p_1$). Cette chute de pression n'a pas lieu pour le modèle à pression constante, car on impose $p_2 = p_1$. Ainsi, la pression avalée 'vue' par le col est plus faible dans le cas de l'équation du moment, et le débit est augmenté car la différence de pression aux bornes du col est plus élevée.

Dans le cas sonique, on note que le modèle de tuyère produit des évolutions de vitesse pratiquement horizontales. Dans le cas du modèle de blocage sonique au col, on note une augmentation de la vitesse adimensionnée, jusqu'à atteindre un état d'écoulement sonique dans le conduit lui-même. On verra plus loin lequel des deux modèles produit une évolution en corrélation avec les mesures expérimentales.

4.2 Modèles non-isentropiques de restrictions : Cas des écoulements sortant du conduit

On rappelle qu'une seule condition limite de fluide sortant d'un conduit via une section partiellement ouverte a été trouvée dans l'étude bibliographique. Cette condition limite est basée sur une hypothèse d'isentropie et est par conséquent systématiquement combinée à des correctifs expérimentaux. Dans le but de réduire la nécessité d'introduire de tels correctifs, il est proposé d'introduire la résolution de l'équation de conservation du moment en lieu et place de l'hypothèse d'isentropie. On obtient alors une condition limite non-isentropique.

Le système isolé est tracé sur la figure 11.6. Afin de résoudre l'équation du moment sous hypothèse de restriction brusque, la distribution de pression en amont de la restriction est non-uniforme : au col, la pression statique est supposée être égale à la pression extérieure ($p_2 = p_0$). Cependant, la pression appliquée sur la paroi de la restriction brusque est considérée comme étant égale à la pression totale (pressions statique + pression dynamique) de l'écoulement du conduit en 1. C'est la théorie de la pression d'arrêt, appliquée sur la paroi par un fluide initialement en mouvement. Cette distribution de pression mène à l'équation de conservation du moment suivante :

$$(p_1 + \rho_1 u_1^2) F_1 = (p_2 + \rho_2 u_2^2) F_2 - (p_1 + \rho_1 u_1^2)(F_1 - F_2)$$

On peut ré-écrire cette équation sous une autre formulation, avec $\phi = \frac{F_2}{F_1}$

$$\frac{p_2}{p_1} = \frac{(2-\phi)+\gamma \frac{u_1^2}{a_1^2}(2-\phi)}{1+\gamma \phi \frac{u_2^2}{a_2^2}}$$

Dans le but de modéliser l'écoulement, on introduit les équations de conservations de l'énergie entre l'extérieur et le col, la conservation de l'énergie entre le col et l'intérieur du conduit et la conservation de la masse entre le col et l'intérieur du conduit

$$A_2^2 + \frac{\gamma-1}{2} U_2^2 = 1$$

$$A_1^2 + \frac{\gamma-1}{2} U_1^2 = A_2^2 + \frac{\gamma-1}{2} U_2^2$$

$$\rho_1 U_1 = \phi \times \rho_2 U_2$$

La combinaison de ces trois équations à l'équation de conservation du moment développée conduit à la relation suivante (voir Eq. 11.35 à 11.43 pour le détail des développements), où $a_{tot}^2 = a_1^2 + \frac{\gamma-1}{2} u_1^2 = a_2^2 + \frac{\gamma-1}{2} u_2^2$ est la vitesse du son totale de l'écoulement :

$$\left(\frac{\gamma-1}{\gamma+1} - \frac{2\gamma}{\gamma+1} (2 - \phi) \right) \left(\frac{u_1}{a_{tot}} \right)^2 + \frac{2}{\gamma+1} \left(\frac{(2-\phi)}{\phi} \left(\frac{a_2}{a_{tot}} \right)^2 \frac{a_{tot}}{u_2} + \gamma \frac{u_2}{a_{tot}} \right) \frac{u_1}{a_{tot}} - \frac{2}{\gamma+1} = 0$$

Il est également possible de prendre en compte des géométries autres qu'une restriction brusque en modifiant l'équation du moment. Considérons que la géométrie de sortie soit un cône d'une certaine inclinaison. Il est possible de modifier le terme de pression dynamique $\rho_1 u_1^2$ qui est appliqué sur la paroi pour prendre en compte la déviation de l'écoulement plutôt que son arrêt sur la paroi. On introduit un terme de correction Ψ qui va modifier le terme de pression dynamique. Ce terme est directement lié à la géométrie du cône de sortie : si l'angle du cône est de 45° , on considère que 50% de la pression dynamique est effectivement appliquée à la paroi, ce qui conduit à $\Psi = 0,5$. L'évolution de la valeur de Ψ en fonction de l'angle du cône de sortie est tracée sur la figure 11.7. Cela conduit à l'équation du moment modifiée suivante :

$$(p_1 + \rho_1 u_1^2) F_1 = (p_2 + \rho_2 u_2^2) F_2 - (p_1 + \Psi \rho_1 u_1^2)(F_1 - F_2)$$

Cette équation, combinée aux trois équation de conservation d'énergie et de masse conduit à la relation suivante :

$$\left(\frac{\gamma-1}{\gamma+1} - \frac{2\gamma}{\gamma+1} (1 + \Psi(1 - \phi)) \right) \left(\frac{u_1}{a_{tot}} \right)^2 + \frac{2}{\gamma+1} \left(\frac{(2-\phi)}{\phi} \left(\frac{a_2}{a_{tot}} \right)^2 \frac{a_{tot}}{u_2} + \gamma \frac{u_2}{a_{tot}} \right) \frac{u_1}{a_{tot}} - \frac{2}{\gamma+1} = 0$$

Création des cartographies : Dans le cas subsonique, on impose une vitesse d'écoulement subsonique au col : $U_2 \in [0; \sqrt{\frac{\gamma+1}{2}}]$. La sixième équation du système est obtenue en considérant que la pression p_2 est égale à la pression extérieure p_0 . Cela conduit à la résolution suivante :

1. U_2 est imposée. A_2 est déterminé en utilisant la conservation de l'énergie entre l'extérieur et le col..
2. Connaissant A_2 , U_2 et ϕ , on résout l'équation du second ordre obtenue pour $\frac{u_1}{a_{tot}}$, ce qui conduit à U_1 . A_1 est calculé en utilisant la conservation de l'énergie entre le col et le conduit.
3. En utilisant le fait que $p_2 = p_0$, la valeur de p_2 est obtenue . Finalement, l'équation de conservation du moment permet d'obtenir la valeur de p_1 .

Dans le cas sonique, on a : $U_2 = A_2 = cst$. Quand on regarde l'équation du second ordre en $\frac{u_1}{a_{tot}}$, on observe que U_2 , A_2 et ϕ sont constants dans le cas sonique. Par conséquent, la solution U_1 sera constante également. Donc, dans le cas d'un écoulement sortant via une section partiellement ouverte, l'état du fluide est figé dès que l'état sonique est atteint.

Analyse des cartographies : En utilisant les développements précédents, on trace les courbes caractéristiques des modèles développés. Sur la figure 11.8, on compare les résultats pour le modèle isentropique d'écoulement sortant provenant de la littérature à ceux du modèle non-isentropique développé, avec $\Psi = 1$. On compare également les résultats du modèle développé pour $\Psi = 1$ et $\Psi = 0,5$. Ce sont les valeurs de la vitesse du fluide adimensionnée U_1 qui sont tracées. Les résultats sont fournis pour différentes valeurs de rapport de section entre le conduit et la restriction $\phi = \frac{F_2}{F_1}$. On note que le modèle isentropique de la littérature fournit systématiquement des vitesses supérieures à celles obtenues avec le modèle non-isentropique et $\Psi = 1$. Comme l'hypothèse d'isentropicité néglige les pertes dans l'écoulement, il apparaît 'normal' d'observer ce comportement. Concernant la comparaison entre $\Psi = 1$ et $0,5$, on note que les vitesses obtenues pour $\Psi = 0,5$ sont supérieures à celles obtenues pour $\Psi = 1$. Cette tendance apparaît comme correcte car dans la réalité, placer un cône en sortie d'un conduit plutôt qu'une restriction brusque réduit les pertes de charge.

4.3 Résolution non-isentropique de l'écoulement en amont et en aval d'une restriction à l'intérieur du conduit.

Dans cette section, une méthode est proposée afin de résoudre l'écoulement en amont et en aval d'une restriction sans introduire d'hypothèse d'isentropicité. On considère l'écoulement tracé sur la figure 11.9 : le fluide provient d'un conduit en amont de section F_3 . Le fluide passe au travers d'une restriction de section F_2 , et rejoint le conduit aval de section F_1 . On introduit les rapports de section suivants : $\phi_1 = \frac{F_2}{F_1}$ et $\phi_3 = \frac{F_2}{F_3}$. Afin de modéliser l'écoulement entre 3 and 1, on considère la restriction comme étant la combinaison d'une restriction brusque et d'un élargissement brusque.

Afin de créer la cartographie de l'écoulement, on adopte la méthode de résolution suivante :

- La vitesse U_2 est imposée au col.
- A partir de cette vitesse, il est possible de résoudre l'état en aval de la restriction en utilisant les développements proposés pour la résolution d'un écoulement entrant via une section partiellement ouverte (section 4.1 du résumé).
- Connaissant U_2 , on résout également l'état en amont de la restriction à partir des développements proposés pour la résolution d'un écoulement sortant d'un conduit au travers d'une section partiellement ouverte (voir la section 4.2 du résumé).
- Au final, cette méthode permet de construire la cartographie de l'écoulement au travers d'une restriction au sein d'un conduit. On note que l'hypothèse d'isentropicité n'est pas du tout introduite au cours de la résolution.

La figure 11.10 rapporte une étude paramétrique effectuée sur les rapports de section de la restriction. On note que plus le rapport de section entre le col et la section $\frac{F_2}{F_x}$ ($x = 1$ ou 3) est faible, moins la vitesse du fluide est importante pour un rapport de pression donné. Ce comportement est en concordance avec le comportement réel rencontré dans un tel écoulement : les contractions ou élargissements brusques tendent à augmenter les pertes de charges. La précision de ce modèle sera validé par rapport à des mesures expérimentales dans le chapitre 5 de cette partie.

4.4 Condition limite de soupape

Dans la section suivante, les modèles associés aux conditions limites de soupapes sont détaillées. Dans les papiers de la littérature, ce sont les modèles d'élargissements ou de restrictions brusques qui sont utilisés pour modéliser l'écoulement aux soupapes. Comme les écoulements au travers des soupapes sont différents des écoulements au travers de restrictions à changement de section brusque, ces modèles nécessitent l'utilisation d'un coefficient correctif expérimental. Dans cette section, il est proposé de prendre en compte la

géométrie des soupapes afin de créer un modèle représentatif des écoulements aux soupapes. Les modèles développés sont inspirés des observations faites à partir des résultats de calculs aérodynamiques numériques multi-dimensionnels. On introduit sur la figure 11.11 les plans et notations introduits afin de définir le système : le plan 0 est situé dans le milieu au repos à l'extérieur du conduit, le plan 2 correspond au col de l'écoulement, qui est défini comme la section minimale disponible pour l'écoulement. Le plan 3 est le plan perpendiculaire à l'écoulement qui fournit la section de passage maximale entre la soupape et la paroi du cylindre. L_t est la distance entre les plans 2 et 3, L_3 et L_2 sont les longueurs associées aux sections d'écoulement en 2 et en 3.

Ecoulement entrant dans un conduit au travers d'une soupape : Dans le cas d'un écoulement entrant au travers d'une soupape, l'écoulement est établi entre le plan 0 et le plan 1. C'est l'écoulement rencontré lors de cycles d'échappement à partir d'un cylindre vers le conduit aval. Des calculs numériques multi-dimensionnels en stabilisé ont été réalisés et ont permis d'observer certaines caractéristiques de l'écoulement :

1. en conditions subsoniques, la pression statique est pratiquement égale entre le col et le conduit : $p_2 \simeq p_1$.
2. l'écoulement peut être supposé isentropique entre les plans 0 et 1.

Par conséquent, on construit le modèle d'écoulement entrant via une soupape de la façon suivante :

- On utilise la relation d'isentropicité entre 0 et 3.
- Les équations d'Euler (masse, énergie, moment) exprimées en stabilisé sont résolues entre 3 et 2. Dans ce cas, on exprime l'équation du moment en fixant la variable de correction de la pression dynamique Ψ de façon à prendre en compte la géométrie de la soupape : $\Psi = \frac{1}{90} \text{atan}\left(\frac{L_3 - L_2}{L_t}\right)$.
- Dans le cas subsonique, on applique le modèle provenant de la littérature d'écoulement entrant sous hypothèse de pression constante (voir la section 4.1 du résumé) entre 2 et 1. Dans le cas où l'écoulement est sonique, on utilise le modèle de la littérature d'écoulement entrant sonique au col entre 2 et 1.

Ecoulement sortant d'un conduit au travers d'une soupape : Dans ce cas, l'écoulement est établi entre le conduit 1 et l'état au repos 0. Ce type d'écoulement est rencontré durant les cycles d'admission sur moteur. Des calculs numériques multi-dimensionnels en stabilisé ont été réalisés et ont permis d'identifier certaines caractéristiques de cet écoulement :

1. en conditions subsoniques, la pression statique p_3 est égale à la pression en aval p_0 .
2. la pression statique au col de la restriction p_2 est inférieure à la pression statique p_3 .

Afin de respecter ces observations, c'est l'assemblage de modèles suivant qui a été utilisé afin de modéliser un écoulement sortant via une soupape :

- Le système d'équations d'Euler (masse, énergie, moment) est résolu entre 1 et 2. C'est le même modèle que celui développé dans le cas d'un écoulement non-homentropique sortant au travers d'une section partiellement ouverte (voir section 4.2). L'équation du moment est écrite avec le terme de correction de pression dynamique égal à 1 ($\Psi = 1$).
- Le modèle d'écoulement entrant utilisant l'hypothèse d'élargissement brusque (section 4.1) est utilisé afin de modéliser l'écoulement entre 2 et 3. Ce modèle satisfait la condition $p_2 < p_3$.
- Finalement, dans le cas subsonique, la pression statique p_3 est fixée égale à p_0 .

Dans le cas d'écoulement sonique, la création de la cartographie est différente : le blocage sonique au col fixe les valeurs de U_2 et A_2 , et par conséquent, les valeurs de U_1 et A_1 sont fixées (voir section 4.2). Le rapport de pression $\frac{p_0}{p_1}$ évolue entre sa valeur critique (celle lorsque l'écoulement devient juste sonique) et 0.

Il est conclut qu'un assemblage de modèles simples a permis la création de modèles de soupapes plus complexes. La méthode utilisée afin de créer les cartographies correspondantes a été détaillée, les résultats sont visibles sur les figures 11.12 et 11.13.

General conclusion

Conclusion and perspectives

The present thesis has proposed developments in order to improve the accuracy and the computational efficiency of the 0D/1D models of the engine airpath. These two parameters have a strong impact on the compliancy of the model-based approach with the engine control development process. The guideline of the thesis can be summed-up as follows :

Including as much physics as possible...

In this thesis, the improvement of the models accuracy has systematically been achieved by introducing the physical equations of the flow processes.

In the case of the turbocharger, the turbomachinery equations have been redeveloped and analyzed in order to build a more physical model. The linear trend of the enthalpy evolution with respect to the mass flow rate has been used to provide some coherence and physical behavior to the mean-value model. This linear evolution has been demonstrated for the compressor and the turbine, which allows to get a similar treatment in both cases. The linear evolution is used to express the turbomachines efficiencies without introducing complex curve fitting methods. More importantly, the proposed method respects the physical relation between the ideal and the actual turbomachines work. The modeling of the heat exchanges within turbochargers has also been investigated. An equivalent thermal resistance scheme of the turbocharger has been built in order to take into account the heat transfers and their impact on the turbocharger performances.

In the case of the flow restrictions, it has been intended to solve the complete Euler's equations set rather than introducing simplifications, such as the isentropic flow assumption. Indeed, it has been seen that flow restriction models are generally based on an isentropic flow assumption, which simplifies the boundary problem resolution. However, this hypothesis is generally not verified experimentally, as flow losses systematically occur through a restriction. In the literature, an experimental discharge coefficient is generally introduced in order to artificially take into account the flow losses. The main drawback of this approach is that experimental measurements must be performed. The isentropic relationship generally replaces the momentum conservation resolution. In order to investigate a possible improvement of the models accuracy without having to introduce a corrective coefficient, the momentum conservation equation has been re-introduced in the boundary equations systems. Additionally, the possibility to assemble the simple inflow/outflow boundary models in order to build more complex boundaries such as poppet valves or diaphragms has been demonstrated.

... without impacting the calculation time.

The optimization of the calculation time has been an important aspect of the proposed work.

In the case of the turbocharger, the introduction of the turbomachinery equations in the extrapolation algorithm has no impact on the calculation time. The physical developments are pre-processed and stored into a datemap. Consequently, the CPU charge remains low while the accuracy has been increased. Regarding the heat exchanges, the proposed model is based on an equivalent resistance scheme of the turbocharger. This system is solved analytically, therefore the additional computation time required by the heat exchange model is almost negligible.

In the case of the flow restrictions, the iterative loops introduced to solve the 1D inflow/outflow boundary problems have been optimized. The Newton-Raphson algorithm has been applied to the resolution of the 1D flow at boundaries. It has been shown that the choice of the convergence variable is crucial, as it has a strong influence on the robustness of the method. Performance datamaps of the flow restrictions have been introduced in order to simplify the development of the derivative functions introduced by the Newton-Raphson algorithm. The proposed method allows to reduce by a factor 4 the number of iterations required to achieve the convergence of the boundary problem.

Experimental validations...

A large part of the thesis has been dedicated to the experimental validation of the proposed developments. In each area of the thesis, experimental benches have been used. Among them, the steady flow benches (the diaphragm bench and the cylinder head bench) have been developed, built and developed during this thesis. The experimental measurements have allowed to validate the accuracy of the models under transient and stabilized conditions.

... leading to the industrial application of the models.

The experimental validation of the models has allowed to ensure the good accuracy of the proposed models. As a consequence, the models have been applied to the development of the EUR05-EURO6 engines control laws at Renault. These applications have lead to the writing of three applied patents (two regarding the estimation of the EGR rates, one regarding the turbocharger control). An example of the application of the turbocharger model has been described in a paper [87], where the datemap-based turbocharger model is coupled to a mean-value model of the engine in order to tune the command of a variable geometry turbocharger.

Future developments :

Future work directions have been identified in order to improve and to generalize the methods developed in the present thesis :

- Interaction between a 1D pipe scheme and a turbocharger : The iterative schemes dedicated to the 1D boundary conditions have been developed in the case of flow restrictions. However, such schemes have not been adapted to the case of turbochargers. The future developments will be based on work by Benson [5] and Winterbone [139], who already proposed entropy correction loops in the case of turbochargers. As in the flow restriction case, it will be intended to optimize these iterative loops in terms of convergence speed. A crucial aspect will be the identification of a convergence variable ensuring the robustness of the Newton-Raphson algorithm.
- Flow restriction boundary models : The proposed flow restriction models have shown that the resolution of the momentum conservation equation and the assembly of simple models allows to reduce the necessity of a discharge coefficient. It is intended to apply these methods in order to model other components. During the thesis, these future developments have been anticipated : for example, the diaphragm steady flow bench is compatible with a future implementation of a throttle device.
- Turbocharger heat exchange model : The proposed turbocharger heat exchange model is heavily dependent on experimental measurements. In order to allow the generalization of the heat exchange model, it is necessary to identify the dependency of the thermal resistances regarding the parameters of the turbocharger. Such a study requires to perform experimental measurements on several turbochargers. Multi-dimensional calculations of the heat exchanges could also be an helpful tool in order to access to non-measurable quantities, such as the local temperature distributions.
- Implementation of the CE-SE numerical scheme : The developments regarding the flow through restrictions have been coupled to a 1D Lax-Wendroff scheme in order to solve the inpipe flow. This numerical scheme has reached a mature level and provides satisfying results. However, it would be in-

teresting to test the interaction between the boundary resolution schemes developed during this thesis and the Conservation Element - Solution Element scheme developed by Chang [20] [21], as it allows a significant reduction of the calculation time. According to Onorati [98], such a scheme runs 20% faster than a Lax-Wendroff scheme.

Résumé : Conclusion et perspectives

La présente thèse a proposé des développements afin d'améliorer la précision et l'efficacité en termes de temps de calcul des modèles 0D/1D de la chaîne d'air des moteurs à combustion interne. Ces deux paramètres ont une forte incidence sur la conformité de l'approche par modèles concernant le processus de développement du contrôle moteur. La ligne directrice de la thèse peut être résumée comme suit :

Inclure autant de physique que possible ...

Dans cette thèse, l'amélioration de la précision des modèles a été systématiquement réalisée en introduisant les équations physiques des phénomènes à prendre en compte.

Dans le cas du turbocompresseur, les équations de turbomachines ont été réaménagées et analysées afin de construire un modèle plus physique. La tendance linéaire de l'évolution d'enthalpie vis à vis du débit massique a été utilisée pour fournir la cohérence et le comportement physique au modèle moyen de turbocompresseur. Cette évolution linéaire a été démontrée pour le compresseur et la turbine, ce qui permet d'obtenir un traitement similaire dans les deux cas. L'évolution linéaire est utilisée pour exprimer l'efficacité des turbomachines sans introduire de méthodes complexes. Plus important encore, la méthode proposée respecte la relation physique entre les puissances idéales et réelles des turbomachines. La modélisation des échanges thermiques dans les turbocompresseurs a également été étudiée. Un système de résistance thermique équivalent du turbocompresseur a été construit afin de prendre en compte les transferts de chaleur et leur impact sur les performances du turbocompresseur.

Dans le cas des restrictions d'écoulement, la résolution des équations d'Euler complètes plutôt que l'introduction d'hypothèses simplificatrices introduction a été la ligne directrice des développements proposés. En effet, on a vu que les modèles de restriction de débit sont généralement basées sur l'hypothèse d'écoulement isentropique, ce qui simplifie la résolution du problème de frontière. Cependant, cette hypothèse n'est généralement pas vérifiée expérimentalement. Dans la littérature, un coefficient expérimental de décharge est généralement mis en place pour prendre en compte les pertes de charge. Le principal inconvénient de cette approche est que les mesures expérimentales doivent être effectuées avant de pouvoir réaliser les calculs. La relation isentropique remplace généralement la résolution conservation du moment. Afin d'enquêter sur une éventuelle amélioration de la précision des modèles sans avoir à introduire un coefficient correcteur, l'équation de conservation du moment a été réintroduite dans les systèmes d'équations aux limites. En outre, la possibilité d'assembler des modèles de restrictions simples afin de construire des conditions limites complexes telles que les soupapes ou les diaphragmes a été démontrée.

... sans impacter le temps de calcul.

L'optimisation du temps de calcul a été un aspect important du travail proposé.

Dans le cas du turbocompresseur, l'introduction des équations des turbomachines dans l'algorithme d'interpolation n'a aucune incidence sur le temps de calcul. Les évolutions physiques sont pré-traitées et stockées dans une cartographie. Par conséquent, la charge CPU reste faible alors que la précision a été augmentée. En ce qui concerne les échanges de chaleur, le modèle proposé est basé sur un schéma de résistances thermiques équivalentes du turbocompresseur. Ce système est résolu analytiquement, donc le temps de calcul

supplémentaires est presque négligeable.

Dans le cas des restrictions d'écoulement, les boucles itératives introduites pour résoudre les problèmes aux limites ont été optimisées. L'algorithme de Newton-Raphson a été appliqué à la résolution de l'écoulement 1D aux frontières. Il a été démontré que le choix de la variable de convergence est essentiel, car il a une forte influence sur la robustesse de la méthode. La méthode proposée permet de réduire par un facteur 4 le nombre d'itérations nécessaires pour atteindre la convergence du problème.

Des validations expérimentales ...

Une grande partie de la thèse a été consacrée à la validation expérimentale des développements proposés. Dans chaque domaine de la thèse, des bancs expérimentaux ont été utilisés. Parmi eux, les bancs de soufflerie en écoulement stabilisé (le banc diaphragme et le banc culasse) ont été mis au point, construits et développés au cours de cette thèse. Les mesures expérimentales ont permis de valider l'exactitude des modèles en régime transitoire et stabilisé.

... conduisant à l'application industrielle des modèles.

La validation expérimentale a permis d'assurer la bonne précision des modèles proposés. Par conséquent, les modèles ont été appliqués à l'élaboration de lois de commande des moteurs EUR05-EURO6 Renault. Ces applications ont conduit à l'écriture de trois brevets déposés (deux en ce qui concerne l'estimation des taux d'EGR, l'une concernant le contrôle turbocompresseur). Un exemple de l'application du modèle de turbocompresseur a été décrite dans un document [87].

Les développements futurs :

De futures orientations de travail ont été identifiées afin d'améliorer et de généraliser les méthodes développées dans cette thèse :

- Interaction entre un conduit 1D et un turbocompresseur : Les schémas itératifs dédiés aux conditions aux limites 1D ont été développés dans le cas de restrictions de débit. Cependant, ces schémas n'ont pas été adaptés au cas des turbocompresseurs. Les développements futurs seront fondés sur le travail de Benson [5] et Winterbone [139], qui ont déjà proposé des boucles de correction d'entropie dans le cas des turbocompresseurs. Comme dans le cas de restriction de débit, l'objectif sera d'optimiser ces boucles itératives en termes de vitesse de convergence. Un aspect crucial sera l'identification d'une variable de convergence assurant la robustesse de l'algorithme de Newton-Raphson.
- Les modèles de conditions limites : Les modèles proposés de restriction de débit ont montré que la résolution de l'équation de conservation du moment et l'assemblage des modèles simples permet de réduire la nécessité d'un coefficient de décharge. Il est prévu d'appliquer ces méthodes afin de modéliser d'autres composants.
- Modèle d'échange de chaleur du turbocompresseur : Le modèle proposé d'échanges thermiques turbocompresseur est fortement tributaire des mesures expérimentales. Afin de permettre la généralisation du modèle d'échange de chaleur, il est nécessaire d'identifier la dépendance des résistances thermiques en fonction des paramètres du turbocompresseur. Une telle étude nécessite d'effectuer des mesures expérimentales sur plusieurs turbocompresseurs. Des calculs multi-dimensionnels des échanges de chaleur pourraient également être un outil utile pour accéder à des quantités non mesurables, telles que les distributions de températures locales.
- Application du schéma numérique CE-SE : Les développements en ce qui concerne l'écoulement au travers des restrictions ont été couplés à un système 1D Lax-Wendroff. Ce schéma numérique a atteint un bon niveau de maturité et donne des résultats satisfaisants. Toutefois, il serait intéressant de tester l'interaction entre les systèmes de résolution des conditions limites développés durant cette thèse et le schéma de Conservation Element - Solution Element développé par Chang [20] [21], car elle permet une réduction significative du temps de calculs.

Appendices

A : Compressible flow similitude

The theory of similitude allows to build new characteristic curves of a turbomachine in the case where some flow parameters are modified. In our case, the compressor and turbine data maps have been built for a given inlet temperature T_{in} . The similitude theory will allow to build new characteristic quantities (mass flow rate, pressure ratio and power) for a different inlet temperature without having to perform additional measurements. The main equations introduced to identify compressible flow similitudes are introduced below.

Pressure ratio

The expression of the pressure ratio across a turbomachine is being developed :

$$\frac{P_{out}}{P_{in}} = \left(1 + \eta \frac{\Delta T}{T_{in}}\right)^{\frac{\gamma}{\gamma-1}} = \left(1 + \frac{\eta}{C_p} \frac{\Delta h}{T_{in}}\right)^{\frac{\gamma}{\gamma-1}} \quad (1)$$

Typical speed components are introduced : U is the tangential blade speed, V is the flow speed, V_θ is the tangential component of V and V_r is the radial component of V . Adimensioning these speed quantities by the reference tangential speed value U_{out} allows to define the following ratios :

$$\alpha = \frac{V_{r,out}}{U_{out}} \quad (2)$$

$$\beta = \frac{V_{r,in}}{U_{out}} \quad (3)$$

$$\sigma = \frac{U_{in}}{U_{out}} \quad (4)$$

$$\zeta = \frac{V_{in}}{U_{out}} \quad (5)$$

Developing the expression of Δh and introducing the previously defined ratios allows to develop the following expression of $\frac{P_{out}}{P_{in}}$:

$$\frac{P_{out}}{P_{in}} = \left(1 + \frac{(\alpha - \sigma\beta)\pi^2}{30^2} \frac{\eta R_{out}^2}{C_p} \frac{N_{turb}^2}{T_{in}}\right)^{\frac{\gamma}{\gamma-1}} \quad (6)$$

Mass flow rate

The mass flow rate across a turbomachine can be expressed as it follows, with the introduction of the isentropic flow speed for a compressible flow through an orifice (Saint-Venant formulation) :

$$Q_m = \rho_{in} S_{in} V_{in} = \frac{P_{in}}{\sqrt{T_{in}}} \frac{S_{in}}{r} M_{in} \sqrt{\gamma r \left(1 + \frac{\gamma-1}{2} M_{in}^2\right)^{\frac{1+\gamma}{1-\gamma}}} \quad (7)$$

Rotational speed

Developing the enthalpy formulation and introducing the Saint-Venant flow formulation and the previously defined speed ratios allow to get the following expression of the rotational shaft speed for a turbomachine :

$$N_{turb} = \frac{\pi}{30} M_{in} \sqrt{\frac{\gamma r}{1 + \frac{\gamma-1}{2} M_{in}^2}} \frac{\sqrt{T_{in}}}{\zeta R_{out}} \quad (8)$$

Similitude requirements

In order to get the same flow around the turbomachine blades (therefore the same isentropic efficiency), the following quantities need to remain constant even though the inlet temperature changes :

- Same Reynolds number.
- Same Mach number.
- Same geometry.
- Same triangle of speeds ($\alpha = cst$, $\beta = cst$, $\sigma = cst$, $\zeta = cst$)

Similitude

The isentropic efficiencies of two turbomachines will be the same at an operating point where their speed triangle and their Mach / Reynolds numbers are equal. Now, we also consider that the two turbomachines have the same geometry and are working with the same fluid ($\gamma = cst$, $r = cst$). Considering these constant quantities and the introduced assumptions, it appears that Eq. 8 can be rewritten as in Eq. 9. It appears that the right term is constant under the similitude hypothesis.

$$\frac{N_{turb}}{\sqrt{T_{in}}} = \frac{\pi}{30} M_{in} \sqrt{\frac{\gamma r}{1 + \frac{\gamma-1}{2} M_{in}^2}} \frac{1}{\zeta R_{out}} = Cst \quad (9)$$

Consequently, the similitude between two turbomachines A and B leads to :

$$\left(\frac{N_{turb}}{\sqrt{T_{in}}} \right)_A = \left(\frac{N_{turb}}{\sqrt{T_{in}}} \right)_B \quad (10)$$

Introducing the previous result into Eq. 6 and considering the constant quantities due to the similarity requirements leads to :

$$\left(\frac{P_{out}}{P_{in}} \right)_A = \left(\frac{P_{out}}{P_{in}} \right)_B \quad (11)$$

Finally, Eq. 7 leads to :

$$\left(Q_m \frac{\sqrt{T_{in}}}{P_{in}} \right)_A = \left(Q_m \frac{\sqrt{T_{in}}}{P_{in}} \right)_B \quad (12)$$

If the characteristics of the turbomachines were plotted on the same data map using the functions expressed in Eq. 10, 11 and 12, their points would be superimposed. This means that the similitude theory allows to build only one data map for a turbomachine, even though its inlet temperature varies. This explains the corrected functions selected by the turbocharger suppliers in order to provide data maps.

B : Compressor and turbine corresponding operating points

Three turbocharger operating points have been plotted in the compressor data map (Fig. B1). The chosen operating points are on the same iso-speed curve and the VGT setting of the turbine is fixed (VGT=100%). In order to find the corresponding operating turbine operating point, it is necessary to take into account that the shaft speed is imposed by the choice of the compressor operating points and that the two turbomachines are linked by the shaft, therefore their shaft power are identical (excluding the shaft power losses). From this, the compressor shaft power is calculated for each operating point. In parallel, the turbine shaft power data map is plotted, and the three previously determined compressor shaft powers are used to read into the data map. This allows to determine the corresponding turbine mass flow rate. It should be noticed that the mass flow rate plotted in the data maps are not corrected. It is intended to allow direct comparison during this study between the compressor and the turbine. Once the turbine mass flow rate, it is possible to determine the corresponding pressure ratio.

Looking at Fig. B1, it appears that while the compressor mass flow rate varies from 0.04 to 0.08 kg.s (variation = 100%), the turbine mass flow rate varies from 0.0755 to 0.078 kg/s, which represents a variation of 4%. This means that, for a constant shaft speed and a fixed VGT setting, a small mass flow rate change has a strong impact on the turbine power. On Fig. B2, one can see that the variation of the turbine shaft power is performed by the mean of the turbine efficiency. Indeed, the turbine efficiency is increased by 60%, as the turbine efficiency is very sensitive to mass flow rate variations.

An other interesting point is that the turbine and the compressor mass flow rates do not match. This is due to the test bench configuration, as the compressor and the turbine air circuits are totally independent. While this case could occur once mounted on an engine under transient conditions, it is impossible to reach such a mass flow rate discrepancy under stabilized conditions. Once mounted on a real engine, the engine control would adjust the VGT setting to allow both the mass flow rate and the shaft power equilibriums. In our study, only the shaft power equilibrium is imposed. By covering the entire VGT setting range, it is therefore possible to cover the entire turbocharger compressor/turbine corresponding operating points range.

Finally, it appears that for a given shaft speed and a given VGT setting, the turbine shaft power is continuous and increasing with respect to the mass flow rate. This means that for a given VGT setting, only one turbine operating point is corresponding to a compressor operating point. One can also notice the compressor shaft power vs. mass flow rate evolution : for the majority of the values of mass flow rates, the compressor shaft power is increasing. However, once the operating points are getting closer to the choking region, the shaft power starts to decrease. Consequently, when covering a compressor iso-shaft speed, the power on the shaft will increase and then decrease. As the turbine shaft power is continuously increasing with respect to the mass flow rate, this means that the turbine mass flow rate will increase and then decrease in order to follow the corresponding compressor shaft power evolution.

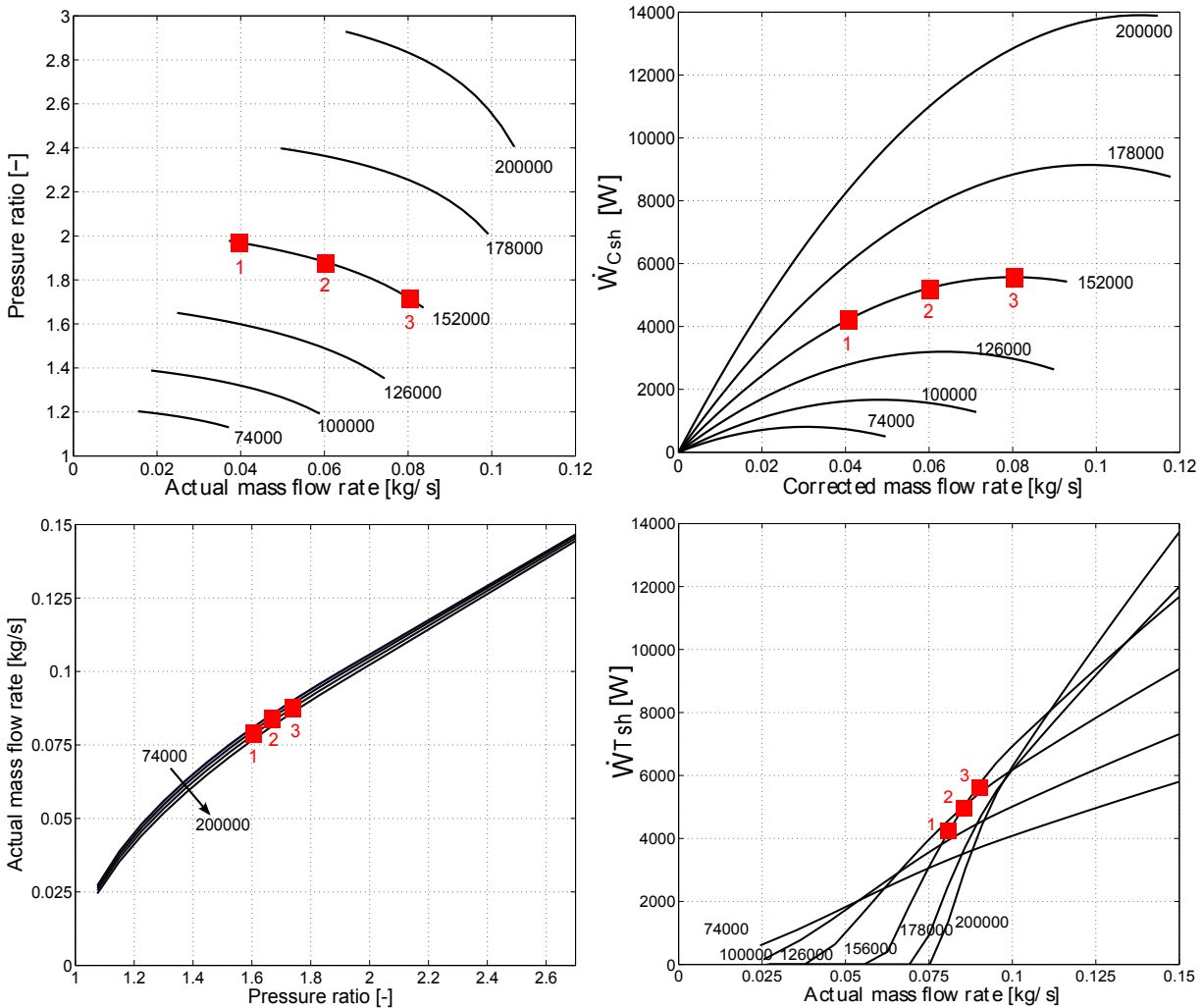


Fig. B1 - Turbocharger operating points plotted in the compressor pressure ratio data map (upper left), in the compressor shaft power data map (upper right), in the turbine mass flow rate data map (lower left) and in the turbine shaft power data map (lower right). Chosen operating points are superimposed in red.

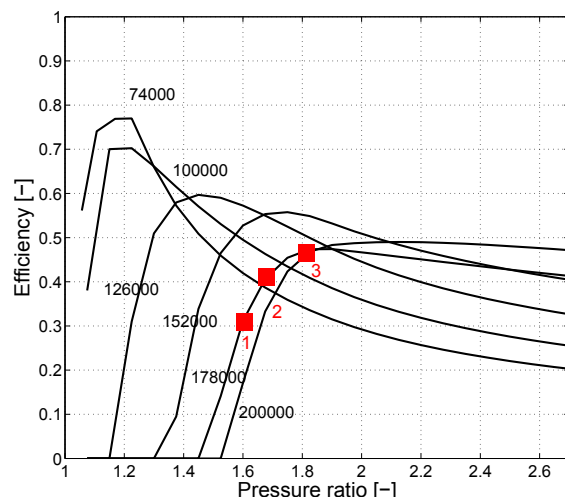


Fig. B2 - Turbine adiabatical efficiency, with the chosen operating points superimposed in red.

C : The Method of Characteristics

Non-homentropic Euler's equations have been expressed in Eq. (8.10). When the following condition is imposed $C(W) = 0$, Euler's equations are written for an homentropic flow (no entropy is created within the flow). In this case, the equations set is strictly hyperbolic, therefore the Jacobi matrix $A(W) = \frac{\partial f}{\partial W}(W)$ is introduced and defined such that :

$$\frac{\partial W}{\partial t} + A(W) \frac{\partial W}{\partial x} = 0 \quad (1)$$

$A(W)$ can be put into a diagonal formulation and all of its eigenvalues are real. Expressing eigenvectors and eigenvalues of $A(W)$ allows to determine the invariant quantities for the Euler's equations. α and β are called the Riemann invariants, and $C+$ and $C-$ their associated characteristic curves.

- α is constant along $C - |\frac{dx}{dt}| = u - a$.
- β is constant along $C + |\frac{dx}{dt}| = u + a$.
- The entropy S is constant along $C0|\frac{dx}{dt}| = u$.

$$\alpha = a_i^{n+1} - \frac{\gamma - 1}{2} u_i^{n+1} = a_R^n - \frac{\gamma - 1}{2} u_R^n = cst \quad (2)$$

$$\beta = a_i^{n+1} + \frac{\gamma - 1}{2} u_i^{n+1} = a_L^n + \frac{\gamma - 1}{2} u_L^n = cst \quad (3)$$

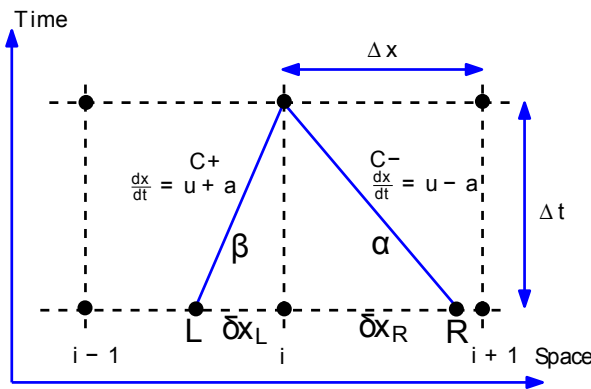


Fig. C1 - Eulers's equations' homentropic characteristics shown on a space-time diagram.

Looking at Fig. C1, the calculation domain has been discretized in space ($i - 1; i; i + 1$) and time ($n; n + 1$). Using the MOC, it appears that in the case where all the quantities are known at time step n , it is possible to calculate the Riemann characteristics α and β and the associated characteristics curves $C+/ -$. Using these information, it is possible to extrapolate the characteristics curves and to determine the quantities at time step $n + 1$. This approach is only valid under an homentropic flow assumption.

D : W_β^α numerical schemes

In their paper, Lerat and Peyret [75] proposed a general class of W_β^α schemes with the following characteristics :

- explicit conservation form.
- two-step predictor/corrector type.
- three point space stencil, two level point stencil.
- second order accuracy in time and space.

This class of numerical schemes is described here, as it is the most widespread type of schemes found in papers dedicated to the simulation of engine pipe flows. These schemes allow a the numerical resolution of the governing equations, which are expressed here in their vectorial formulation :

$$\frac{\partial W}{\partial t} + \frac{\partial F(W)}{\partial x} + C(W) = 0 \quad (1)$$

The W_β^α are two-step schemes of predictor-corrector type. This means that during a first step, an intermediate solution located by α and β is introduced, while the final solution is calculated during the second step (corrector). This is illustrated on Fig. E1.

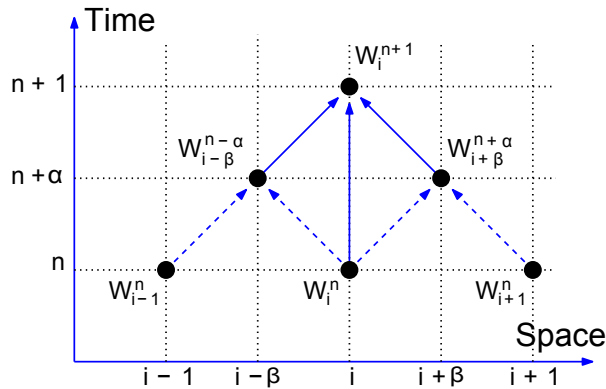


Fig. E1 - Two steps Lax-Wendroff stencil

The schemes have the following general form :
First step :

$$\begin{aligned} W_{i+\beta}^{n+\alpha} &= (1-\beta)W_{i+1}^n + \beta W_i^n - \alpha \frac{\Delta t}{\Delta x} [F(W_{i+1}^n) - F(W_i^n)] \\ &\quad - \alpha \frac{\Delta t}{2} [C_{i+1}^n + C_i^n] \end{aligned} \quad (2)$$

$$\begin{aligned} W_{i-\beta}^{n+\alpha} &= (1-\beta)W_i^n + \beta W_{i-1}^n - \alpha \frac{\Delta t}{\Delta x} [F(W_i^n) - F(W_{i-1}^n)] \\ &\quad - \alpha \frac{\Delta t}{2} [C_i^n + C_{i-1}^n] \end{aligned} \quad (3)$$

Second step :

$$\begin{aligned} W_i^{n+1} &= W_i^n - \frac{\Delta t}{2\alpha\Delta x} [(1-\alpha-\beta)F(W_{i+1}^n) + (2\beta-1)F(W_i^n)] \\ &\quad - \frac{\Delta t}{2\alpha\Delta x} [(1-\alpha-\beta)F(W_{i-1}^n) + F(W_{i+\beta}^{n+\alpha}) - F(W_{i-1+\beta}^{n+\alpha})] \\ &\quad - 2\alpha\Delta t C_i^n \end{aligned} \quad (4)$$

Such numerical schemes are stable for a Courant-Friedrichs-Lowy [30](CFL) number lower than 1. The values set to α and β allows to determine from the previous equations the numerical schemes developed by Lax and Wendroff, Rubin and Burstein, Lerat and Peyret and McCormack. The corresponding α and β values are detailed in the following table :

Scheme	α	β
Lax-Wendroff	0.5	0.5
Rubin-Burstein	1	0.5
Lerat-Peyret	$1 + \sqrt{\frac{5}{2}}$	0.5
MacCormack 0	1	0
MacCormack 1	1	1

TAB. 1 – Predictor-Corrector numerical schemes and the corresponding α and β values.

E : Gas models

Perfect gas equations

The density ρ , the pressure p , the temperature T and the internal energy e characterize the equilibrium state of a thermodynamical system. In this thesis, the main developments have been achieved under the assumption that the air is considered as a perfect gas, which means that the intra-molecular forces are neglected. A perfect gas complies to the following law :

$$p = \rho r T \quad (1)$$

where r is a constant of the gas $r = \frac{R}{M}$ where R is the universal constant of the perfect gases and M is the molar mass of the gas. Under the conditions considered in this study, the air is composed of 21% of oxygen and 79% of azote, leading to a molar mass of 28.97 and a constant r equal to :

$$r = 287.06 \text{ J.kg}^{-1}.\text{K}^{-1} \quad (2)$$

The internal energy e can be linked to (ρ, T) by the mean of the calorific state equation : $e = e(\rho, T)$. It is also possible to write $e = e(v, T)$ where v is the specific volume of the gas ($v = \frac{1}{\rho}$). It is therefore possible to write a differential relationship expressing the variation of the internal energy with respect to the temperature and volume variations :

$$de = \left(\frac{\partial e}{\partial v} \right)_T dv + \left(\frac{\partial e}{\partial T} \right)_v dT \quad (3)$$

In the case of a perfect case, one gets $\left(\frac{\partial e}{\partial v} \right)_T = 0$, therefore the internal energy is only dependent on the temperature. The specific heat capacity for a constant volume Cv is introduced :

$$Cv = \left(\frac{\partial e}{\partial T} \right)_v \quad (4)$$

In the case of the air, Cv remains constant for temperatures lower than 600K, with $Cv = 717 \text{ J.kg}^{-1}.\text{K}^{-1}$. In the case where Cv is assumed to be constant the internal energy is a linear function of the temperature :

$$e = Cv T \quad (5)$$

The enthalpy $h = e + \frac{p}{\rho}$ is also a state variable, dependent on the pressure and the temperature $h = h(p, T)$. It is therefore possible to build a differential relationship expressing its variation regarding the variations of pressure and temperature :

$$dh = \left(\frac{\partial h}{\partial p} \right)_T dp + \left(\frac{\partial h}{\partial T} \right)_p dT \quad (6)$$

Going back to the enthalpy definition, one can write :

$$\begin{aligned} dh &= de + d\left(\frac{p}{\rho}\right) \\ &= CvdT + rdT \\ &= (Cv + r)dT \end{aligned} \quad (7)$$

One deduces from this development that the enthalpy is only dependent on the temperature $h = h(T)$, therefore : $\left(\frac{\partial h}{\partial p}\right)_T = 0$. The specific heat capacity at constant pressure is introduced :

$$Cp = \left(\frac{\partial h}{\partial T}\right)_p \quad (8)$$

In the case of the air, Cp remains constant for temperatures lower than 600K, with $Cp = 1004 \text{ J.kg}^{-1}.\text{K}^{-1}$. Under the assumption that Cp and Cv are constant, it is possible to define ratio of the specific heat capacities :

$$\gamma = \frac{Cp}{Cv} \quad (9)$$

γ is equal to 1.40 in the case the temperatures are not higher than 600K. Combining this expression to the Mayer relationship ($Cp - Cv = r$), it is possible to build the following relationships :

$$Cv = \frac{r}{\gamma - 1} \quad \text{and} \quad Cp = \frac{\gamma r}{\gamma - 1} \quad (10)$$

Consequently, the state equation 1 can reformulated as follows :

$$\begin{aligned} p &= \rho r T \\ &= (\gamma - 1)\rho e \end{aligned} \quad (11)$$

Extension to higher temperatures

The previous developments include the hypothesis that the gas temperature is lower than 600K, which allows to consider Cp and Cv as constants. However, the exhaust gas temperature will generally be higher than 600K. It is therefore not valid anymore to consider the gas to be perfect. However, the properties of various gases have been tabulated with respect to the temperature, leading to polynomial approximations of their properties with respect to the temperature. These tables can be found in many thermodynamical or engine modeling-related books ([61], [5], [138]). In the case of a perfect gas, it has been seen that $Cv = cst$, and therefore, the internal energy can be expressed as follows, with a_1 a constant value :

$$e = a_1 T \quad (12)$$

In the case where the perfect gas hypothesis is not satisfied, the tabulations allow to express the internal energy as follows, where $(a_1 \dots a_n)$ are the tabulated coefficients.

$$e = a_1 T + a_2 T^2 + a_3 T^3 + a_4 T^4 \dots \quad (13)$$

Now :

$$Cv = \left(\frac{\partial e}{\partial T}\right)_v = a_1 + 2a_2 T + 3a_3 T^2 + 4a_4 T^4 \dots \quad (14)$$

Viscosity model

The fluid dynamical viscosity μ is dependent on the considered fluid, but also of the local thermodynamical properties of the flow. For temperatures lower than 3000K, the viscosity can be assumed to be independent of the pressure, therefore only the temperature dependency needs to be taken into account. This dependency is well taken into account by the Sutherland law :

$$\mu(T) = C_1 \frac{T^{1.5}}{T + C_2} \quad (15)$$

where C_1 and C_2 are tabulated coefficients with respect to the gas. In the case of the air, $C_1 = 1.458 \times 10^{-6} \text{ kg.m}^{-1}.\text{s}^{-1}.K^{-\frac{1}{2}}$ and $C_2 = 110.4 \text{ K}$.

Bibliography

- [1] ACEA website *Statistics section* <http://www.acea.be>
- [2] A. Albrecht et al. *Towards a stronger simulation support for engine control design : a methodological point of view* Oil & Gas Science and Technology, Rev. IFP, Vol.62 (2007), No.4, pp. 437-456
- [3] R. Baar, M. Lucking, M. Sievert *Die Turboladermodellierung für Prozessrechnungen bei erweiterter Leistungsbilanz* Motorprozesssimulation und Aufldung, Berlin, 2005.
- [4] R.S. Benson, N.D. Whitehouse *Internal Combustion Engines vol.2* Pergamon Press, 1979.
- [5] R.S. Benson *The Thermodynamics and Gas Dynamics of Internal Combustion Engines vol.1* Clarendon Press Oxford, 1982.
- [6] A.J. Blair, G.P. Blair *Gas flow modelling of valves and manifolds in car engines* International Conference computers in Engine Technology, 24-25 march, Robinson Cambridge, pp. 131-144, 1987.
- [7] G.P. Blair, F.M. Drouin *The relationship between discharge coefficient and the accuracy of engine simulation* SAE paper 962527.
- [8] G.P. Blair, D. McBurney, P. McDonald, P. McKernan, R. Fleck *Some fundamental aspects of the discharge coefficients of cylinder porting and ducting restrictions* SAE paper 980764.
- [9] G.P. Blair, E. Callender, D.O. Mackey *Maps of discharge coefficients for valves ports and throttles* SAE paper 2001-01-1798.
- [10] P. Brejaud *Convergence of entropy correction MOC scheme* Institut Prisme, Internal publication, 2009.
- [11] D. Bohn, T. Heuer, K. Kusterer *Conjugate flow and heat transfer investigation of a turbocharger* ASME Journal of Engineering for Gas Turbines and Power vol.127, pp. 663-669, 2005.
- [12] D. Bohn *Conjugate flow and heat transfer investigation of a turbocharger Part II : Experimental results* ASME Conference Paper GT2003-38449, 2003.
- [13] D. Bohn *Conjugate calculation of flow field and heat transfer in compressor, turbine and casing of a gas turbine* VGB Powertech, vol.83 n°11, pp. 54-59, 2003.
- [14] F. Bozza, A. Gimelli, R. Piazzesi, F. Fortunato et al. *The prediction of the performance and gasdynamic noise emitted by a medium-size spark-ignition engine by means of 1D and 3D analyses* SAE paper 2007-01-0380, 2007.
- [15] F. Bozza, A. Gimelli *Unsteady 1D simulation of a turbocharger compressor* SAE paper 2009-01-0308, 2009.
- [16] S. Busam, A. Glahn, S. Witting *Internal bearing chamber wall heat transfer as a function of operating conditions and chamber geometry* ASME Journal of Engineering for Gas Turbines and Power, vol.122, 2000.
- [17] W.L. Cahoon *Unsteady gas flow through a naturally aspirated two-stroke Internal Combustion Engine* Ph. D thesis, Department of mechanical engineering, The Queen's University of Belfast, 1971.
- [18] S. Carballes *Les véhicules particuliers en France*. Publication ADEME www.ademe.fr, 2010.

- [19] D. Chalet *Etude et modélisation des ondes de pression dans les géométries complexes. Application à la simulation du fonctionnement d'un moteur à combustion interne* Thèse de l'Université de Nantes, 2003.
- [20] S. Chang, W. To *A brief description of a new numerical framework for solving conservation laws : the method of space-time cosnervation element and solution element.* NASA technical memorendum 105757, 1992.
- [21] S. Chang, X. Wang, C. Chow *The method of space-time conservation element and solution element : application to one-dimensional and two-dimensional time -marching flow problems* NASA technical me- morendum 106915, 1995.
- [22] A. Chen , K.C. Lee, M. Yianneskis *Velocity characteristics of steady flow through a straight generic inlet port* International Journal for Numerical Methods in Fluids, Volume 21, n°7, pp. 571-590, 1995.
- [23] R.S.W Cheung, S. Nadarajah, M.J. Tindal, M. Yianneskis *An experimental study of velocity and reynolds stress distributions in a production engine inlet port under steady flow conditions* SAE Transactions, Volume 99, n°3, pp. 334-353, 1990.
- [24] P. Chesse, J.F. Hetet, X. Tauzia, P. Roy, B. Inozu *Performance simulation of sequentially turbocharged marine diesel engines with applications to compressor surge* Transactions ASME Journal of engineering for gas turbines and power, vol. 122, pp.562-569, 2000.
- [25] CITEPA *Inventaire des émissions de polluants atmposphériques en France - Format SECTEN.* Rapport national d'inventaire, www.citepa.org, 2010.
- [26] M. Cormerais *Caractérisation expérimentale et modélisation des transferts thermiques au sein d'un turbocompresseur automobile. Application à la simulation du comportement transitoire d'un moteur Diesel à forte puissance spécifique* Thèse de l'Université de Nantes, 2007.
- [27] C. Corre *Aérodynamique Fondamentale* Cours de l'Ecole Nationale des Arts et Métiers Paris, 2006.
- [28] R. Courant, K.O. Friedrichs *Supersonic flow and shocks* Interscience New-York.
- [29] R. Courant, E. Isaacson, M. Rees *On the solution of non-linear hyperbolic differential equations by finite differences* Commun. Pure Appl. Math., 5, 243-249.
- [30] R. Courant, K.O. Friedrichs, H. Lewy *On the partial difference equations of mathematical physics* IBM J. Res. Dev., Volume 11, pp. 215-234, 1967.
- [31] R.C. Jr Dean, D.D. Wright, P.W. Jr Runstadler *Fluid mechanics analysis of high-pressure-ratio centrifugal compressor data* USAAVLabs Technical report 69-76, AD872 161, 1970.
- [32] M. Demoulin *Transvasements gazeux dans les moteurs thermiques.* Techniques de l'ingénieur, B-2-600.
- [33] G. Descombes, Q. Duan, J. Jullien, N. Parkinson *Study of the performance of a variable geometry turbocharger* 22nd Cimac, Copenhaguen, 18-21 May 1998.
- [34] G. Descombes, F. Maroteaux, J. Jullien, M. Pluviose *Modelling of flow within a vaned channel in thermal engine* Internal journal of thermal sciences 44, 1000-1012, 2005.
- [35] C. Depcik, D. Assanis *A universal heat transfer correlation for intake and exhaust flows in a spark-ignition internal combustion engine* SAE paper 2002-01-0372, 2002.
- [36] C. Donitz, I. Vasile, C. Onder, L. Guzella *Modelling and optimizing two- and four-stroke hybrid pneumatic engines* IMechE Part D - Journal of Automobile Engineering, Vol. 223, No. 2, pp. 255-280, 2009.
- [37] P.A. Durbin *Separated flow computations with the k- ϵ -v² model* AIAA Journal, 33(4), 659-664, 1995.
- [38] S.H. El Thary *k-epsilon equation for compressible reciprocating engine flows.* Am. Inst. Aeronaut. Astronaut. J. Energy, 0146-0412, 7(4), 345-353, 1983.
- [39] L. Eriksson *Modeling and control of turbocharged SI and DI engines* Oil and gas science and technology - Rev.IFP, Vol.62 (2007), No. 4, pp523-538, 2007.

- [40] Eurachem-Citac *Quantifier l'i dans les mesures analytiques* deuxième édition, Editeurs S.L.R Ellison, M.Rosslein, A.Williams, 2000.
- [41] T.B. Ferguson *The centrifugal compressor stage* Butterworths 1963.
- [42] P. Ferreri, C. Venezia *UNIAIR variable valve actuation system modelling and integration to the engine in the GT-SUITE environment* GT-SUITE european conference, Frankfurt am Main, 2008.
- [43] S.A. Nelson, Z.S. Filipi, D.N. Assanis *The use of neural networks for matching compressors with diesel engines* Spring technical conference, vol. ICE-26-3 p.35-42 1996.
- [44] R. Flierl, M. Kluting *The third generation of valvetrains - New fully variable valvetrains for throttle-free load control* SAE paper 2000-01-1227, 2000.
- [45] Fluent Incorporated *Fluent V.5 user's guide* Centerra Resource Park, Lebanon, NH, 1998.
- [46] A. Frenk *A slip factor calculation in centrifugal impellers based on linear cascade* Turbo and jet laboratory faculty of space, Oral presentation report, <http://jet-engine-lab@technion.ac.il>, 2005.
- [47] M.Frelin *Prévision des caractéristiques d'une turbine radiale à partir des données géométriques* Thèse de doctorat de l'Université Paris VI, 1991.
- [48] M.Friberg, M.Mahieddine, M.Toussaint, M.Frelin *Prévision des caractéristiques des turbomachines. Application à une pompe centrifuge, un compresseur centrifuge et une turbine centripète* Revue Française de Mécanique n°1988-4, 1988.
- [49] R.I. Gault, D.J. Thornhill, R. Fleck et al. *Analysis of the steady flow characteristics through a poppet valve* SAE paper 2004-01-1676.
- [50] P. Giansetti *Contrôle moteur à allumage commandé. Estimation / prédition de la masse et de la composition du mélange enfermé dans le cylindre* Thèse de doctorat. Université d'Orléans, 2005.
- [51] S.K. Godunov *A difference method for the numerical computation of discontinuous solutions of hydrodynamic equations* Mat. Sb., 47, 271-306.
- [52] E.M. Greitzer *Surge and rotating stall in axial flow compressors. Part 1 : Theoretical compression system model* Transactions ASME, Journal of engineering for gas turbines and power, vol. 98, pp. 190-198, 1976.
- [53] E.M. Greitzer *Surge and rotating stall in axial flow compressors. Part 2 : Experimental results and comparison with theory* Transactions ASME, Journal of engineering for gas turbines and power, vol. 98, pp. 199-217, 1976.
- [54] Gamma Technologies *GT-ISE User's manual* Gt-Power v.6.1, 2004.
- [55] M. Guillou, C. Bradley *Fuel consumption testing to verify the effect of tire rolling resistance on fuel economy* SAE paper 2010-01-0763.
- [56] Z. Guzovic, B. Matijasevic, M. Rusevljian *Generalized correlations for heat transfer determination in turbine cascades* Strojnicki Vestnik vol.47 n°8, 2001.
- [57] L. Guzzella, A. Amstutz *Control of diesel engines* IEEE Contr. Syst. Mag., 18, 53-71, 1998.
- [58] L. Guzzella, C. H. Onder *Introduction to modeling and control of internal combustion engine systems* Springer, 2004.
- [59] P. Gyan *Etude expérimentale du comportement thermique des moteurs en régime transitoire* Thèse de doctorat. Ecole Centrale de Lyon, 2003.
- [60] A. Harten *High resolution schemes for hyperbolic conservation laws*. J. Comp. Phys., 49, 357-393.
- [61] J.B. Heywood *Internal Combustion Engine Fundamentals* McGraw Hill Ed., 1988.
- [62] P. Higelin, A. Charlet, Y. Chamaillard *Thermodynamic simulation of a hybrid pneumatic-combustion engine concept* Journal of Applied Thermodynamics, Vol 5, No. 1, pp 1 - 11, 2002.

-
- [63] J.H. Horlock, D.E. Winterbone *The Thermodynamics and Gas Dynamics of Internal Combustion Engines vol.2* Clarendon Press Oxford, 1986.
 - [64] H. Hugoniot *Mémoire sur la propagation du mouvement dans les corps et spécialement dans les gaz parfaits* Journal de l' Ecole Polytechnique, 58, 1-125.
 - [65] D. Japikse *Assessment of single- and two-zones modeling of centrifugal compressors, studies in component performance : part 3* ASME paper85-GT-73, 1985.
 - [66] D. Japikse *Turbomachinery performance modeling* 2008 Cliff Garrett turbomachinery and applications engineering award, published under SAE paper number 2009-01-0307, 2009.
 - [67] E.Jenny *Berechnungen und modellversuche über druckwellen grosser amplituden in auspuff-leitungen* ETHZ thesis, 1949.
 - [68] J.P. Johnston, R.C. Jr Dean *Losses in vaneless diffusers of centrifugal compressors and pumps* ASME paper 65-FE-1, 1965.
 - [69] J.P. Jensen, A.F. Kristensen, S.C. Sorenson and N.Nouback *Mean value modeling of a small turbocharged diesel engine* SAE Paper 910070, 1991.
 - [70] T.V. Jones *Definition of heat transfer coefficients in the turbine situation* Imech Paper C423/046, 1991.
 - [71] I.P.Kandylas, A.M.Stamalos *Engine exhaust system design based on heat transfer computation* Energy Conversion and Management 40, 1999.
 - [72] S.J. Kirkpatrick *An evaluation of one-dimensional simulation techniques for predicting unsteady gas flow in engine ducting* Ph. D thesis, Department of mechanical and manufacturing engineering, The Queen's University of Belfast, 1994.
 - [73] P.D. Lax *Weak solutions of non-linear hyperbolic equations ans their numerical computation* Commun. Pure Appl. Math., 7, 159-193.
 - [74] P.D. Lax, B. Wendroff *Difference schemes for hyperbolic equations with high order of accuracy* Commun. Pure Appl. Math., 17, 381-398.
 - [75] A. Lerat, R. Peyret *Non-centered schemes and shock propagation problems* Comp. Fluids, 2, 35-52.
 - [76] A. Lerat *Ecoulements compressibles instationnaires* Cours de l'Ecole Nationale Supérieure des Arts et Métiers, 2005.
 - [77] Ligier *Lubrification des paliers moteurs* Editions Technip Publications. Institut français du pétrole. ISBN 2-7108-0713-0, 1997.
 - [78] J. Liu, N. Schorn, C. Schernus, L.Peng *Comparison studies on the method of characteristics and finitie difference method for one-dimensional gas flow through IC engine manifold.* SAE paper 960078.
 - [79] Lotus Engine Simulation *Online help : 'Theory of turbochargers'* Lotus Engine Simulation V5.05 freeware, 2004.
 - [80] R. MacCormack, B.S. Baldwin *A numerical method for solving the Navier-Stokes equations with application to shock-boundary layer interaction* AIAA paper 75-1.
 - [81] J.H. McDonnell *Unsteady gas flow through a naturally aspirated four-stroke Internal Combustion Engine* Ph. D thesis, Department of mechanical engineering, The Queen's University of Belfast, 1974.
 - [82] J. Macek, J. Vávra, O. vítek *1-D model of radial turbocharger turbine calibrated by experiments* SAE paper 2002-01-0377, 2002.
 - [83] J. Macek, O. vítek *Simulation of Pulsating Flow Unsteady Operation of a Turbocharger Radial Turbine* SAE paper 2008-01-0295, 2008.
 - [84] J. Macek, O. vítek, S. Srinivasan, F.X. Tanner *1D modeling of transient engine operations using data generated by a CFD code.* SAE paper 2008-01-0357, 2008.

- [85] J. Macek, O. vítek, V. Doleček, S. Srinivasan, F.X. Tanner *Improved simulation of transient engine operations at unsteady speed combining 1D and 3D modeling* SAE paper 2009-01-1109, 2009.
- [86] G. Martin, V. Talon, P. Higelin, A. Charlet, C. Caillol *Implementing turbomachinery physics into data map-based turbocharger models* SAE Int. J. Engines 2(1) : 211-229, 2009.
- [87] G. Martin, V. Talon, T. Peuchant, P. Higelin, A. Charlet *Physics-based diesel turbocharger model for control purposes* SAE paper 2009-14-0123, 2009.
- [88] G. Martin, P. Brejaud, P. Higelin, A. Charlet *Pressure ratio-based method for non-isentropic inflow valve boundary conditions resolution* SAE paper 2010-01-1052, 2010.
- [89] M. Matsuki, K. Nakano, T. Amemiya, Y. Tanabe, D. Schimizu, I. Ohmura *Development of a lean-burn engine with a variable valve timing mechanism* SAE paper 960583.
- [90] Mian *Design and analysis of engine lubrication systems* SAE paper SAE 970637, 1997.
- [91] G. Montenegro, A. Onorati, F. Piscaglia, G. D'Errico *Integrated 1D-multiD fluid dynamic models for the simulation of ICE intake and exhaust systems.* SAE paper 2007-01-0495, 2007.
- [92] G. Montenegro, A. Onorati *Modeling of Silencers for I.C. Engine Intake and Exhaust Systems by Means of an Integrated 1D-MultiD Approach* SAE Int. J. Engines 1(1) : 466-479, 2008.
- [93] F.K. Moore, E.M. Greitzer *A theory of post-stall transients in axial compression systems. Part 1 : Development of equations* Transactions ASME, Journal of engineering for gas turbines and power, vol. 108, pp.68-76, 1986.
- [94] P. Moraal and I. Kolmanovsky *Turbocharger modeling for automotive control application* SAE Paper 1999-01-0908, 1999.
- [95] M. Mueller *Mean value modeling of turbocharged spark ignition engines* master's thesis DTU, Denmark, 1997.
- [96] S.H. Nasser, BB. Playfoot *A turbocharger selection computer model* SAE paper 1999-01-0559, 1999.
- [97] A. Onorati, D.E. Winterbone, R.J. Pearson *A comparison of the Lax-Wendroff technique and the method of characteristics for engine gas dynamic calculations using fast Fourier transform spectral analysis* SAE paper 930428 ,1993.
- [98] A. Onorati, G. Ferrari *Modeling of 1-D unsteady flows in IC engine pipe sytems : numerical methods and transport of chemical species* SAE paper 980782 , 1998.
- [99] A. Onorati, G. Montenegro, G. D'Errico *Prediction of the attenuation characteristics of IC engine silencers by 1D and multiD simulation models* SAE paper 2006-01-1541, 2006.
- [100] A. Onorati, G. Montenegro, G. D'Errico, F. Piscaglia *Integrated 1D-3D Fluid Dynamic Simulation of a Turbocharged Diesel Engine with Complete Intake and Exhaust Systems* SAE paper 2010-01-1194, 2010.
- [101] S. Pagerit, P. Sharer, A.Rousseau *Fuel economy sensitivity to vehicle mass for advanced vehicle power-trains* SAE paper 2006-01-0665.
- [102] R.J. Pelton, D.Japikse, D. Maynes, K.N. Oliphant *Turbomachinery performance models (2005B)* ASME paper IMECE2005-79414, 2005.
- [103] B.J. Peters, R.J. Wanker, ,A. Münzer, J.C. Wurzenberger *Integrated 1D to 3D Simulation Workflow of Exhaust Aftertreatment Devices* SAE paper 2004-01-1132, 2004
- [104] V. Picron, Y. Postel, E. Nicot, D. Durrieu *Electro-magnetic valve actuation system : first steps toward mass production* SAE paper 2008-01-1360, 2008
- [105] F. Piscaglia, A. Montorfano, A. Onorati, G. Ferrari *Modeling of pressure wave reflection from open-ends in ICE duct systems* SAE paper 2010-01-1051

-
- [106] M. Pluviose *Machines à fluides Ellipses*, 2002.
 - [107] PSA website *Annual reports 2000-2009* <http://www.psa-peugeot-citroen.com>, Publications section
 - [108] W.J.M. Rankine *On the thermodynamic theory of waves of finite longitudinal disturbance* Phil. Trans. R. Soc., 160, 277-288.
 - [109] M. Rautenberg, A. Mobarak, M. Molababic *Influence of heat transfer between turbine and compressor on the performance of small turbochargers* JSME Paper 83-Tokyo-IGTC-73, International Gas Turbine Congress, 1986.
 - [110] M. Rautenberg, N. Kammer *On the thermodynamics of non adiabatic compression and expansion process in turbomachines* Proceedings of the 5th International Conference for Mechanical Power Engineering, Cairo, Egypt, 1984.
 - [111] Renault SAS website *Annual reports 2000-2009* <http://www.renault.com>, Finance publications section
 - [112] B. Riemann *Gesammelte mathematische werke* Second edition, (Teubner Leipzig).
 - [113] P.L. Roe *Approximate Riemann solvers, parameter vectors and difference schemes* J. Comp. Phys., 43, 357-372.
 - [114] E.L. Rubin, S.Z. Burstein *Difference methods for the inviscid and the viscous equations of a compressible gas* J. Comput. Phys., Vol. 2, pp. 178-196, 1967.
 - [115] R. Sinclair, T. Strauss, P. Schindler *Code Coupling, a New Approach to Enhance CFD Analysis of Engines* SAE paper 2000-01-0660, 2000.
 - [116] N.M. Salas *Modélisation des échanges thermiques dans une turbine radiale* Thèse de doctorat. Ecole Nationale Supérieure des Arts et Métiers, 2006.
 - [117] S.Shaaban, J.R.Seume *Analysis of Turbocharger non-adiabatic performance* ImechE Turbocharger and Turbocharging, 2006.
 - [118] S.Shaaban *Experimental investigation and extended simulation of turbocharger non-adiabatic performance* Doktor-Ingenieur Dissertation, Hannover Univsersity, 2004.
 - [119] W. Spannhake *Centrifugal pumps, turbines and propellers : basic theory and characterisitcs* Cambridge MA : the technology press, MIT, 1934.
 - [120] W.L. Stewart *Analysis of two-dimensional compressible flow loss characteristics downstream of turbomachine blade rows in terms of basic boundary layer characterisitcs* NACA TN-3515, 1955.
 - [121] A. Stodola *Steam and Gas Turbines, Vols I and II* McGraw-Hill, NewYork, 1927.
 - [122] V.Talon *Modélisation 0-1D des moteurs à Allumage Commandé'* Thèse de doctorat. Université d'Orléans, 2004
 - [123] V.Talon *Engine control model-based design with Achille library*, E-COSM - Rencontres Scientifiques de l'IFP - 2-4 Octobre 2006, pp. 35-51.
 - [124] G. Theotokatos, N.P. Kyrtatos *Diesel engine transient operation with turbocharger compressor surging* SAE paper 2001-01-1241.
 - [125] D. Thornhill, L. Hongyan, R. Fleck, G. Cunningham *Modelling od unsteady gas-dynamics flow in a pipe at its exit using CFD*. Proc. IMechE Vol. 220 Part D : J. Aut. Eng, pp. 1153-1162, 2006.
 - [126] B. van Leer *Towards the ultimate conservative difference scheme I : the quest of monotonicity*. Lecture notes in physics, 18, Springer Verlag, pp.163-168.
 - [127] B. van Leer *Towards the ultimate conservative difference scheme II : monotonicity and conservation combined in a second-roder scheme*. J. Comp. Phys., 14, 361-376.
 - [128] B. van Leer *Flux-vector splitting of the Euler equations*. Proceeding of the eighth international conference on numerical methods in fluid dynamics, 170, pp.507-512

- [129] M.J. van Nieuwstadt, I.V. Kolmanovsky, P.E. Moraal, A. Stephanopoulou, M. Jankovic *EGR VGT control schemes ; Experimental comparison for high-speed diesel engine* IEEE Contr. Syst. T., 8, 288-299.
- [130] J. von Neumann *Proposal and analysis of a numerical calculation of hydrodynamics shocks* National Defence and research comitte report.
- [131] J. von Neumann, R. Richtmeyer *A method for nor numerical calculation of hydrodynamics shocks* J. Appl. Phys., 21, 232-250.
- [132] Volkswagen AG website *Volkswagen AG annual reports 2000-2009* <http://www.volkswagenag.com>, Publications section
- [133] N. Watson *Turbocharging developments on vehicle diesel engiens* SAE paper 850315, 1985.
- [134] N. Watson, M.S. Janota *Turbocharging the internal combustion engine* MacMillan publishers, ISBN 0333242904, 1986.
- [135] F. Westin, J. Rosenqvist, H-E Angström *Heat Losses from Turbine of a Turbocharged SI-Engine- Measurements and Simulation* SAE paper 2004-01-0996, 2004.
- [136] F.J. Wiesner *A review of slip factors for centrifugal impellers* Trans. ASME, J. Eng Pwr 89, 558-572, 1967.
- [137] G. Winkler *Steady state and dynamic modeling on engine turbomachinery systems* Phd Thesis, University of Bath, 1977.
- [138] D.E. Winterbone *Advanced thermodynamics for engineers* Edward Arnold, London.
- [139] D.E. Winterbone, R. J. Pearson *Theory of Engine Manifold Design* SAE Int, 2000.
- [140] W.A. Woods, S.R. Khan *An experimental study of flow through poppet valves* Proc. I. MECH.E. Vol. 180, Pt.3N, p.32, 1965-1966.
- [141] W.A. Woods, S.R. Khan *Discharge from a cylinder through a poppet valve to an exhaust pipe* Proc. I. MECH.E. Vol. 182, Pt.3H, p.126, 1967-1968.
- [142] V. Yakhot, S.A. Orszag *Renormalization group analysis of turbulence- I Basic theory* J. Sci. Comp., 1(3), 1-51, 1986.
- [143] V. Yakhot, S.A. Orszag, S. Thangam, T.B. Gatski, C.G. Speziale *Development of turbulence models for shear flows by a double expansion technique* Phy. Fluids, A4(7), 1510-1520, 1992.
- [144] H. Zhang, S. Widener *An integrated engine cycle simulation model with species tracking in piping system* SAE paper 960077, 1996.

Guillaume MARTIN

Modélisation 0D - 1D de la Chaîne d'Air des MCI dédiée au Contrôle

La présente thèse porte sur la modélisation dédiée au contrôle des phénomènes physiques se produisant au travers des restrictions de la chaîne d'air du moteur. L'objectif est d'assurer la précision des modèles tout en limitant les temps de calcul associés. En effet, les modèles dédiés au contrôle nécessitent un temps de calcul court (proche du temps réel) afin d'être exploitables dans un processus de développement. En parallèle de cela, les normes concernant les rejets polluants sont de plus en plus drastiques, et nécessitent de prendre en compte finement les phénomènes physiques mis en jeu.

Dans une première partie, les équations des phénomènes physiques liés aux turbocompresseurs radiaux sont introduites dans une approche cartographique. Les équations fondamentales des turbomachines sont développées et utilisées afin de construire une méthode d'interpolation / extrapolation de champs turbocompresseur expérimentaux incomplets. Dans un second temps, les résultats d'essais réalisés lors de la thèse sont utilisés pour identifier les transferts thermiques au sein des turbocompresseurs. Un modèle dynamique d'échange thermique est ensuite construit. Le modèle final permet d'obtenir une cartographie complète des champs compresseur et turbine, tout en prenant en compte l'impact des transferts thermiques sur les performances des turbomachines.

La seconde partie porte sur la modélisation des restrictions (soupapes, changements de section...) rencontrées sur les MCI. Une méthode pour la résolution quasistatique des équations Euler 1D complètes (masse, énergie, moment) est proposée afin de construire les cartographies associées aux restrictions considérées, sans introduire de coefficient de correction expérimental. Ces cartographies sont utilisables en tant que modèles moyens ou utilisées comme conditions limites de codes aérodynamiques 1D. En cas de couplage avec un code 1D, une méthode de correction d'entropie basée sur un algorithme de linéarisation est proposée afin de réduire le temps de convergence aux conditions limites du domaine de calcul. Finalement, les développements sont validés expérimentalement en écoulements stabilisés et transitoires.

Mots clés : Moteur, Aérodynamique, Modèle, Turbocompresseur, Soupape.

0D - 1D Modeling of the Airpath of IC Engines for Control Purposes

The present thesis will focus on the modeling of the airpath components for the development of the control laws. The goal is to ensure the accuracy of the models while liming the associated calculation time. Indeed, models associated to the development of control laws must ensure law calculation time in order to be compliant with automotive development processes. In the same time, pollutant emissions regulations are increasingly restrictive, which has a direct impact on the required accuracy level of the models.

In a first part, the physical equations of the radial turbocharger are introduced in a datemap-based approach. The fundamental equations of turbomachines are developed and processed in order to build an interpolation / extrapolation method for incomplete turbocharger datamaps. Then, measurements from tests realized during the thesis are analyzed in order to identify the heat exchanges occurring within turbochargers. A dynamical heat exchange model is then built. The final turbocharger model allows to build complete turbocharger datamaps, while taking into account the effect of thermal exchanges.

The second part focuses on the modeling of ICE flow restrictions (valves, change of pipe area...). A method is proposed in order to solve the quasistatic formulation of the Euler 1D equation (mass, energy, momentum). This allows to build datamaps associated to the studied components, without having to introduce an experimental corrective coefficient. These datamaps can be used as mean-value models or as boundary conditions of a 1D numerical scheme. In case of coupling with a 1D scheme, an entropy correction scheme based on local linearization has been developed in order to improve the convergence speed at the boundary condition. Finally, proposed developments are validated experimentally under stabilized and transient flow conditions.

Keywords : Engine, Aerodynamics, Model, Turbocharger, Valve.



Laboratoire PRISME – Université d'Orléans
8, rue Leonard de Vinci
45072 Orléans Cedex 2
FRANCE

